



MagAO-X

Preliminary Design Review

	MagAO-X Preliminary Design	Doc #:	MagAOX-001
		Date:	2017-Apr-23
		Status:	Rev. 0.0

Table of Contents

1 Introduction and Overview

2 Optical and Mechanical Design

- 2.1 Overall Design**
- 2.2 WFS Design**
- 2.3 Alignment Plan**
- 2.4 Shipping Plan**
- 2.5 MES Specification and Status**
- 2.6 MEMS DM Environment and Safety**

3 Electronics, Computers, and Software

- 3.1 Electronics Design**
- 3.2 Computers and Data Management**
- 3.3 Software Design**

4 AO Control and Simulations

- 4.1 AO Control and Simulations**
- 4.2 Low-Order and Focal-Plane Wavefront Sensing and Control**

5 Optical Performance

- 5.1 Optics Specifications**
- 5.2 vAPP Coronagraph Design**
- 5.3 Fresnel Propagation Analysis**
- 5.4 System Throughput**

6 Management and Budget

Appendix

A Telescope Interfaces

- A.1 Optical**
- A.2 Mechanical**
- A.3 Electrical**
- A.4 Cooling**
- A.5 Software**

Note: Each section is individually paginated.



1.0 Overview and Science Justification

Jared Males, Laird Close and the MagAO-X Team

1 Introduction

AO systems are now in routine use at many telescopes in the world; however, nearly all work only in the infrared (IR, $\lambda > 1 \mu\text{m}$) due to the challenges of working at shorter wavelengths. The Magellan AO (MagAO) system was the first to routinely produce visible-AO science on a large aperture telescope. In Figure 1, we show an example of the power of large diameter visible-AO. Other large telescopes with visible AO systems include the 5 m at Palomar (Dekany et al., 2013) and ESO’s 8 m VLT with the ZIMPOL camera behind the Spectro-Polarimetric High-contrast Exoplanet REsearch (SPHERE) (Roelfsema et al., 2014).

MagAO-X is a *new* visible-to-near-IR “extreme” AO (ExAO) system. When completed, MagAO-X will consist of: (1) 2048 high-order actuators controlled at (up to) 3.7 kHz; (2) cutting-edge coronagraphs to block a star’s light; and (3) a suite of focal plane instruments including imagers and spectrographs enabling high-contrast and high-resolution science.

MagAO-X will deliver high Strehls ($\gtrsim 70\%$ at $\text{H}\alpha$), high resolutions (14–30 mas), and high contrasts ($\lesssim 10^{-4}$) from ~ 1 to $10 \lambda/D$. Among many compelling science cases, MagAO-X will revolutionize our understanding of the earliest stages of planet formation, enable high spectral-resolution imaging of stellar surfaces, and could take the first images of an exoplanet in reflected light.

1.1 Existing MagAO and 2000 Hz: Our current MagAO system combines a second-generation 585 actuator adaptive secondary mirror (ASM) and a cutting-edge pyramid wavefront sensor (PWFS). MagAO is mounted on the 6.5 m Magellan Clay telescope at Las Campanas Observatory (LCO), Chile. MagAO has two science cameras, namely the Clio IR camera (1–5 μm) (Morzinski et al., 2015) and VisAO (0.6–1 μm). The combination of fine spatial sampling (300 to 400 modes), up to 2 kHz speed, the excellent site, and the ASM and PWFS has enabled—for the first time—filled-aperture, diffraction-limited imaging at visible wavelengths on a large telescope: at wavelengths as blue as r' ($\lambda_0 = 624\text{nm}$, Fig. 1).

We have recently completed an upgrade of the existing MagAO system, improving the loop speed from 1000 Hz to 2000 Hz. In 0.6” to 0.7” seeing (somewhat worse than median at LCO), we measured the improvement in z' (0.9 μm) image quality. The results are shown in Figure 2. These results show the benefits of increased AO loop speed.

1.2 Introduction to MagAO-X: MagAO-X will be an ExAO system optimized for working in the optical ($\lambda < 1 \mu\text{m}$) while (eventually) providing imaging and spectroscopic capabilities out to H band (1.6 μm). In its final form, it will consist of a 2000 actuator Boston Micromachines Corp. (BMC) deformable mirror (DM) controlled by a PyWFS operating at up to 3.63 kHz. Diffracted starlight will be suppressed using coronagraphs, and using techniques such as Low-order and focal-plane wavefront sensing (LOWFS and FPWFS) in real-time

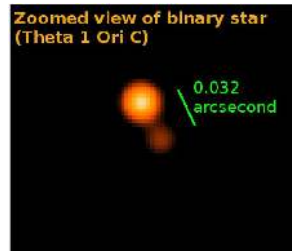


Figure 1: MagAO/VisAO r' image of the 32 mas binary θ^1 Ori C (Close et al., 2013).

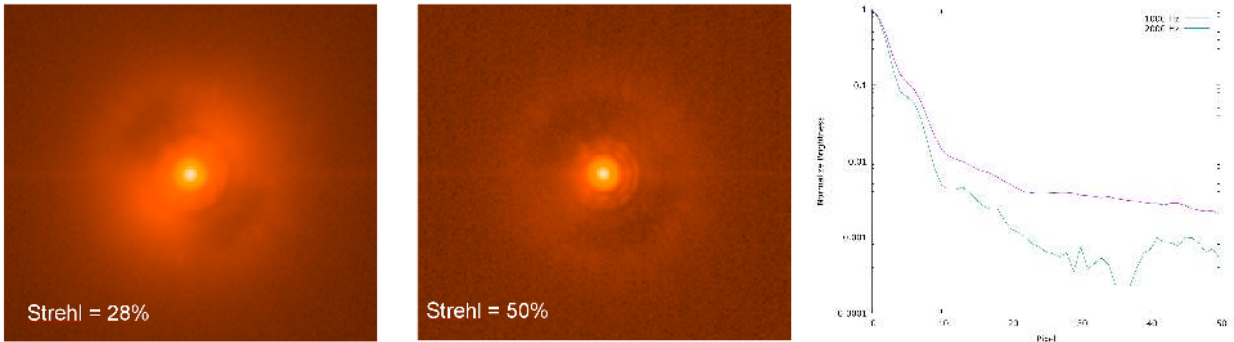


Figure 2: The benefits of speed. Here we show the improvement realized when speeding the existing MagAO system up from 1 kHz to 2 kHz. The PSF images are for z' ($0.9 \mu\text{m}$) in slightly worse than median conditions at LCO ($0.7''$ seeing) on a cloudy night. The improvement in Strehl is obvious. The cuts plotted at right show the improvement in the full-width at half maximum and dark hole contrast (even without a coronagraph).

the impact of static and non-common path (NCP) aberrations will be minimized. Finally, we make use of post-processing techniques such as simultaneous differential imaging and angular differential imaging to achieve the highest possible contrasts.

We have organized MagAO-X into 3 phases. This approach will allow us to manage the complexity and risk more effectively than possible if the entire instrument were delivered at once. It also more efficiently uses telescope allocations during commissioning, as it provides time to analyze critical on-sky results and re-optimize the instrument between runs. Each of the three phases will be scientifically productive, ensuring that the MagAO-X project will have a **major science impact early on** while we build to our ultimate scientific goals.

NOTE: only Phase I and Phase II are the subjects of this PDR. Phase III is described here for context, but we are deferring preliminary design of the final phase to a future effort.

Briefly, the three phases are:

Phase I: A new visible-wavelength vector apodizing phase plate (vAPP) coronagraph, optimized for $H\alpha$, will be introduced. We will exploit the vAPP leakage term (explained in detail below) to perform LOWFS. This phase will employ the main optical train of MagAO-X, but use the *existing* MagAO system for high-order wavefront control without using the new MEMS DM. While this will provide only moderate Strehl ratio to the coronagraphic system, it will still be an advance over existing MagAO+VisAO, which has no diffraction-rejecting coronagraphic capabilities. The LOWFS will employ offloading to the Pyramid via slope offsets, a standard technique for the LBT/MagAO architecture. Importantly, this phase will provide an on-sky test of the optical train, and test the vAPP LOWFS on-sky. We will also perform a fit and alignment check of the f/11 feed using our on-board woofer (in preparation for Phase II).

Science focal plane instrumentation will initially include two electron multiplying CCDs (EMCCD) for $\lambda \lesssim 1 \mu\text{m}$, with $J-H$ bands ($1.2-1.6 \mu\text{m}$) being sensed by our existing Clio camera. This capability will allow initial observations in the MaXProtoPlanets survey (described below) on the brightest targets where existing MagAO achieves moderately good correction at $H\alpha$.

By getting the basic instrument on-sky at the telescope as early as possible, we will retire risk associated with the optics design and layout, the coronagraph architecture, the LOWFS strategy (crucial for rejecting instrumental



quasi-static speckles at small separations), and our shipping and handling plan. This phase will be scientifically productive, kicking off one of our major science projects.

Phase II: The main new goal of the second phase is to bring the new high-order (HO) wavefront control system on-line. This will consist of a new woofer (an Alpa DM97) and a new tweeter (a Boston Micromachines 2k), along with a new PWFS using an OCAM-2K EMCCD camera. This new hardware will be integrated with the coronagraph, which will now be fed with wavefronts having Strehl ratios of $\sim 70\%$ at $H\alpha$ on brighter guide stars. Significantly, this will allow high contrast imaging on guide stars as faint as 12th mag. This then enables the MaXProtoPlanets survey, a census of low-mass accreting proto-planets around all of the T Tauri and Herbig Ae/Be stars accessible from LCO.

The initial development and testing for Phase II will be conducted in the ExAO and Coronagraphy lab on a separate optical bench. This will enable Phase II to start in parallel with the later stages of Phase I. Once Phase I is complete and the instrument has been shipped back to Steward, the new hardware will be integrated on the MagAO-X bench.

It is during this phase of the project that we will begin the MaXProtoPlanets survey in earnest.

Phase III: In the final phase of the project we will introduce a new coronagraph and spectrographic capabilities. The phase induced amplitude apodization complex-mask coronagraph (PIAACMC) and lyot-based LOWFS will be integrated in the system. The PIAACMC is capable of achieving a high throughput design (say 78% off-axis) small IWA $< 1\lambda/D$, over a broad 20% bandpass on a complex aperture (including spiders, etc.) Here we will also employ an energy-resolving microwave kinetic inductance detector (MKID) array, which provides integral field spectroscopy (IFS) from 0.7–1.4 μm . An important goal of this instrument is to use the MKIDS as FPWFS to achieve the highest possible speckle suppression. Finally, “RHEA@MagAO-X” a 9-element, visible light, single-mode fiber, $R \sim 60,000$ spectrograph will be used for high spatial and spectral resolution science behind MagAO-X. As noted above, the preliminary design of Phase III is not being presented here.

2 Science Justification

For the purposes of this review, we are focusing on one main science case: a survey of nearby T Tauri and Herbig Ae/Be stars for newly formed accreting planets in $H\alpha$. We describe this science case in the following section and present the high level performance requirements we derive from it.

2.1 A Survey of the Low Mass Distribution of Young Gas Giant Planets: We now know that wide (> 30 AU) massive ($> 4 M_{Jup}$) giant planets (EGPs) are rare (e.g. Biller et al., 2013). Yet there are hints of a major population of lower mass ($0.5\text{--}2 M_{Jup}$) EGPs closer in, from $\sim 5\text{--}20$ AU (Sallum et al., 2015). Such EGPs may well determine the delivery of volatiles to potentially habitable inner terrestrial planets (Raymond et al., 2004; Matsumura et al., 2015). A key goal of the decadal Astro2010 survey is the *characterization of habitable planets*, as well as understanding planet formation. MagAO-X will image protoplanets in $H\alpha$ (for H recombination $H\alpha$ is $\sim 1760\%$ stronger than the best near-IR line $\text{Pa}\beta$) in the luminous accretion phase of formation to address these goals (not possible with GPI’s IR IFS).

2.1.1 Proof-of-concept – Imaging LkCa 15 b at $H\alpha$: We used MagAO’s simultaneous differential imaging (SDI) mode (Close et al., 2014) to discover $H\alpha$ from a forming protoplanet (LkCa 15 b) for the first time (Sallum et al., 2015) (see Fig. 3), detecting an accretion stream shock from a 90 mas (15 AU) protoplanet. Dynamical stability places the mass of LkCa 15 b at $2^{+3}_{-1.5} M_{Jup}$. Correcting for extinction we found an accretion rate of $\dot{M} = 1.16 \times 10^{-9} M_\odot/\text{yr}$ (Sallum et al., 2015). Observed $H\alpha$ rate was $\sim 0.5e/s$ at the peak pixel at Strehl $\sim 5\%$.

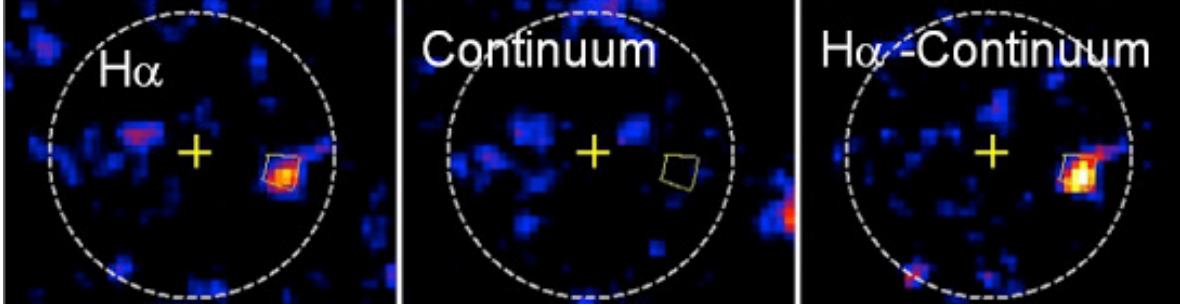


Figure 3: LkCa 15 b, a protoplanet imaged with SDI at $H\alpha$. Sallum et al. 2015.

2.1.2 MagAO-X $H\alpha$ Protoplanet Survey (MaXProtoPlanetS): While LkCa 15 (145 pc; 1–2 Myr) is fairly faint ($I \sim 11$ mag) there are many brighter, closer similarly young accreting targets. In the η Cha (Mamajek et al., 1999), ϵ Cha (Murphy et al., 2013), ρ Oph (Luhman & Rieke, 1999), TW Hya (Mamajek, 2005), and Upper Sco (de Zeeuw et al., 1999) clusters, which are all <5 – 10 Myr old within $\lesssim 150$ pc, there are **exactly 160 individually vetted accreting targets with $I \leq 10$ mag**. These are good guide stars for Phase I of MagAO-X. Around all these target stars a planet like LkCa 15 b would be at ~ 100 – 200 mas separations (~ 15 AU), but instead of $\Delta H\alpha = 5.3$ mag it could (conservatively) be 5 mag fainter still — due to extra dust extinction (no disk gaps like LkCa 15), and/or lower mass of the planet. The worst case $\Delta H\alpha \sim 11$ mag contrast is too high for the *existing* MagAO but will be achievable with MagAO-X. Utilizing MagAO-X’s SDI+vAPP mode, we will observe the $H\alpha/H\beta$ line ratio that can be compared to Case-B recombination theory (Hummer & Storey, 1987); hence, the line of sight extinction (A_R) can be estimated (Close et al., 1997). As a result, the true $H\alpha$ line strength can be measured and protoplanet masses estimated (Close et al., 2014), see Fig. 4. An $I=10$ mag star in median conditions with a $0.5 M_{Jup}$ EGP and 2.5 mag greater A_R and the same \dot{M} as LkCa 15b ($\Delta H\alpha = 10.3$ mag) will have peak pixel S/N ~ 11 in 2 hrs with our KLIP (Soummer et al., 2012) pipeline (accounting for EMCCD excess noise, MagAO-X+vAPP throughput, Strehl and contrast).

There are six (2 of spectral type A and 4K spectral types) $I < 10$ mag targets in the η Cha cluster (50 pc, ~ 10 Myr) (Mamajek et al., 1999), 15 $I < 10$ targets (1B, 4A, 2G, and 8K SpT) in the ϵ Cha cluster (100 pc, 3 – –5 Myr) (Murphy et al., 2013), two $I < 10$ targets (1B and 1A SpT) in the ρ Oph cluster (140 pc, 1 Myr) (Luhman & Rieke, 1999), 17 $I < 10$ targets (2A, 3K, and 12M SpT) in the TW Hya cluster (50 pc, ~ 10 Myr) (Mamajek, 2005), and finally an additional 120 $I < 10$ targets (49B, 34A, 22F, 9G, 4K, and 2M SpT) in the Upper Sco cluster (150 pc, 5–10 Myr) (de Zeeuw et al., 1999). **So there are a total of 160 < 10 Myr old accreting D < 150 pc targets all with $I < 10$ mag for the MaXProtoPlanets survey—all bright enough for good AO correction.** There are also many slightly fainter targets $I < 12$ mag that will be dis.

Extrapolating from our initial (3/10 = 30%) success rate for the young star GAPplanetS $H\alpha$ survey having accreting objects (Follette et al., 2016) the 160 stars yield ~ 48 new protoplanet systems using just 5 nights per semester.

In Phase II we can achieve the same contrasts on fainter $I=12$ stars which yields 33 more (ϵ Cha, ρ Oph) targets, yielding ~ 11 more detections —raising the total to ~ 59 systems. **MaXProtoPlanetS’s $\sim 59 \times$ larger sample of detected protoplanet systems will define the population of low-mass outer EGPs, and will help reveal where/how gas planets actually form and grow.** Integrating over the secure members of the above youngest

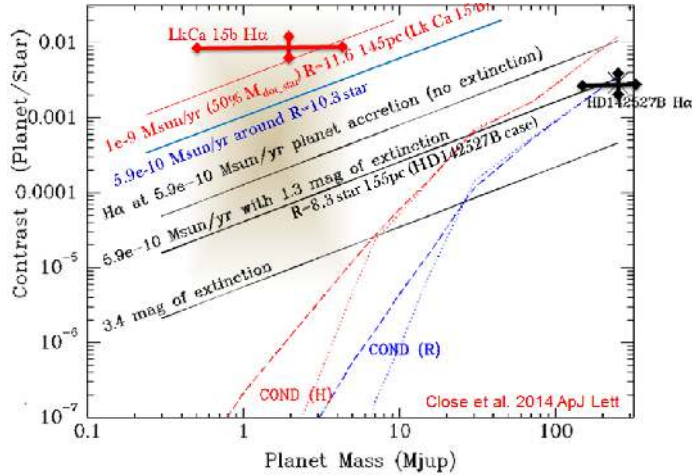


Figure 4: Relation between the mass of the $H\alpha$ planet to the observed contrast (as a function of M_{Rstar} , A_R , & \dot{M} of the planet).

clusters (ϵ Cha, ρ Oph) yields exactly 16 and 17 (respectively) more 1–3 Myr targets from $10 < I < 12$ mag. These 32 targets should yield another ~ 11 discoveries, raising the total to ~ 60 . **This would increase the number of known protoplanets systems by $\sim 60\times$, define the population of low-mass outer EGPs, and for the very first time reveal where gas planets actually form.**

2.1.3 High Level Performance Requirements: From the MaXProtoPlanets survey we derive the high level performance requirements for MagAO-X. These are present in Table 1. The main requirement is to achieve the contrast at the given separation. This places requirements on WFC at specific spatial frequencies. Strehl ratio, which is a global image quality metric, is a “soft” requirement – we need high image quality but do not need to achieve an exact Strehl ratio so long as the contrast is achieved.

Table 1: The high level performance requirements derived from the MaXProtoPlanets $H\alpha$ SDI survey.

Targets			Performance		
I mag	d [pc]	Numb.	Sep [mas]	$\Delta H\alpha$ mag	Strehl ¹ [%]
5	225	6	75	12.0	70
8	150	25	100	9.0	50
10	150	129	100	7.0	30
12	150	44 ²	100	5.0	20

¹ At $H\alpha$, $\lambda = 656$ nm.

² not complete, there are likely more

3 Other Science Cases

Here we present a short summary of several additional science cases. These are generally spanned by the parameters of the $H\alpha$ survey in terms of guide star brightness and separations, and are less-demanding, and so



we do not specifically derive requirements for these. Rather, they are presented to give an idea of the breadth of use-cases for this new instrument.

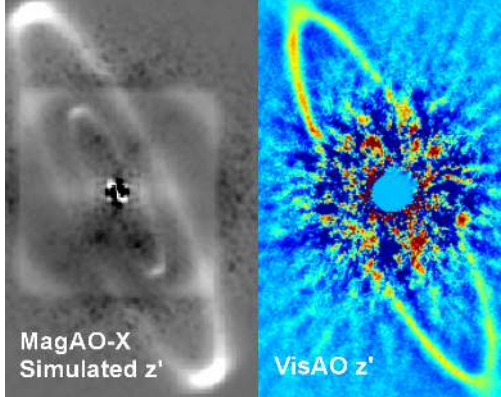


Figure 5: The HR 4796A disk. Left: simulated MagAO-X image at z' ($0.9 \mu\text{m}$) (includes hypothetical inner disk suggested by Rodigas et al. (2015)), just 5 seconds of data with simple PSF subtraction. Right: actual MagAO+VisAO image (Rodigas et al., 2015). MagAO-X will significantly enhance our ability to probe the regions closest to the star.

3.1 Circumstellar Disks: Disk science is a challenging application of AO, with low surface brightness and characteristics similar to the uncorrected seeing halo, so high-Strehl high-contrast ExAO is critical. MagAO-X will push the two frontiers in circumstellar disk science. The first is detailed imaging of geometry, particularly in the 5-50 AU region analogous to the outer part of the solar system. Most disks sit at 50-150 pc, so reaching radii comparable to the giant planet region requires imaging at 50-120 mas. Existing systems push in to at best ~ 150 mas. For some disks, an inner working angle of ~ 100 mas will push to the exozodiacal light region for the first time. For example, in the well-known HR 4796A disk, SED fits show that the $8\text{-}20 \mu\text{m}$ flux cannot be fully explained by the outer, ~ 100 K, ring, suggesting a ring at 3-7 AU (Wahhaj et al., 2005). MagAO-X has the potential to image this inner ring. The second frontier is multiwavelength study of disks to derive the chemical make-up and dynamical state (Rodigas et al., 2015; Stark et al., 2014). This requires a large wavelength grasp from visible through near-infrared so MagAO-X's ability to image at $\sim 0.45 \mu\text{m}$ complements existing systems.

3.2 Fundamental Properties of Young Solar-System-like EGPs: Dedicated exoplanet-imagers GPI and SPHERE are now operational, and GPI has discovered the first planet of this new era: 51 Eri b is a 600-K $\sim 2 M_{\text{Jup}}$ exoplanet imaged 13 AU from its 20-Myr-old, 30-pc-away F-type host star (Macintosh et al., 2015). This planet is different from other exoplanets (whether imaged or analyzed by transit spectroscopy): its atmosphere is the closest analog yet to solar system atmospheres because of its Saturn-scale orbit, Jupiter-scale mass, and cool temperature such that CH₄ was detected in the GPI spectrum.

We have conducted a prototype experiment with existing MagAO using the exoplanet β Pic b, which can be imaged with the current VisAO due to its brightness (youth and mass) and its 300-400 mas separation. Fig. 6 shows images of β Pic b taken with the MagAO+VisAO camera (Males et al., 2014). Fig. 7 demonstrates using such measurements to empirically measure the fundamental properties of this solar-system-scale exoplanet—the luminosity of β Pic b (Morzinski et al., 2015). **MagAO-X will extend these observations to shorter wavelengths, and to smaller mass, smaller separation planets such as 51 Eri b.** MagAO-X will also enable characterization of such planets with the DARKNESS and RHEA@MagAO-X spectrographs.

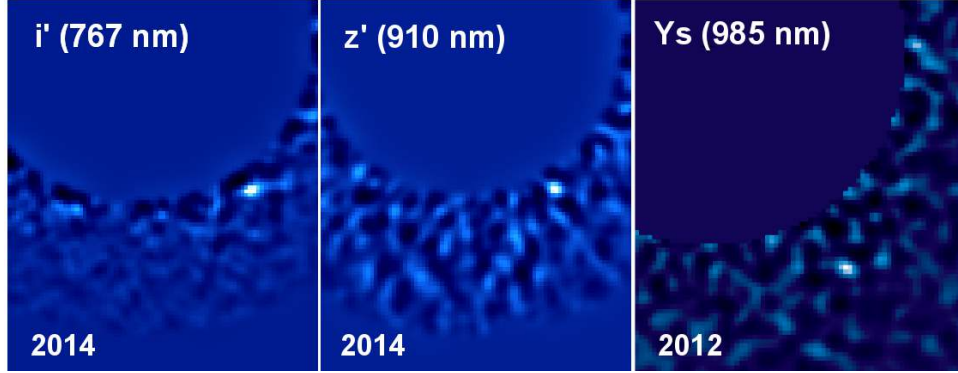


Figure 6: The exoplanet β Pic b imaged with VisAO, in i' & z' (Males et al, in prep) and Y_s (separation 470 mas, $\Delta Y_S = 11.97$ mag, Males et al., 2014). MagAO-X will extend these observations to shorter wavelengths, and fainter, smaller-separation planets such as 51 Eri b.

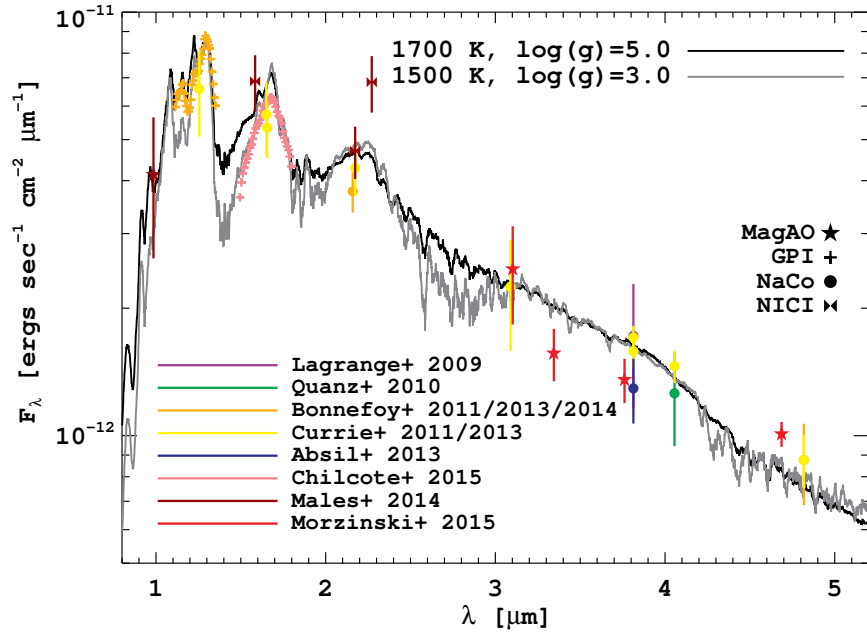


Figure 7: SED of young super-Jupiter β Pic b, with which we measured its bolometric luminosity, empirically for the first time (Morzinski et al., 2015). Plotted black and gray lines are degenerate BT Settl models with identical fits but different temperatures and gravities. MagAO-X will measure the Wien's slope in the visible to give the temperature for this and other young EGPs.

3.3 Resolved Stellar Photospheres: The 3x3 single-mode fiber-fed IFS, RHEA@MagAO-X, with $R \sim 60,000$ spectral resolution, will be provided by collaborator Mike Ireland. The combination of the ExAO resolution and contrast with high spectral resolution enables many exciting science cases. For instance: the largest resolvable non-Mira stars accessible from MagAO include Betelgeuse (~ 50 mas), Antares (~ 40 mas), Arcturus (~ 21 mas), Aldebaran (~ 20 mas) and α Boo (~ 19 mas). These stars lose mass through a complex process in an interplay between a hot ($\sim 10,000$ K) corona and a cool (~ 2000 K), slow (~ 10 km/s) molecular wind. These states can



not co-exist so asymmetries of some kind are expected. Resolving the photosphere in lines and molecular bands enables the multi-dimensional structure of these regions to be imaged. Upwelling and downwelling velocities on the surface are of order a few km/s, separable at sufficient resolution. A single image of a stellar photosphere would be the *first ever direct measurement of convection in a star other than the Sun*.

3.4 Asteroids: MagAO-X will have resolutions of 14–21 mas in *g-r* bands, which correspond to \sim 20–30 km on a main-belt asteroid (MBA). On a typical night more than 80 MBAs brighter than I=13 (implying \gtrsim 50 mas) will be resolvable by MagAO-X. This will provide true dimensions, avoiding degeneracies in light-curve analysis. MagAO-X will enable sensitive searches for and orbit determination of MBA satellites. In combination, these directly measure density and hence estimate composition (Britt et al., 2002). This will directly inform the theories of terrestrial planet formation (Mordasini et al., 2011).

4 Preliminary Design Review

The MagAO-X team has completed our preliminary designs of the following items:

- The optical design of Phase I and II
- Optical component specifications
- The mechanical design of Phase I and II
- The electronics design
- The shipping and handling plan
- The real-time and control software design
- The data management plan
- Wavefront control plan (as described with simulations)
- Management plan

Each of these areas are addressed in detail in the following sections, with specific requirements the designs are intended to meet.

References

- Biller, B. A., Liu, M. C., Wahhaj, Z., et al. 2013, ApJ, 777, 160
- Britt, D. T., Yeomans, D., Housen, K., & Consolmagno, G. 2002, Asteroids III, 485
- Close, L. M., Roddier, F., Hora, J. L., et al. 1997, ApJ, 489, 210
- Close, L. M., Males, J. R., Morzinski, K., et al. 2013, ApJ, 774, 94
- Close, L. M., Follette, K. B., Males, J. R., et al. 2014, ApJL, 781, L30
- de Zeeuw, P. T., Hoogerwerf, R., de Bruijne, J. H. J., Brown, A. G. A., & Blaauw, A. 1999, AJ, 117, 354



**MagAO-X Preliminary Design
1.0 Overview and Science Justification**

Doc #: MagAOX-001
Date: 2017-04-24
Status: Rev. 0.0
Page: 9 of 9

Dekany, R., Roberts, J., Burruss, R., et al. 2013, ApJ, 776, 130

Follette, K. B., Miller Close, L., Males, J., et al. 2016, in American Astronomical Society Meeting Abstracts, Vol. 227, American Astronomical Society Meeting Abstracts, #106.05

Hummer, D. G., & Storey, P. J. 1987, MNRAS, 224, 801

Luhman, K. L., & Rieke, G. H. 1999, ApJ, 525, 440

Macintosh, B., Graham, J. R., Barman, T., et al. 2015, Science, 350, 64

Males, J. R., Close, L. M., Morzinski, K. M., et al. 2014, ApJ, 786, 32

Mamajek, E. E. 2005, ApJ, 634, 1385

Mamajek, E. E., Lawson, W. A., & Feigelson, E. D. 1999, ApJL, 516, L77

Matsumura, S., Brasser, R., & Ida, S. 2015, ArXiv e-prints, 1512.08182

Mordasini, C., Alibert, Y., Klahr, H., & Benz, W. 2011, in European Physical Journal Web of Conferences, Vol. 11, European Physical Journal Web of Conferences, 04001

Morzinski, K. M., Males, J. R., Skemer, A. J., et al. 2015, ApJ, 815, 108

Murphy, S. J., Lawson, W. A., & Bessell, M. S. 2013, MNRAS, 435, 1325

Raymond, S. N., Quinn, T., & Lunine, J. I. 2004, Icarus, 168, 1

Rodigas, T. J., Stark, C. C., Weinberger, A., et al. 2015, ApJ, 798, 96

Roelfsema, R., Bazzon, A., Schmid, H. M., et al. 2014, Proc. SPIE, 9147, 91473W

Sallum, S., Follette, K. B., Eisner, J. A., et al. 2015, Nature, 527, 342

Soummer, R., Pueyo, L., & Larkin, J. 2012, ApJL, 755, L28

Stark, C. C., Schneider, G., Weinberger, A. J., et al. 2014, ApJ, 789, 58

Wahhaj, Z., Koerner, D. W., Backman, D. E., et al. 2005, ApJ, 618, 385



MagAO-X PDR

2.1 Optical Mechanical Design Overview

Laird Close & Jared Males
University of Arizona
4/18/2017

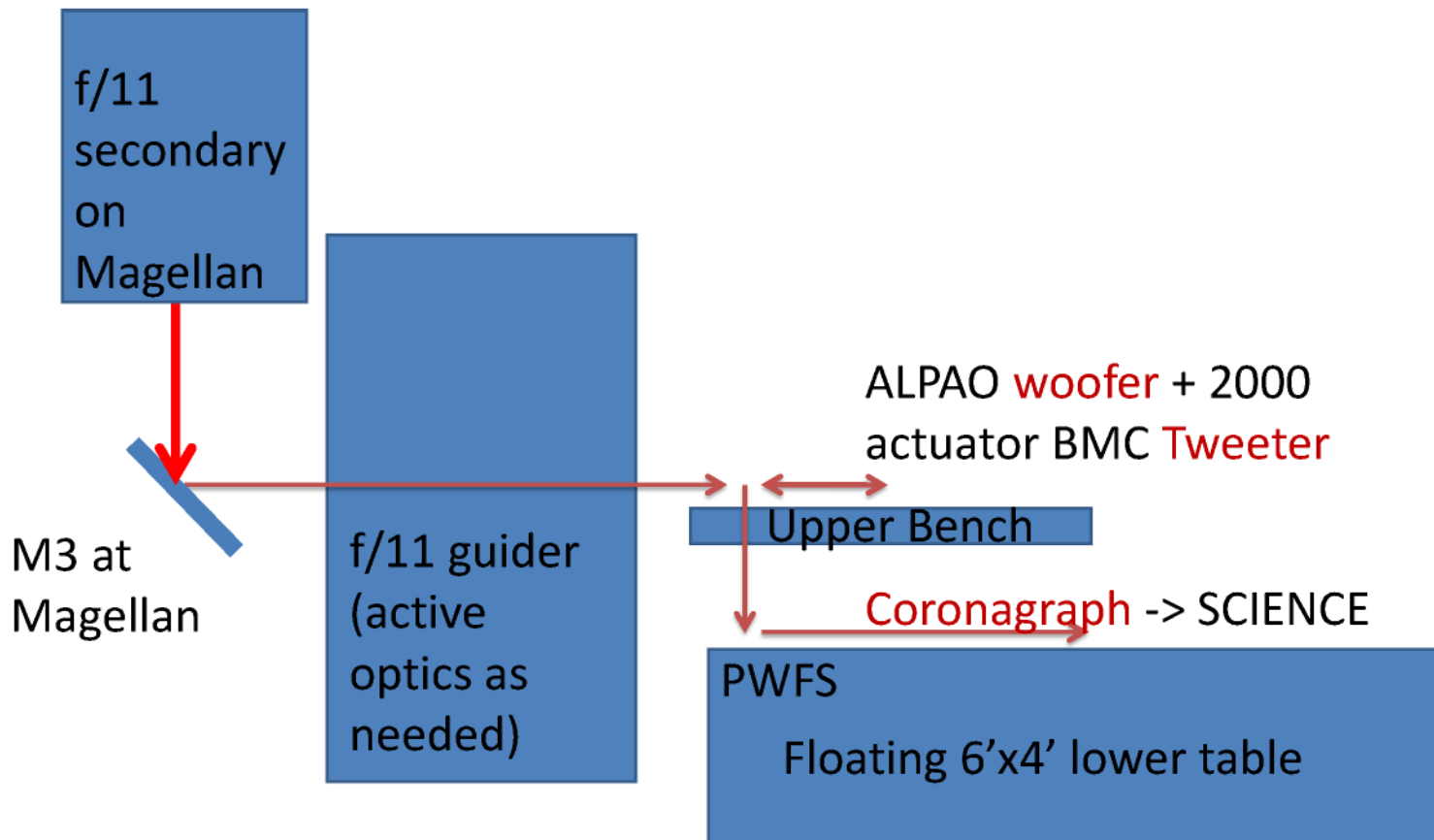
MagAO-X OptoMech Design Philosophy

The MagAO-X PDR design is based on our experiences with 5 years of high-contrast AO at Magellan and lessons learned from the current generation of ExAO systems (like SECxAO)

1. **MINIMIZE FLEXURE and NCP VIBRATIONS:** The design almost eliminates issues with NCP vibrations through use of a [stiff floating optical table](#). It is gravity invariant. Our [LOWFS should track and mitigate any NCP vibrations that are missed by the PWFS](#).
2. **MINIMIZE NCP WAVEFRONT ERRORS:** The design limits NCP errors by building the PWFS feed deep into the heart of the instrument. Also post-coronagraphic errors can be sensed with our flexible LOWFS concept which is common path with almost all the powered optics.
3. **MINIMIZE OPTICAL AND CHROMATIC ERRORS:** All reflective (silver) optics design with very tight polishing specs. Use an advanced triplet ADC design without on-axis ghosts.
4. **MINIMIZE MISALIGNMENT ERRORS:** Use all 2inch (or smaller) [stainless steel mounts on Stainless table](#) to minimize temperature effects (which are small at Magellan). Automatic pupil sensing and correction. Automatic re-alignment of masks and wheels.
5. **MINIMIZE DUST CONTAMINATION:** Use [completely sealed instrument](#) that doesn't need to be opened during regular observations
6. **MINIMIZE INSTALLATION AND CALIBRATION COMPLEXITY:** Must be able to work with either [the f/11 facility secondary](#) or the MagAO f/16 ASM. Must be able to have internal interaction matrices that can be made in daytime at scope (internal, deployable fiber source).
7. **ALLOW DIFFERENT CORONAGRAPHS AND LOWFSs TO BE TESTED:** we have [2 focal plane wheels](#) and [2 pupil plane wheels](#) allowing a wide range of coronagraphs to be remotely deployed (From Simple vAPPs to PIAACMCs systems).
8. **ALLOW DIFFERENT SCIENCE CAMERAS AND SPECTROGRAPHS:** while the initial science camera is a pair of EMCCD SDI cameras there is room (post coronagraph) to deploy fiber fed spectrographs like RHEA or MKIDs cameras.
9. **SHIPPING SHOULD BE ROUTINE:** The instrument must be safe and easy to pack and unpack.



Conceptual design of f/11 MagAO-X optics with Coronagraph



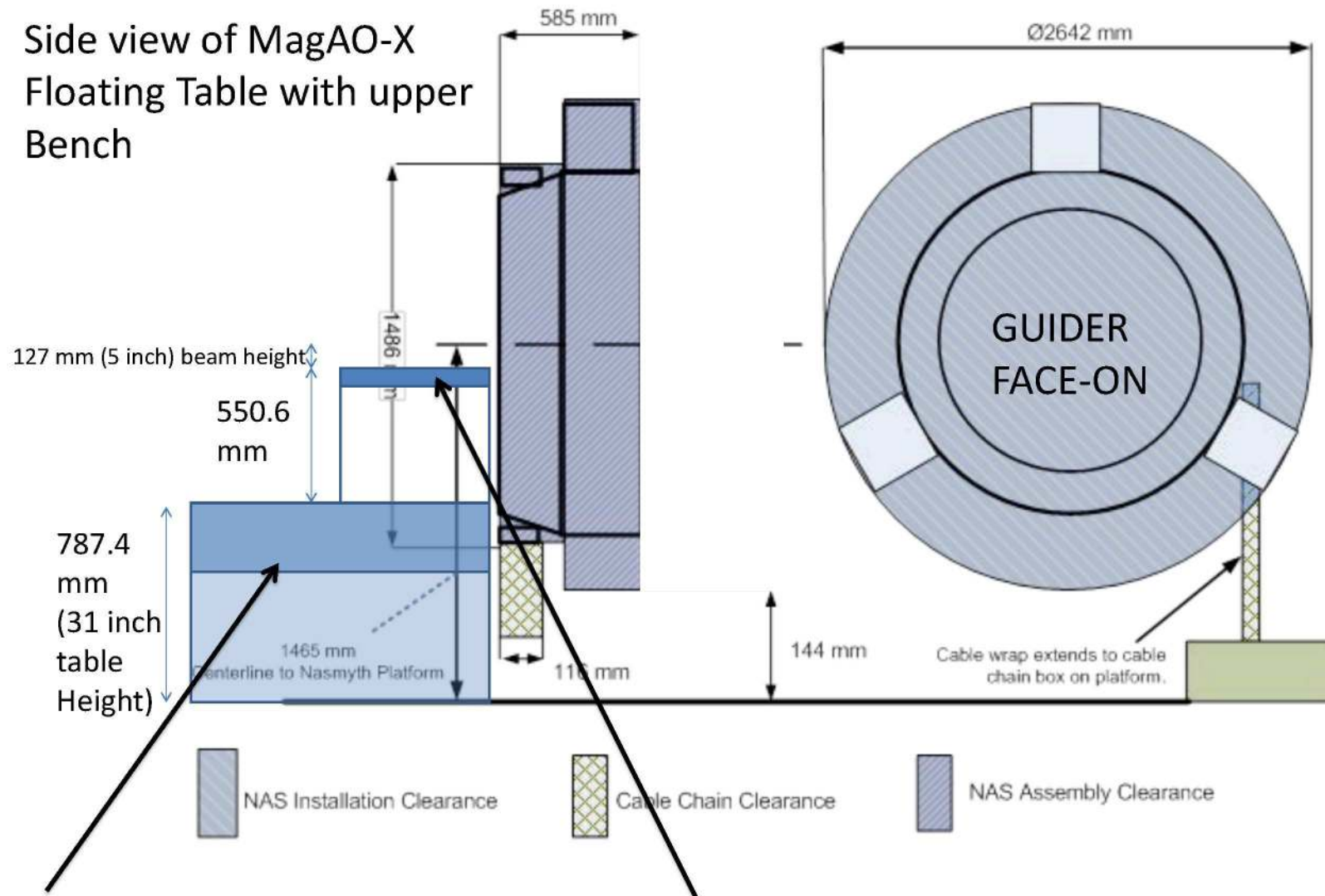
MagAO-X Summary:

~80% Strehl at 0.65 microns + PIAACMC coronagraph with **Contrasts of 10^{-5} -@50 mas and 10^{-6} @150 mas** on a 5th mag star in median conditions. Also can feed MKID or RHEA IFS R=60,000 (PI Ireland)



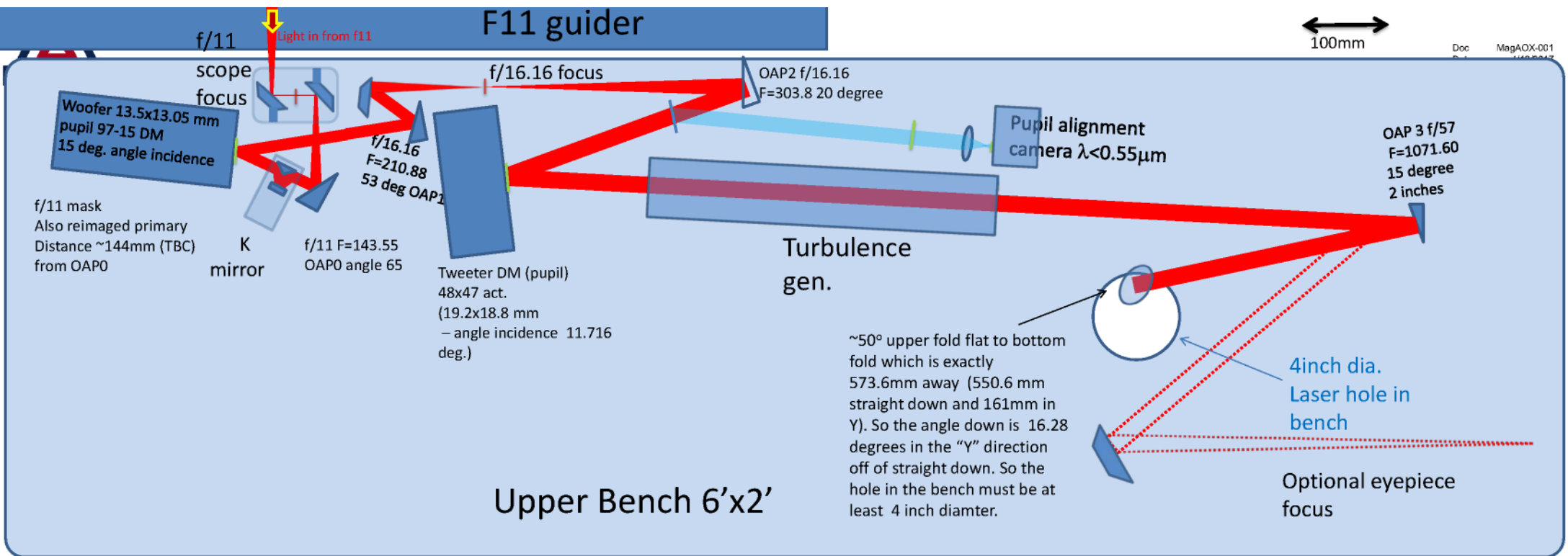
9.6mm air gap between table and f/11 guider

Side view of MagAO-X
Floating Table with upper
Bench



Lower 6'x4'x1' TMC research
grade optical top

Upper 2'x6'x4" TMC research grade optical
breadboard (aligned with Table)

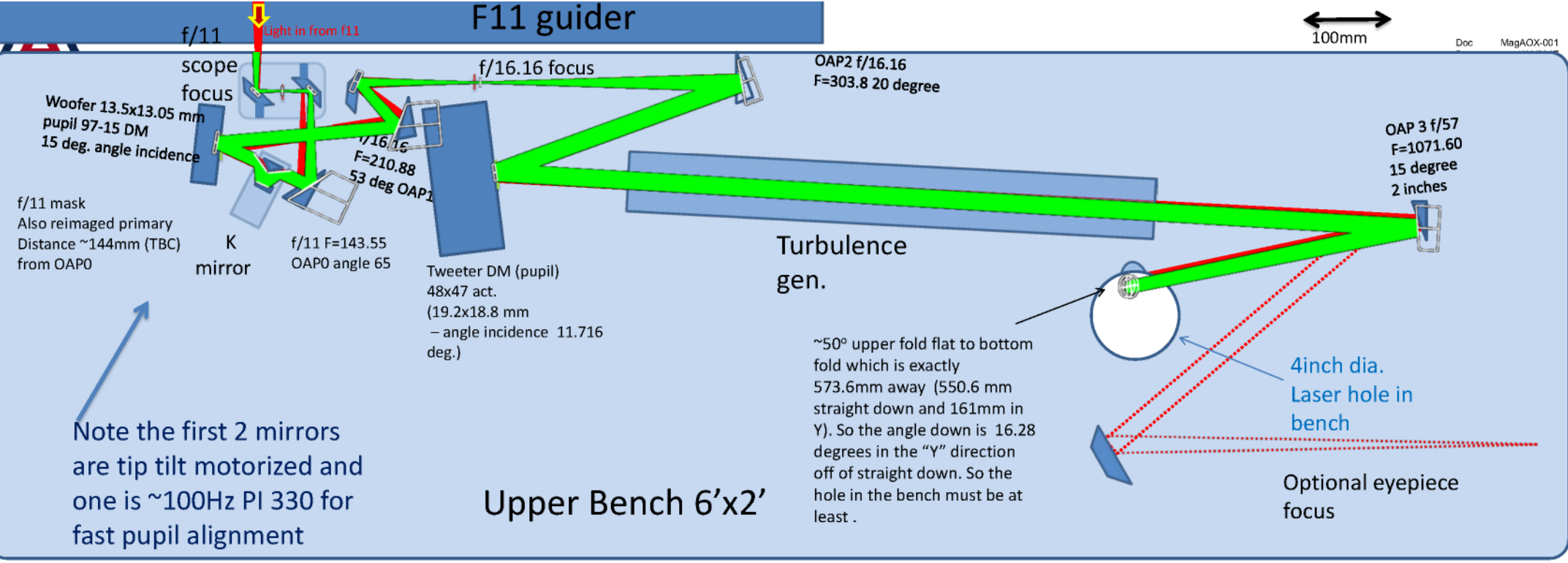


Analytical concept of the f/11
feed to the Woofer and Tweeter
on the upper bench

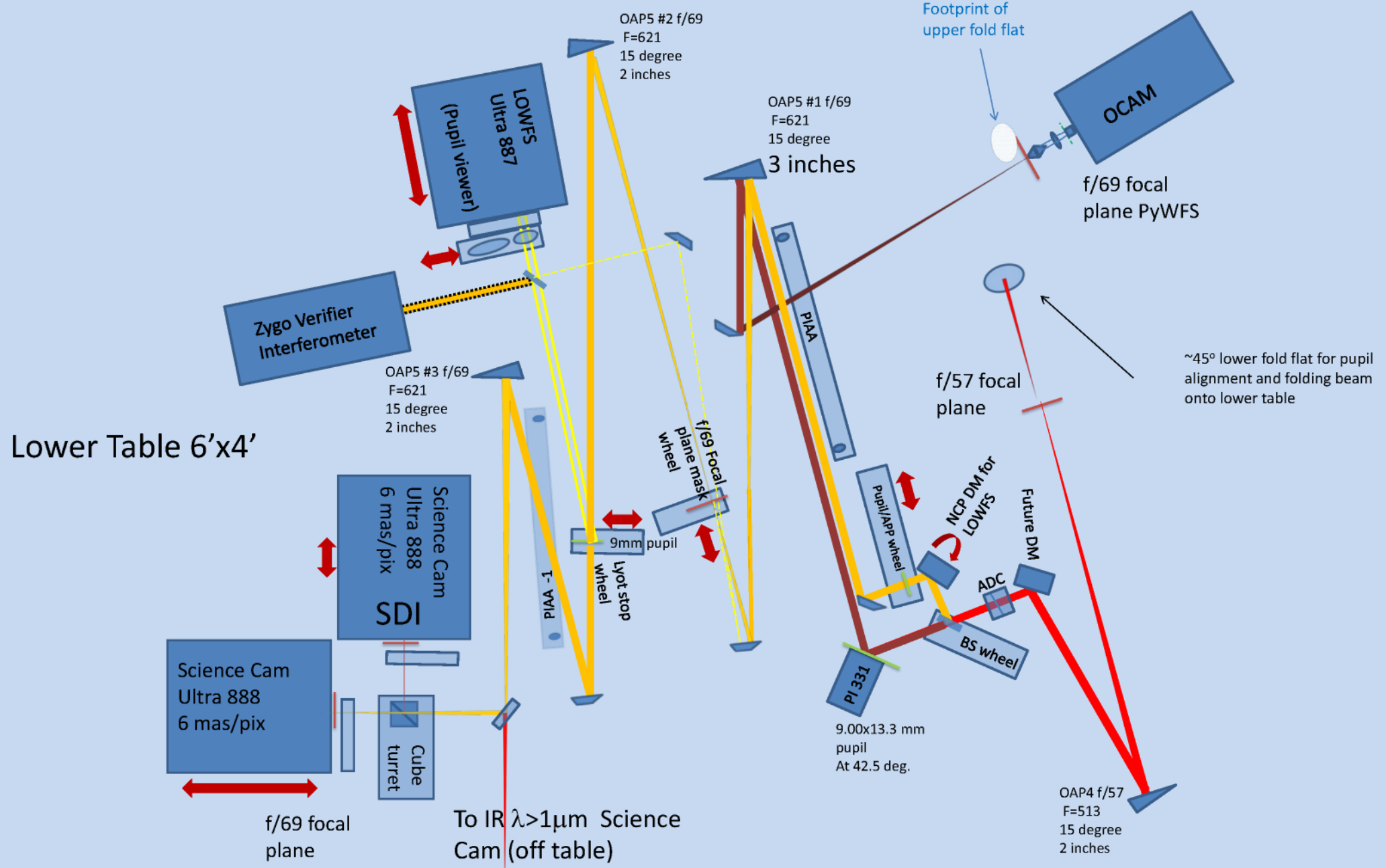
F11 guider

100mm

Doc MagAOX-001



Zemax design in Green – agrees with our analytical optical design, OAPs and pupils correct in ZEMAX.





Selected Key MagAO-X Components

Based on our experiences with MagAO we could identify “tried and tested” sets of controllers/motors/gears/wheels/pinons that already perform well at Magellan for many years maintenance free.

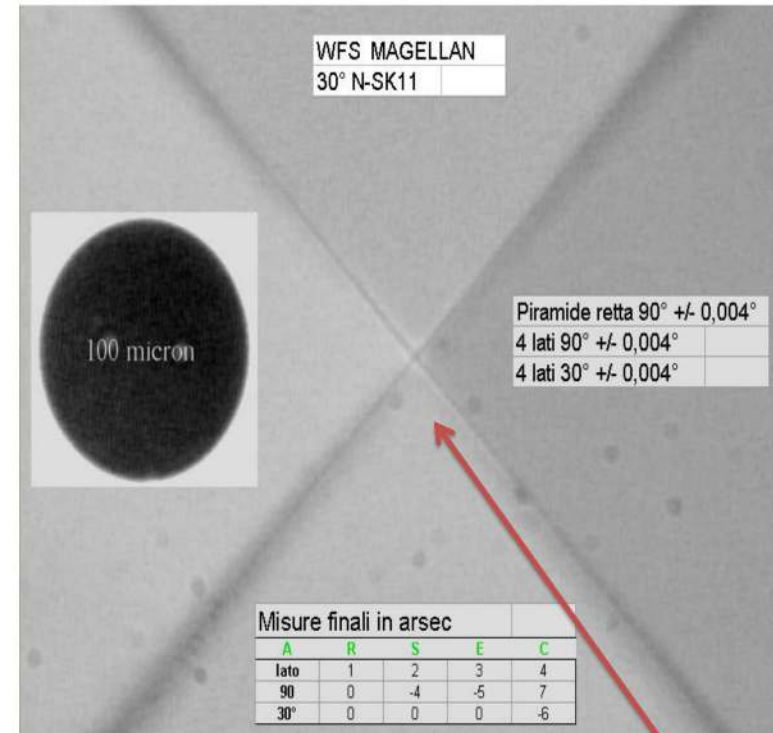
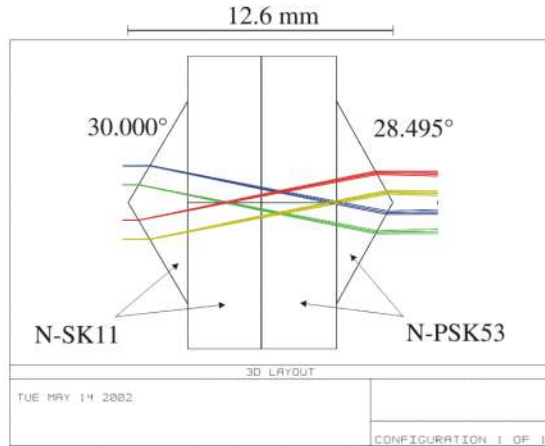
We have also identified long lead time optics (such as the pyramid optic for the PWFS) and have that fabricated ahead of time.

We also identified a series of low thermal drift stainless steel optical mounts, that were also low stress for our flats and OAPs.

Also we have identified a vendor with excellent coatings for our SDI differential H α camera. Moreover we will feed the 2 SDI cameras at 90 degrees through a dichroic beamsplitter cube. Hence we should be able to image at H α and the continuum simultaneously with around ~95% transmission of the H α photons (this is a large improvement over MagAO’s ~20% transmission of its current SDI optics).



Pyramid Optics for PWFS: In Hand



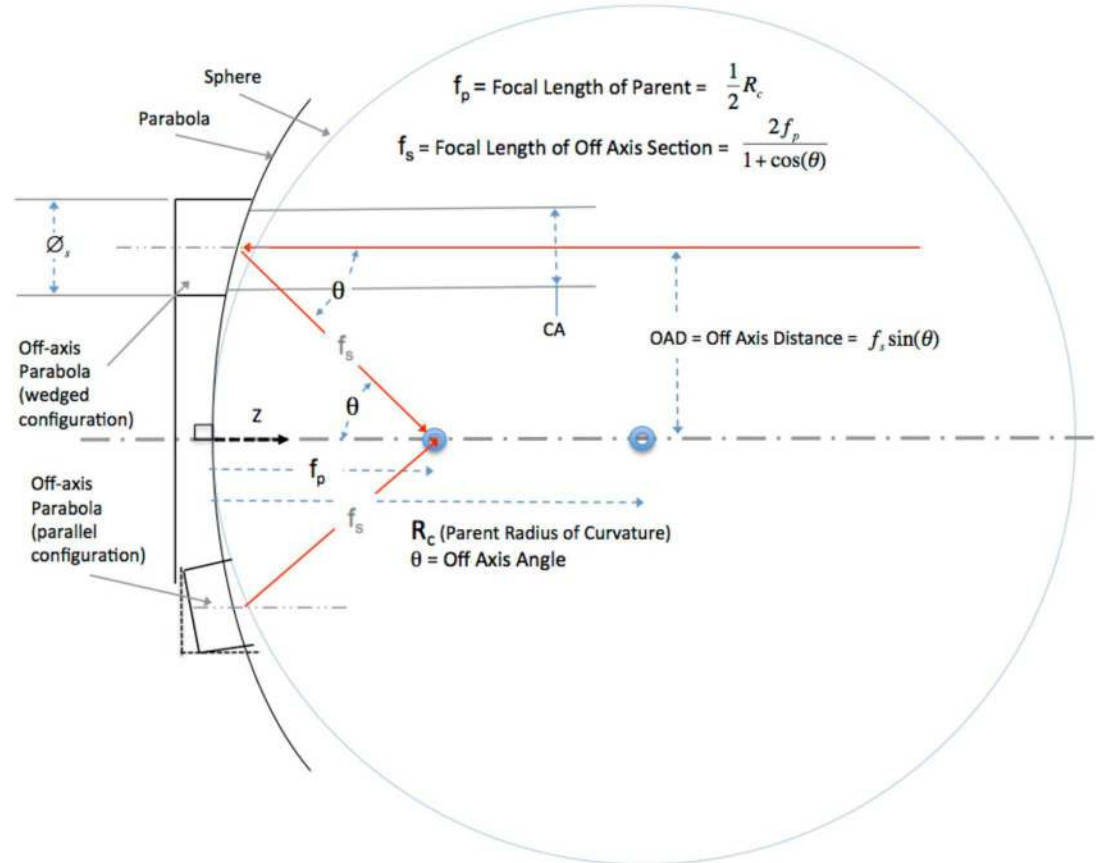
Very high quality tip



All powered Optics are OAPs



Aperture Optical Sciences (AOS) OAP



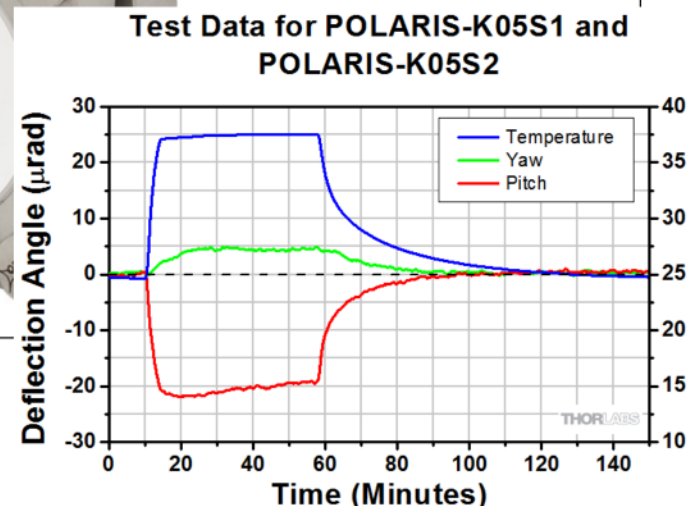
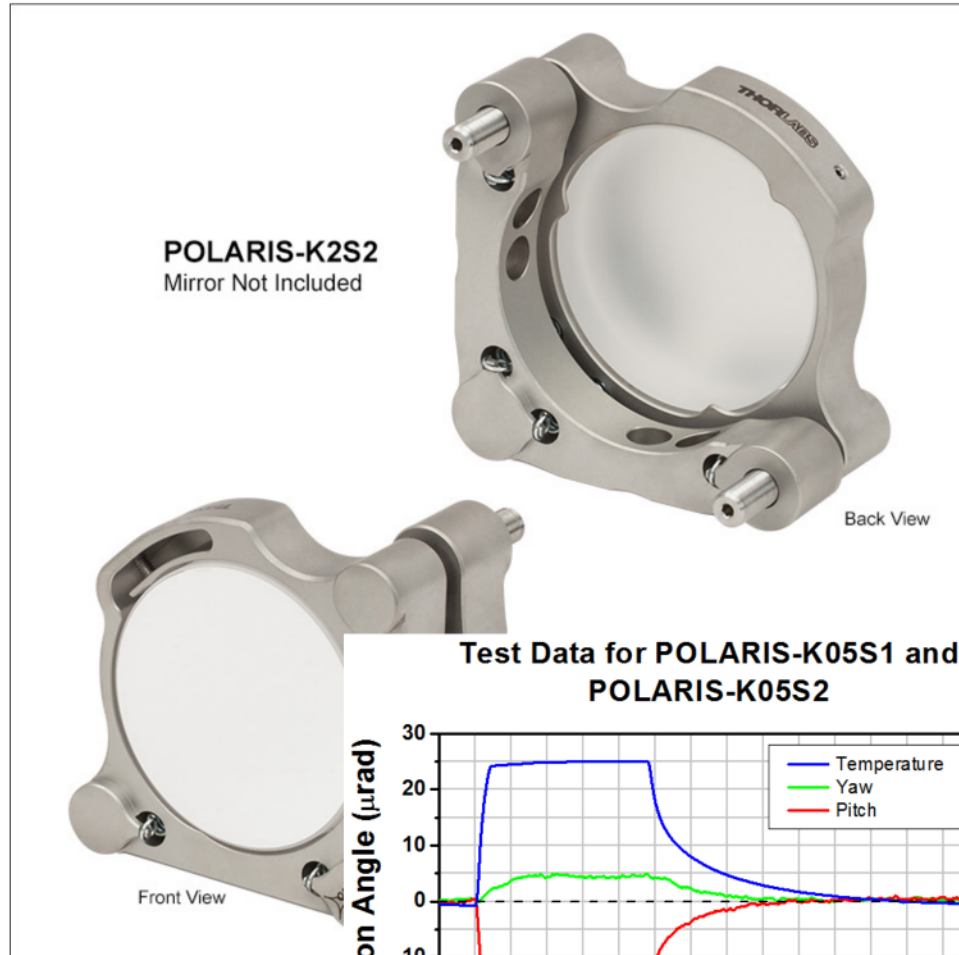
Main Parameters of AO Design *****

AO ASM f/ratio	dia. of 48 act tweeter to have 47 act dia	Second f/#	dia. of Corona beam	Final f#	f11 f/#	dia. of Woofer	Ang. Inc. on woofer
16.16	19.2	57	9	69	11.02	13.5	15

FS (vertex focus) mm	theta (deg)	FP (parent focus) mm	Off Axis Dist. OAD	OAD to inner edge of 2in effective f/	optic size	name	
143.7007616	65	102.2154911	130.2372804	104.8372804	11.02	2inch	OAP0 f/11 collimates 13.05mm pupil
210.7263437	53	168.7721295	168.2938153	142.8938153	16.16	2inch	OAP1 makes f/16.16 focus
303.8078076	20	294.6468388	103.9086229	78.5086229	16.16	2inch	OAP 2 -- f/16 collimator to 18.8mm tweeter
1071.599321	15	1053.342306	277.3509467	251.9509467	57	2inch	OAP3 -- makes f/57 focus
513	15	504.2599338	132.7744735	107.3744735	57	2inch	OAP4 collimates 9mm pupil
621	15	610.4199199	160.7269942	135.3269942	69	2inch	OAP5 x3 for Corona



2inch OAP & Fold Mirror Mounts



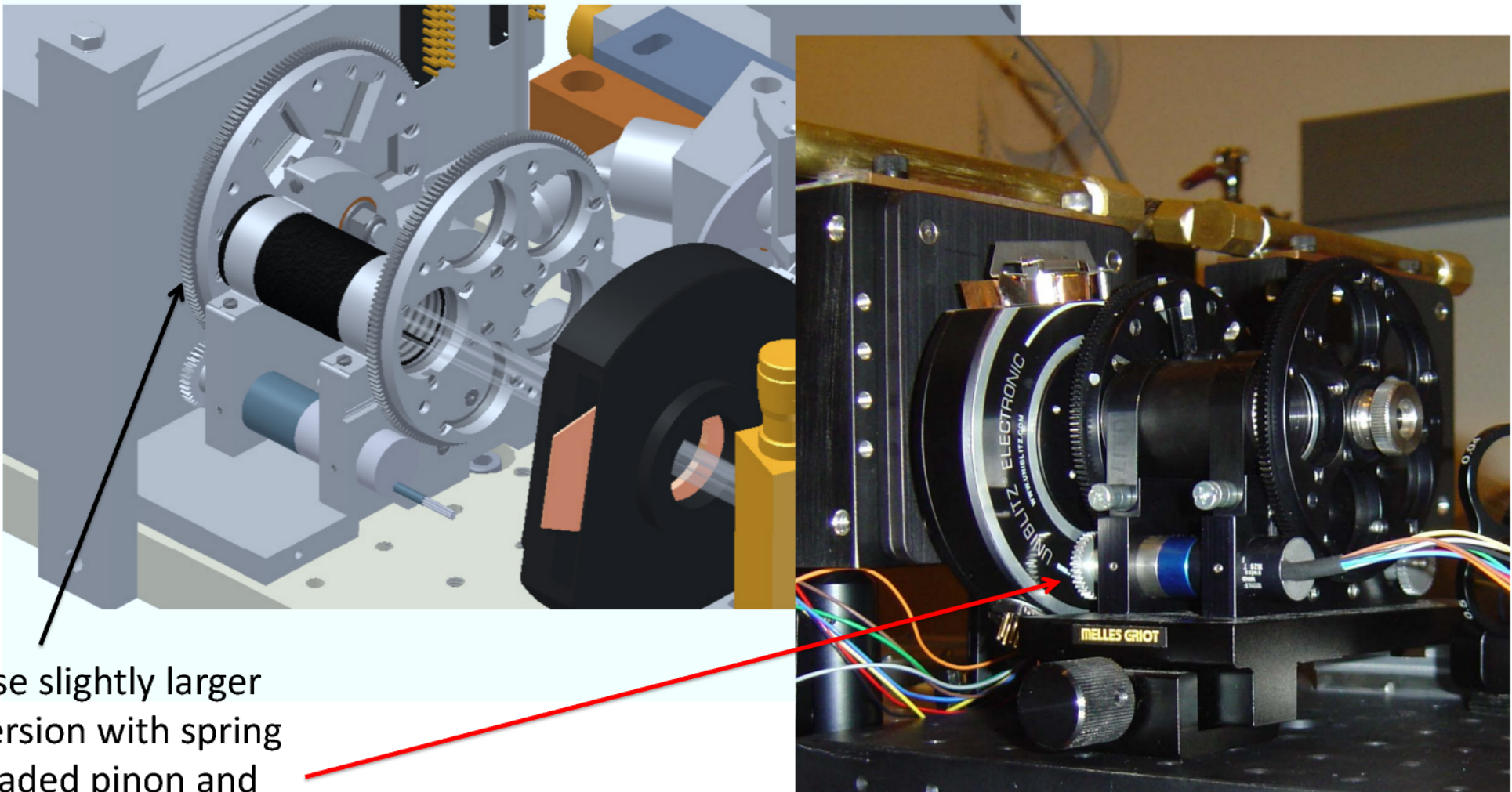
- Monolithic and Spring Flexure Arms Provide Highly Stable Mirror Retention
- Matched Actuator Threading Minimizes Drift and Backlash
- Heat Treating Stainless Steel Minimizes Temperature-Dependent Hysteresis
- Sapphire Seats Ensure Long-Term Stability

HOW MUCH TILT DUE TO TEMP CHANGES?

- in one MagAOX night only expect 5C change hence only 4μrad of tilt
- 4μrad/night of tilt is 57μm over the whole 8.2m pathlength which is just over a pixel/night of drift (open loop)
 - with the loop closed it is only 0.6m of NCP path -and so just 4 μm / night.
 - This very slow motion can easily be completely corrected by stacking the SDI images post-detection.

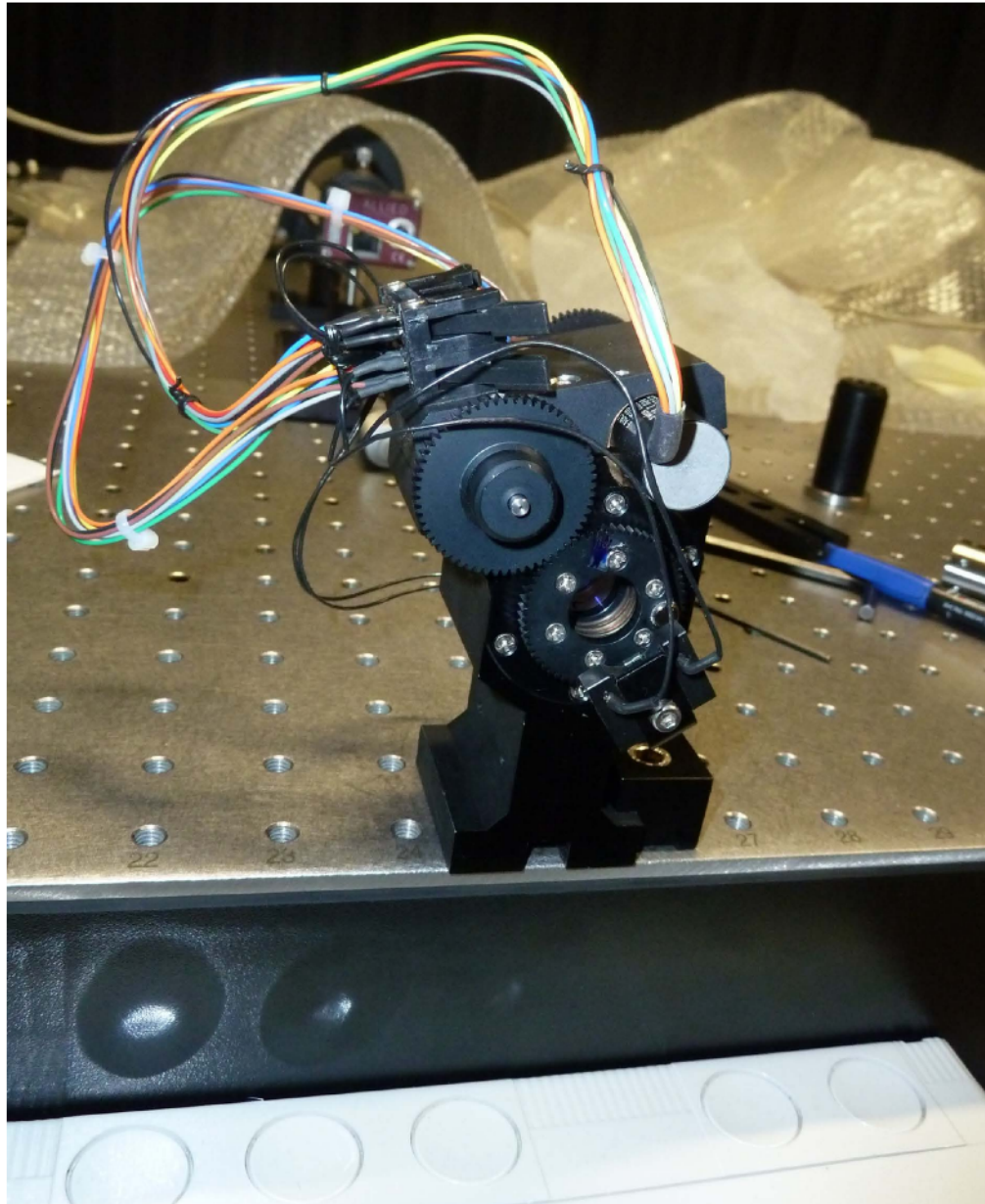


Wheels & Motors --versions of our current VisAO wheels

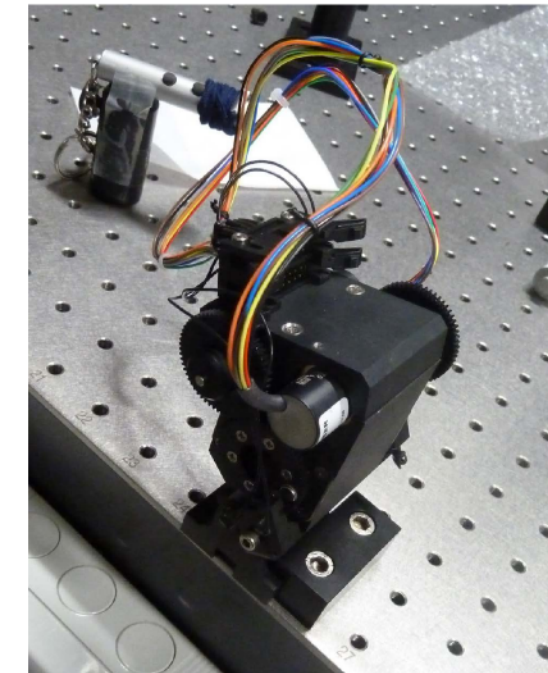


Use slightly larger
version with spring
loaded pinon and
Faulhaber motors with
1:66 gear reducers

ADC (modified version of MagAO ADC)



- Very Compact
- Well understood optomech design
- Same motors





Linear Stages



**PI M-406 Precision Linear Stage
Cost-Effective With High Guiding
Accuracy –high load crossed
bearings**

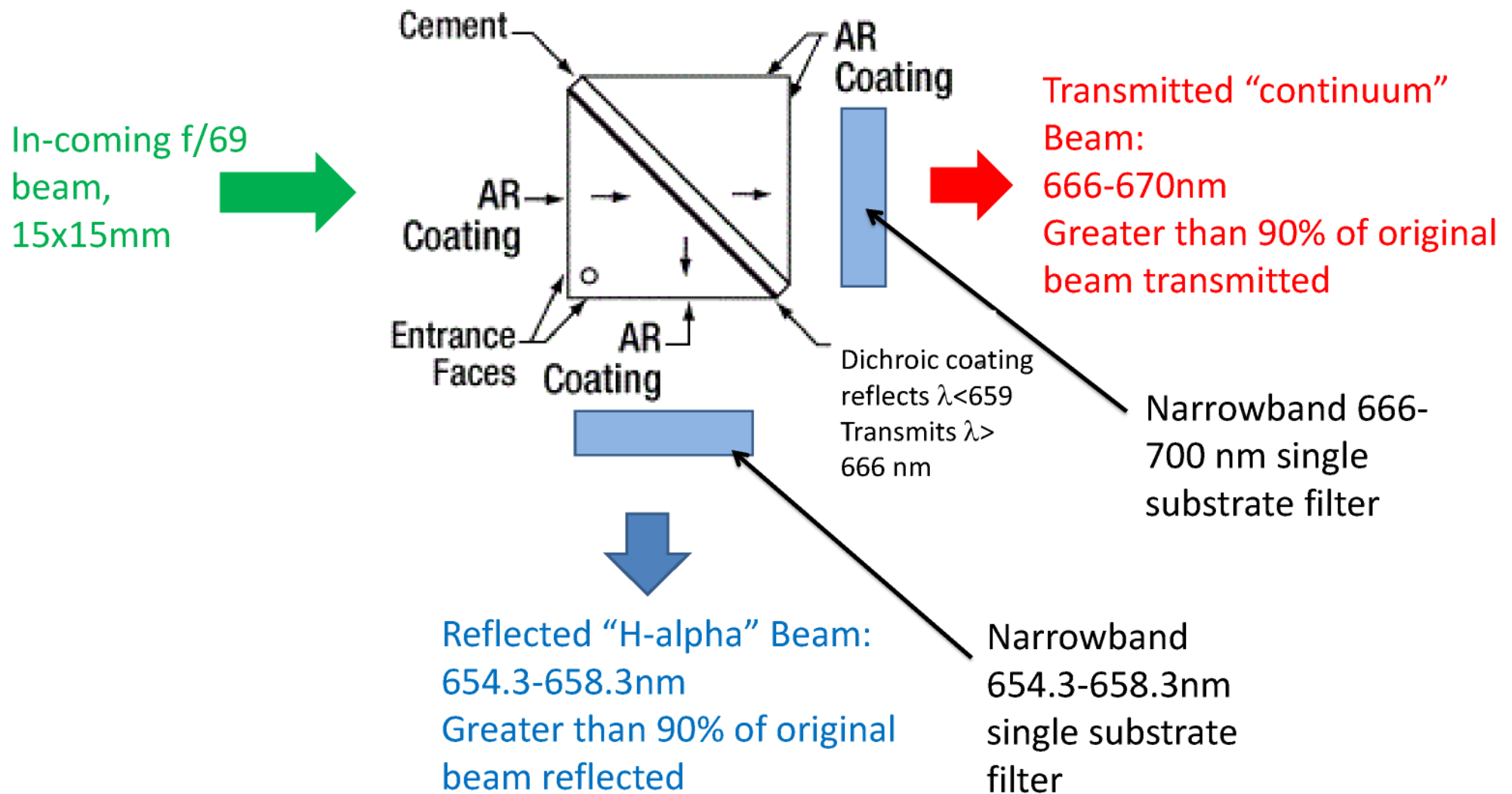
Can Drive the LOWFS and Main
Ultra 888 EMCCDs 150 mm for
phase diversity and focus uses



**PI N-565 Linear Positioner with the
Highest Precision
NEXACT® Piezo Stepping Drive with
Subnanometer Encoder Resolution**
will drive all the Pupil & mask wheels by
up to 13mm with no vibration or heat
when powered off.

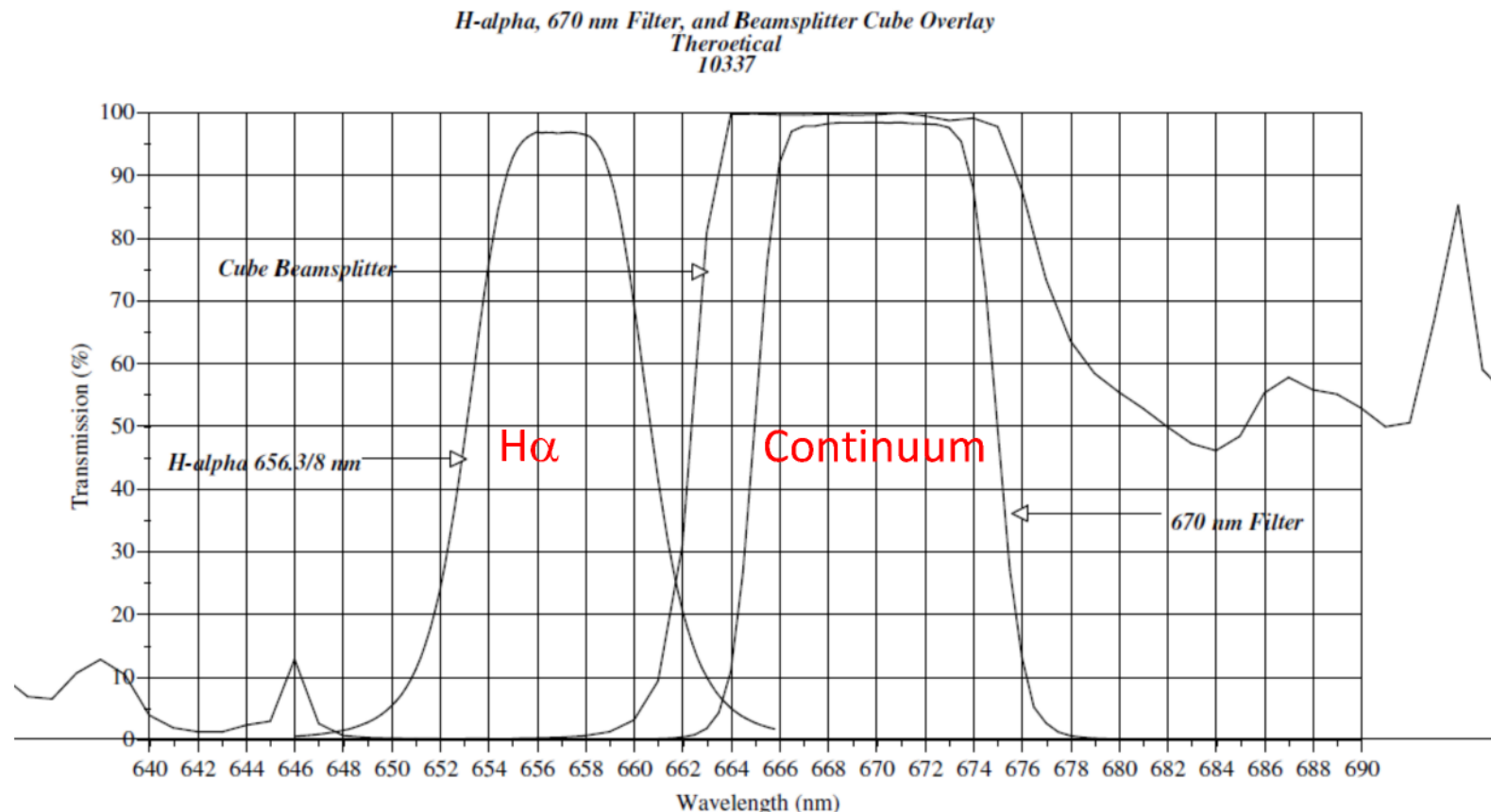


SDI Beamsplitter ($H\alpha$, also r' & i' SDI)





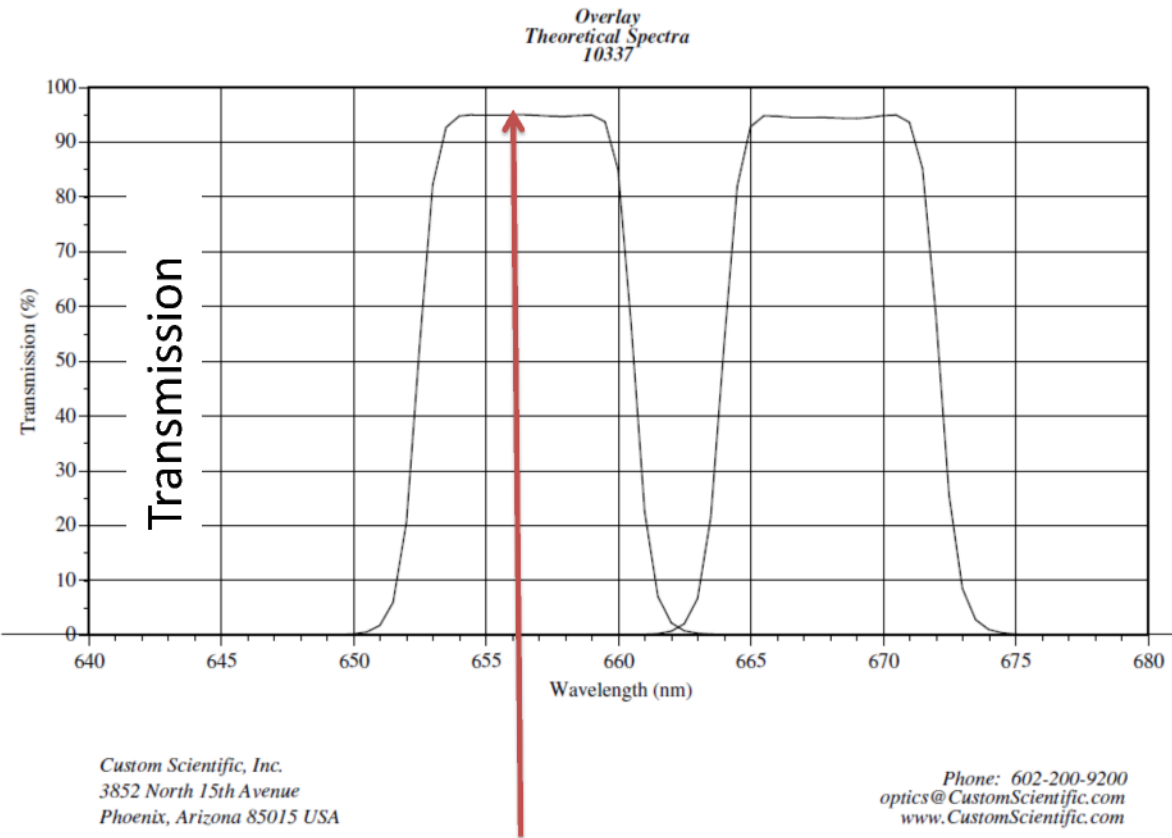
Halpha SDI design with ~95% Throughput



Custom Scientific, Inc.
3852 North 15th Avenue
Phoenix, Arizona 85015 USA

Phone: 602-200-9200
optics@CustomScientific.com
www.CustomScientific.com

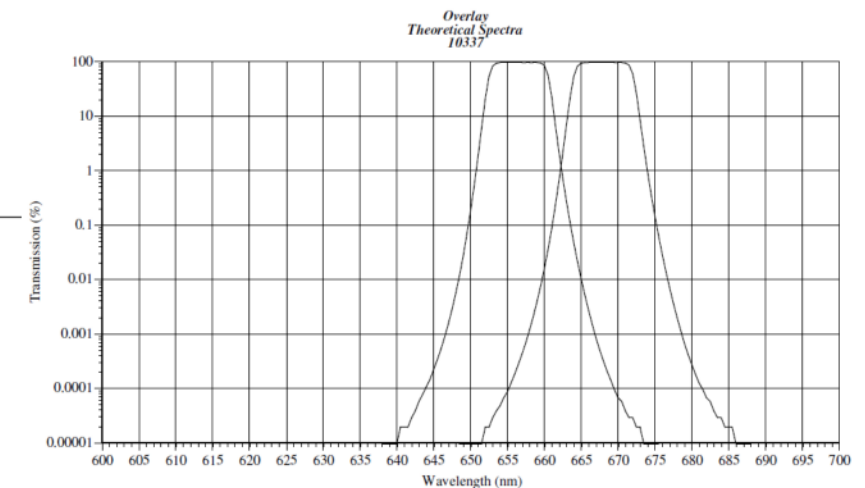
SDI H α (656nm) and (668 nm) Continuum Cube Filters



H α at 656.3 nm
at >95% Transmission

Phone: 602-200-9200
optics@CustomScientific.com
www.CustomScientific.com

Blocking <0.01% leak at H α



Phone: 602-200-9200
optics@CustomScientific.com
www.CustomScientific.com

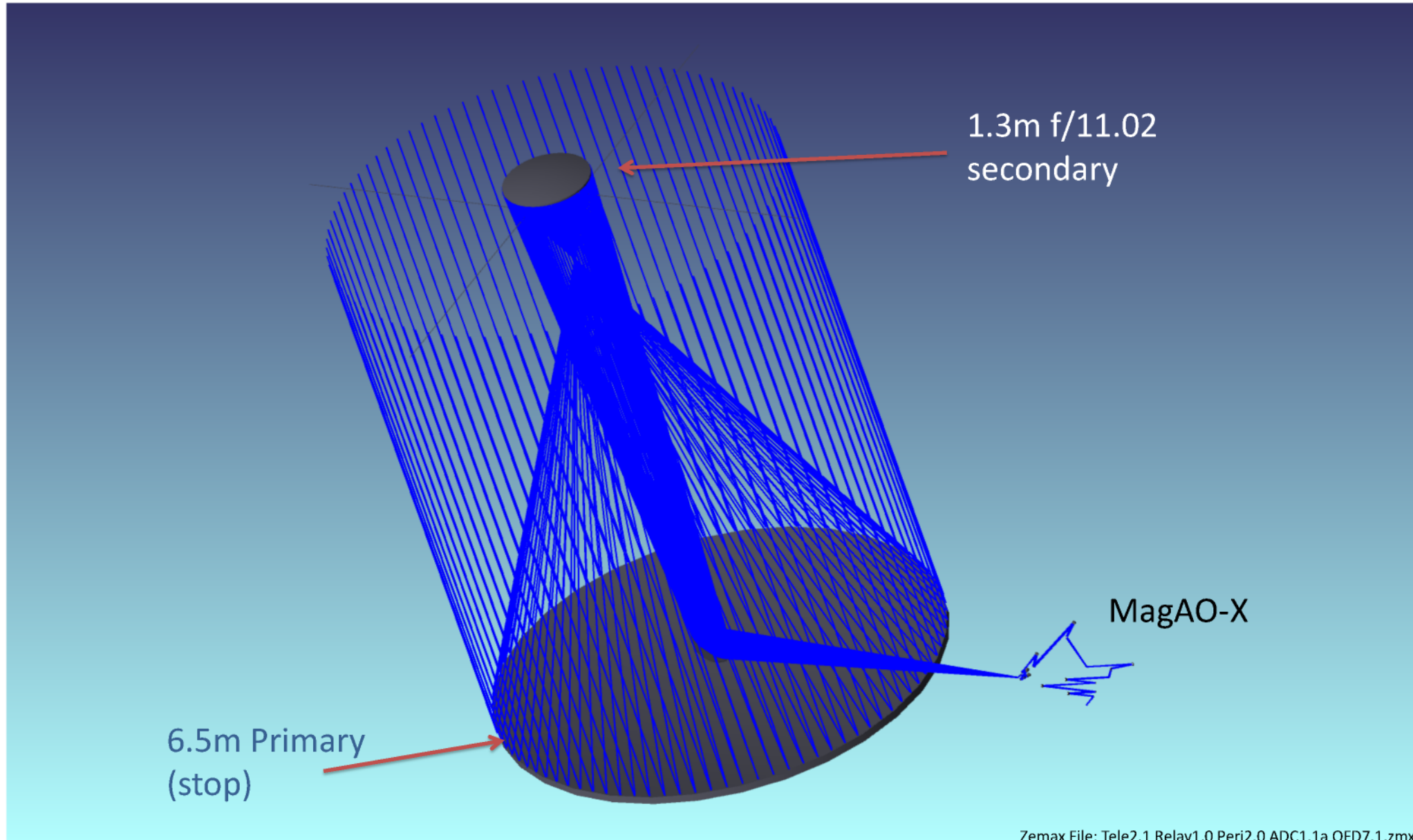


OPTICAL DESIGN

- Zemax design by Oli Durney (Senior Optical Engineer Steward Observatory) from initial analytical design
- The design is all reflective (save the ADCs)
- All the powered optics are OAPs (eliminates ghosts and chromaticity)
- The ADC design is diffraction-limited from 1-2 airmasses and from 0.6 to 1.8 microns. The ADC is commonpath with the PWFS and the science cameras.
- The design was first analytically done by Laird Close and then done with zemax by Oli Durney. Both designs are in excellent agreement.
- The true aperture stop (the primary mirror) is relayed to the Woofer pupil to the Tweeter pupil to the first coronagraphic pupil to the Lyot stop.
- The first coronagraphic focal plane is f/67 and is the location of the coronagraphic mask
- The final focal plane is after the Lyot stop and is also f/67 yielding a 6mas/pixel platescale on the Ultra 888 science camera.
- The optical quality of the on-axis beam has a Strehl 100% (with perfect optics) over any broad band astronomical filter that we would use (such as r',i',z',J, H).

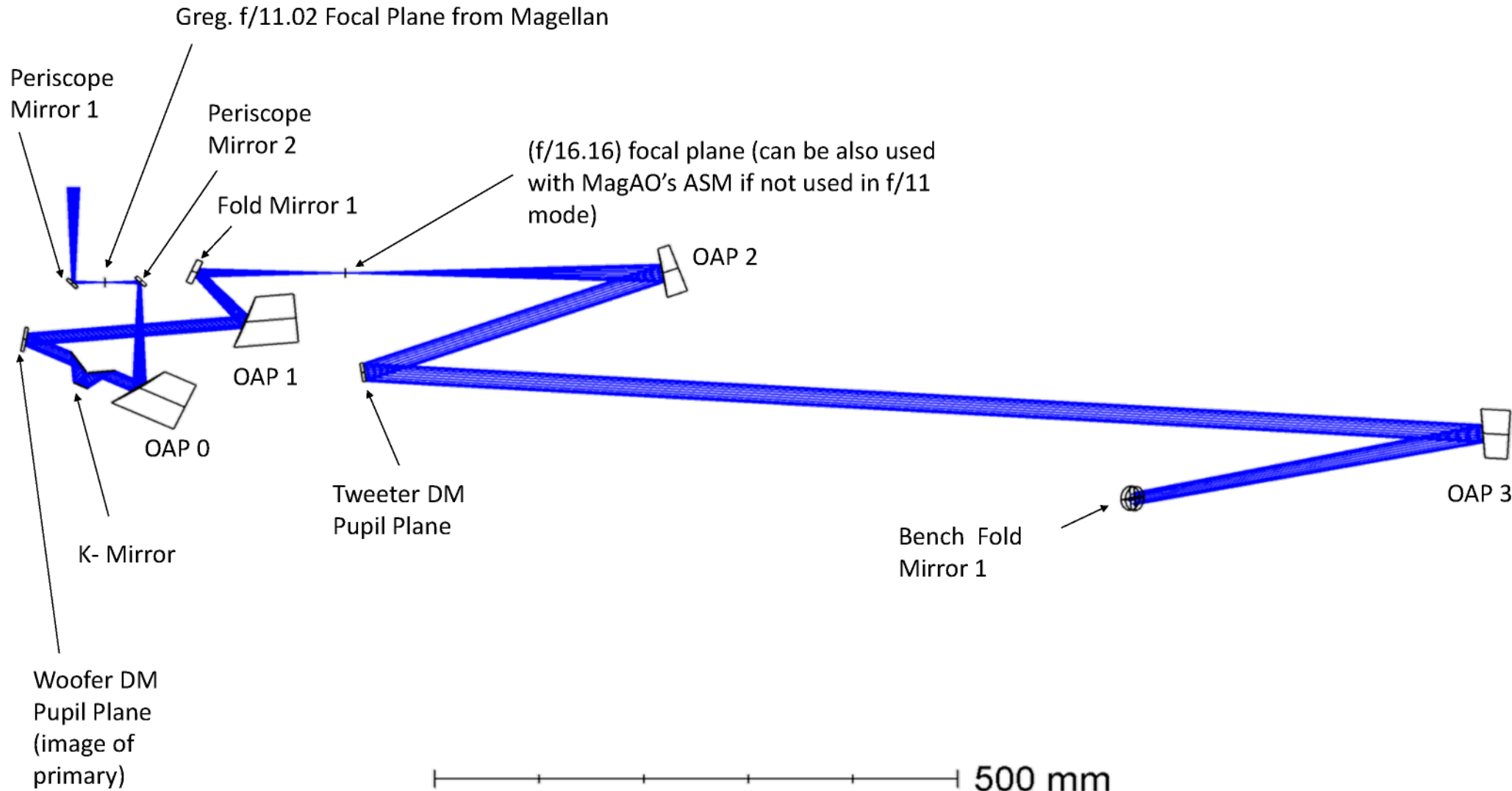


Shaded Model of f/11 + MagAO-X



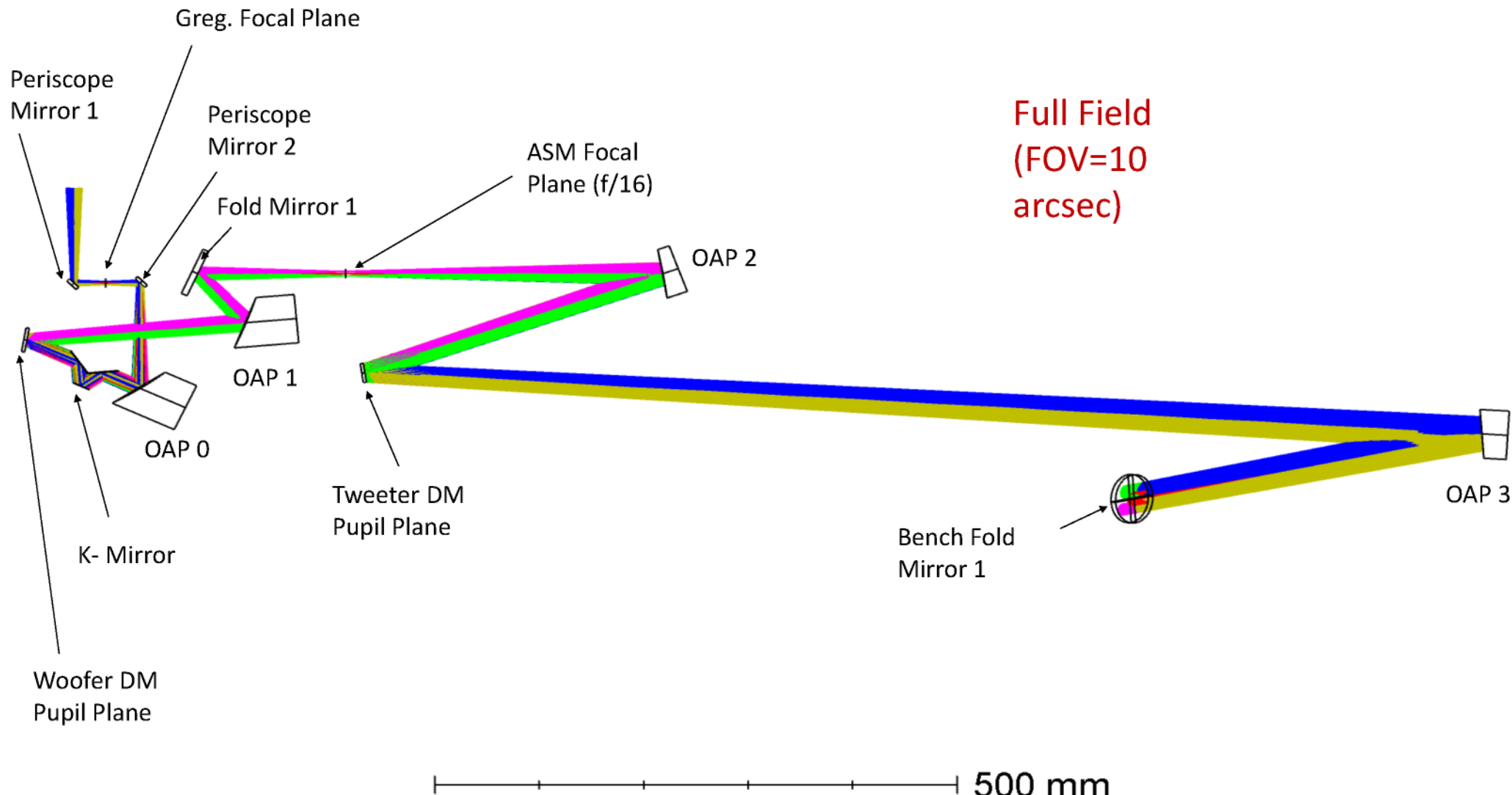


Upper Bench Optical Design (on-axis)





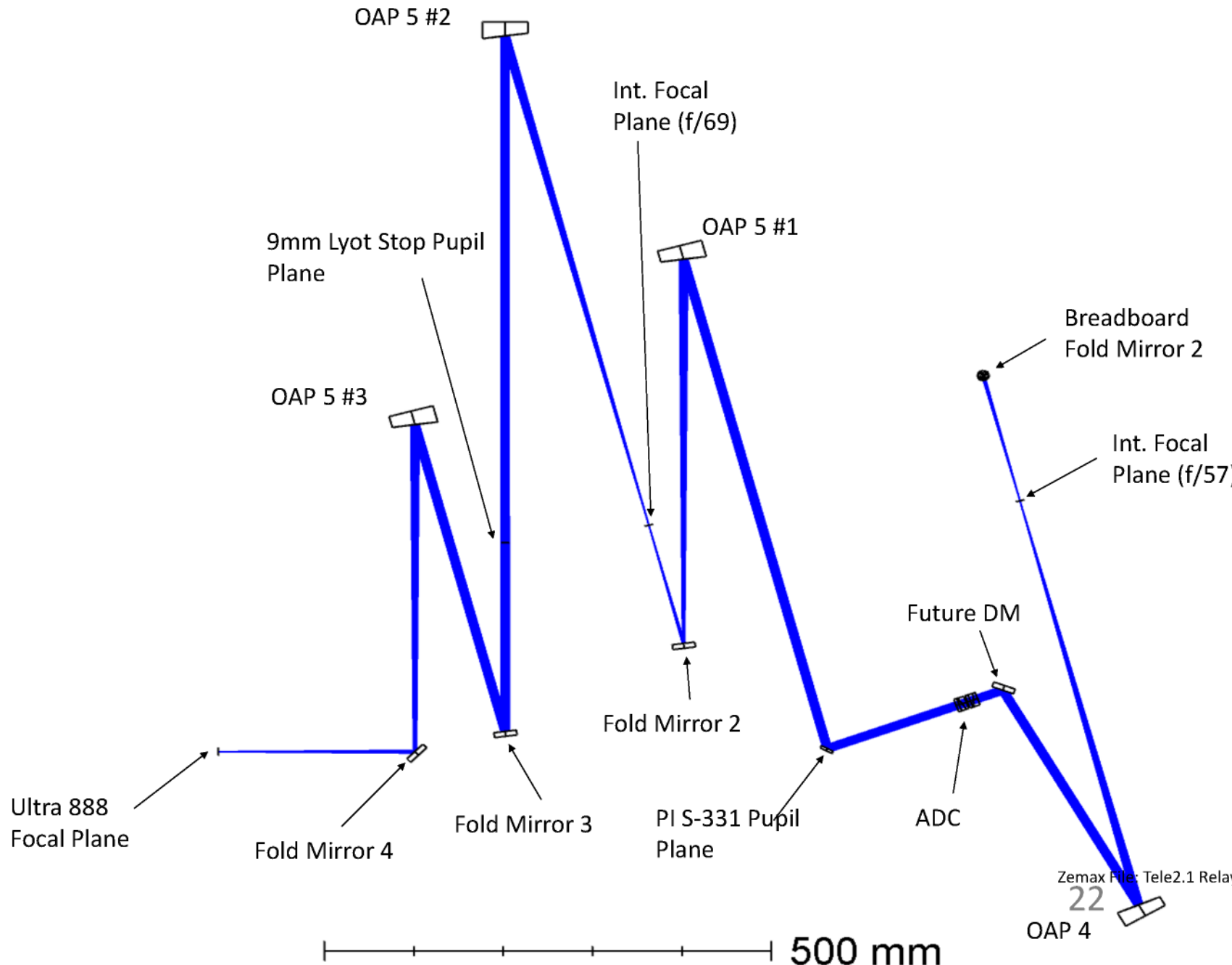
Upper Bench Optical Design (10" FOV)



Full Field
(FOV=10
arcsec)

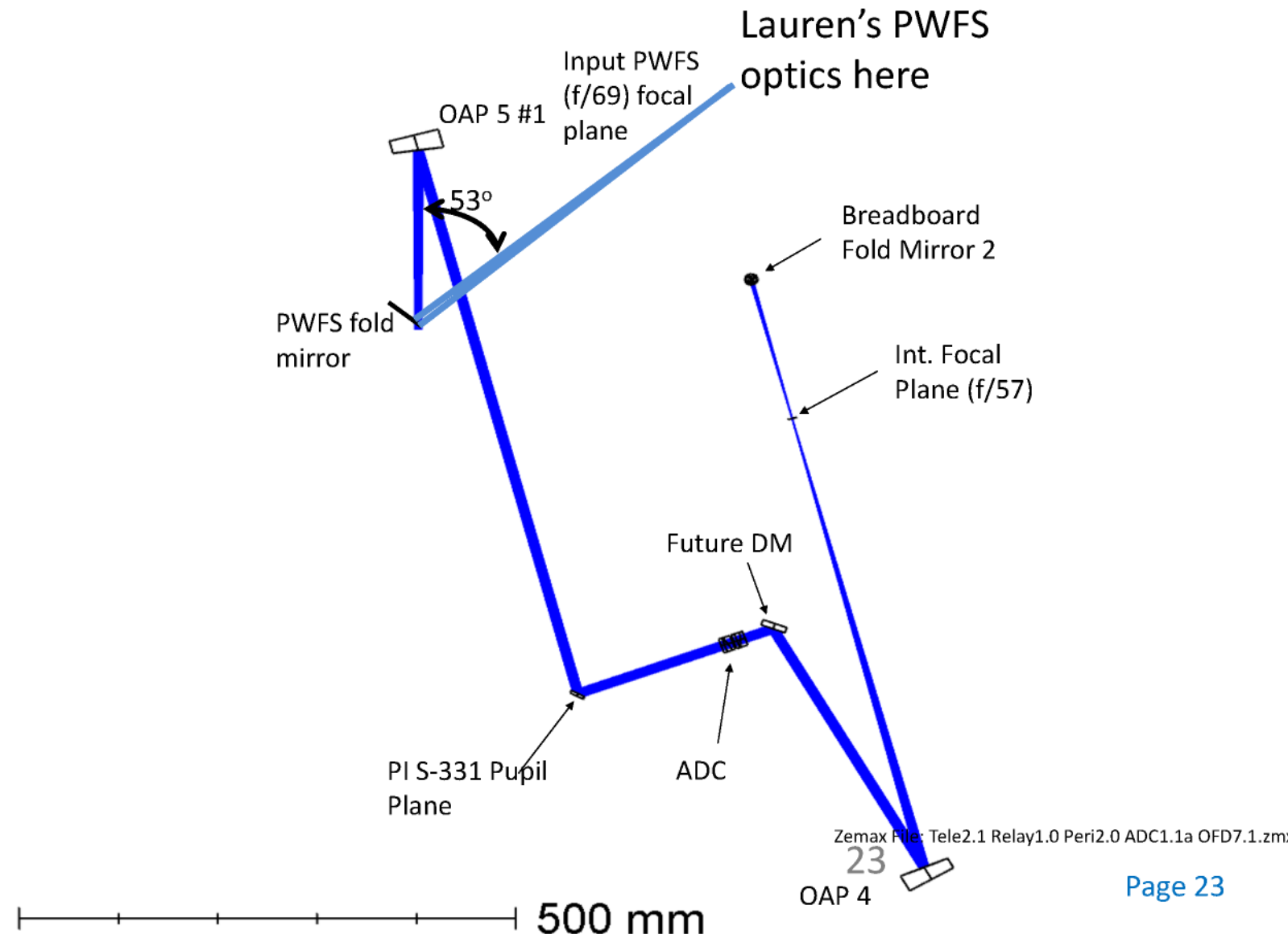


Lower Table Optical Design On-Axis



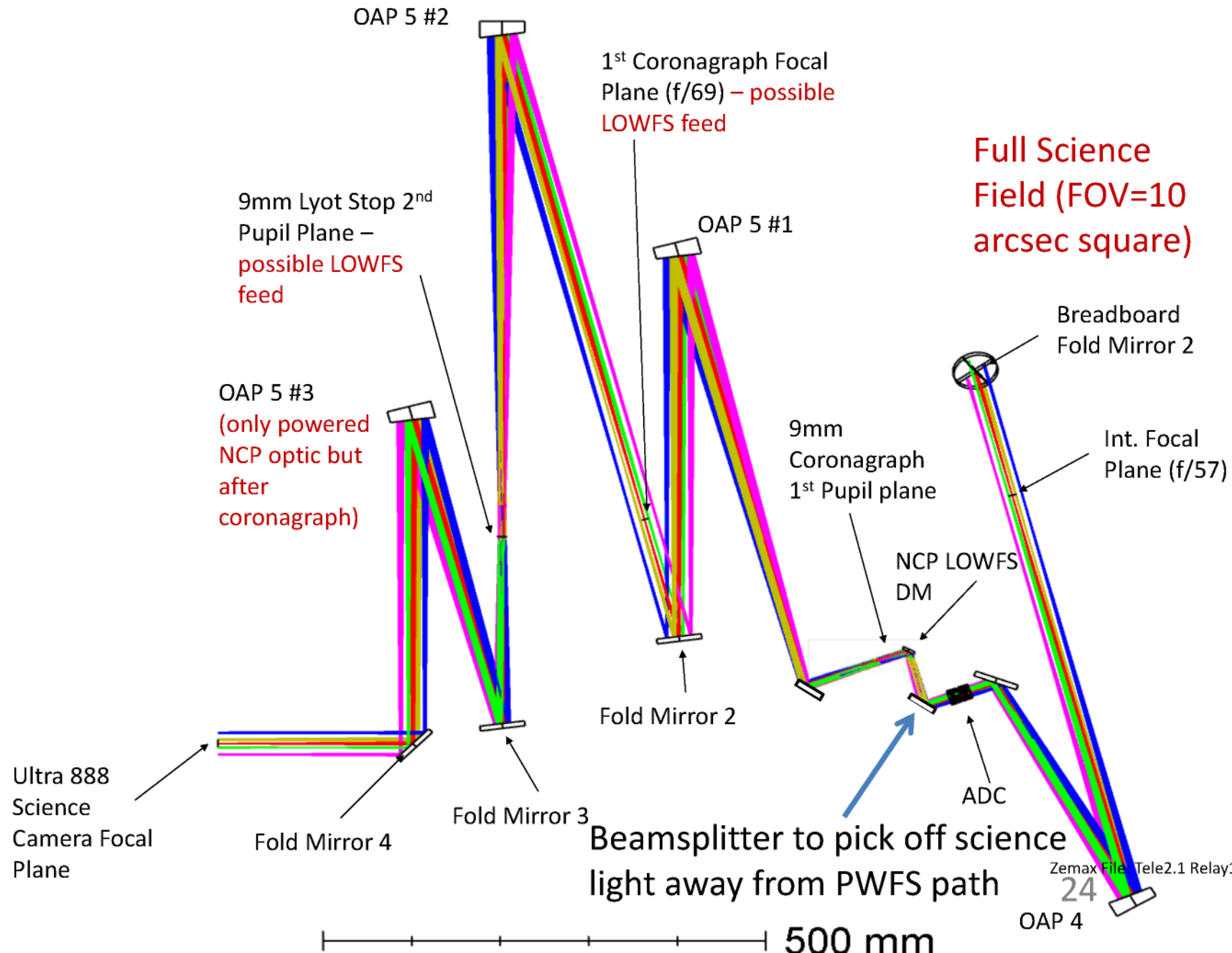


Lower Table Optical Design with PWFS



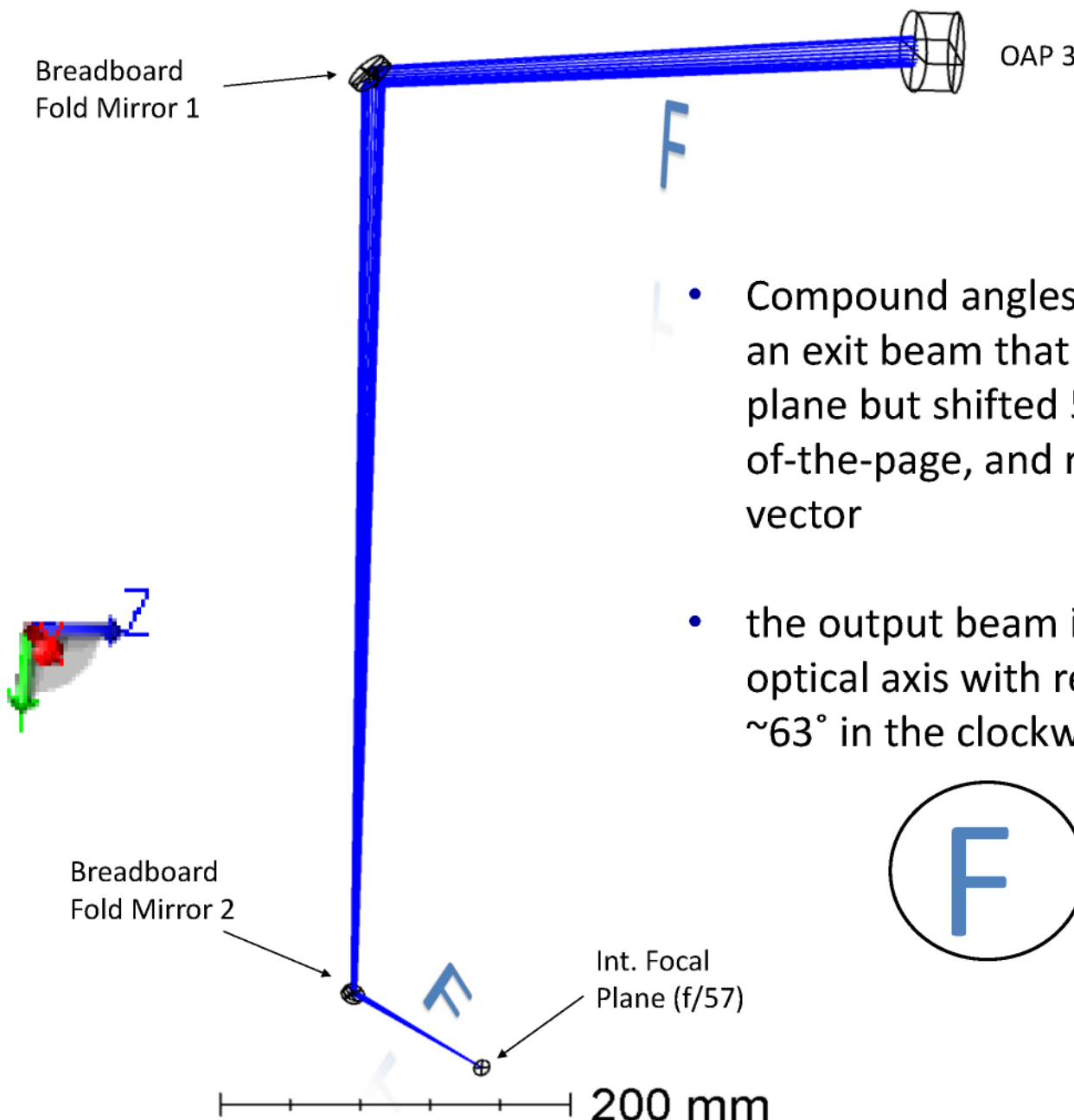


Lower Table Science Full FOV

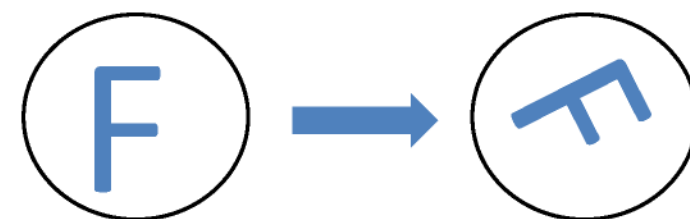




Bench to Table Periscope



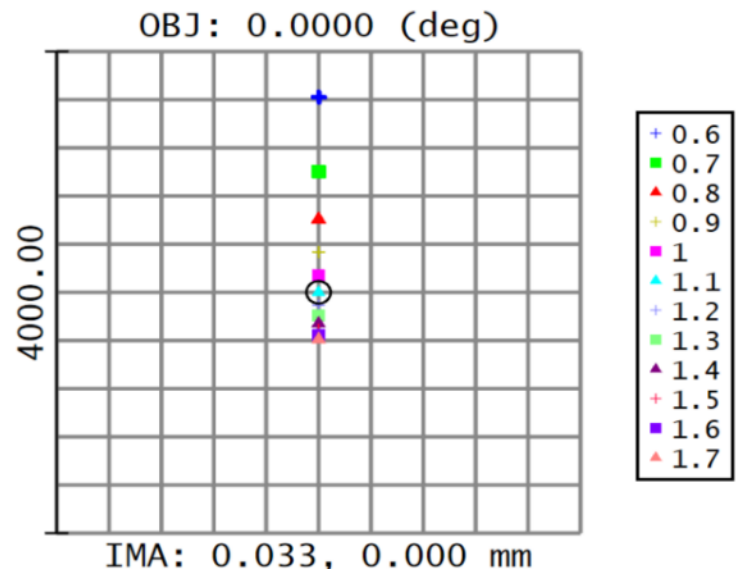
- Compound angles for both BBFM1 & 2 result in an exit beam that is parallel with the input beam plane but shifted 550.6 mm lower, 161 mm out-of-the-page, and rotated in its output direction vector
- the output beam is also rotated about the optical axis with respect to the input beam by ~63° in the clockwise direction.



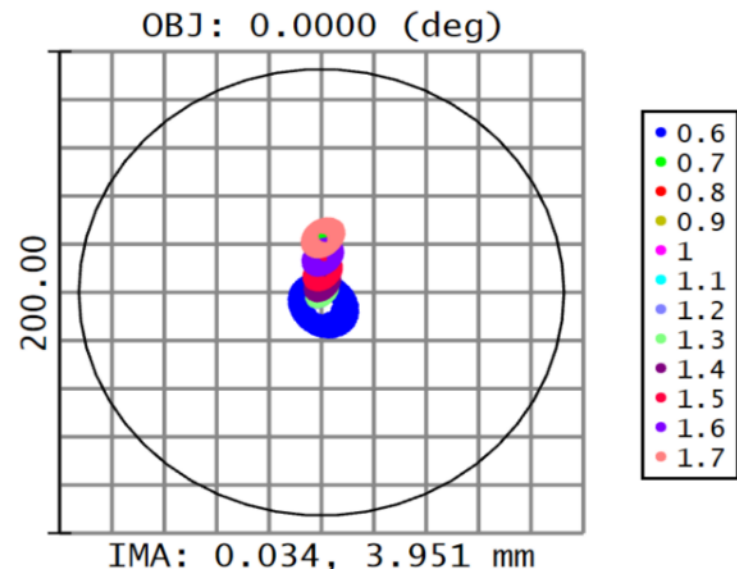


Spot Diagrams for Zenith Z=40° w/ ADC

No ADC Correction



ADC Correction (Current Design)



Surface TMA: Ultra 888 Focal Plane

Spot Diagram

Magellan With f/11 Secondary
2/16/2017
Units are μm . Airy Radius: 92.64 μm . Legend items refer to Wavelengths
Field : 1
RMS radius : 620.382
GEO radius : 1635.77
Scale bar : 4000 Reference : Chief Ray

Steward Observatory
933 N. Cherry Ave.
Tucson, AZ 85721

Tele2.1 Relay1.0 Peri2.0 ADC1.1a OFD5.5.zmx
Configuration 7 of 7

Surface TMA: Ultra 888 Focal Plane

Spot Diagram

Magellan With f/11 Secondary
2/16/2017
Units are μm . Airy Radius: 92.65 μm . Legend items refer to Wavelengths
Field : 1
RMS radius : 12.594
GEO radius : 30.627
Scale bar : 200 Reference : Chief Ray

Steward Observatory
933 N. Cherry Ave.
Tucson, AZ 85721

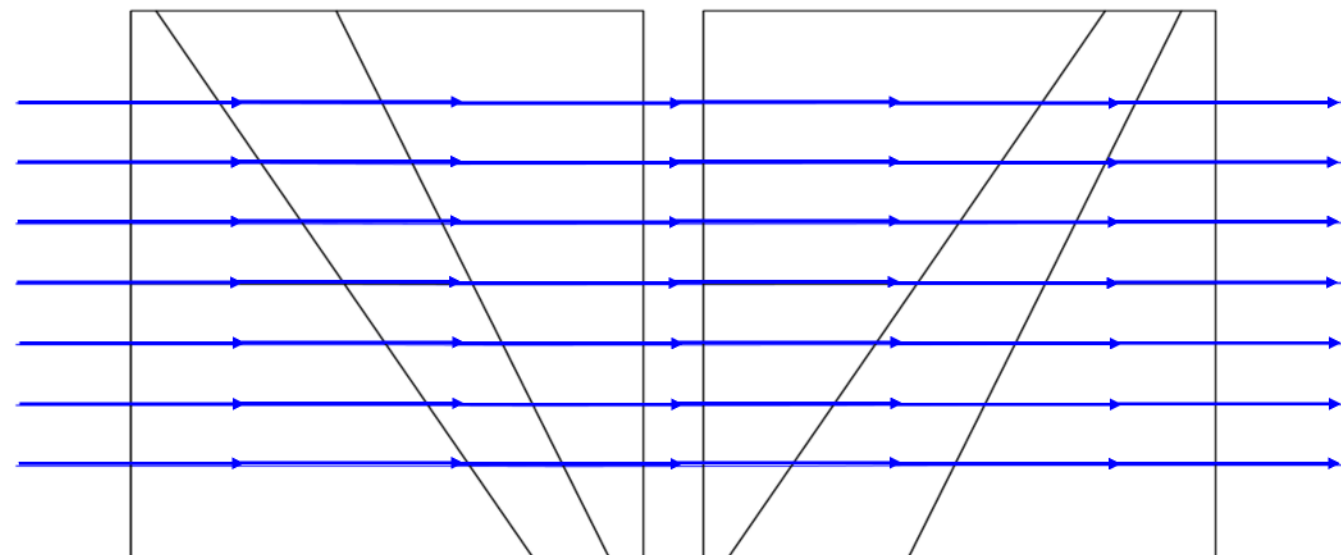
Tele2.1 Relay1.0 Peri2.0 ADC1.1a OFD5.5.ZMX
Configuration 7 of 7



ADC Prism Design Layouts

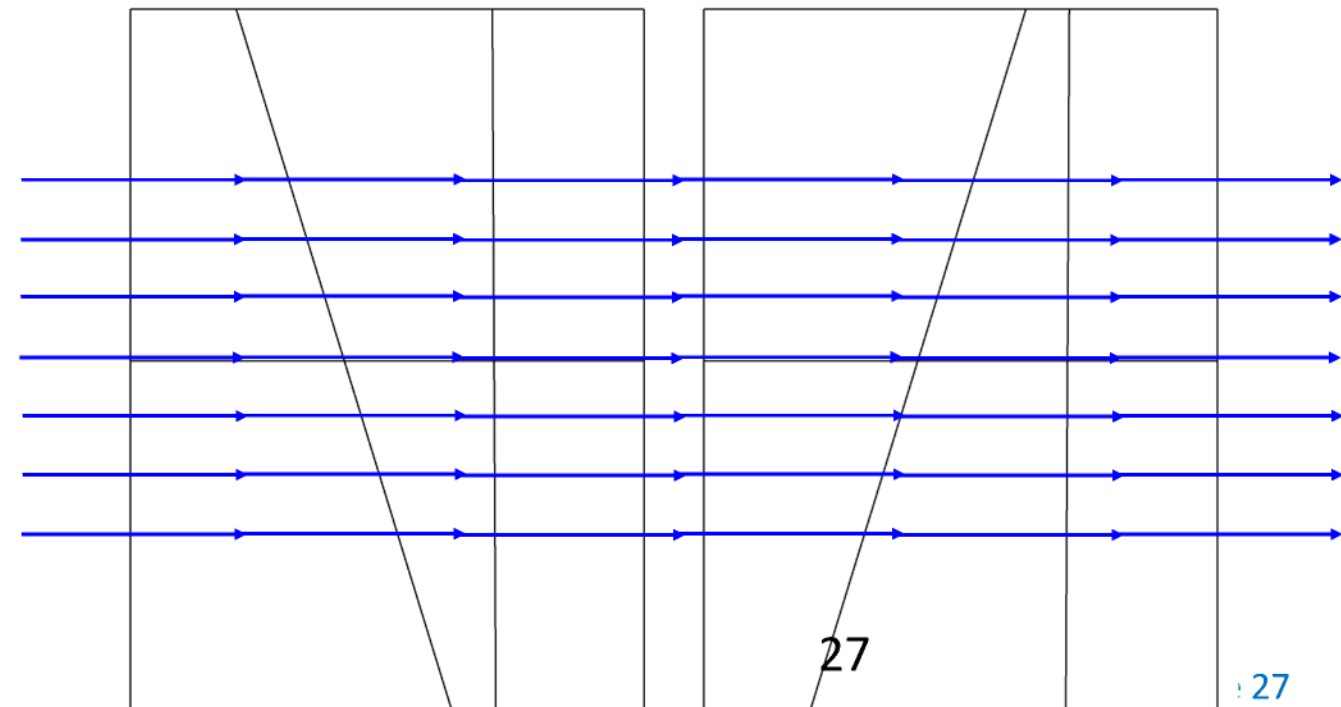
Current ADC Design

- $\phi = 14 \text{ mm}$
- S-PHM53, S-TIM8, N-KZFS4
- CT = 5.0, 3.0, 4.0 mm
- $\theta = 57.785^\circ, 65.474^\circ$



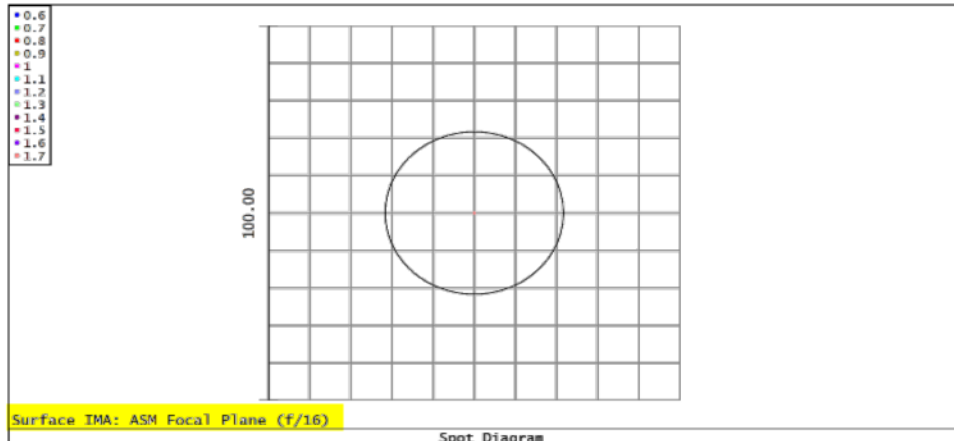
New ADC Design

- $\phi = 18 \text{ mm}$
- S-PHM53, S-TIM8, N-KZFS4
- CT = 5.0, 3.5, 3.5 mm
- $\theta = 73.687^\circ, 0.260^\circ$





Spot Diagrams at Focal Planes

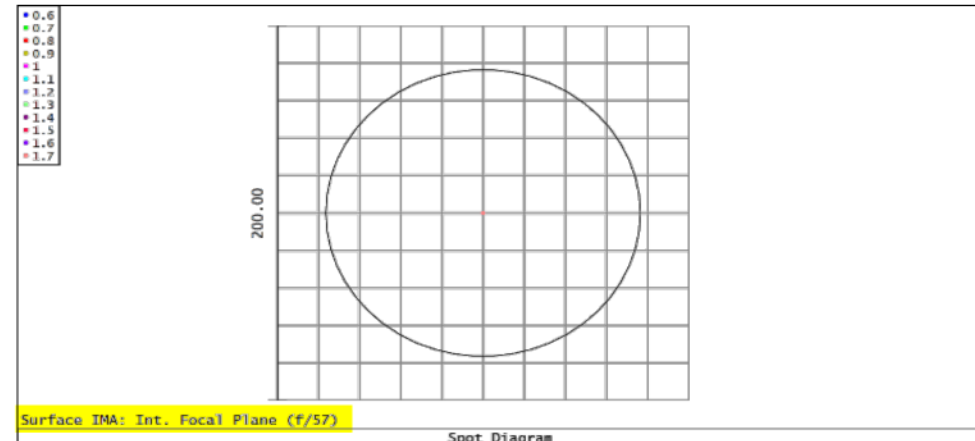


Surface IMA: ASM Focal Plane (f/16)

Spot Diagram

Magellan With f/11 Secondary
2/16/2017
Units are μm . Airy Radius: 21.69 μm . Legend items refer to Wavelengths
Field : 1
RMS radius : 0.099
GEO radius : 0.187
Scale bar : 100 Reference : Chief Ray

Steward Observatory
933 N. Cherry Ave.
Tucson, AZ 85721
Tele2.1 Relay1.0 Periz.0 ADC1.1a OFD5.5.ZMX
Configuration 2 of 7

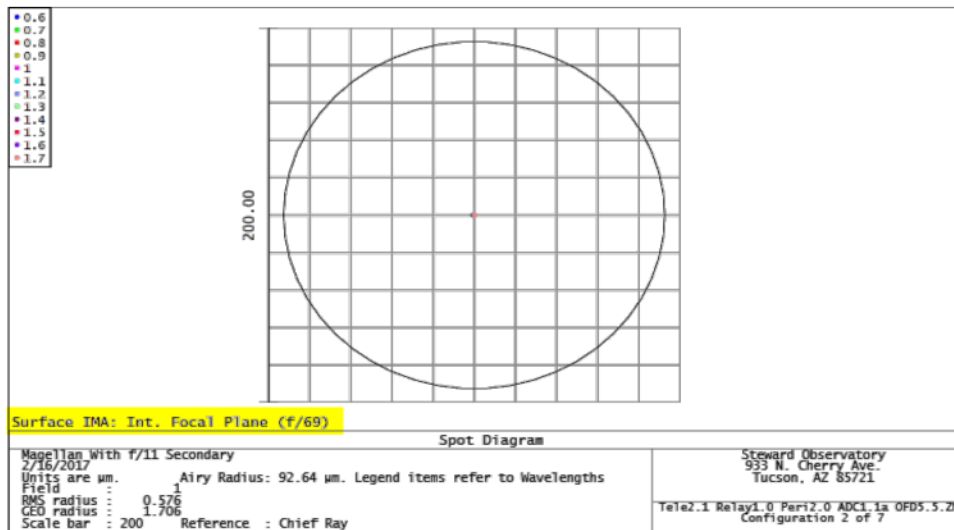


Surface IMA: Int. Focal Plane (f/57)

Spot Diagram

Magellan With f/11 Secondary
2/16/2017
Units are μm . Airy Radius: 76.48 μm . Legend items refer to Wavelengths
Field : 1
RMS radius : 0.349
GEO radius : 0.671
Scale bar : 200 Reference : Chief Ray

Steward Observatory
933 N. Cherry Ave.
Tucson, AZ 85721
Tele2.1 Relay1.0 Periz.0 ADC1.1a OFD5.5.ZMX
Configuration 2 of 7

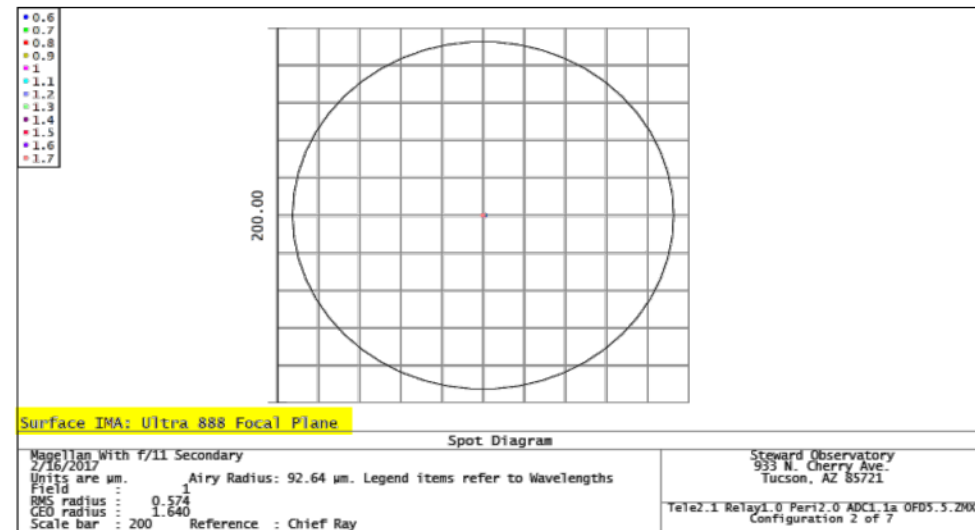


Surface IMA: Int. Focal Plane (f/69)

Spot Diagram

Magellan With f/11 Secondary
2/16/2017
Units are μm . Airy Radius: 92.64 μm . Legend items refer to Wavelengths
Field : 1
RMS radius : 0.576
GEO radius : 1.706
Scale bar : 200 Reference : Chief Ray

Steward Observatory
933 N. Cherry Ave.
Tucson, AZ 85721
Tele2.1 Relay1.0 Periz.0 ADC1.1a OFD5.5.ZMX
Configuration 2 of 7



Surface IMA: Ultra 888 Focal Plane

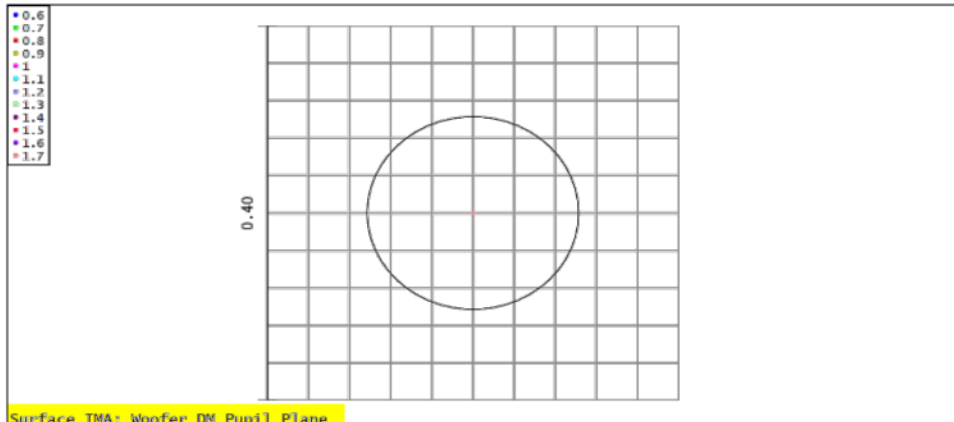
Spot Diagram

Magellan With f/11 Secondary
2/16/2017
Units are μm . Airy Radius: 92.64 μm . Legend items refer to Wavelengths
Field : 1
RMS radius : 0.574
GEO radius : 1.640
Scale bar : 200 Reference : Chief Ray

Steward Observatory
933 N. Cherry Ave.
Tucson, AZ 85721
Tele2.1 Relay1.0 Periz.0 ADC1.1a OFD5.5.ZMX
Configuration 2 of 7

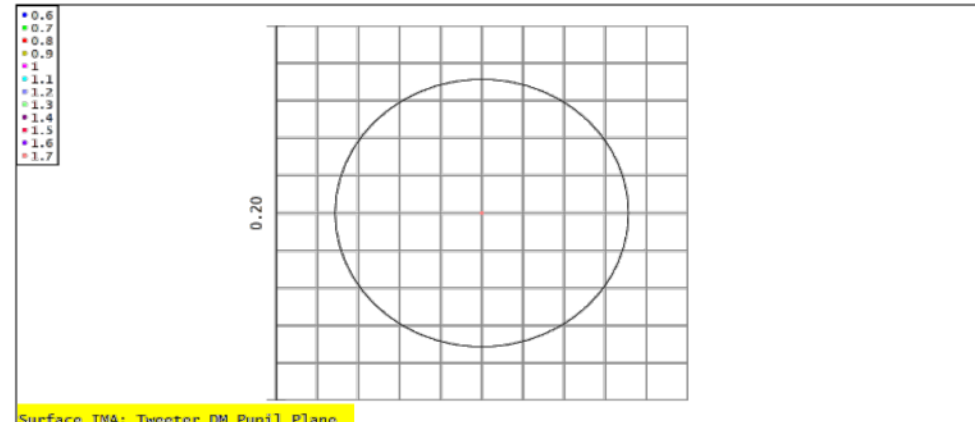


Spot Diagrams at Pupil Planes



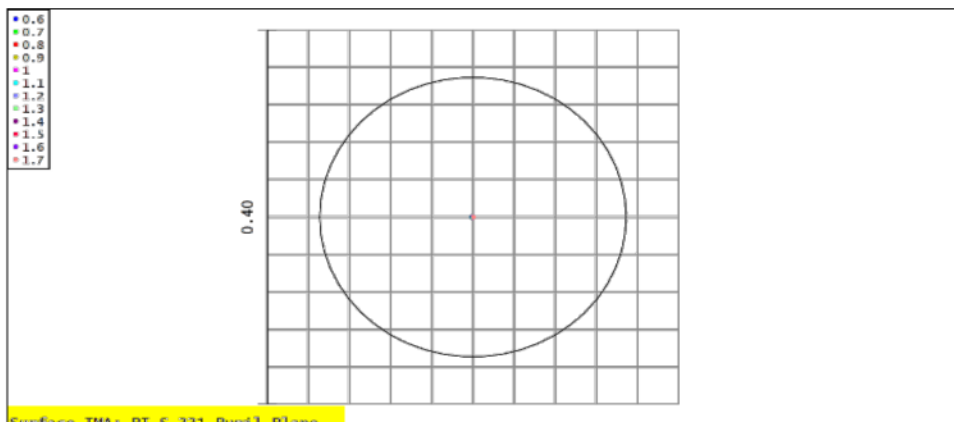
Surface IMA: Woofer DM Pupil Plane

Spot Diagram	
Magellan With f/11 Secondary	
2/16/2017	Airy Radius: 0.1029 mr. Legend items refer to Wavelengths
Units are mr.	
Field : 1	
RMS radius : 0.000	
GEO radius : 0.001	
Scale bar : 0.4	Reference : Chief Ray



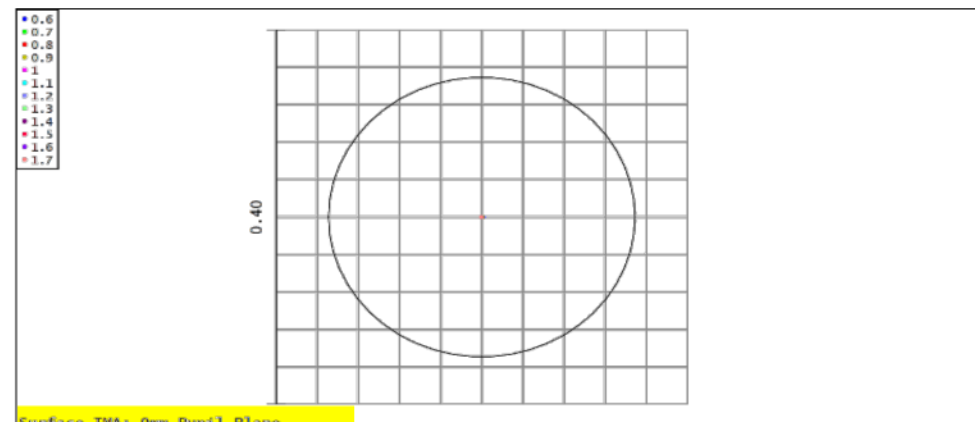
Surface IMA: Tweeter DM Pupil Plane

Spot Diagram	
Magellan With f/11 Secondary	
2/16/2017	Airy Radius: 0.07137 mr. Legend items refer to Wavelengths
Units are mr.	
Field : 1	
RMS radius : 0.000	
GEO radius : 0.001	
Scale bar : 0.2	Reference : Chief Ray



Surface IMA: PI S-331 Pupil Plane

Spot Diagram	
Magellan With f/11 Secondary	
2/16/2017	Airy Radius: 0.1491 mr. Legend items refer to Wavelengths
Units are mr.	
Field : 1	
RMS radius : 0.001	
GEO radius : 0.003	
Scale bar : 0.4	Reference : Chief Ray

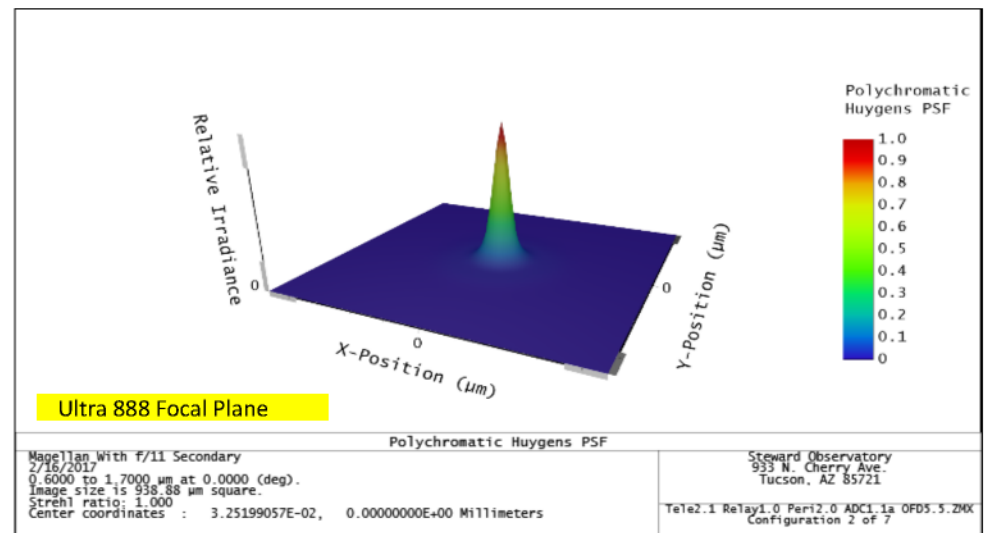
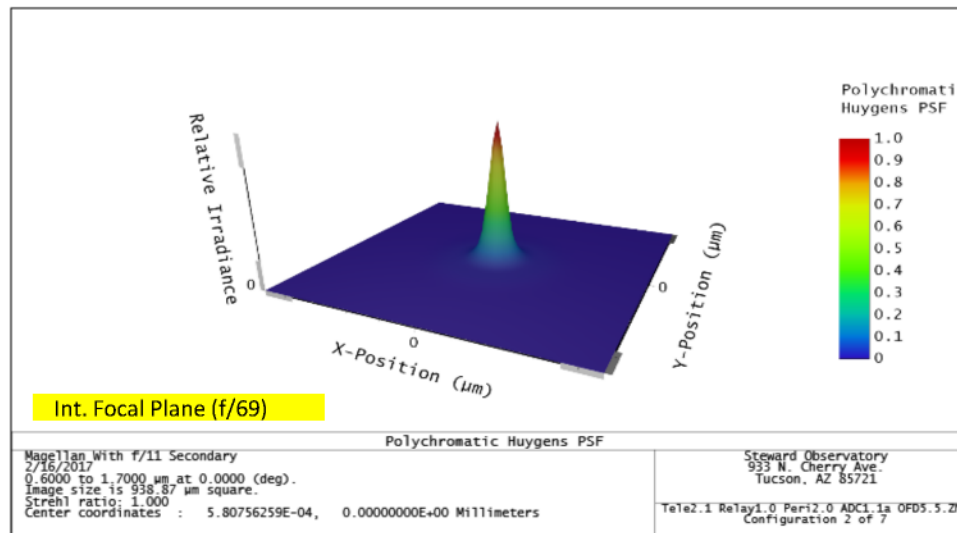
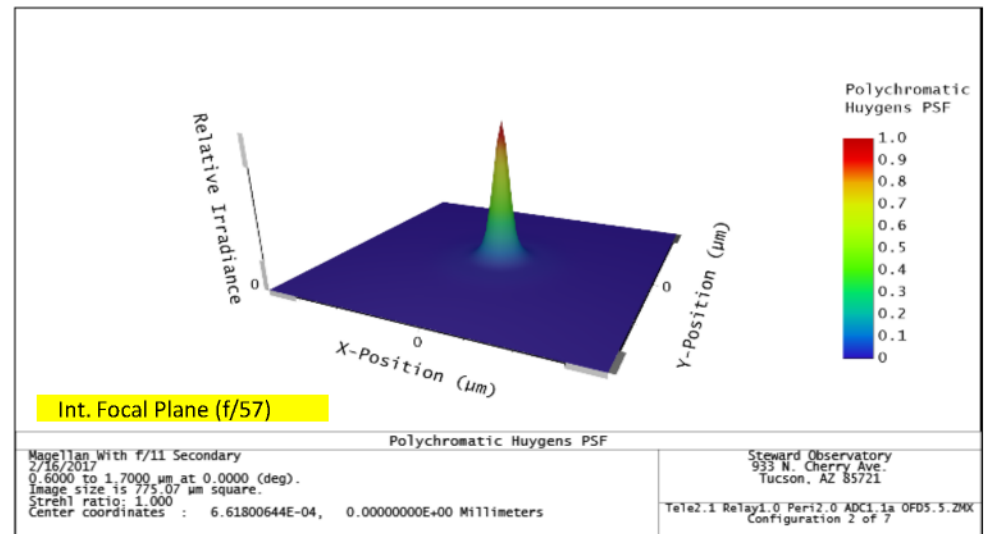
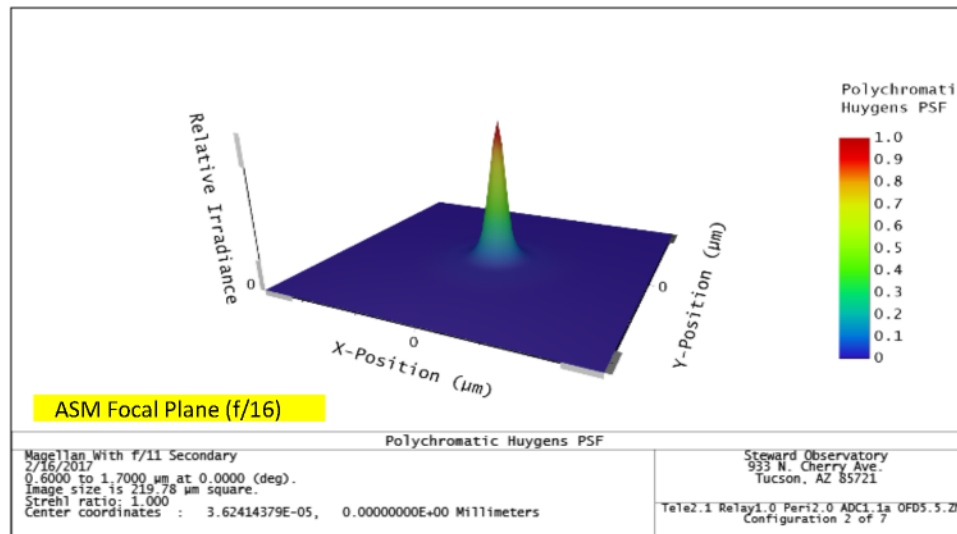


Surface IMA: 9mm Pupil Plane

Spot Diagram	
Magellan With f/11 Secondary	
2/16/2017	Airy Radius: 0.1491 mr. Legend items refer to Wavelengths
Units are mr.	
Field : 1	
RMS radius : 0.001	
GEO radius : 0.003	
Scale bar : 0.4	Reference : Chief Ray

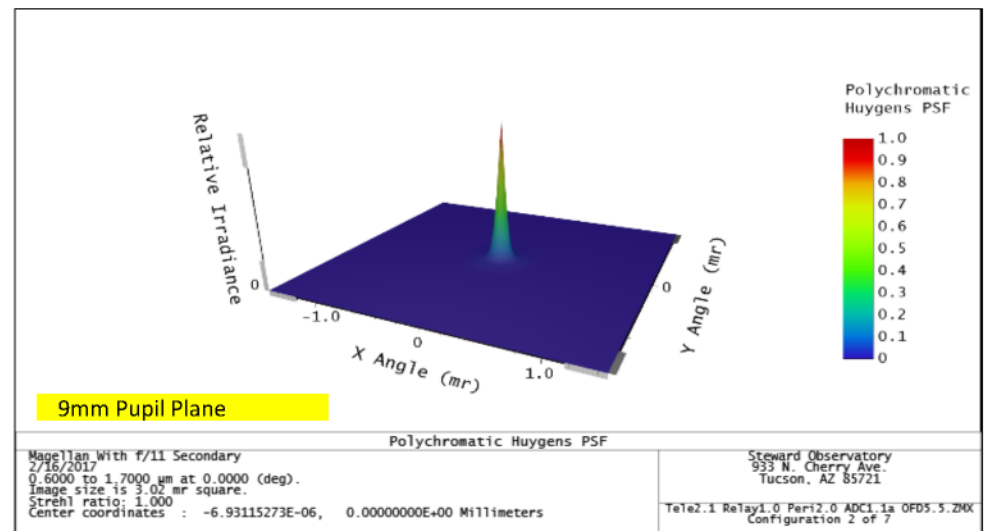
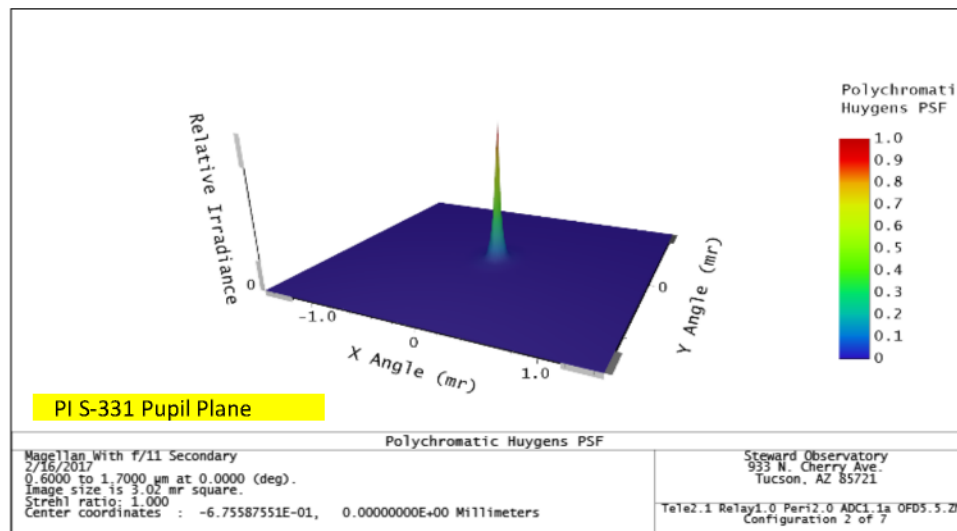
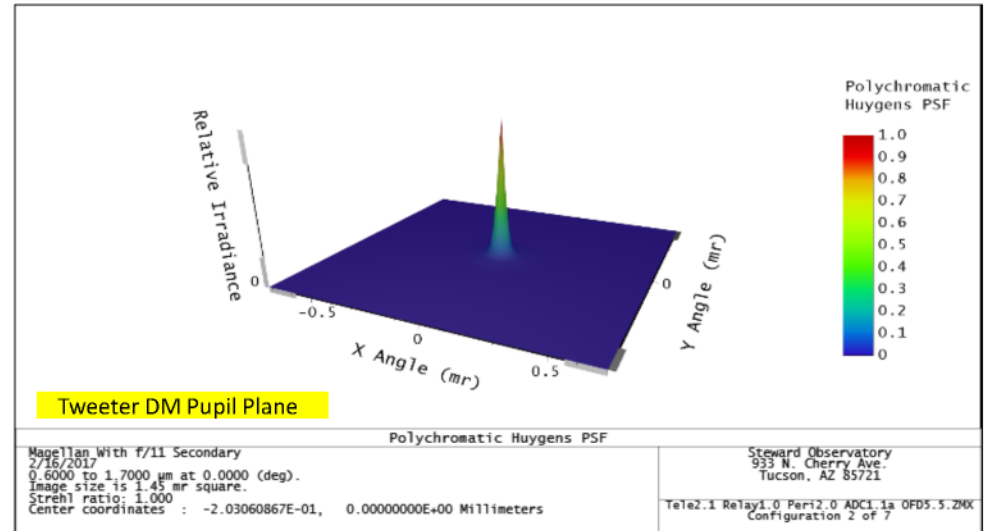
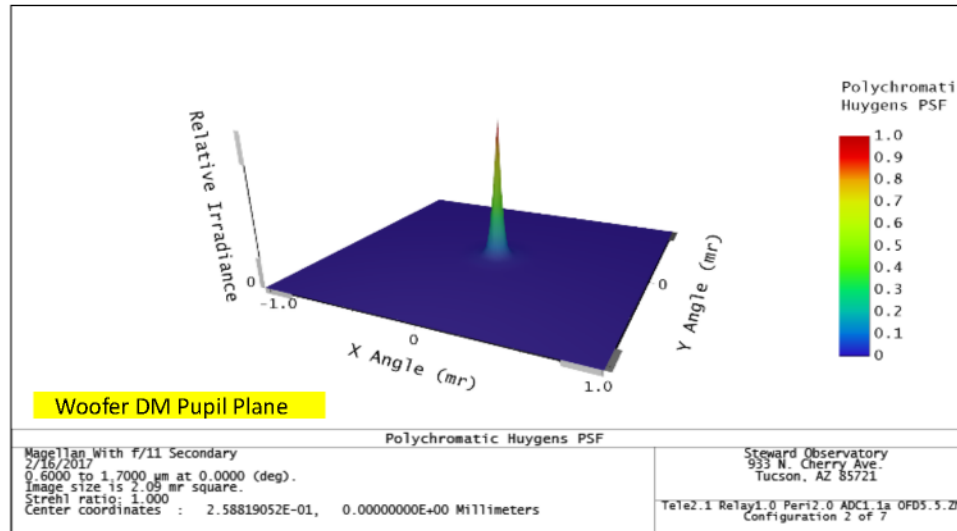


PSF at Focal Planes





PSF at Pupil Planes





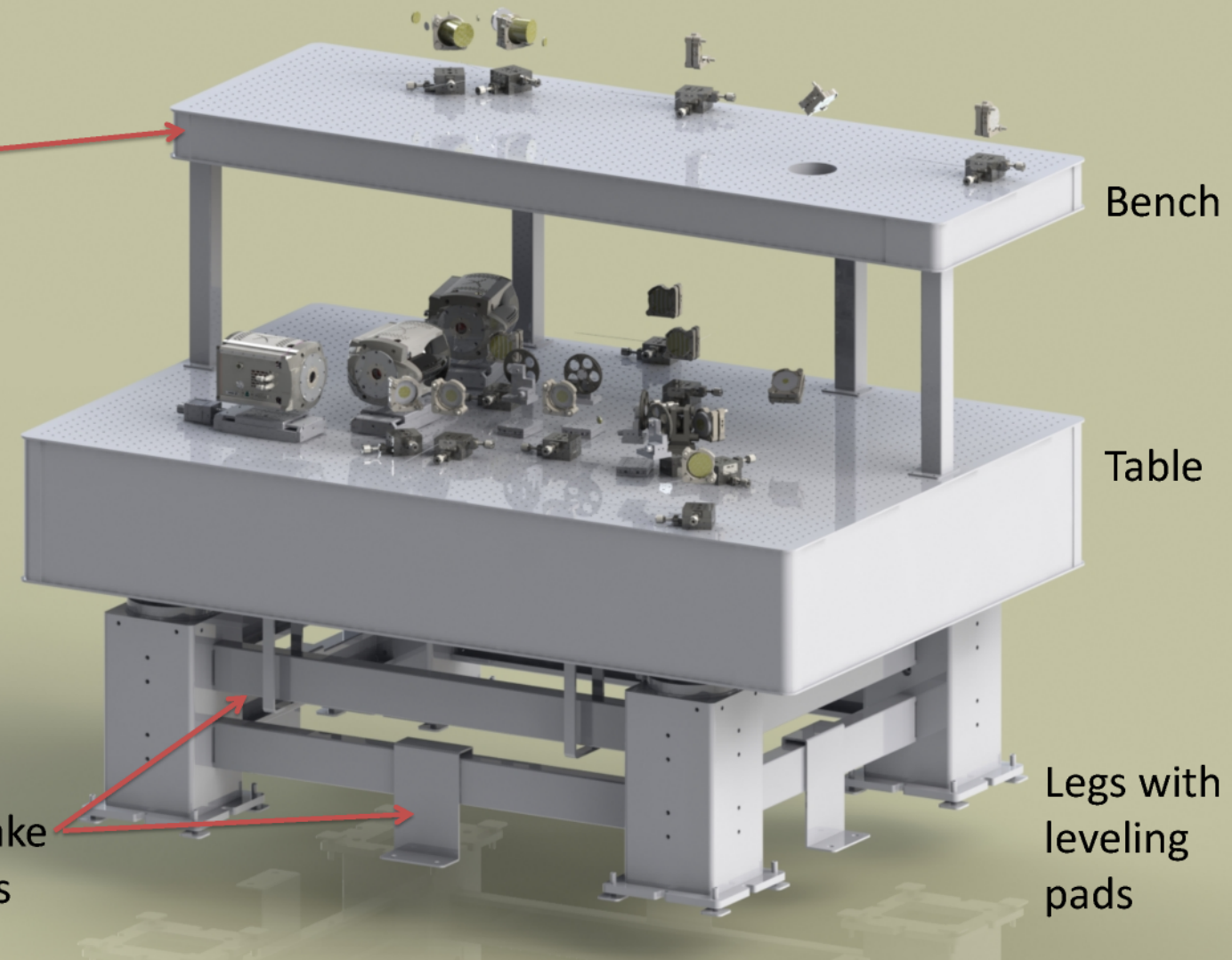
Mechanical Solid Model

Solid works design by Corwynn (Cork) Sauve, Steward Observatory



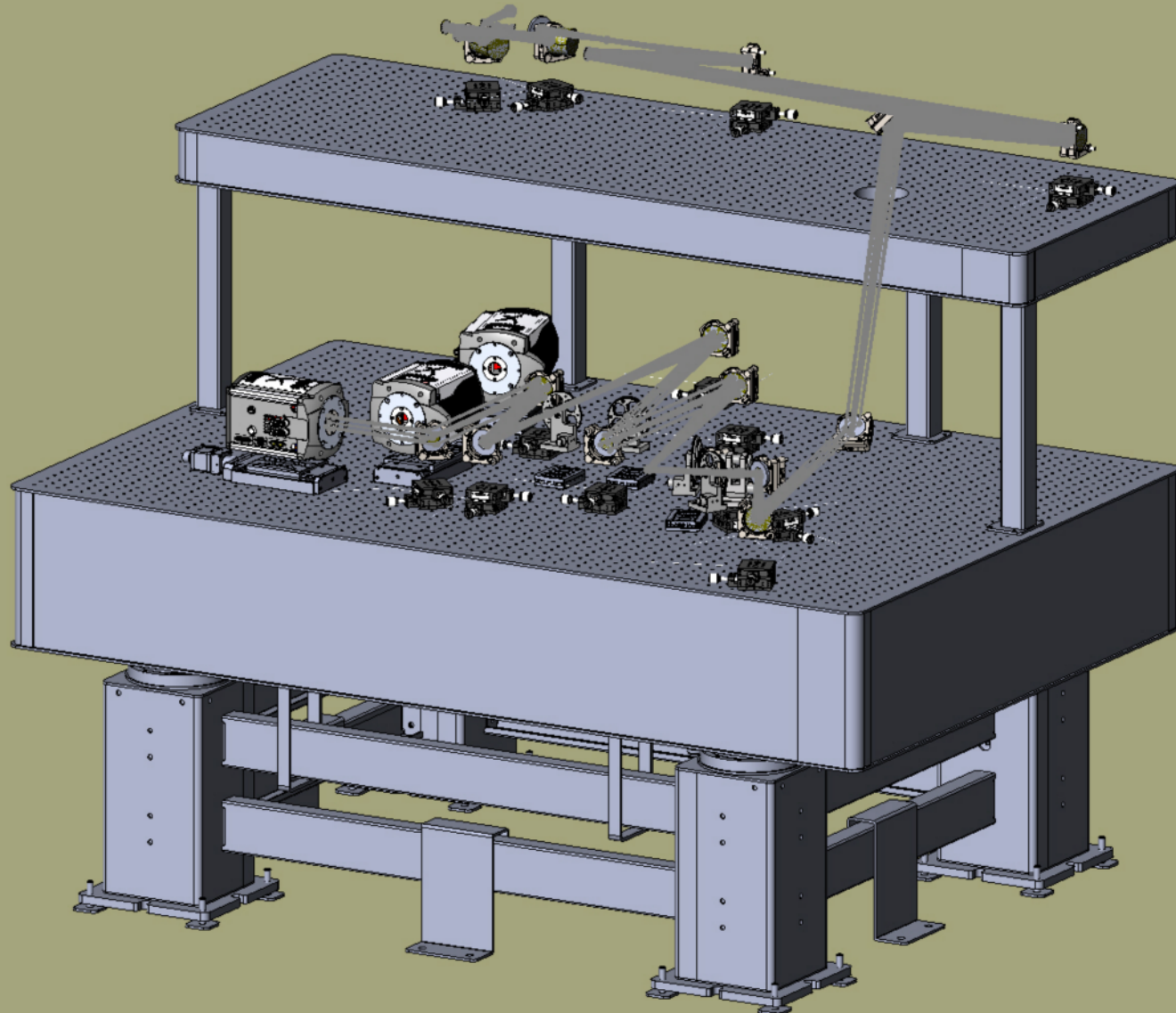
Mechanical Solid Model With TMC Table

All gray components (bench, table, and legs) are a single custom build, of our design, offered by TMC



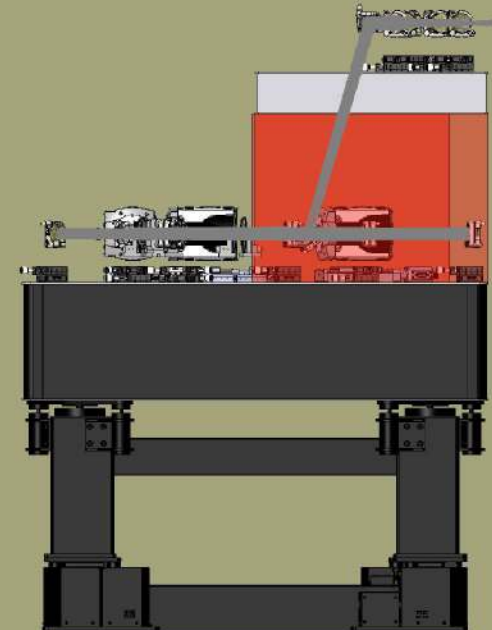
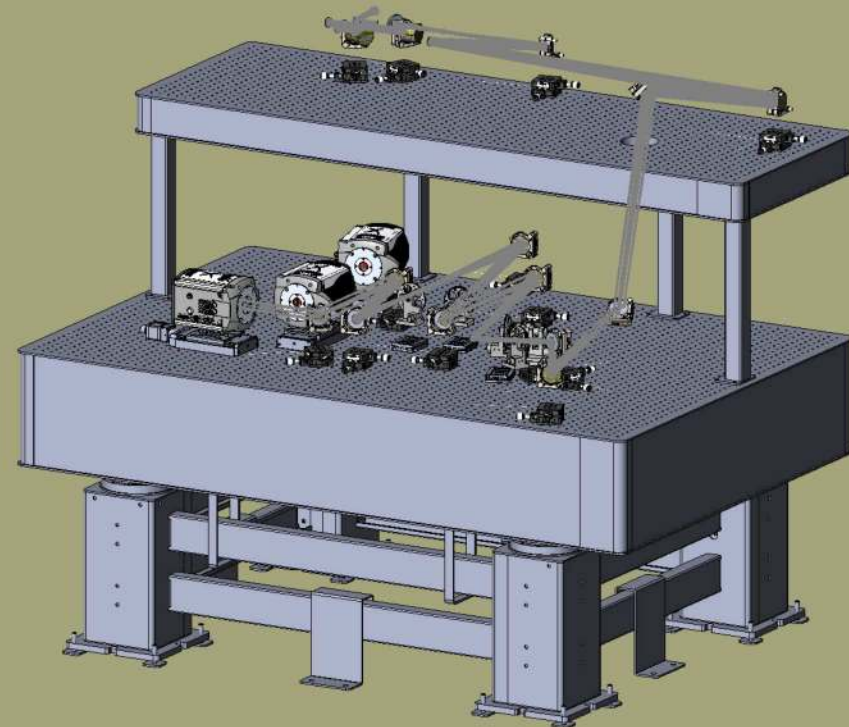


Full Science FOV (10") Rays

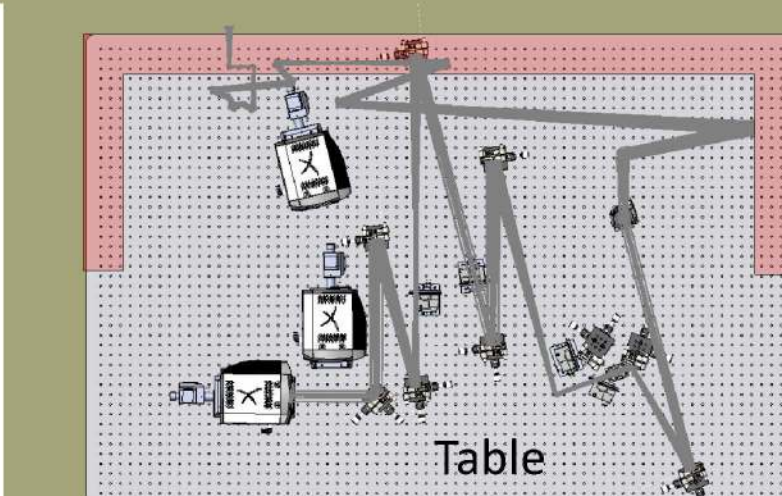




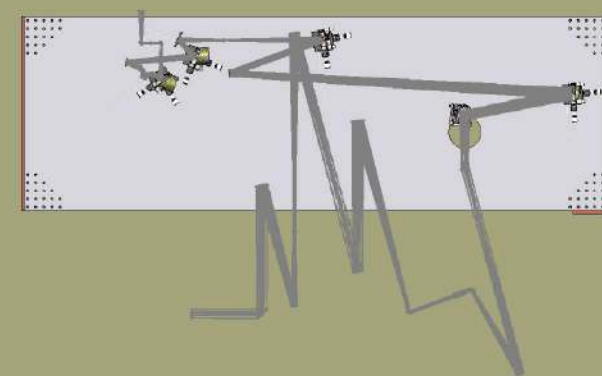
10" Rays



5 inch b
height
through



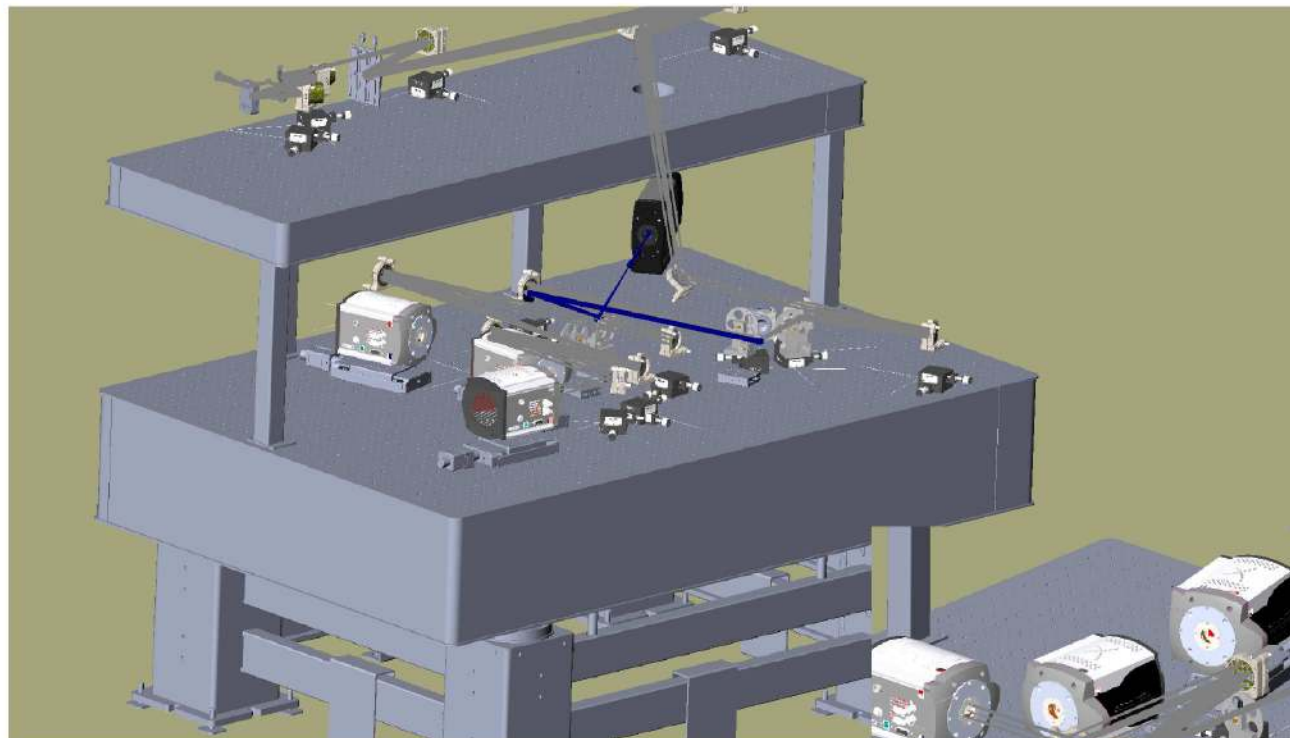
All the optics,
mounts, and
cables fit on
the bench and
Table



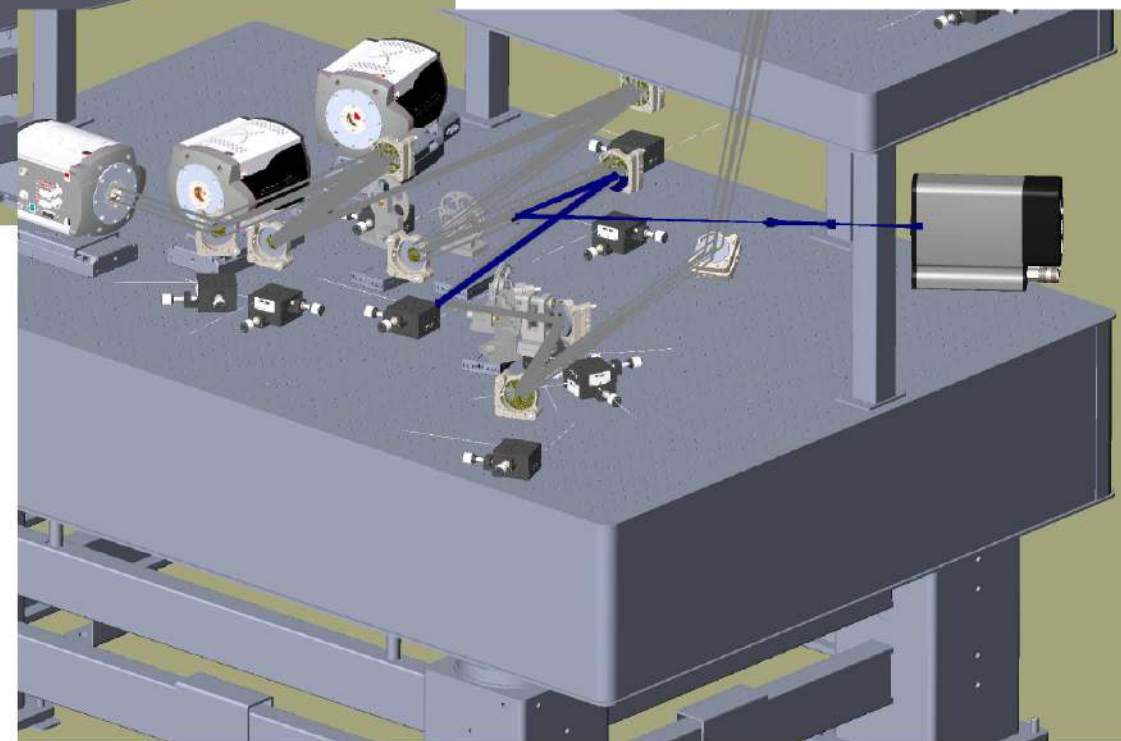
Bench

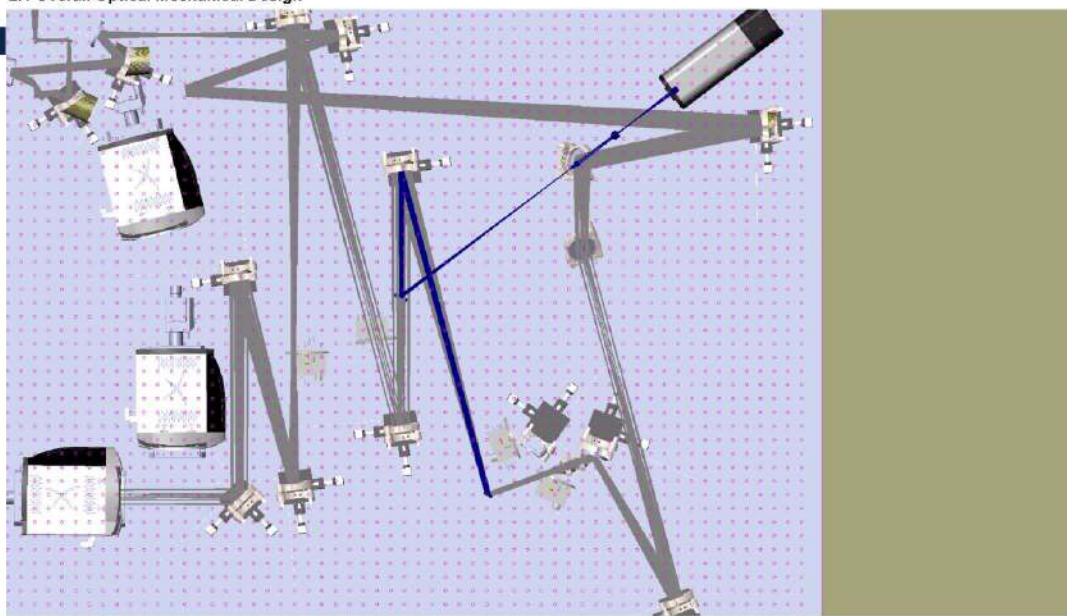


With PWFS



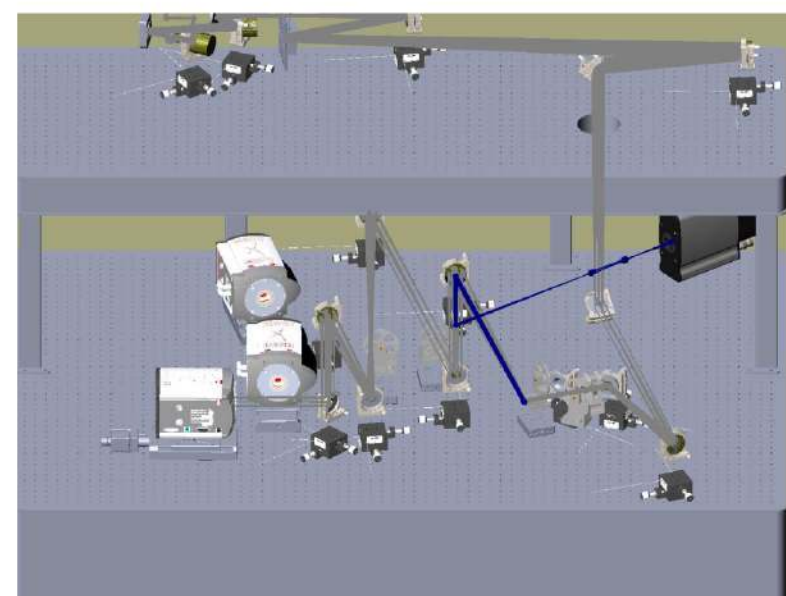
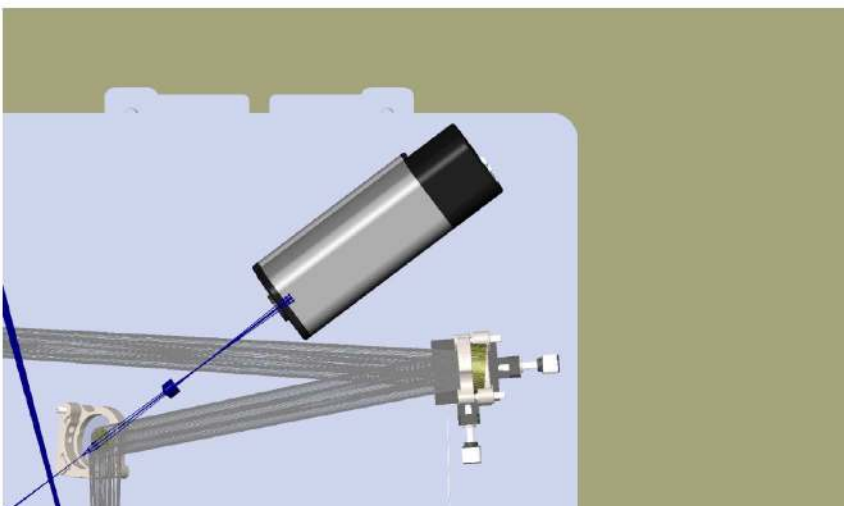
NCP rays for PWFS in blue





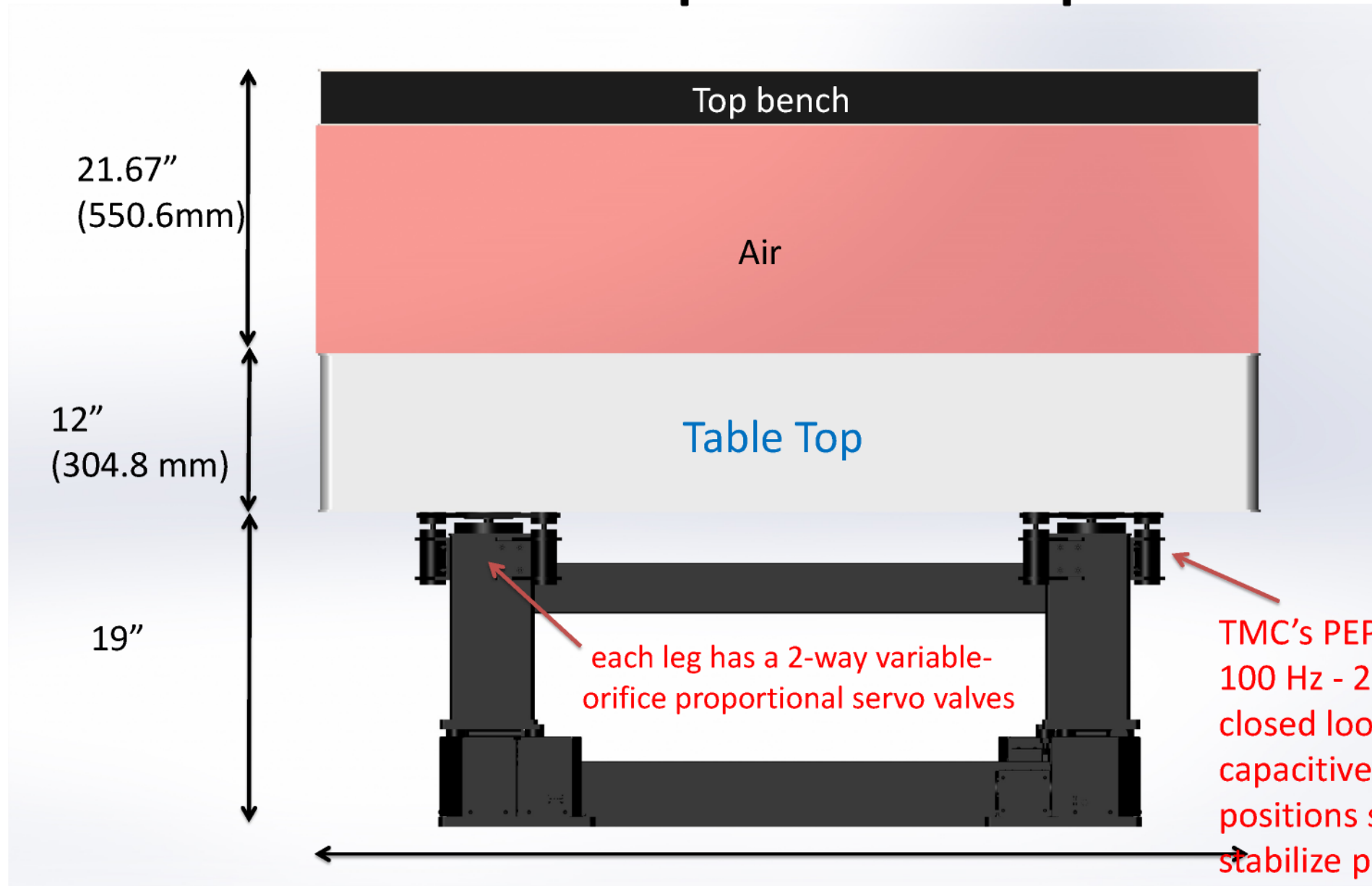
With PWFS

NCP rays for PWFS in blue



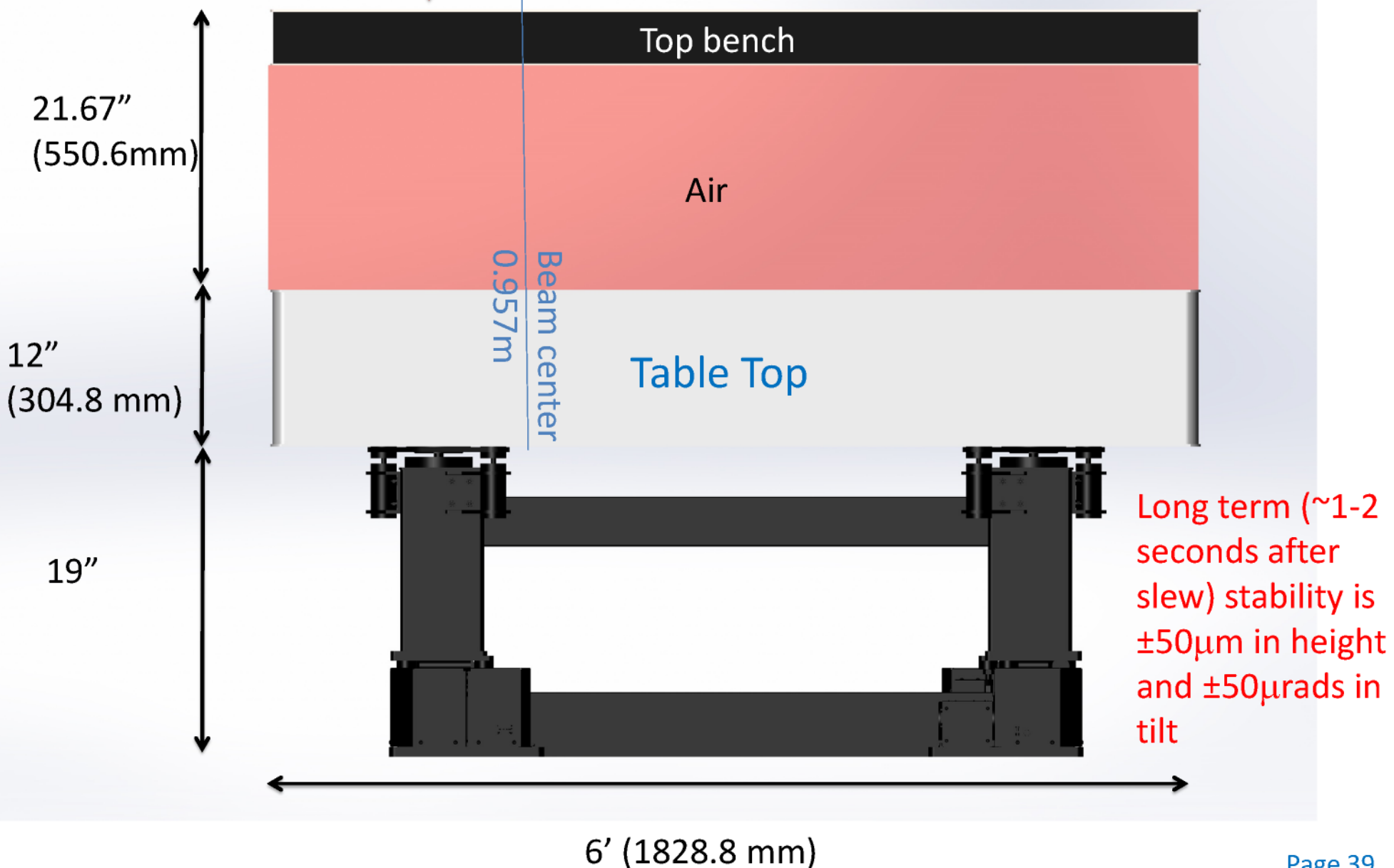


The Closed-loop Air Damped Table



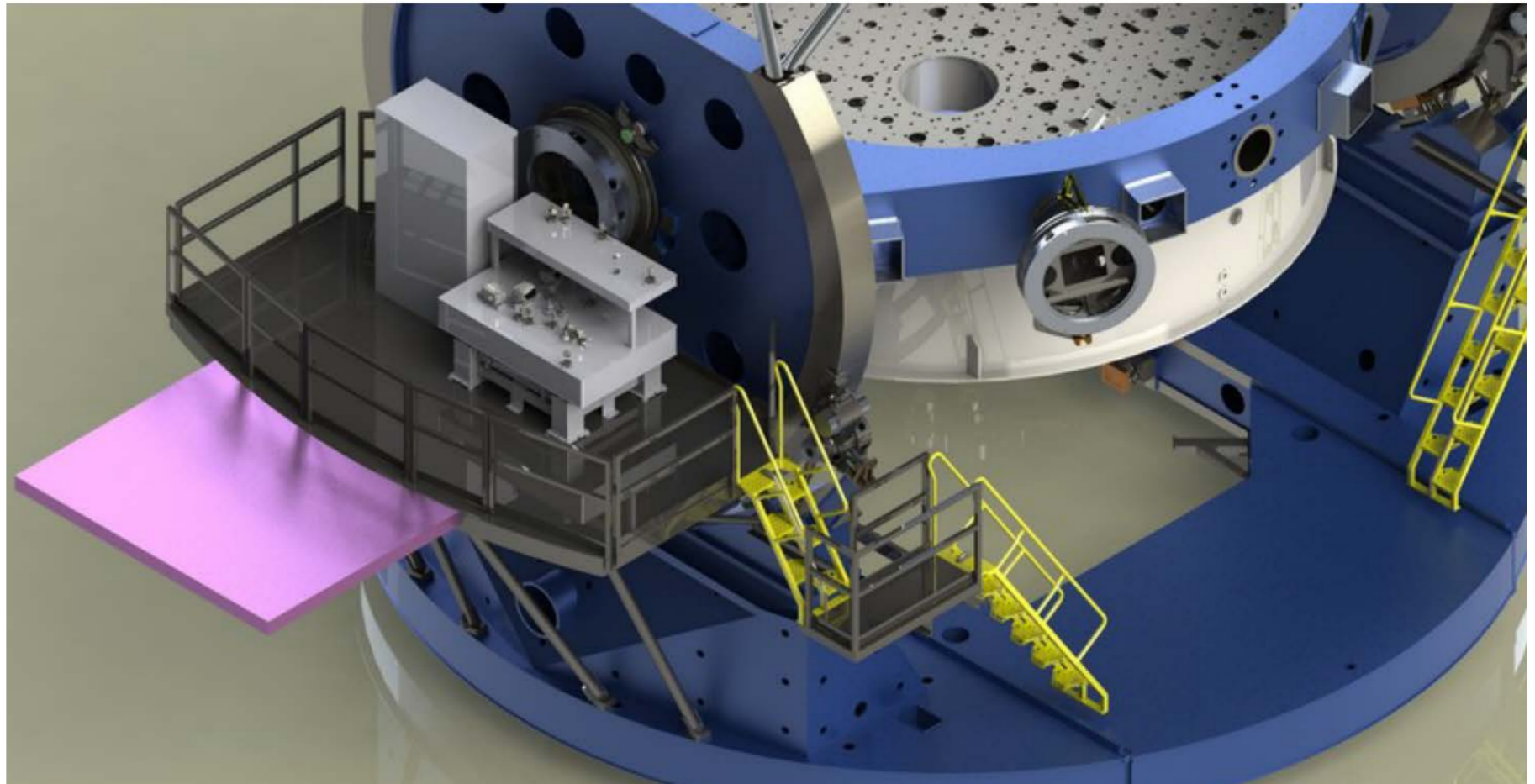


$\pm 50\mu\text{m}$ Long term Stability w.r.t. Telescope with **PEPS® II – Specifications** $\pm 50\mu\text{m}$ Variation of height \leftrightarrow $\pm 47\mu\text{m}$ with $\pm 50 \mu\text{radians}$ of tilt variation



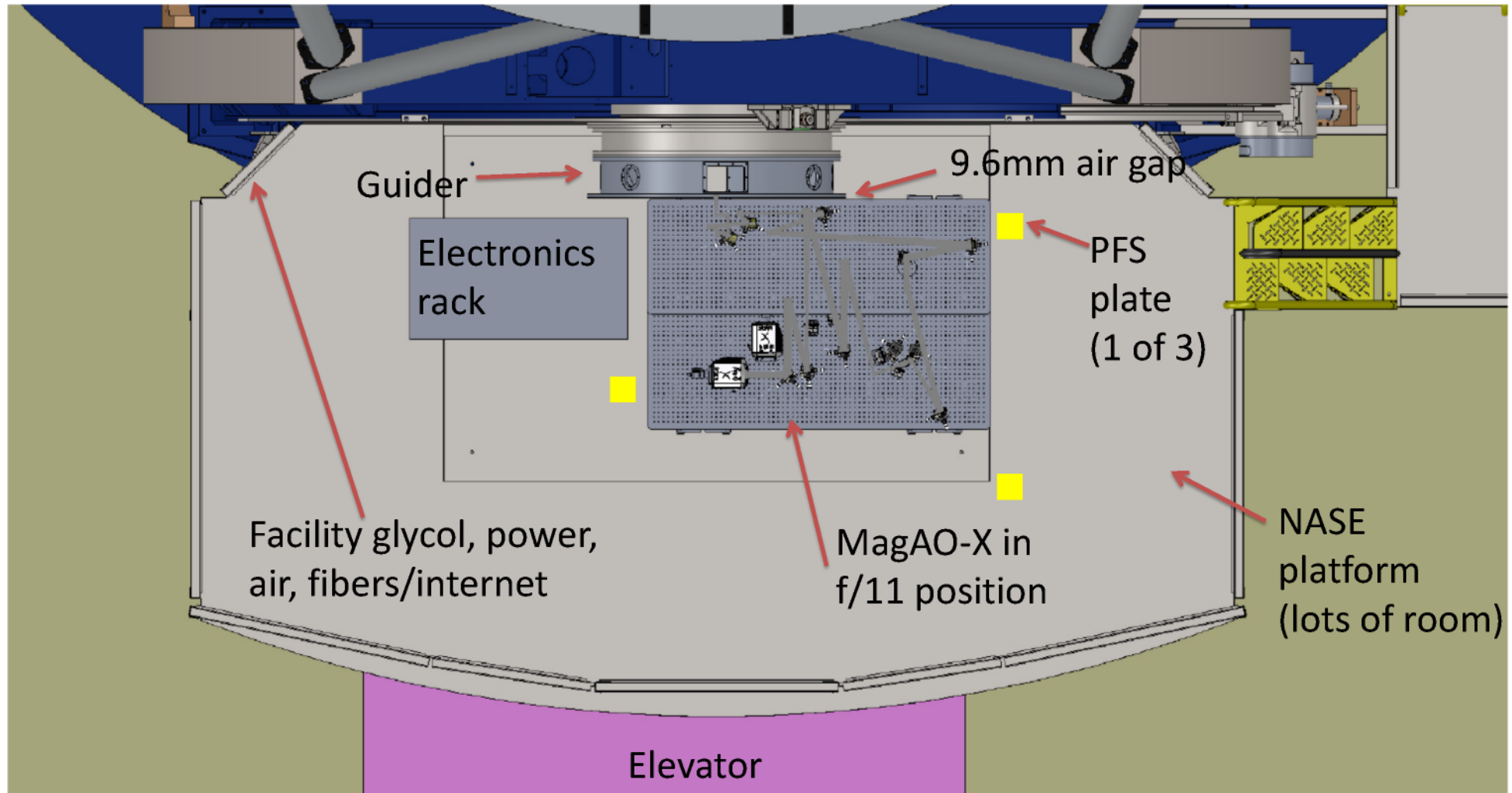


Completed Design At Magellan





MagAO-X fits on the NASE





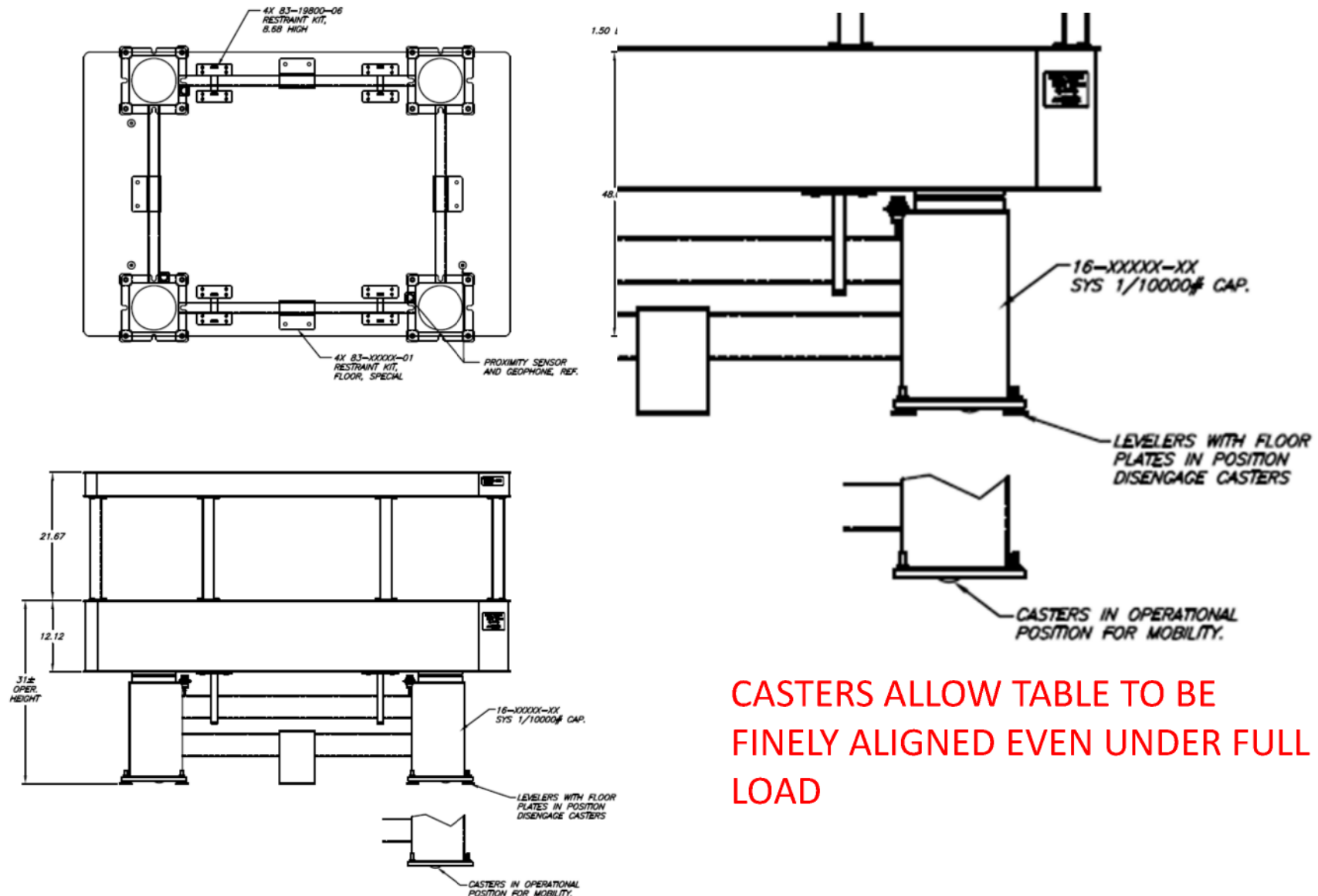
Unpacking and Alignment at Telescope

START: Use the Isuzu truck to move the shipping box to the lift gate at summit, then hand truck to elevator, then:

- 1)** hand truck shipping box to telescope observing floor off of the elevator
- 2)** Independently, position our legs (on their casters) to the correct X position of the legs w.r.t. the guider center of the NASE platform. So all that is needed is a straight push (in Y) towards the guider, rotate the casters in the Y direction.
(Note: we could use a simple piece of angle bar bolted to the hatch to guarantee the casters motion in Y only once the Table is attached- TBD)
- 3)** lift up the 5 sided top of the shipping box -- rotate dome and place beside Table.
- 4)** pull bench out of shipping box base with overhead jib crane and lifting triangle
- 5)** lower the Table onto the legs with crane, remove Triangle.
(NOTE: the Table/Legs alignment is guaranteed with alignment pins (that slide into the tiebars on legs) that are bolted onto in the tapped holes for earthquake brackets -- these pins are already attached when we are shipping the bench)
- 6)** Now slowly push the whole assembly on the casters towards the guider until the air gap is 9.6mm then stop.
- 7)** Carefully engage all 16 leveling pads (disengaging the casters)
- 8)** remove alignment pins and add the missing 2 upper earthquake brackets.
- 9)** Add the lower earthquake brackets
- 10)** cable up the system, etc.



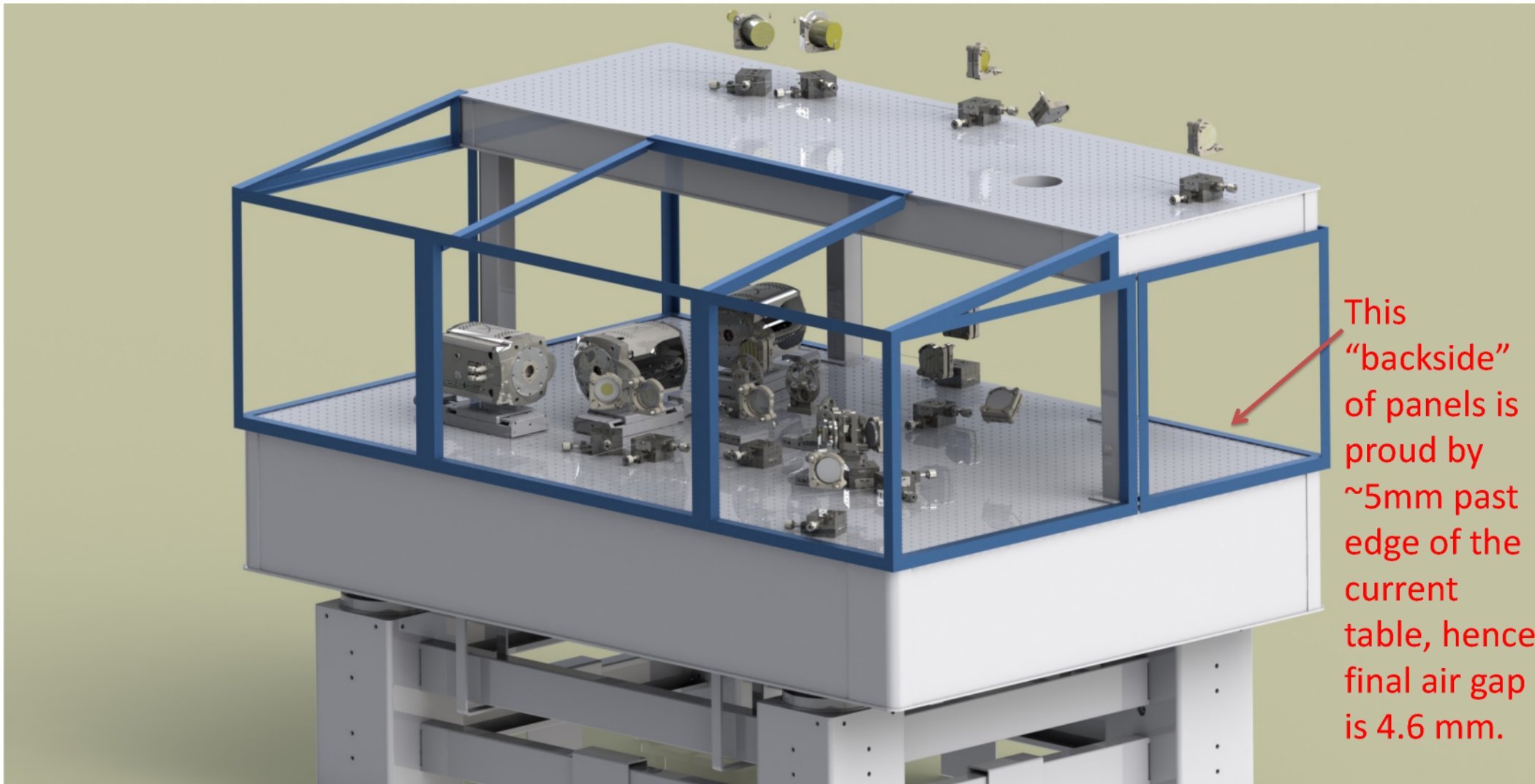
Unpacking and Alignment at Telescope



CASTERS ALLOW TABLE TO BE
FINELY ALIGNED EVEN UNDER FULL
LOAD

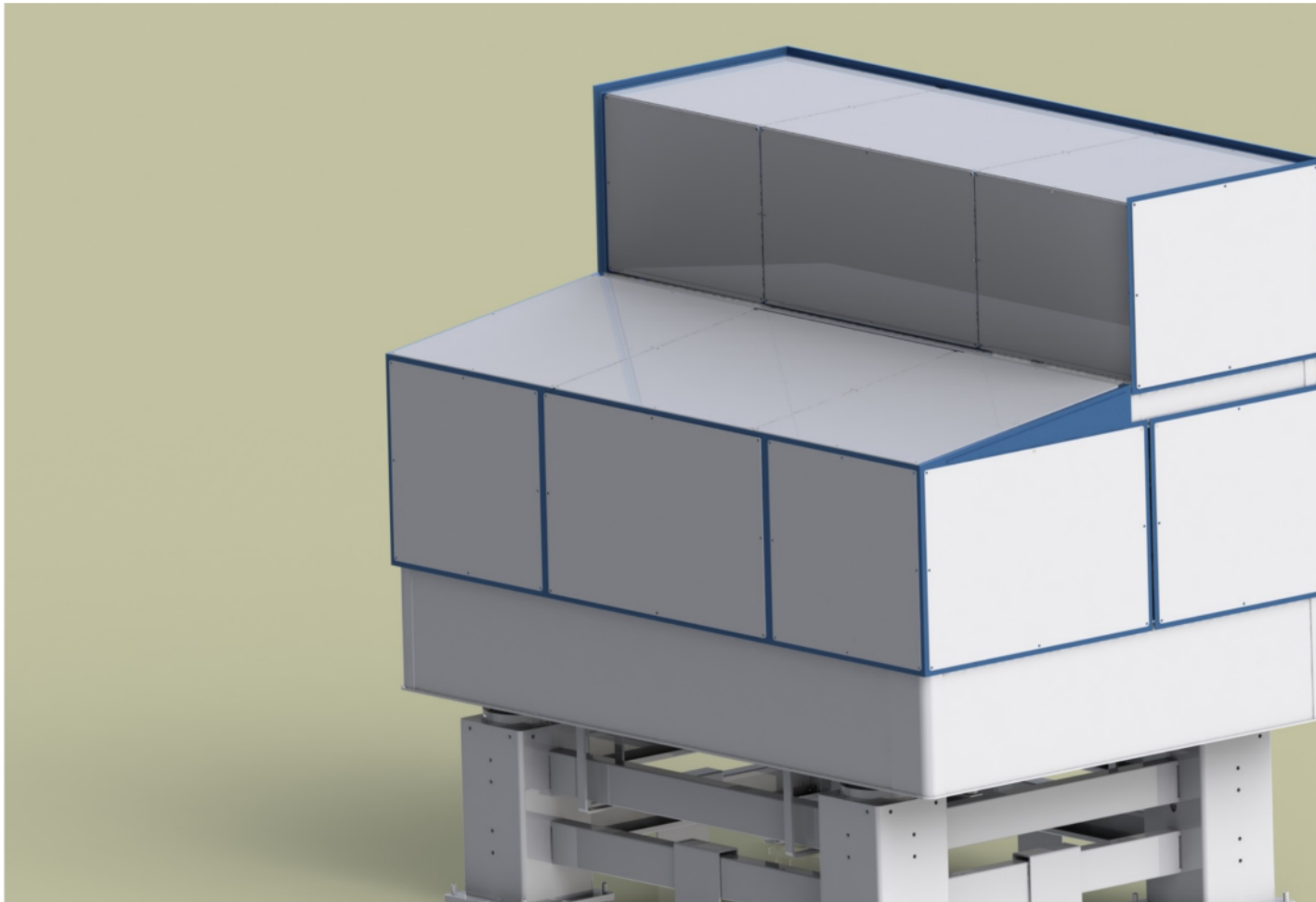


Wind/dust screen





Wind/dust screen



MagAO-X as
it will
appear for
observing
(or shipping)
with dust
covers
attached



2.2 Wavefront Sensor Design

Lauren H. Schatz, Oli Durney, Jared Males

1 Pyramid Wavefront Sensor Overview

The MagAO-X system uses a pyramid wavefront sensor (PWFS) for high order wavefront sensing. The wavefront sensor delivers four pupils sampled by 56 pixels across, giving 2662 illuminated sub-apertures, to control the 2048 actuators on the Boston Micromachines DM tweeter, and 97 actuators on the ALPAO woofer.

2 System Requirements

The pyramid wavefront sensor of the MagAO-X system consists of a prism pyramid, a camera lens, and a OCAM²K EMCCD detector. We use the same four sided double pyramid as the MagAO and LBTAO systems. The MagAO-X pyramid wavefront sensor is designed to operate from 600-1000nm bandwidth. Figure 1 is the bandpass of the MagAO PWFS. We expect a similar transmission for the MagAO-X PWFS.

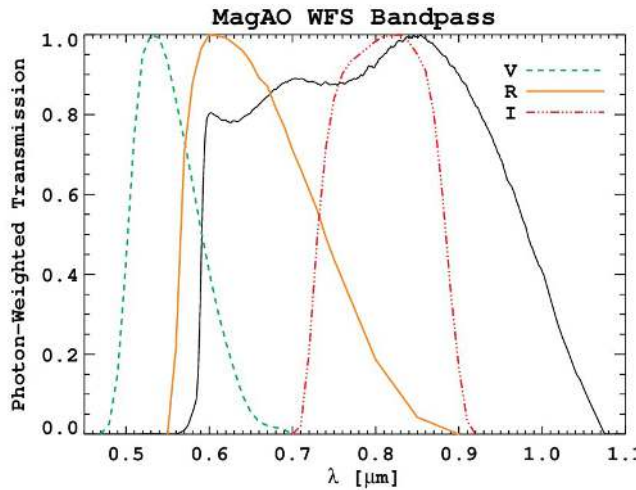


Figure 1: The MagAO pyramid wavefront sensor bandpass.

A new camera lens is designed to meet the requirements of the MagAO-X system. These requirements



are listed below. The OCAM²K will be used in 2x2 binning mode, giving us a 48 μm pixel size.

Parameter	Requirement
Wavelength Range	600- 1000 nm
Pupil Size	56 pixels; 2.688 mm
Pupil Separation	60 pixels; 2.880 mm
Pupil Tolerances	$\Delta < 1/10$ th pixel; 2.4 μm
Lens Diameter	10 mm < D < 20 mm

2.1 Pyramid Design: MagAO-X will be using a copy of the pyramid prism used in both the LBTAO and MagAO systems. The pyramid is already in hand. A picture of the pyramid is shown in Figure 2. Details of the design done by Tozzi et. al. are summarized here.(1) The pyramid used in the WFS is a double pyramid, consisting of two four sided prisms aligned back to back. The schematic of the double pyramid is given in Figure 3. The total deviation angle needed for the pyramid wavefront sensor is hard to manufacture. Combining two pyramids makes the polishing process easier and at the same time allows us to control chromatic aberrations by using two different glass types. The glass types were chosen using an I.D.L. optimization routine that selected glass combinations from the Shott and Hoara catalog that would give a suitable deflection angle of the double pyramid. The front prism is made from Shott N-SK11, and the back prism is made from Shott N-PSK53.

2.2 Wavefront Sensor Design: A design of the wavefront sensor was done in Zemax. A table of the element thicknesses (or distances), and radii of curvatures pulled from Zemax is shown in table 2. The wavefront sensor consists of the double pyramid. A F/69 focus created by OAP5#1 is imaged onto the pyramid tip. A custom achromatic triplet images four pupils onto our OCAM²K wavefront sensor camera. A layout of the wavefront sensor optical path done in both Zemax and SolidWorks is shown in Figure 5. Upstream not shown is the wavefront sensor dichroic pickoff. Except for the high precision flat and dichroic, the light to the wavefront sensor uses the same optical surfaces as the rest of the upstream system to reduce non common path errors. The double pyramid was modeled by the Arcetri team in Zemax, and that same model is used here. A custom achromatic triplet was designed to give the correct pupil size and separation. The two windows in the OCAM²K detector are included in the design for completeness. The expected pupil footprint on the image plane for 800 nm wavelength is given in Figure 4.

2.3 Achromatic Triplet Design: Pupil sizes and separation are a vital parameter in the operation and performance of pyramid wavefront sensors. A custom achromatic triplet was designed in Zemax, and optimized to give the same pupil size and separation from the 600-1000 nm wavelength range. A schematic of the lens is shown in Figure 6. The OPD error expected from the triplet is expected to be less than 0.5 waves across our wavelength band. The OPD fan is given in Figure 7.

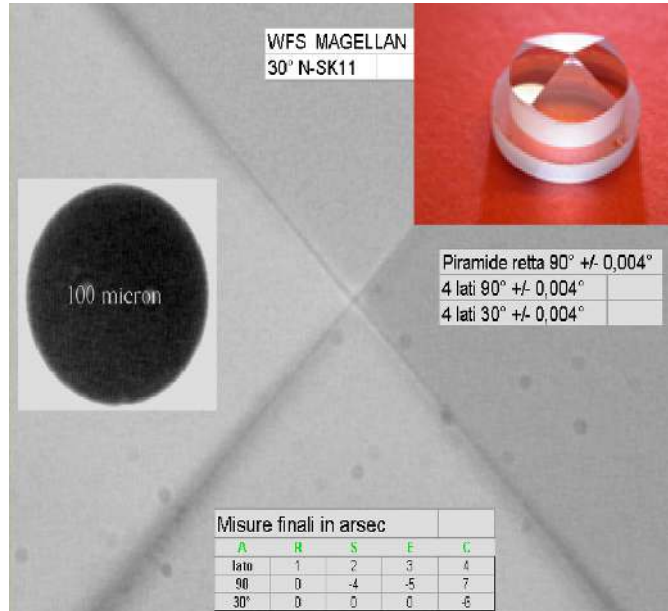


Figure 2: Fabricated pyramid made in Arcetri.

A tolerance analysis was performed to determine lens performance as a function of wavelength and manufacturing constraints. The tolerancing was done using parameters from the Precision grade Optimax manufacturing tolerancing chart. Reasonable values of alignment errors were estimated and included in the tolerancing analysis. The figure of merit used was the RMS angular radii of the lens because the pyramid is an afocal system. A 500 trial Monte Carlo simulation was done for three wavelengths, 600nm, 800nm, and 1000nm. At each wavelength the nominal, mean, and worst RMS angular size (twice the angular radii) was recorded. The difference of the mean and worst angles with respect to the nominal value was calculated. That change in angle was propagated through the system to estimate the change in size we would expect. The propagation is shown in Figure 8, where θ_n is the nominal RMS angular size, and θ_Δ is the change in RMS angular size we use to calculate the estimated change Δy . The distances $x_1 \dots x_5$ were taken from the Zemax design, and the indices n_1, n_2, n_3 correspond to air, BK-7, and Sapphire respectively. The index of refraction was adjusted for the different wavelengths when the propagation was calculated. The propagation was calculated using trigonometry and Snell's law. The results are summarized in Figure 9, where the change in size in nanometers is graphed against wavelength. At worst we expect about a 45 nm change in pupil size and separation, and no change on average. Both are well within our tolerance of the change being no greater than 1/10th a pixel, or $2.4\mu\text{m}$.



MagAO-X Preliminary Design 2.2 Wavefront Sensor Design

Doc #: MagAOX-PDR-001
Date: 2017-04-21
Status: Rev. 0.0
Page: 4 of 8

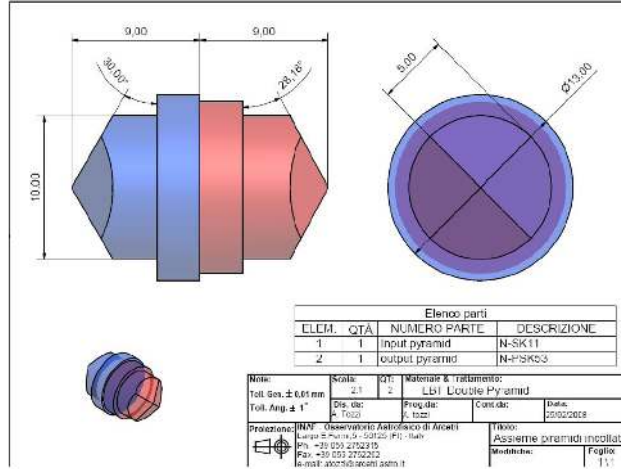


Figure 3: Mechanical design of the DP for LBT. The selected glass are produced by Schott. The diameter of the two pyramid bases are different to distinguish them and to facilitate the mounting.

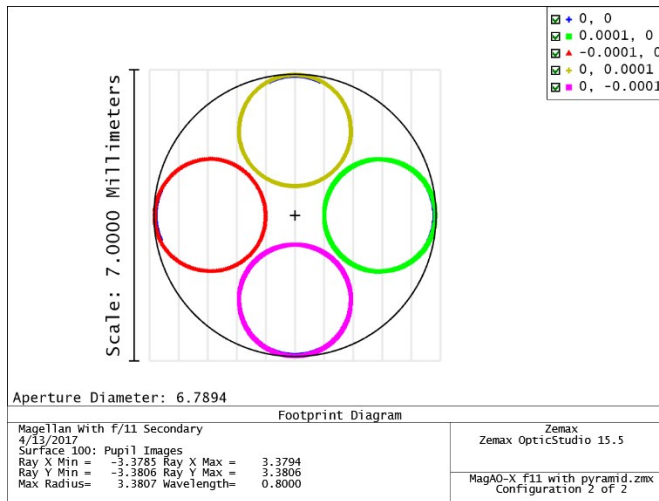


Figure 4: Beam footprint at the image plane done in Zemax.

3 System Performance

A simulation of the expected partial illumination of pupil pixels was done in MATLAB. A binary model of the MagAO-X pupil was generated with 10 times the spatial sampling than our expected PWFS



MagAO-X Preliminary Design

2.2 Wavefront Sensor Design

Doc #: MagAOX-PDR-001
Date: 2017-04-21
Status: Rev. 0.0
Page: 5 of 8

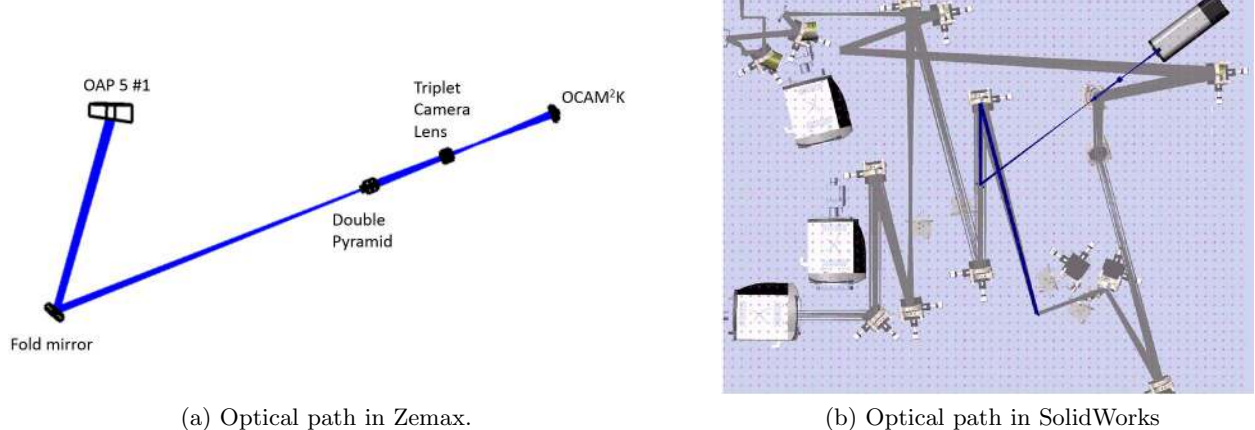


Figure 5: Optical path of the pyramid wavefront sensor. The Zemax ray trace was imported into SolidWorks for the optomechanical design.

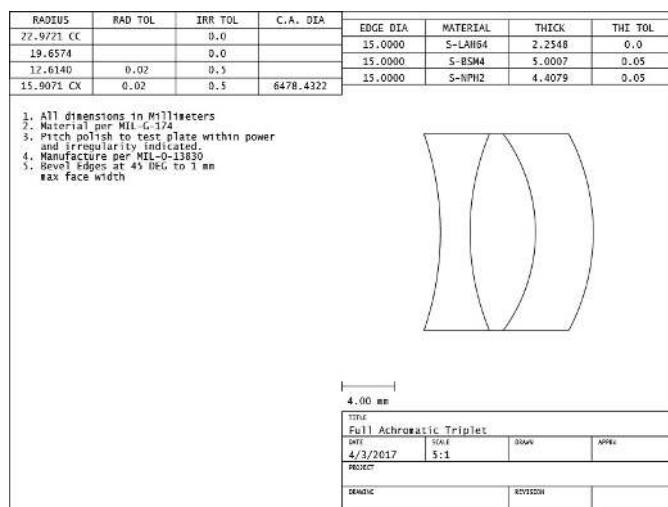


Figure 6: Achromatic triplet.

pupil. We then bin down to the expected pupil sampling of our PWFS. That is we start with a pupil of 560 by 560 pixels, and bin down to a 56 by 56 pixel pupil by summing 10 by 10 pixel bins and normalizing. The expected illumination pattern is given by Figure 10.a. A table of the pixel counts are given in Table 1. where the pixel value is given on the X-axis, and the number of pixels with that value are given on the Y-axis. We expect 1958 fully illuminated pixels across our pupil.



MagAO-X Preliminary Design

2.2 Wavefront Sensor Design

Doc #: MagAOX-PDR-001
Date: 2017-04-21
Status: Rev. 0.0
Page: 6 of 8

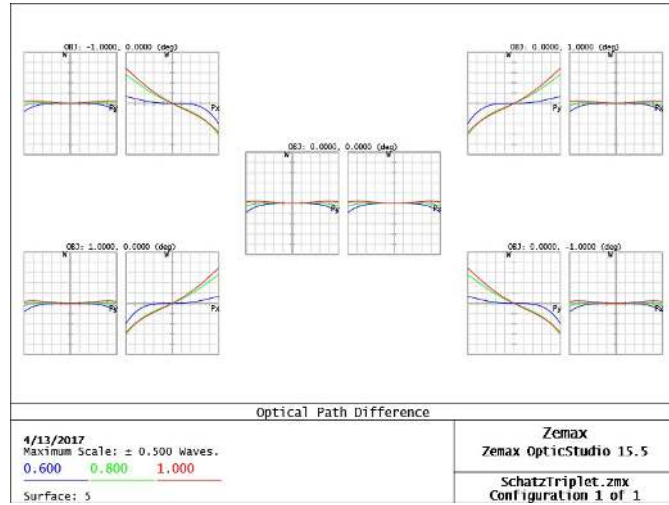


Figure 7: OPD fan of the achromatic triplet.

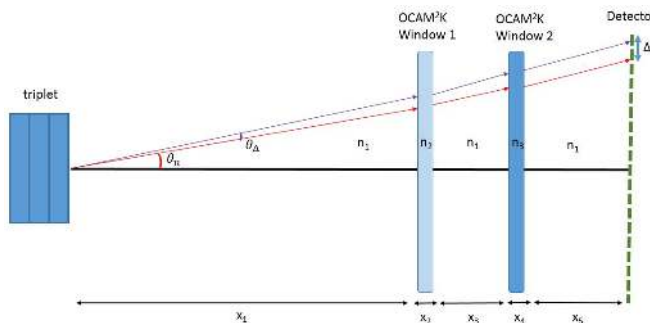
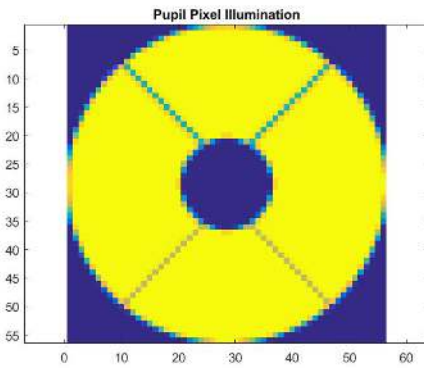


Figure 8: Diagram of the light propagation path used to calculate the change in pupil size.



% Illumination	# of Actuators
100%	1958
90%	166
80%	24
0%	46
60%	20
50%	18
< 50%	904

Figure 10: Expected pupil illumination on the PWFS.

Table 1: Pixel illuminations in the 56 by 56 pixel pupil.

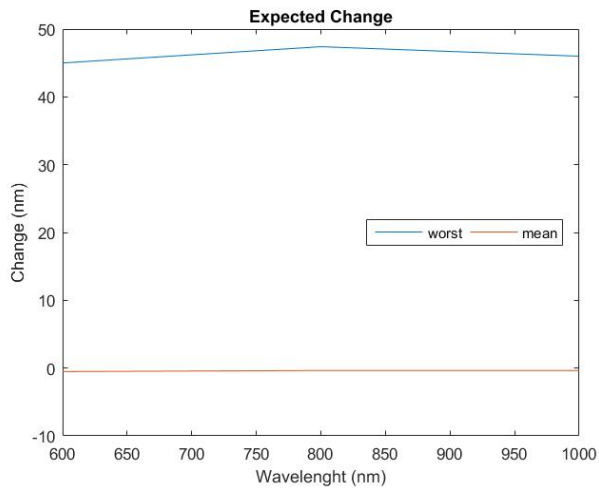


Figure 9: Expected change in pupil size as a function of wavelength.

References

- [1] A. Tozzi, P. Stefanini, E. Pinna, S. Esposito, "The Double Pyramid wavefront sensor for LBT", in Adaptive Optics Systems, Proceedings of SPIE, (2008). Vol. 7015, 701558



MagAO-X Preliminary Design
2.2 Wavefront Sensor Design

Doc #: MagAOX-PDR-001
Date: 2017-04-21
Status: Rev. 0.0
Page: 8 of 8

Element #	Surface	Radius of Curvature	Thickness
76	OAP5#1	1220.83984	0
77	Propagation #1	Infinity	200
78	Coordinate Break	Infinity	0
79	Fold Mirror 2	Infinity	0
80	Coordinate Break	Infinity	-389.625
81	Int. Focal Plane (f/69)	Infinity	0
82	dummy Pyramid Entrance	infinity	-1.5
83	PYR 30°	Non-Sequential	0
84	Dummy Out	Non-Sequential	0
85	PYR 30° Base	Non-Sequential	-6.16384
86	PYR 28° base	Non-Sequential	-6.23166
87	Dummy In	Non-Sequential	0
88	PYR 28°	Non-Sequential	0
89	Dummy Out	Non-Sequential	0
90	Propagation	Infinity	-80
91	Triplet Front Surface	-15.88071497	-4.41266
92	Triplet	-12.61981892	-5.00127
93	Triplet	19.13048337	-2.21407
94	Triplet Back Surface	-23.03743881	0
95	propagation	Infinity	-130
96	OCAM window	Infinity	-3
97	propagation	Infinity	-0.82
98	CCD 220 OCAM window	Infinity	-0.9
99	Focal Plane	Infinity	-2.83

Table 2: Table of Zemax surface elements



2.3 Alignment Plan

Kelsey Miller

1 Introduction to OAPs

The optics requiring the highest level of precision alignment within the MagAO-X beam path are the off-axis parabolic mirrors (OAPs). OAPs are fundamental to the design of MagAO-X because they are capable of delivering diffraction limited imaging (used to both collimate and focus the incoming beam at different points in the system) while deviating the incoming beam off-axis at a designed reflection angle (see Figure 1).(1) This deviation provides access to the system focal point without obstruction to the beam. OAPs also have the added benefit of being non-wavelength dependent, meaning they are free of aberration across a broad wavelength range.(2) To benefit from the high quality imaging OAPs provide, they must be precisely aligned. Below we discuss plans for initial system alignment as well as a plan to maintain that alignment after moving the MagAO-X instrument.

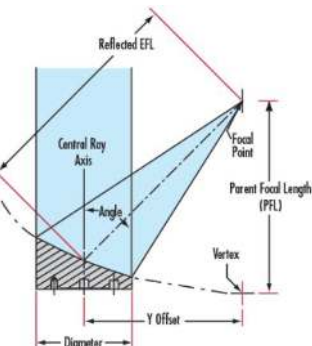


Figure 1: OAP diagram demonstrating the ability to focus an incoming collimated beam while deviating the beam off-axis at a designed reflection angle.

2 Initial Alignment

2.1 Degrees of freedom: OAPs have five degrees of freedom (DOF) accessible to the user for alignment: tip, tilt, translation in height, lateral translation, and translation along the optical path. A sixth degree of freedom key to OAP alignment is the rotation of the OAP around the optical axis; this is also referred to as clocking. This DOF however, is dealt with by having all OAPs permanently mounted by the manufacturer in the correct orientation before delivery. The remaining five degrees of freedom, however, are very sensitive and require an iterative approach to correctly adjust for ideal alignment.

2.2 Mounting: To have access to all five adjustable DOFs, the OAP will be mounted in a kinematic mount with three actuators to allow for tip and tilt. The kinematic mount is placed in an adjustable post holder to allow for height alteration. (It should be noted that OAPs are heavy optics and tend to sink into the adjustable post holders



over time; it is therefore crucial that a c-clamp is added to maintain the OAP height after alignment.) For lateral translation and translation along the beam path, the mounted OAP is then placed on two translation stages: one along the beam path and one perpendicular to the beam path. This allows for precise, easy translation of the OAP; these stages will be locked into place after initial alignment. With the optic properly mounted, an iterative approach is used to align the OAP.

2.3 Iterative alignment approach: OAP alignment requires a few essential tools: an iris for height verification, as well as a narrowband* spatially-coherent light source and a shear plate interferometer to check for collimation and misalignment-induced optical aberrations. (*Note: the internal source must be narrowband to allow for the use of the shear plate interferometer which uses interference fringes created by a temporally-coherent source to diagnose optical aberrations.) In this section, we layout the steps required to align an OAP in two ways: (1) using an incoming light source that is diverging (so that the OAP collimates the light), and (2) using an incoming light source that is collimated (so that the OAP brings the light to a focus). Recalling that OAPs are used both to focus and collimate light, both alignment schemes will be used to align the MagAO-X instrument since it implements a cascading system of OAPs which will each be aligned one by one in a successive fashion.

2.3.1 Aligning to a diverging light source: The following steps describe how to align an OAP to a diverging light source: (1)

1) Verify the angle of the incoming beam

a. Prior to the first OAP, make sure that the incoming beam is at the desired system height and is propagating parallel to the reference surface (in many cases an optical bench). This can be done by placing two irises set to the system beam height in the beam path: one close to the source and one further down the beam path. The source height and angle with respect to the table can then be adjusted until the beam passes straight through both irises without clipping.

2) Adjust the height of the OAP mount

a. The center of the OAP in the vertical direction should match the center of the beam.

3) Position the OAP

a. Place the horizontal center of the OAP at a distance of one OAP focal length from the light source. Be sure to use the reflected focal length of the OAP, not the parent focal length.

b. Approximate the angle of the OAP to match the designed reflection angle. This can be approximated by eye using a mounted protractor placed in front of the OAP in the beam path such that the incoming and reflected beam pass over the protractor, thereby allowing the user to see the angle between the two beams.

4) Check collimation using a shear plate interferometer



a. Position a shear plate interferometer in the path of the reflected beam. The shear plate will produce straight fringes parallel to the reference line when the beam is perfectly collimated and without aberrations. It is therefore important to orient the reference line towards the incident beam. The angle of the fringes relative to the reference line tells the user about the state of collimation. If the lines are tilted, the beam is defocused, meaning that the OAP must be translated along the beam path. If the fringes are not straight, there is some aberration in the wavefront, which is usually caused by a tilt or de-centering of the OAP. Adjust the tip/tilt and lateral position of the OAP as necessary to achieve straight fringes parallel to the reference line.

5) Check collimation in the orthogonal direction

a. Rotate the shear plate by 90 degrees to check collimation in the tangential or sagittal plane. Make the same adjustments to achieve collimation.



Figure 2: Shear plate interferometer showing straight line fringes indicating the light reflecting off of the OAP is collimated and free of aberrations.(1)

6) Iterate steps 4 and 5

a. Adjustments of collimation in the two orthogonal planes are not entirely decoupled. When you make an adjustment in one plane, it is likely to affect collimation in the other. Alignment is therefore an iterative process of minor adjustments and checking collimation in both planes. The OAP is well-aligned when the fringes in both directions are straight and parallel to the reference line as shown in Fig 2 .

7) Check the angle of the output beam

a. The output beam should be parallel to the reference surface, just like the input beam. This can again be done using two irises set at the system beam height: one placed near the OAP and one placed further away. Tilt the OAP until the beam passes straight through both irises.

2.3.2 Aligning to a collimated light source: The following steps describe how to align an OAP to a collimated light source: (1)



1) Verify the angle of the incoming beam (same as above)

2) Adjust the height of the OAP mount (same as above)

3) Position the OAP (same as above)

4) Check the image

a. Look at the focused spot formed by the OAP using a detector. Adjust the angle of the OAP relative to the incoming beam (tilt) to achieve good imaging quality. By adjusting the OAP angles in small increments you can minimize the aberrations observed in the focal plane.

5) Check the angle of the output beam (same as above)

2.4 High precision adjustments: Some small residual error can be expected at the end of this alignment scheme given the precision of the above methods. To deal with this residual, a Zygo Verifire interferometer will be placed at the end of the system which will allow for high-precision adjustments of each OAP to be made to fine-tune the alignment. This interferometer ensures reliable "ripple-free" phase measurements in vibration-prone environments, and will allow for small residual errors in the alignment to be removed by small final adjustments made to the OAPs.(3)

3 Maintaining Alignment

Initial alignment of the system is crucial, and maintaining the same quality of alignment over time and after shipping the MagAO-X instrument is essential to maintain system performance. Misalignment is expected to occur in shipping, and it is important to minimize the amount of time required to realign the system before going on-sky. We have therefore developed a rough alignment strategy to quickly realign the system.

For maintaining alignment, we propose using three methods: (1) a series of irises placed along the beam path to check for tip/tilt and height variation, (2) an individual reference for each OAP to monitor any changes in the OAPs position with respect to its initial, ideal-alignment orientation, and (3) a series of flip mirrors and cameras to check PSF quality and beam location.

3.1 Method 1: Irises: A series of irises will be centered on the beam along the optical path after initial alignment of the instrument and epoxied in place to keep them from moving during shipment (see Figure 3).(?) The irises will be oversized and fully opened while the instrument is in operation to avoid affecting the beam. For alignment, the irises will be stopped down to check for beam misalignment that will result in clipping by the iris. These irises can be fully epoxied to remain in place, will have no moving parts, and will therefore be the least likely of the three methods to be affected by shipping.

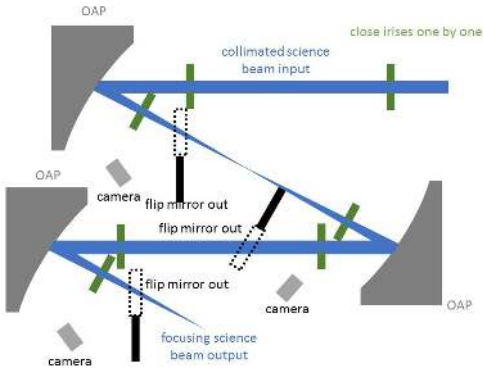


Figure 3: Iris method: close down each iris individually in succession down the beam path (with the flip mirrors out of the beam). Misalignment on the iris will give tip/tilt misalignment information for the preceding OAP.

3.2 Method 2: Laser/back reflection/camera: The back surface of each OAP will be polished to allow for a 4% reflection off the uncoated back surface. (Note: the OAP mounts are designed to be open in the back, thereby allowing access to the back surface of the optic. For specifics on these mounts, see Section 2.1: Overall Design) A small laser will then be set up and epoxied in place to reflect off the back of the OAP and onto a camera (also epoxied in place with a square post and post holder to avoid rotation in the mount during transit). (See Figure 4)

The rough alignment maintenance strategy will proceed as follows:

- 1) Initial alignment of the full optical system
- 2) Set-up a laser and camera (one of each per OAP) behind each OAP to reflect the laser off the polished back surface of the OAP and onto the camera.
- 3) For each OAP, take an image of the laser beam footprint with the camera and save as the ideal reference image for each OAP.
- 4) After shipping, or at any given time after the initial alignment, turn on the laser for each OAP and take an image of the beam footprint on the camera.
- 5) Measure the shift in position of the beam with respect to the reference image. (See Figure 5) This will provide information on how the OAP has tipped and tilted since the initial alignment. (Note: these are the two most sensitive DOFs and are therefore the most likely misalignments to occur during shipping. The OAPs will be locked in place in height, in position along the beam path, and laterally with respect to the beam, and will therefore be less likely to move.)
- 6) Use the actuators on the OAPs kinematic mount to adjust the OAPs tip and tilt to return the beam to its reference position on the camera.
- 7) To ensure that the OAPs, not the laser/camera system has moved in transit, this procedure will be augmented



by iterating on the initial alignment steps 3 - 5, checking the centering of the beam on each OAP, the input and output angle of the beam, and the beam height along the optical train.

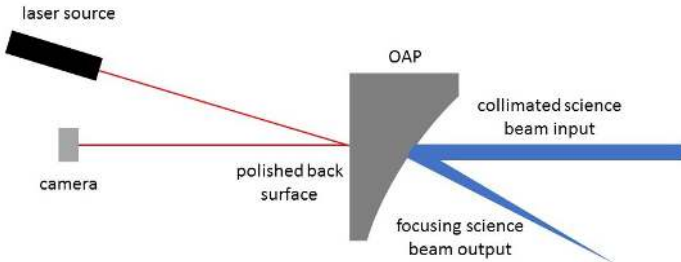


Figure 4: OAP layout for rough alignment strategy using a laser reflection of the polished back surface of each OAP reflected back to a camera

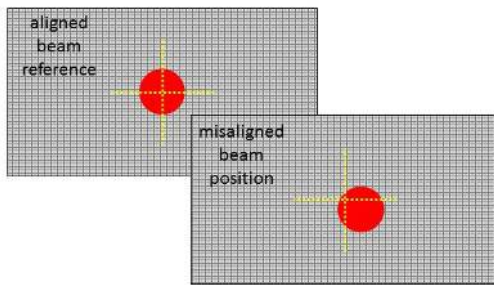


Figure 5: Beam displacement used to adjust tip/tilt OAP actuators to realign the OAP.

This strategy will bring the OAPs back into alignment. However, OAPs are sensitive optics, so it is possible some residual aberration may remain after this rough alignment. If this is the case, it will be seen in the image quality at the end of the optical system. Smaller, more precise adjustments of the OAPs will then be required to fine tune the final image quality. This can be achieved by checking the beam height throughout the optical system with an iris or target set to the beam height, checking for wavefront aberrations using a shear plate interferometer, and adjusting the OAPs accordingly (see previous section for initial alignment).

3.3 Method 3: Flip-mirrors/camera: Flip mirrors will be placed along the optical path after each OAP that will be out of the beam during operation and flipped into the beam, reflecting it back to a camera, one at a time starting at the beginning of the system. In collimated space, the beam footprint location on the camera will be used as in Method 2 to determine any tip/tilt that has been induced on the OAP before it (see Fig 5). After OAPs where the light is coming to converging, the camera will be placed at focus. The position of the beam at the camera will be again be used to identify tip/tilt, but the beam at the camera will now be a PSF, the quality of which can be used to more precisely diagnose optical aberrations induced by the preceding OAPs. This method, as well as method 1, has been demonstrated successfully at Subaru Coronagraphic Extreme Adaptive Optics (SCExAO) by Nemanja Jovanovic, whose expertise and on-sky experience have contributed significantly to this alignment scheme.(?)

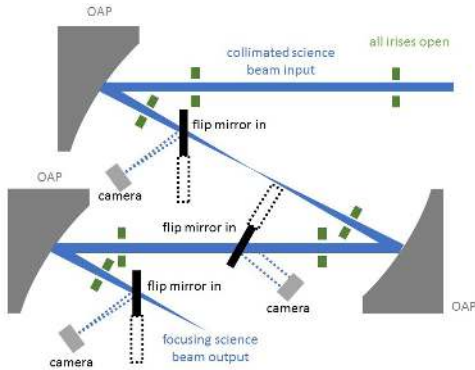


Figure 6: Flip mirror method: flip each flip mirror into the beam in succession down the beam path (with the irises fully open). The reflected beam, both collimated and the PSF, will give tip/tilt error information for the preceding OAP, and the PSF will give higher precision error information for the preceding OAP.

4 Laser Safety

The internal broadband light source for MagAO-X is a class IIIb Fianium Whitelase micro laser(?) with a total power output $> 200\text{mW}$ and a bandwidth of 400 – 2200 nm, with a significant fraction of the total power lying outside of the visible band. Specular reflections as well as direct exposure to this laser can be harmful to the eye. This makes laser safety an important topic for consideration. The upper bench of the MagAO-X instrument is designed to be 1.465 m tall, making it below the average eye level. To further mitigate safety concerns, a near-infrared (NIR) filter will be used to cut off all light past 800 nm, ensuring that all light delivered to the instrument is within the visible spectrum. This filter decreases the total output power being delivered to the instrument to less than 5mW, downgrading it to a class IIIa. This beam will therefore be eyesafe and will allow for personnel to align the instrument without the use of safety goggles. Standard procedure for operating this laser will still include avoiding direct eye exposure to the beam (straight from the source as well as any reflections) by keeping the users eyes above the level of the beam at all times. Should the NIR filter need to be removed at any time for instrument testing, personnel working on the optical bench will be required to wear laser safety goggles with high OD (optical density) in the lasers peak wavelength regimes. The same Fianium Whitelase micro source that will be used for the MagAO-X bench is currently in use at the University of Arizona's Extreme Adaptive Optics Lab, and the above safety precautions, including procedures and hardware, have been and are currently being successfully implemented.

References

- [1] K. Newman, "An introduction to off-axis parabolic mirrors," tech. rep., 2013.
- [2] E. Optics, "Off-axis parabolic first surface metal mirrors," tech. rep., 2017.
- [3] Zygo, "Verifire," tech. rep., 2017.



2.4 Shipping Plan

The MagAO-X plan envisions accommodating a total of six air-shipments of the instrument from Tucson to LCO and five return air-shipments to Tucson. As explained previously the idea is that improvements and upgrades to the instrument can be made in between commissioning runs. Where it makes sense we will buy/fabricate duplicate hardware such as the table legs and the table lifting fixture to reduce shipping costs.

The table and optical components will be aligned in the lab in Tucson and then packaged in a special wooden handling crate see fig 2.4-1. The only component not shipped in the crate will be the critical BMC DM, which will be hand carried for each run. The crate is equipped with wire rope isolators sized to reduce the shock load of an 18" drop to 15g. The box construction is such that the table is bolted to a steel frame that is attached to the isolators which is in turn bolted to a steel sub-frame that attaches to the bottom of the crate. Additionally we will have impact indicators (e.g. Drop-N-Tell) attached to the crate to record any actual events during shipment. Also, desiccant will be added to the crate to prevent moisture buildup.

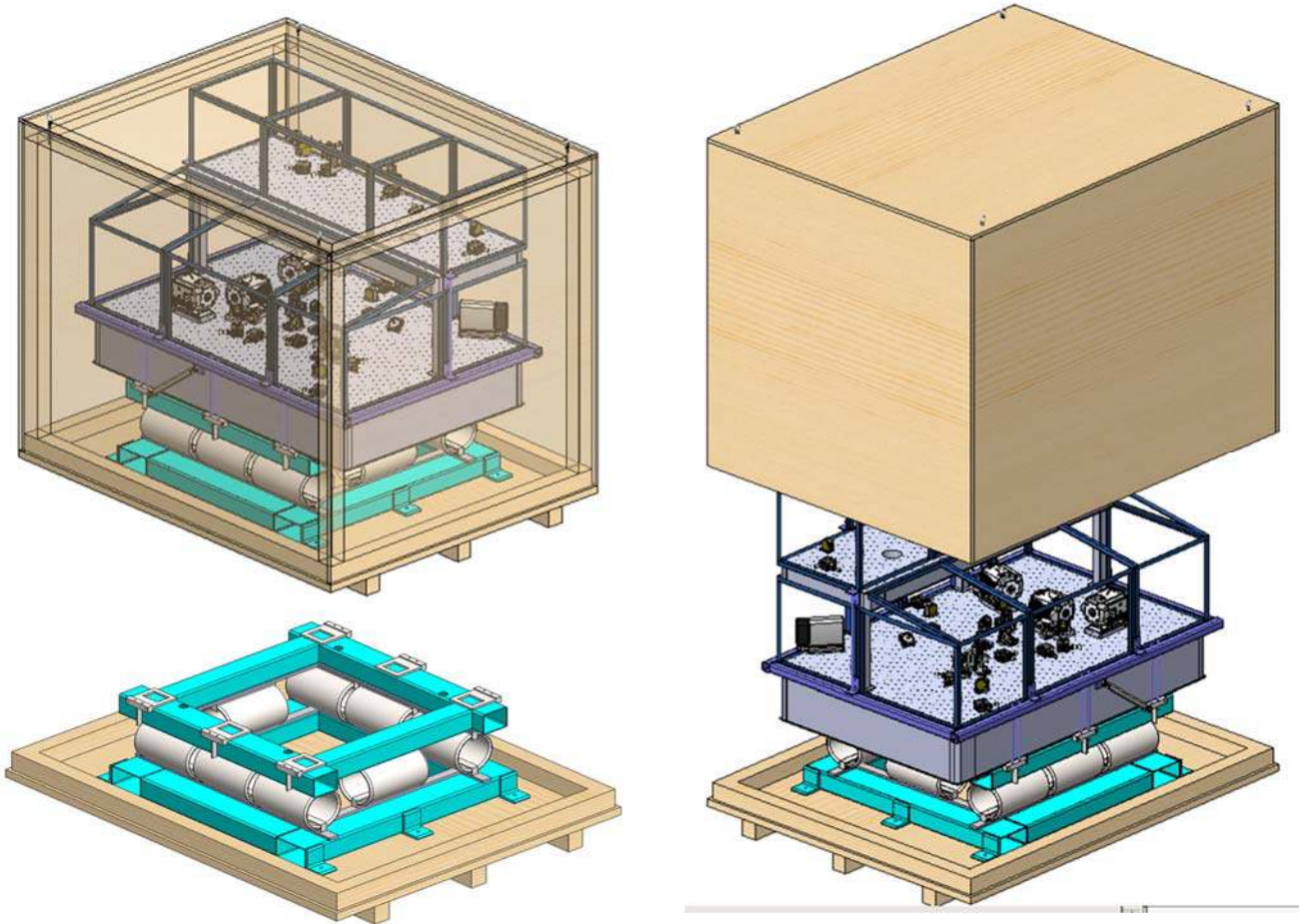


Figure 2.4-1: Special handling crate for the table and components. Top-left view shows the full assembly. Right-hand view shows the removal of the top of the crate to access the table. Bottom-left shows the assembly of the steel frames and wire rope isolator configuration mounted to the bottom of the crate.



The electronics rack, table legs and lifting fixture will be packaged in their own separate wooden crates. The electronics rack will have a crate that will be reusable, similar to the crate for the table. The rack will be bolted to the bottom of the crate and the lid will be lifted off similar to the table crate see fig 2.4-2. The lid and rack will be lifted using the four lifting eyes on the top of the box lid and electronics rack. The electronics rack crate will also have impact indicators and desiccant. The table legs will likely be dropped shipped from the manufacturer to Carnegie in Pasadena for shipment to LCO. The lifting frame will be palletized and shipped to Carnegie from Tucson for shipment, ideally concurrent with the legs, to the site. Table 2.4-1 contains a list of the crate dimensions.

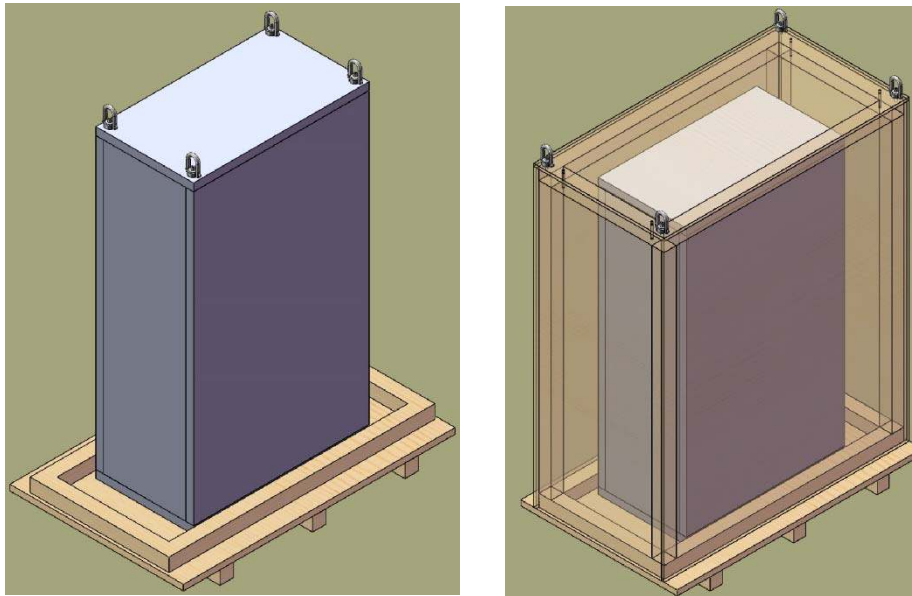


Figure 2.4-2: Electronics rack crate.

Table 2.4-1: MagAO-X Shipping Crates

Crate	Contents	Dims (LxWxH) (Inches)	Weight (Lbs.)
1	TMC Optics Table populated with components	88.5 x 70.5 x 77.2	3250
2	Electronics Rack fully populated	70.5x45x91	1140
3	TMC Optical Table Legs	72 x 62 x 30	800
4	Lifting Fixture	83 x 74 x 16	840
5	Miscellaneous Computers and Equipment	48 x 45 x 34	500

Optics Table Crate Design Details

The optics table crate is designed to handle a 18" drop and reduce the shock the table sees to 15g. We believe this is sufficient attenuation to make the drop survivable for the table and reduce chances for damage to the components. After such an event the optics may need to be realigned. The following is the shipping environment and subsequent deflections (see Table 2.4-2) based on the use of 8ea. John Evans' Sons HM08875-5 7/8" wire rope isolators and a 2000 lb load (load may be 1500 lbs, but design provides some margin). The table is constrained to the wire rope isolators via the upper shipping frame and lower clamps.

- Ref. Mil-STD-810D Environmental Test Methods and Engineering Guidelines



- Transit Drop, Method 516.3 Procedure III (Weight > 1000 Lbs)
 - 18" drop on base or skids
 - One edge on 5 to 6" blocks, the other raised 18" above floor and dropped.
- Basic transportation Method 514.3 Category 1 (land, air and sea)
 - Vertical: $.015 \text{ g}^2/\text{Hz}$ from 5 to 50 Hz rolling off to $.00015 \text{ g}^2/\text{Hz}$ at 500 Hz
 - Transverse: less than $0.0007 \text{ g}^2/\text{Hz}$ from 5 to 500 Hz
 - Fore and aft: less than $.007 \text{ g}^2/\text{Hz}$ from 5 to 500 Hz

Table 2.4-2: Optical table shipping deflections.

Load Case on Shipping Box, 2000 lb breadboard, 8 isolators	Max Deflection (inch)
18" Drop	3.6
Vertical Shipping Vibrations	.57
F&A Shipping Vibrations	.97
Transverse Shipping Vibrations	.18
F&A Shipping Vibrations with Rolled Isolator	1.38

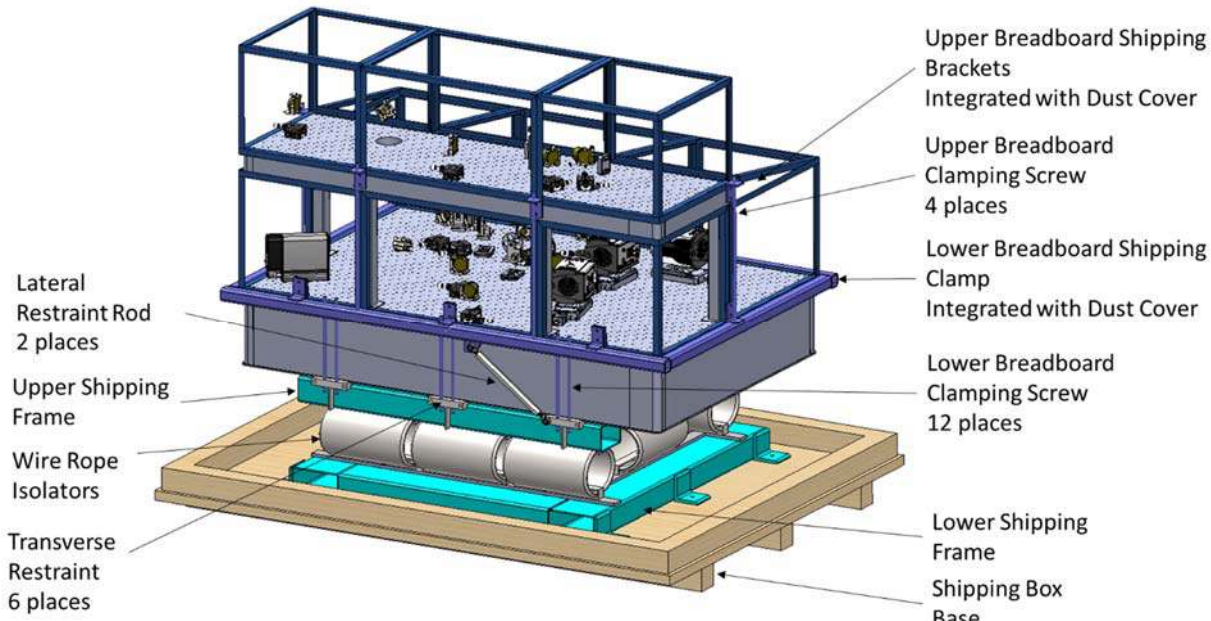


Figure 2.4-3: Optical table crate design details.

Optical Table Handling

A special lifting fixture has been designed to lift the optical table in and out of the crate and onto the legs both at the telescope and in the lab (see fig 2.4-4). The steel fixture can be disassembled for storage, handling and shipping and then reassembled with the aid of a crane as needed. The overall weight is 540 lbs. The crane lifting point will be nominally set to coincide with the cg of the table and fined tuned with adjustable bumpers.

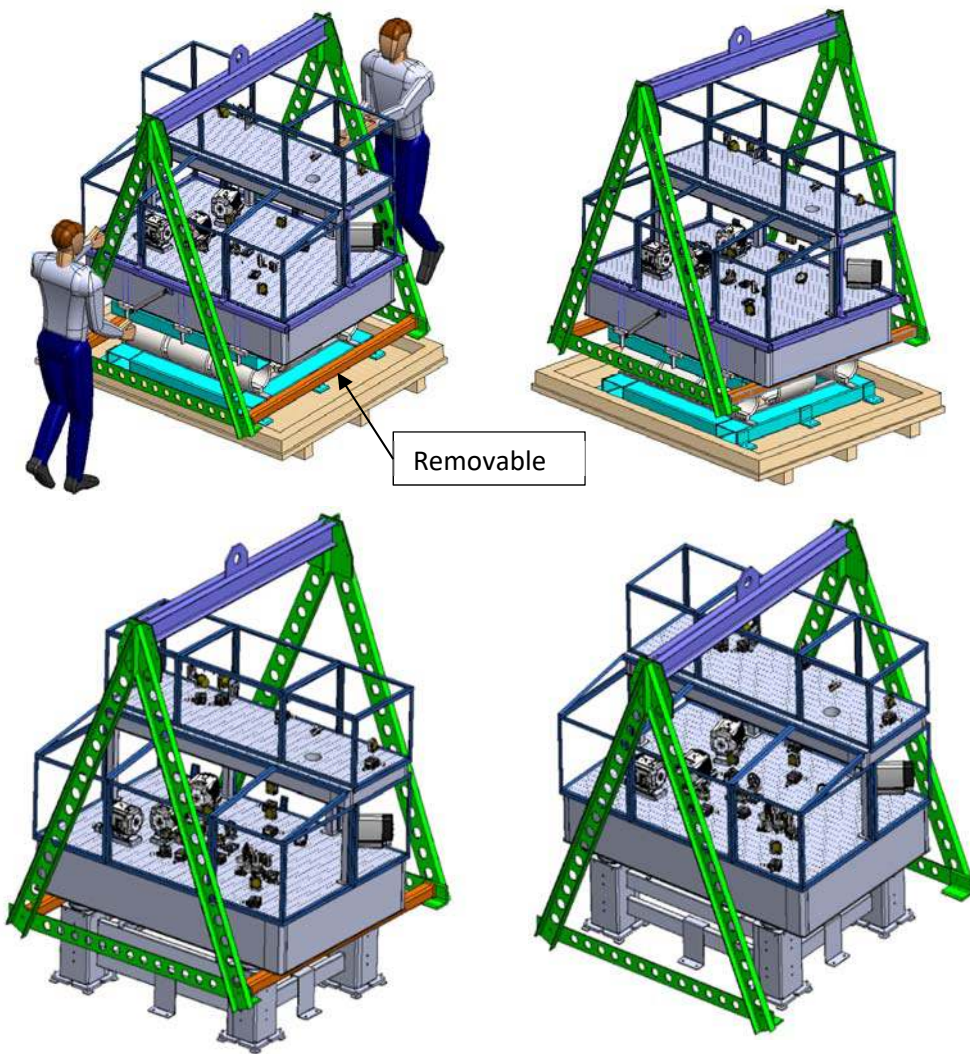


Figure 2.4-4: Optical table lifting frame. Top-left and top-right view shows the configuration when lifting the table out of the crate. Bottom-left and bottom-right views shows the configuration when lowering the table onto the legs. Red bars are removed prior to lowering upper frame onto and off of table.

Handling in Lab

The process to load the optical bench crate will be to:

- 1) Lift the table off the legs, using the lifting fixture, in the lab with a gantry crane and onto an industrial moving dolly (see fig 2.4-5).
- 2) The table is then rolled down the hall to the freight elevator and moved to the first floor and out on to the loading dock. (Note: that the dust covers will be installed during the entire operation.)
- 3) We then employ a industrial moving company to lift the table onto the shipping frame and lower crate assembly.
- 4) Lift the lid onto the lower crate and secure.
- 5) Then when the truck arrives to pick up the shipment the crate will be loaded into the truck.

The opposite steps will be used to unload the crate when returning to the lab.



Figure 2.4-5: Industrial moving dolly. It is three point support that eliminates the possibility of a skate to slip out due to uneven loading when traversing uneven and discontinuous flooring. Wide rollers prevent wheel from getting stuck. Model shown has a 6 ton capacity.

Handling at the Site

The crate will be moved to the summit with the Isuzu truck and unloaded using the lift. Then:

- 1) Use a hand truck shipping box to telescope observing floor off of the elevator.
 - 2) Independently, position our legs (on their casters) (see figure 2.4-6) to the correct X position of the legs w.r.t. the guider center of the NASE platform. So all that is needed is a straight push (in Y) towards the guider, rotate the casters in the Y direction.
 - 3) Lift up the 5 sided top of the shipping box -- rotate dome and place beside table.
 - 4) Pull table out of shipping box base with overhead jib crane and lifting fixture.
 - 5) Lower the table onto the legs with crane, remove lifting fixture.
- (NOTE: the Table/Legs alignment is guaranteed to within +/- 0.1mm with alignment pins (that slide into the tiebars on legs) that are bolted onto in the tapped holes for earthquake brackets -- these pins are already attached when we are shipping the bench)
- 6) Now slowly push the whole assembly on the casters towards the guider until the air gap is 9.6mm then stop.
 - 7) Carefully engage all 16 leveling pads (disengaging the casters).
 - 8) Remove alignment pins and add the missing 2 upper earthquake brackets.
 - 9) Add the lower earthquake brackets.
 - 10) Cable up the system, etc.

See section 2.1 for details of instrument layout on the NASE platform.

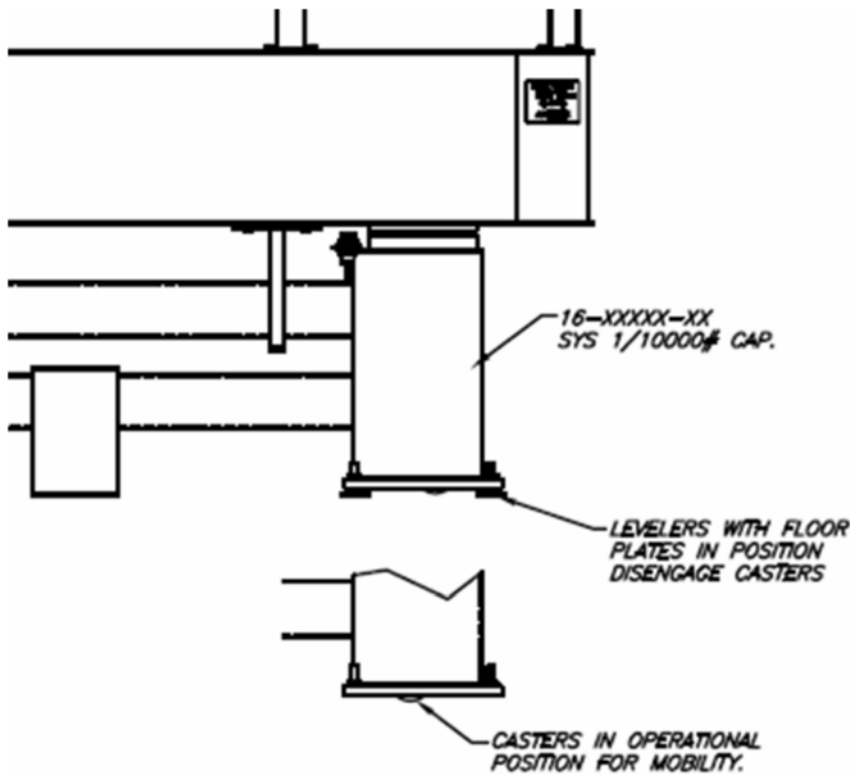


Figure 2.4-6: Table casters allow fine alignment under load.

Export Licenses

The University of Arizona will arrange for the export licenses to Chile for the BMC DM and OCAM-2K camera, since they are both EAR classified equipment, 6A004.a.1 and 6A003.b.4.c respectively. We see no show stoppers and we are already in the process of applying for both of the licenses. We expect to have them well ahead of the first planned shipments.



2.5 MEMS Specification and Status

Jared R. Males

1 Introduction

The Boston Micromachines Corporation MEMS deformable mirror (DM) is the perhaps the most important component in the MagAO-X system. We have identified high-yield as the most important characteristic, that is we desire 0 bad actuators within the illuminated portion of the mirror. BMC has not yet delivered a device to this specification, but are confident that their process has matured to the point that they have guaranteed it. Nevertheless, we recognize this as a schedule and performance risk.

As we have now developed the f/11+woofer option, a further interesting possibility is to obtain a MEMS device with $3.5 \mu\text{m}$ of stroke (compared to $1.5 \mu\text{m}$ for the nominal one). This could potentially obviate the need for a woofer to deal with Kolmogorov turbulence. This would significantly simplify the control problem.

Given these points, we have begun procurement of a BMC MEMS 2040 actuator (2K) DM. BMC has agreed to attempt to first produce a $3.5 \mu\text{m}$ stroke device meeting our yield requirements *at no extra cost* using already fabricated die. If this is not successful, BMC has guaranteed us a $1.5 \mu\text{m}$ stroke device which meets our yield requirements.

2 MEMS Specifications

Here we list the minimum specifications of the MEMS DM which BMC has agreed to deliver:

- Continuous Surface
- 2040 Actuators
- 50 Actuators across circular active aperture
- 100% Yield in specified area
- For bad actuators adjacent to (edge or corner) the specified area or under a spider, no more than 1 bad actuator per 3×3 square
- For bad actuators not adjacent to the specified area, waiver required for more than 1 bad actuator per 3×3 square.
- Spiders: the center of any bad actuator must fall under a 400 micron wide (± 200 micron from spider) mask centered on the spider
- The spider pattern can be rotated.
- A waiver is possible for non-functioning actuators which are not stuck up or down.



- $1.5 \mu\text{m}$ Max Stroke (minimum)
- 12-18% influence functions
- $0.85 \mu\text{m}$ inter-actuator Stroke (minimum)
- Temporal response: 5-95% rise/fall < 65 microseconds (single actuator 100 nm step)
- 19.6 mm aperture
- $400 \mu\text{m}$ pitch
- Gold Coating
- Surface finish after coating $< 20 \text{ nm rms}$ after applying a high pass filter with a cutoff frequency of $1.25/\text{mm}$
- For potential $3.5 \mu\text{m}$ device: $2.5 \mu\text{m}$ of stroke after device is flattened (all terms). $3 \mu\text{m}$ of stroke after flattening without correcting for focus
- Protective Window on 6° Wedge w/ AR Coating: 550-2400 nm (both sides) with specifications:
 - MATERIAL: UVFS
 - PARALLELISM: $\leq 5 \text{ arcsec}$
 - THICKNESS TOLERANCE: 0.3 mm
 - DIAMETER TOLERANCE: $+0.0/-0.2 \text{ mm}$
 - SURFACE QUALITY: 20-10 SCRATCH-DIG
 - SURFACE FLATNESS: $\lambda/10$ AT 633nm
 - CLEAR APERTURE: $> 90\%$ OF DIAMETER
 - COATINGS: Ravg $< 1\%$ 550-2500 (as in infinite optics scans 7-2956R S1 and 7-2957R S2)
 - Scan to be provided after coating.



2.6 MEMS CARE AND OPERATION

Katie Morzinski and Nemanja Jovanovic

1 Introduction

MagAO-X will use a micro-electro-mechanical systems (MEMS) deformable mirror (DM) from Boston Micro-machines Corporation (BMC) for high-order wavefront correction. We have experience handling and controlling MEMS DMs from the Center for Adaptive Optics (CfAO) Laboratory for Adaptive Optics (LAO), from the “Villages” on-sky AO testbed at Lick Observatory’s 1-m “Nickel” telescope, from the Gemini Planet Imager (GPI), and from the Subaru Coronagraphic Extreme AO (SCEExAO) testbed and instrument. Here we present our plan for MEMS operation and safety of the equipment during development, deployment, and operations of MagAO-X.

Much of this document is based on KMM’s version of a “MEMS handbook”, entitled *MEMS practice, from the lab to the telescope* by Morzinski et al. (Photonics West invited paper, Proc. SPIE, 2012).

2 Lab testing

2.1 Verification of the MEMS: Upon receipt of the MEMS device from BMC, we will conduct a visual inspection of the surface, wire traces, and pins on the back. We will then carefully insert the MEMS in the ZIF socket while wearing an anti-static strap. After ensuring that the maximum voltage is limited in hardware on the electronics to the BMC-specified value, we will power on the control electronics. Here we assume that BMC will specify the max voltage as 300 V, but the exact value will be determined upon receipt.

MEMS devices are controlled via a voltage applied to a capacitor which pulls the actuator down; there is no inverse “push” motion, so the device is operated at a bias voltage to allow for displacement in both directions. The bias is determined by lab testing to discover which voltage is in the mid-displacement range for the majority of the actuators. MEMS have limited stroke so selection of the bias voltage is important to maximize the stroke in both directions (Fig. 1). Furthermore, because MEMS devices have a stiff and broad influence function (Fig. 2), the best choice of bias voltage varies based on whether a single actuator is being poked or a larger region of actuators are being displaced. To start with, we will extrapolate the best bias voltages for lower-powered previous LAO generation MEMS devices, as seen in Tab. 1.

Table 1: Suggested bias voltages for single-actuator and full-device displacement.

Maximum voltage	Mid-displacement voltage (single actuator)	Mid-displacement voltage (3x3 region)
160	110	90
200	140	120
225	160	140
~300*	~210*	~190*

* Maximum voltage to-be-determined (T.B.D.) as specified by BMC.

* Bias voltage T.B.D. for 300-V bias based on lab testing.

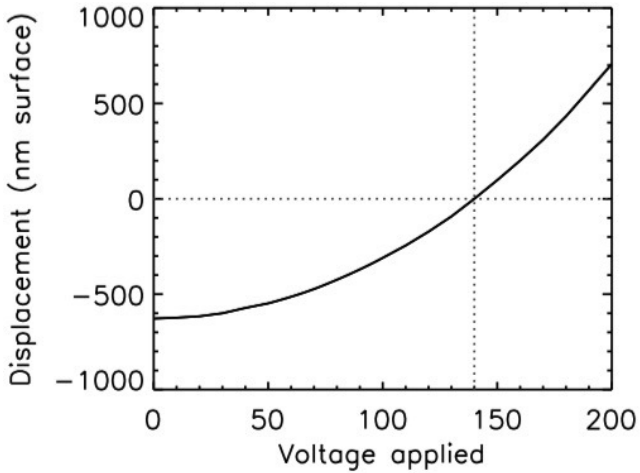


Figure 1: Displacement vs. applied voltage, 1 actuator (Villages MEMS).

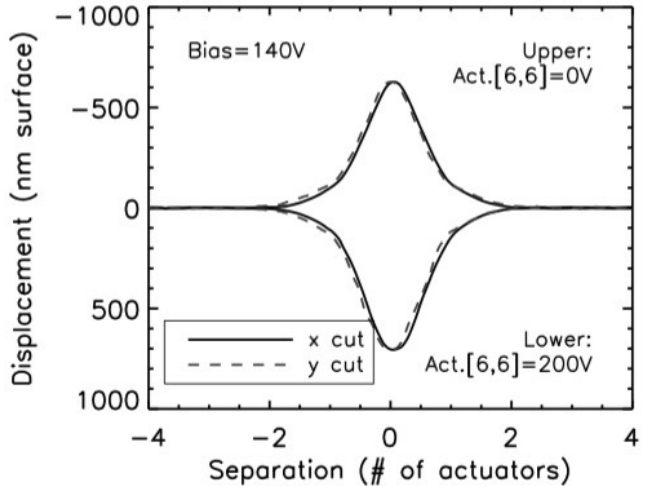


Figure 2: Influence function, 1 actuator (Villages MEMS).

We will apply a uniform bias voltage to the MEMS (~ 190 V) and take an image with our Zygo interferometer. We will also take an image at 0V and at the maximum voltage (~ 300 V). These images give us the un-powered shape, test the basic electronics and control, and identify “dead” actuators that do not move as identified by subtracting the 0 V and 300 V images. The next step will be to verify the mapping of the actuators and begin to test their response to voltage. We will carry out the LAO-standard “rows-and-columns” test where we apply ~ 300 V to each row and then each column, sequentially, while the rest of the device is at a bias voltage of ~ 210 V. We will measure the surface with the Zygo interferometer in the lab, which is aligned to achieve a spatial resolution of ~ 20 pixels across each actuator. The Zygo images will be inspected to find mis-mapped rows or columns.

2.2 Actuator characterization: Actuator functionality will be characterized in detail by measuring the displacement as a function of voltage for each actuator. To characterize each actuator, we will step up the voltage on each actuator individually from 0 to 300 V in steps of 30 V and take a Zygo image at each step. Because the influence function falls to zero at a spacing of a couple actuators (precise value T.B.D. in the lab), each actuator can be measured independently by applying a voltage to every 4th actuator across a row and down a column.

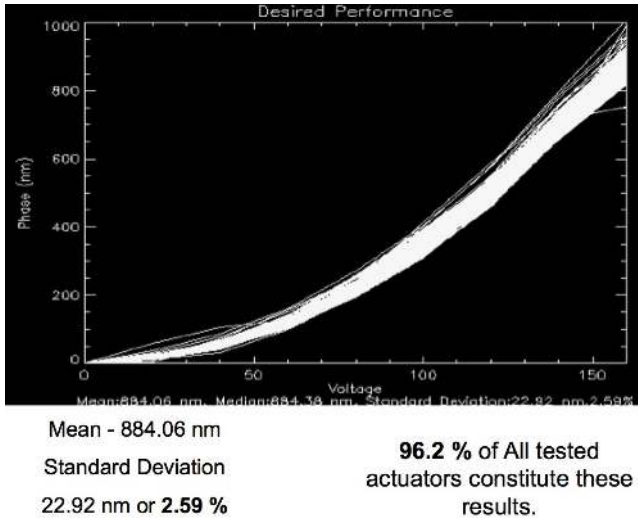
Irregular actuators can be non-responsive (“dead”), under- or over-responsive, coupled to a neighbor (“floating”), or responsive only to the level of the bias. In 2005 CfAO summer student Layra Reza did a thorough characterization of the zoology of actuator failures. She found that in 2005, a 1024-actuator BMC device had 96.2% well-functioning actuators. Of the remaining 3.8% irregular actuators, 78% were coupled pairs. The other irregular actuators included under- or over-responsive actuators (not a quadratic displacement curve), or actuators that moved up to the bias and then stopped. Her results are shown in Figs. 3 and 4. We have contracted with BMC for a device free of actuator irregularities within the clear pupil; the actuator characterization test will be important to investigate the functionality of each individual actuator.

2.3 Calibrating the MEMS: To shape the wavefront, the MEMS must be calibrated for its voltage response. The influence function is the displacement of the entire MEMS surface when a voltage is applied to a single actuator. Because the MEMS has a stiff continuous facesheet, the neighboring actuators are displaced somewhat as well. Figure 2 shows the influence function of the 144-MEMS used in Villages. The single actuator influence function

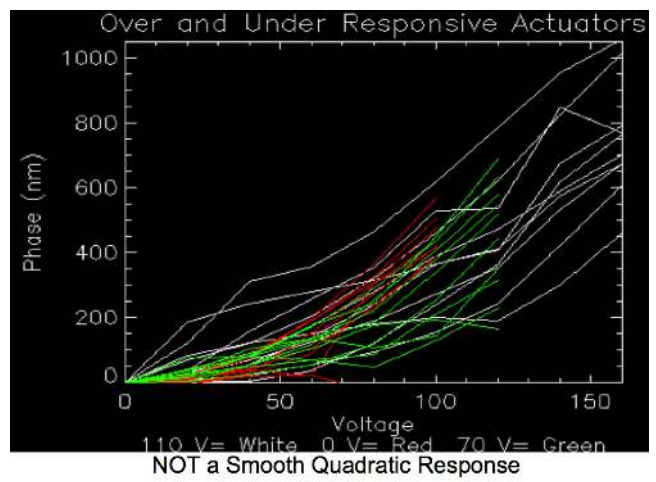


MagAO-X Preliminary Design MEMS CARE AND OPERATION

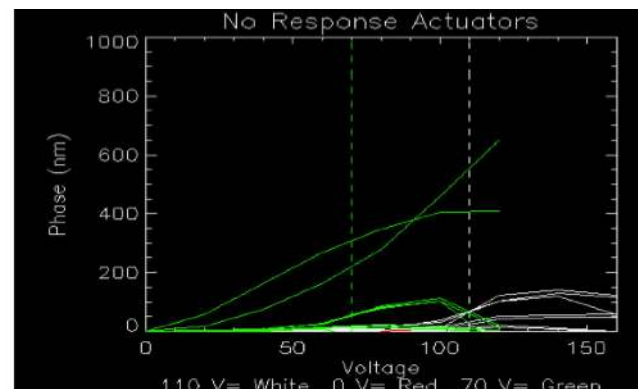
Doc #: MagAOX-001
Date: 2017-04-23
Status: Rev. 0.0
Page: 3 of 6



Desired performance: These actuators have quadratic displacement curves.



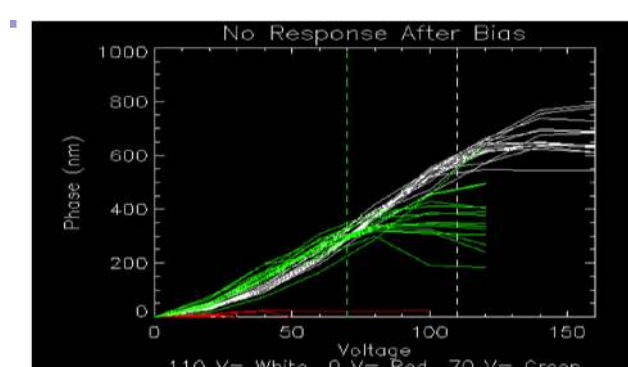
These irregular actuators are over- or under-responsive.



Float with Bias

- Problem with Electronics (Digital-to Analog-Converter)
- MEMS Short Circuit
- Variability

These actuators are not “dead” but float with their neighbors.



Actuators do not move beyond the surface level

- Does the Bias determine the maximum voltage?
- Mechanical Problem

These actuators do not move above the surface level.

Figure 3: The zoology of good and bad BMC MEMS actuators as characterized by CfAO summer student Layra Reza (2005). This was an early-generation device and BMC’s yield improved over time, from 97.9% to 99.5% in 2005–2012 for the old 1k-MEMS devices. We will conduct the same tests to measure the individual displacement curve of each actuator on the MagAO-X MEMS. This will both identify irregular actuators as well as calibrate the displacement curve for use in closed-loop control.

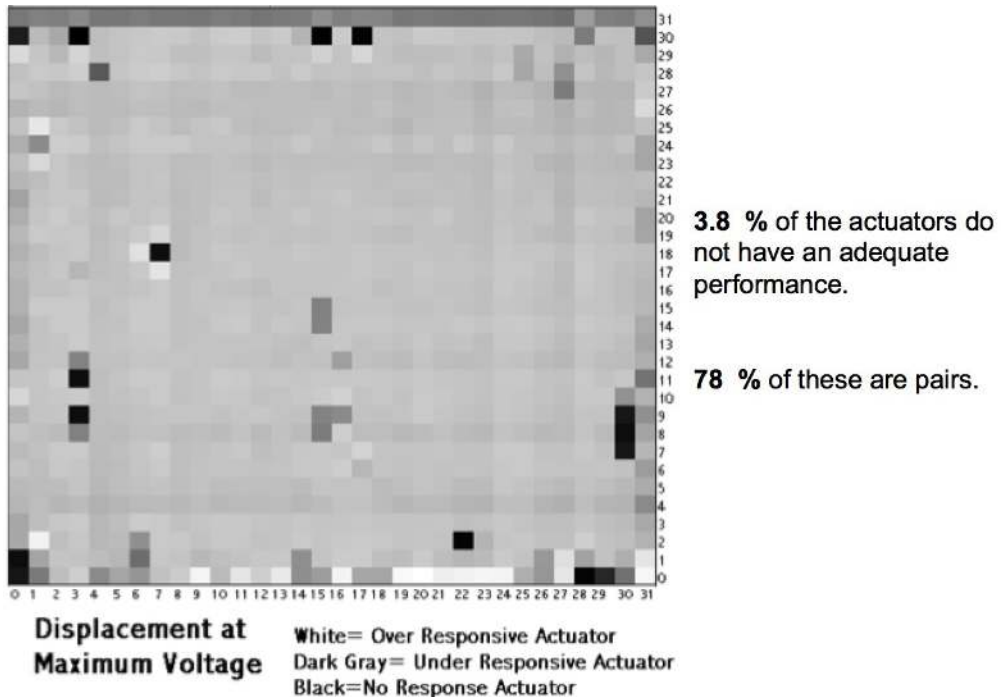


Figure 4: Results of a 2005 test on a 1024-actuator BMC MEMS DM for actuator functionality. We will similarly test each actuator of the MagAO-X MEMS to verify receipt of a device free of actuator irregularities within the clear pupil.

for a 1k-MEMS falls to 26% at one actuator distance and 4% at two actuators distance, and is uniform with varying bias voltage and applied voltage. This will be measured in the lab with the Zygo for the MagAO-X MEMS.

The displacement as a function of voltage is needed for applying shapes. The voltage that gives the displacement in the middle of the range is used as the bias. Figure 1 shows the single-actuator displacement curve for the 144-actuator Villages MEMS. Stroke has improved with advanced designs, after trading with facesheet thickness, surface curvature, and actuator spacing. See previous document for our MEMS specifications.

When calibrating the voltage-displacement curve (recall Fig. 1), in the LAO we would usually test only four actuators, fit a quadratic, and take the average curve for the entire device. However, if one takes the time to calibrate all actuators individually, there is an effect. Fully-functional actuators show a 23% variation in their displacement curves. This effect would account for 2030 nm rms wavefront error in an open-loop control model using an average rather than individual voltage-displacement curve for each actuator. Furthermore, closed-loop performance can be tweaked with an individual voltage-displacement curve for each actuator. Thus for MagAO-X it may be worthwhile to individually calibrate the voltage-displacement curve of each actuator, which we will do in the lab with the Zygo.

3 Care and Handling

There are two common failure mechanisms for MEMS actuators: snap down and humidity damage. In a snap-down failure the actuator has had too much voltage applied and the electrostatic force overcomes the restoring spring force and the actuator gets stuck in the highest-volt position. It is possible but not recommended that snapped down actuators can be freed by poking them with a probe. Snap-down is prevented with hardware and software safety stops to the maximum voltage that can be applied.



3.1 Power: At the LAO we had a device early on in testing on which we often left the same 4 actuators (used for alignment) strongly poked in the maximum voltage position with the rest of the device at a lower bias, on occasion for hours to days at a time. Over time these actuators did not return completely to the zero-volts position, but bumped slightly when unpowered. This cause still remains unknown, but the actuators remain functional. We modified our habits to unpower the device when not in use, and this has not been a problem with subsequent devices. At MagAO-X we will leave the MEMS powered off when not in use.

3.2 Humidity Safety: Voltage in the presence of humidity can induce dissociation of water, causing anodic oxidation of poly-silicon. Water dissociates into OH and H⁺; the negatively-charged OH ions are attracted to the positive anode, where they react with the poly-silicon to form non-conducting SiOH and SiO₂, also known as glass. Over time with a combination of high voltage and high humidity, the connections for the actuators oxidize and the actuator gets stuck in the zero-volts position. It is possible that if there is oxidation on the device it would be visible under a microscope. Here we describe how we will protect the MEMS from humidity damage.

The deformable mirror must only have high voltage applied to it in low humidity conditions (<20%). The chamber around the deformable mirror is not perfectly sealed; a dry atmosphere could not be maintained in the chamber in a static fashion (drying it out and sealing it). Instead, dry air should be flowed through the deformable mirror chamber constantly. Figure 5 illustrates the set-up for SCExAO.

Air from an oil-free compressor is passed through a desiccant to dry it before entering the gas monitoring system. The gas will typically arrive from the compressor at a pressure of 60-100 psi. To ensure the deformable mirror is not damaged by over pressure, a low-pressure regulator will be used which limits the maximum output pressure to 1.4 psi above ambient. A flow regulator will be used to restrict the flow to a dribble. After the regulator a pressure sensor and a pressure relief valve will be used to monitor the pressure and ensure that an overpressure cannot occur (doubly redundant with the regulators). The gas will be sent to the DM and the humidity of the gas returning from the DM will be monitored upon return.

A vacuum pump will be connected to the end of the line to (1) reduce the pressure in the chamber to about 80 Torr and (2) pull the dry air through the chamber to ensure that wetter air that leaks in through the joints does not raise the humidity in the chamber. 80 Torr is required to remove the damping effect of the air in the chamber and allow for the deformable membrane to be modulated at its maximum speed. Going below this significantly (down to 10-20 Torr) could result in electric breakdown and permanent damage. A Venturi pump could easily be used that is driven by the same compressed air line.

An interlock based on both the pressure and humidity will be used to switch the electronics to the deformable mirror off in case the pressure gets below 80 Torr, or the humidity gets above 20%. An software interlock will also be established which reduces the signal set to the deformable mirror to 0 in case nothing has been applied for the last hour. This is to prevent someone leaving something on the deformable mirror, going home and finding out the various interlocks failed.

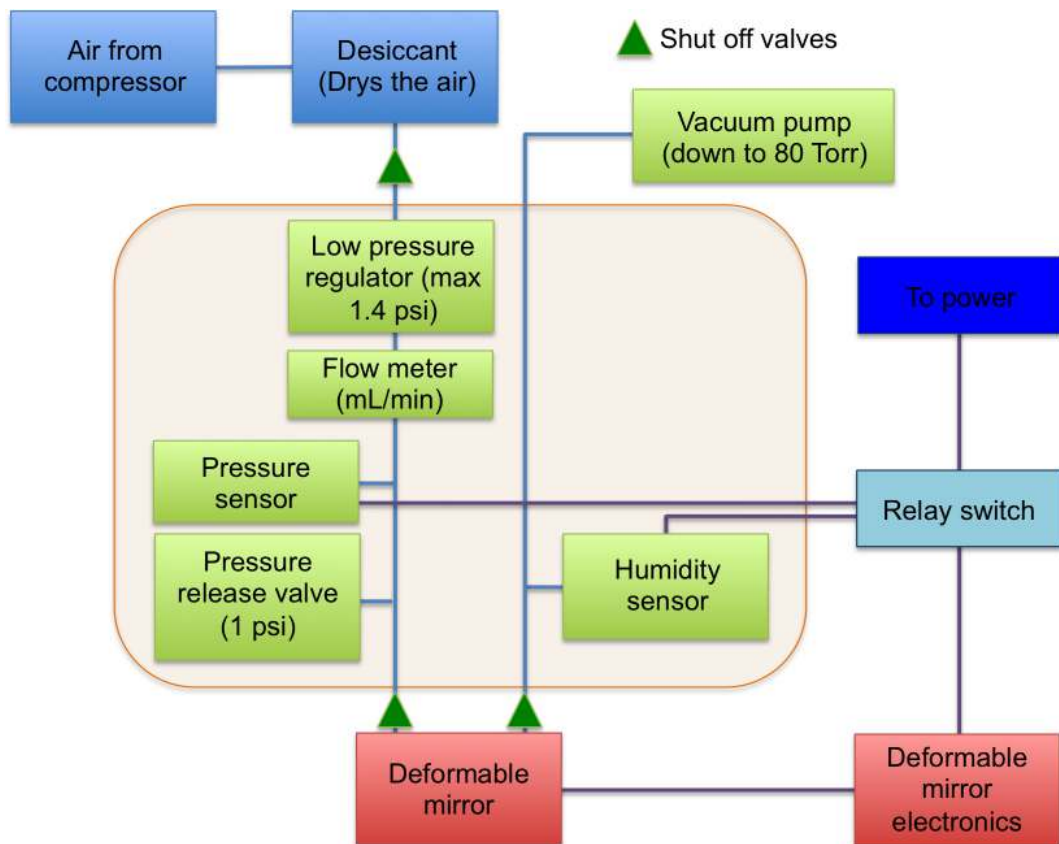


Figure 5: Keeping the MEMS dry at SCExAO. We will use the same set-up for the MagAO-X MEMS to continuously flow dry air through the pseudo-hermetically-sealed MEMS window to ensure the poly-silicon is protected from humidity damage.



3.1 Electronics Enclosure Design

Daniel Alfred

Requirements

The electronics enclosure for the MagAO-X Adaptive Optics instrument is designed according to the following requirements.

1. Operating temperatures shall be between -5°C and 25°C.
2. Storage temperatures shall be between -20°C and 50°C.
3. Maximum allowable heat leak from the electronics rack and instruments to the observatory is 60W.
4. Heat shall be removed with facility-supplied water/glycol coolant that can be assumed to be within 2°C of observatory ambient air.
5. The minimum usable depth of the rack shall be 30". The minimum usable width shall accommodate 19" rack equipment.
6. Transmitted vibration shall be contained by using vibration isolation and minimizing the use of fans in the enclosure.
7. The rack shall provide the following interface capabilities:
 - a. Manage cabling and hoses to minimize connecting and disconnecting effort
 - b. Access ports for components
 - c. Jack wheels
 - d. Lifting eyes
 - e. Bulkhead connections

Design

In order to meet the temperature and heat leak requirements, an electronics rack is designed that is based on a standard 19" electronics rack. However, 2" of rigid foam insulation encloses each side of the equipment rack. The rack and its dimensions are shown in figure 1.

To reduce transmitted vibration, the equipment rack will make use of direct liquid cooling for as many components as possible in order to minimize the use of fans. This includes the GPUs, CPUs, and motor controller components, which can be conductively sunk to a liquid cold plate. The rack, however, includes an air-liquid heat exchanger to remove heat from the components that are designed to sink heat convectively to ambient air. The rack is placed in line with the benchtop cameras that are liquid cooled. A diagram of the system cooling scheme is shown in figure 2.



The electronics rack waste heat is removed by the facility-supplied water/glycol coolant. The GPUs, CPUs, and motor controller components exchange heat conductively with packages and mounting plates that are directly liquid cooled. The DM drivers, computers (ICC and RTC), controllers, and other network devices and power supplies exchange heat with recirculating enclosure air that is driven and cooled by a ThermoCore 5360 air-liquid heat exchanger with two axial fans. The rack thermal management scheme is shown in figure 3.

The components in the electronics rack that are directly liquid cooled include the GPUs, CPUs, and motor controller components and devices. Liquid coolant is plumbed to the RTC, ICC, PCIe expansion, and motor controller units. The RTC, ICC, and PCIe expansion units contain GPUs and CPUs that are packaged with EKWB water blocks. Based on thermal performance and flow data for the water blocks, the CPUs and GPUs will each be plumbed in parallel pairs in order to optimally balance thermal performance with pressure loss. For an expected minimum coolant flow rate of 1.5 GPM (346 L/h), the GPUs and CPUs will be sufficiently cooled and each GPU and CPU water block pair will represent a pressure loss of .61psi and .44 psi, respectively. This is shown in figures 4 and 5.

The motor controller components are mounted to a 19" wide, 26" deep aluminum plate. The plate will be liquid cooled with two Wakefield-Vette 4-pass cold plates. The components will be mounted on either side of the cold plates, which are sandwiched by aluminum mounting plates. The two cold plates are mounted in series, with all of the coolant flow passing through both. This design is shown in figure 6.

The maximum heat leak from the electronics rack is determined by considering the maximum temperature difference between the inside of the rack enclosure and ambient air, as well as the thermal resistances of the enclosure insulation and natural convection at the exterior of the rack. Unless it is shown to result in a violation of the requirement, it is sufficient to perform a calculation that is both relatively simple but addresses the problem at hand conservatively. In this case, the interior temperature of the wall of the enclosure is assumed to be very close to the maximum air temperature ($T_{hx,in}$), which is calculated from the following equation:

$$T_{hx,in} = T_{c,avg} + \frac{\dot{Q}}{TP}$$

$T_{hx,in}$ is the temperature of the air entering the heat exchanger, $T_{c,avg}$ is the average coolant temperature in the heat exchanger, TP is the stated thermal performance of the heat exchanger, and \dot{Q} is the heat being removed by the heat exchanger. The heat flux (q'') through the rack enclosure can then be calculated from $T_{hx,in}$, T_{amb} (ambient temperature),



enclosure insulation R value (R_{encl}), and the enclosure-ambient natural convection coefficient (h_{amb}) from the following equation:

$$q'' = \frac{T_{amb} - T_{hx,in}}{R_{encl} + \frac{1}{h_{amb}}}$$

In order to calculate h_{amb} , a temperature difference between the exterior of the enclosure and ambient air must be assumed. This calculation is repeated until the assumed temperature difference and the calculated temperature difference match, since natural convection is driven by temperature difference and not ambient air conditions alone. For the worst-case hot condition, with the rack fully populated and operating at 100% duty cycle with ambient air at 25°C, the heat leak is 40W. For the worst-case cold condition, with the rack populated with the components it will be initially shipped with and ambient air at -5°C, the heat leak is 32W.

The operating temperatures of the air-cooled components can be determined from the temperature of the rack recirculating air that flows past it or over it. The operating temperatures of the liquid-cooled components are determined from temperatures of their mounting interfaces, which is a function of how much heat is added to the coolant, coolant properties, and coolant mass flow rate. The chip temperatures of the CPUs and GPUs are also determined from the thermal performance of the water blocks and the temperature of the coolant flowing through the water blocks. A summary of the temperatures for the worst-case hot condition (25°C ambient and 100% populated), as well as temperatures for the same condition but at 20°C is shown in table 1.

A summary of component operating temperatures is shown for the worst-case cold condition (-5°C ambient, rack populated in as-shipped condition, motors at 10% duty cycle), and the same condition but with ambient air at 0°C in table 2.

The temperature violations indicated for the worst-case hot and worst-case cold conditions can be addressed by opening up the doors of the rack when it experiences a daytime temperature higher than 20°C, or by turning off the heat exchanger fans when the outside ambient temperature drops below 0°C. This prevents the RTC and ICC motherboards from experiencing an operational temperature that is either hotter or colder than what they are rated for. This table also shows a temperature violation for the Andor cameras at ambient temperatures below 0°C. However, the risk to the Andor cameras and the motherboards is mitigated by the low probability that the observatory will actually experience these temperatures. A histogram of temperature data is shown in figure 7. The histogram also shows the limiting ambient temperatures for the motherboards (labeled “mobo”) and the SMC100CC and C-863 motor controllers.



Additional testing of the motherboards can be performed in order to qualify them for operation in a larger temperature range than what they are currently rated for. The motherboards can be placed in a thermal chamber whose ambient temperature can be set to temperatures outside of the specified operating range of the motherboards (10°C-35°C) and functional tests can be performed to verify its operation at these temperatures. This would also reduce the risk carried by implementing off-the-shelf motherboards.

To further mitigate risk at worst-case cold operation, a heater can be placed on the motor controller plate, and can be temperature-controlled so that the plate does not drop below 5°C during periods when the heat exchanger fans are shut off. The minimum operating temperature of the motor controllers is 5°C, and the risk that the mounting interface for these components approaches this temperature increases when the heat exchanger fans are shut off, since the coolant stops carrying heat from the heat exchanger when that occurs. Also, the motor controllers are operating at a significantly reduced duty cycle (as low as 10%), thereby reducing the heat input to the mounting interface. Both of these effects can be easily counteracted with a temperature-controlled heater.

Each of the features indicated by the interfaces requirement (requirement 7) will be implemented in the design of the electronics rack, though those details are not presented here. This will include casters, removable sections or doors in the rack, proper cable management, lifting eyes attached to the top of the enclosure, and bulkhead connections for electronics and coolant hoses.

Figure 1

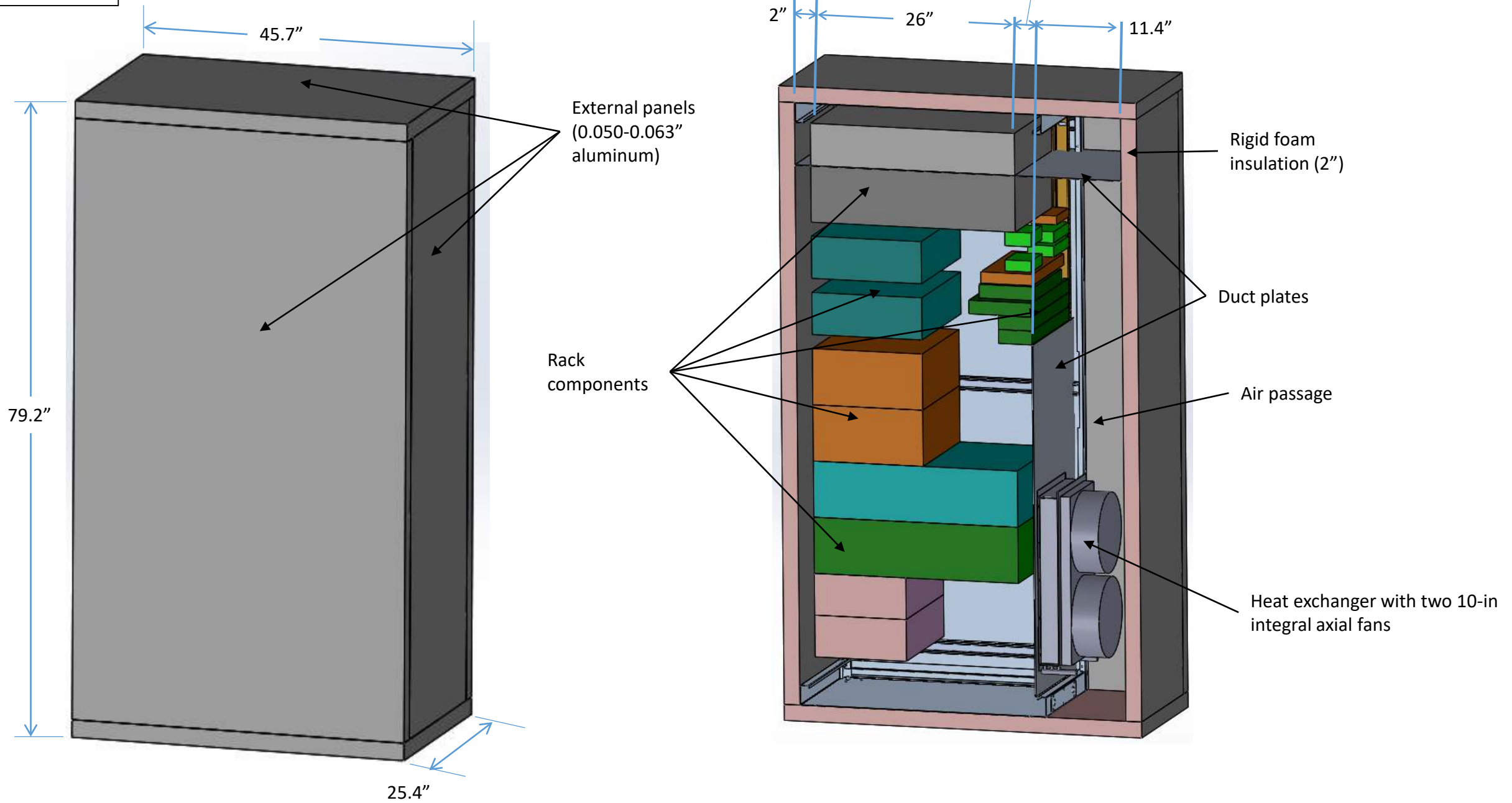


Figure 2

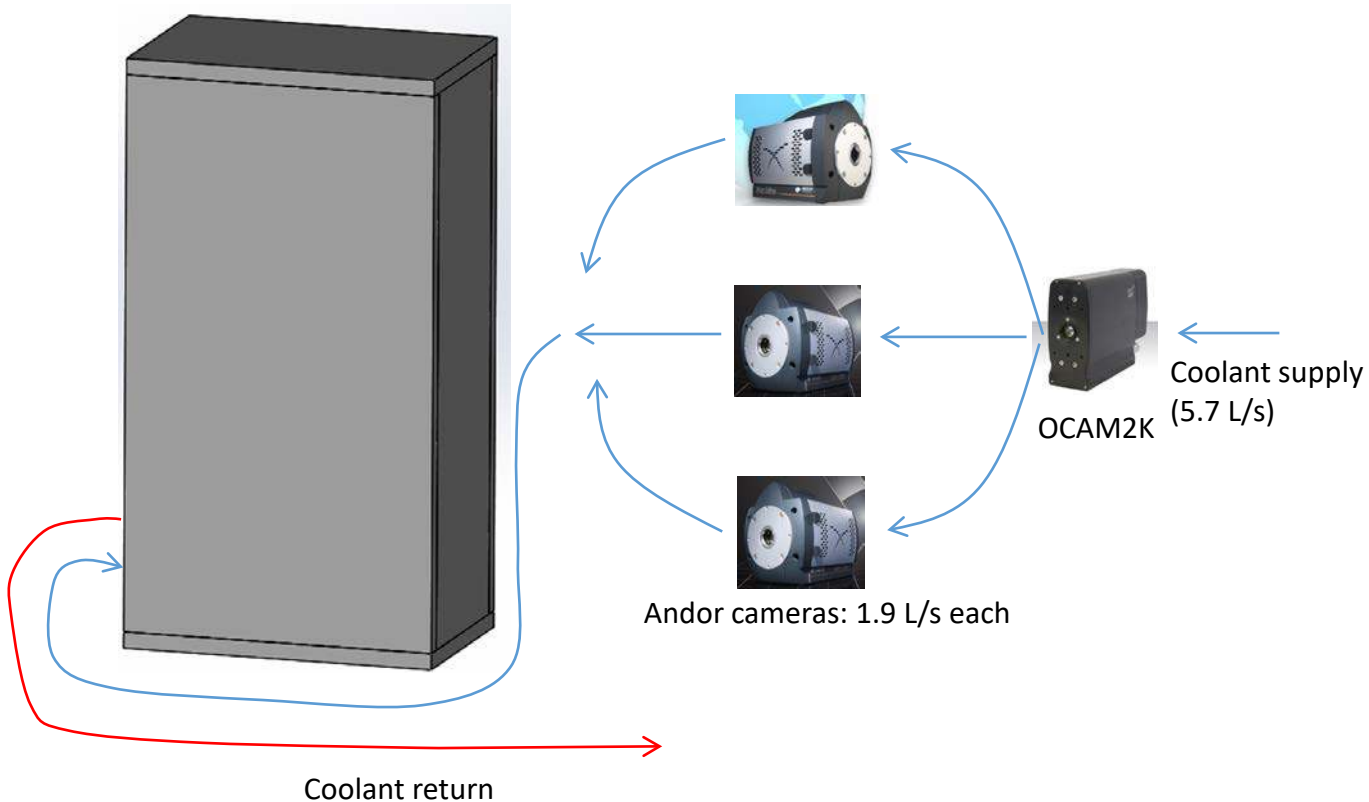


Figure 3

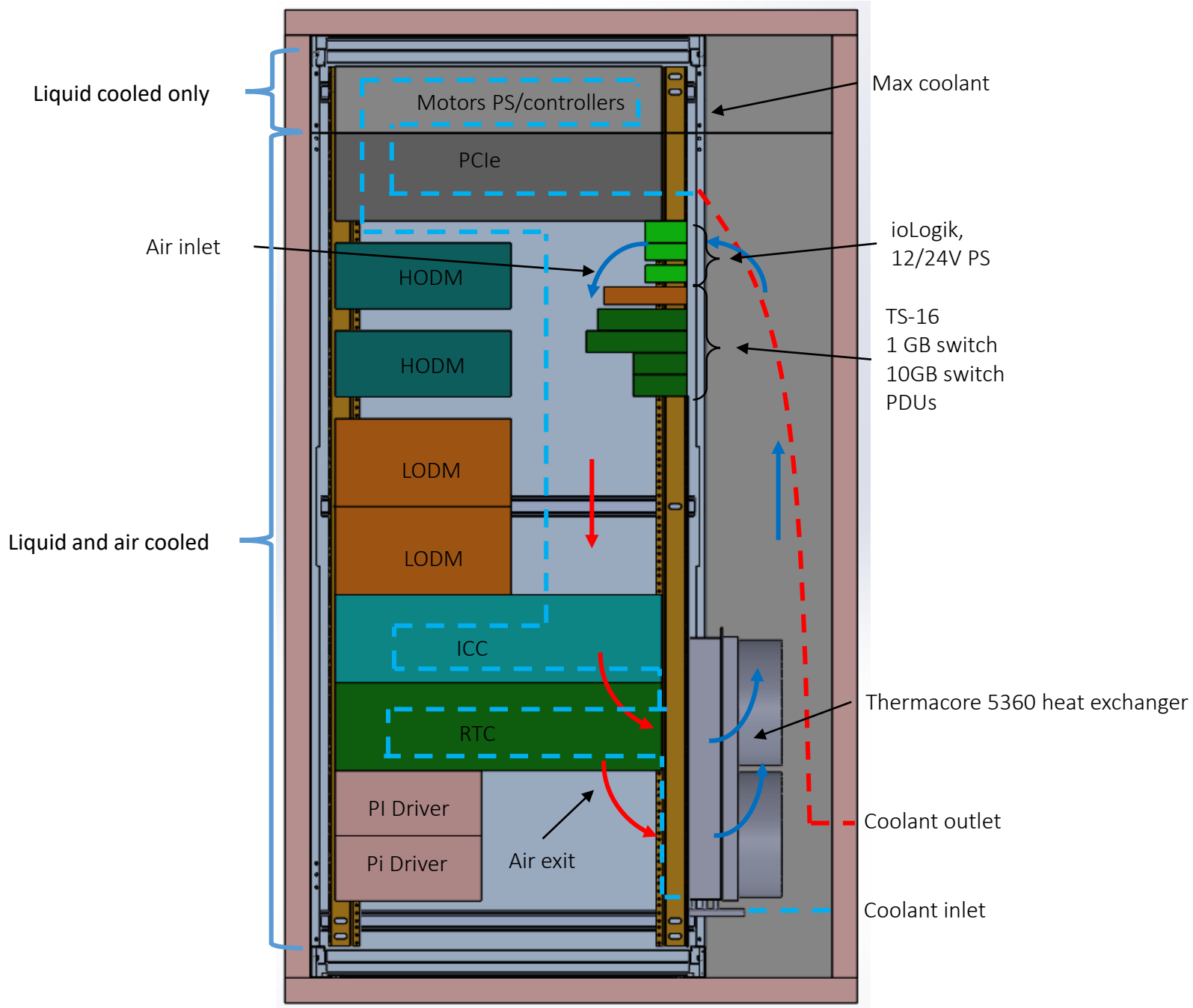


Figure 4

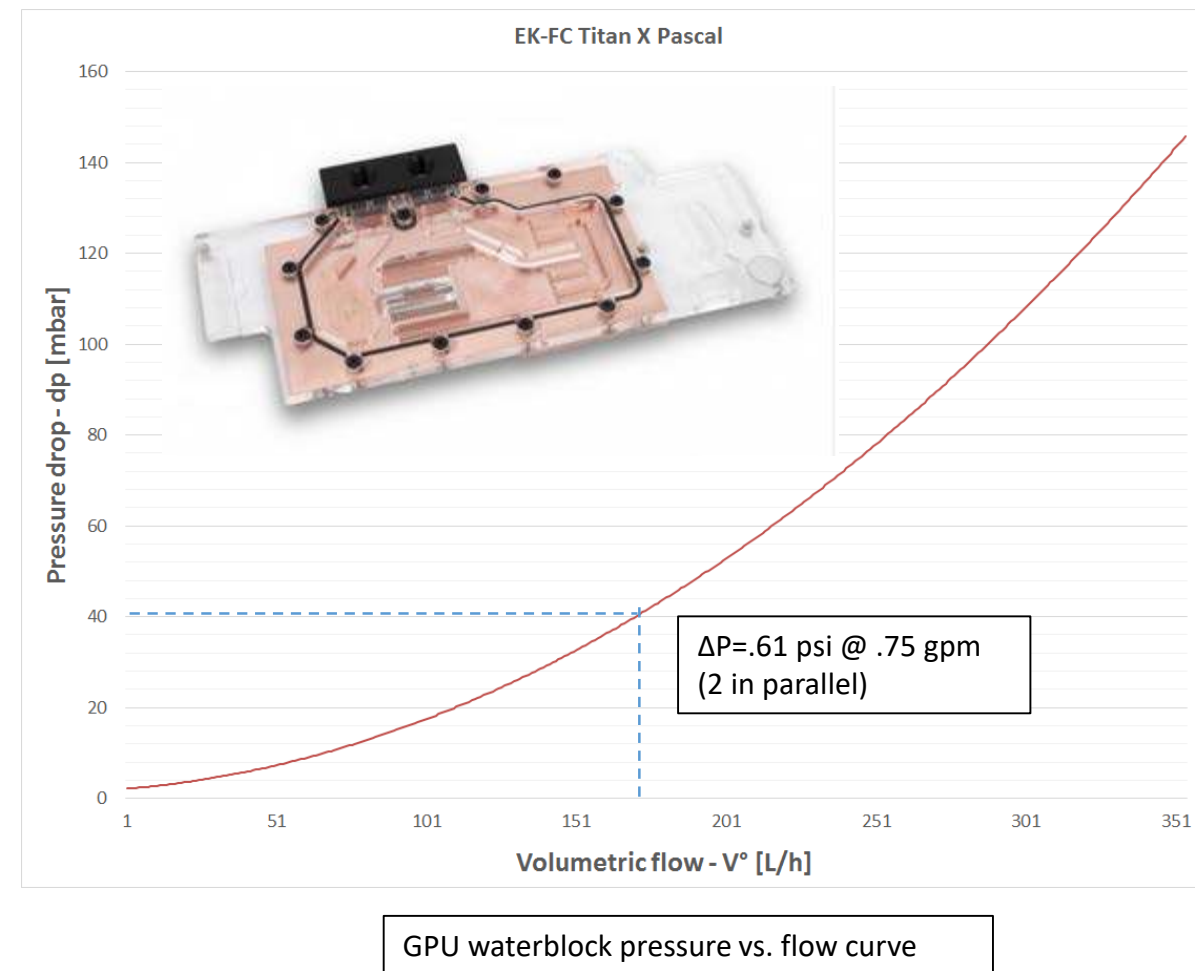


Figure 5

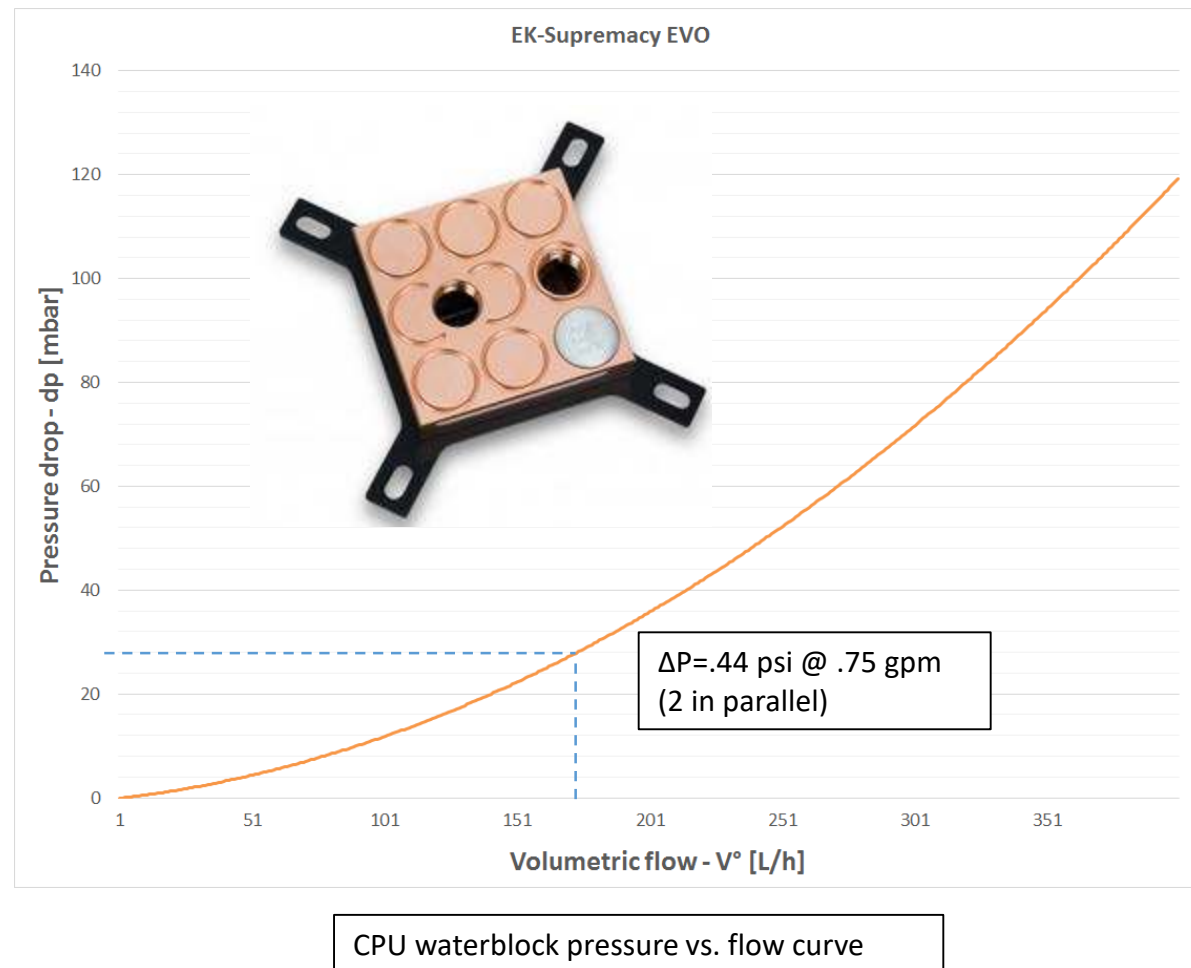


Figure 6

Motor Controllers and Drivers

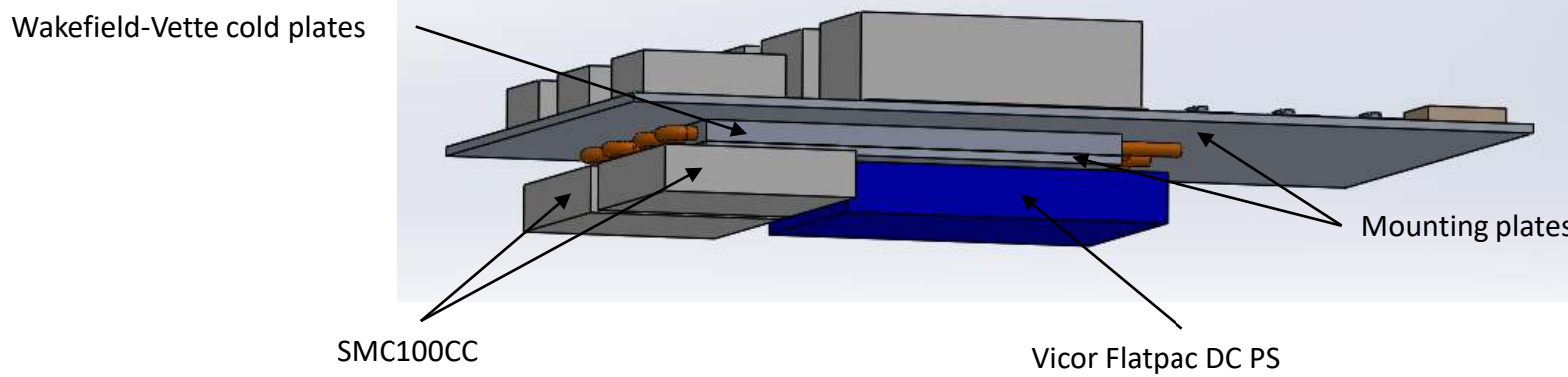
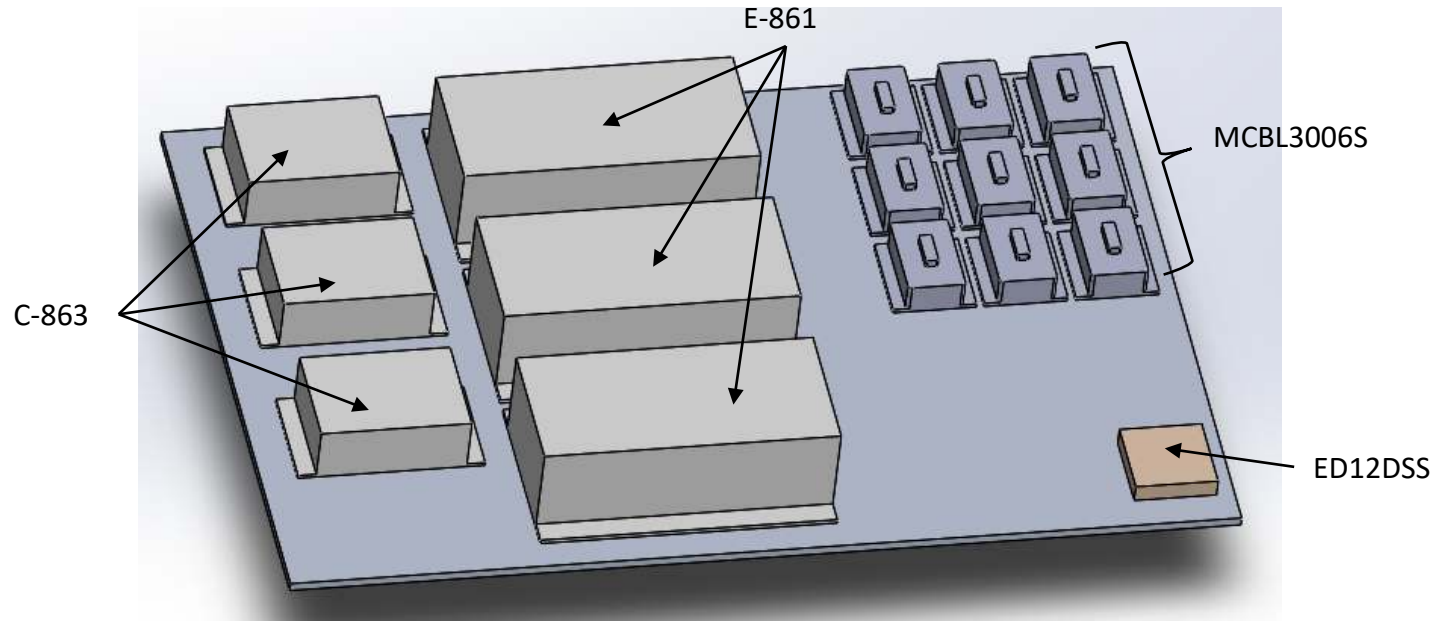


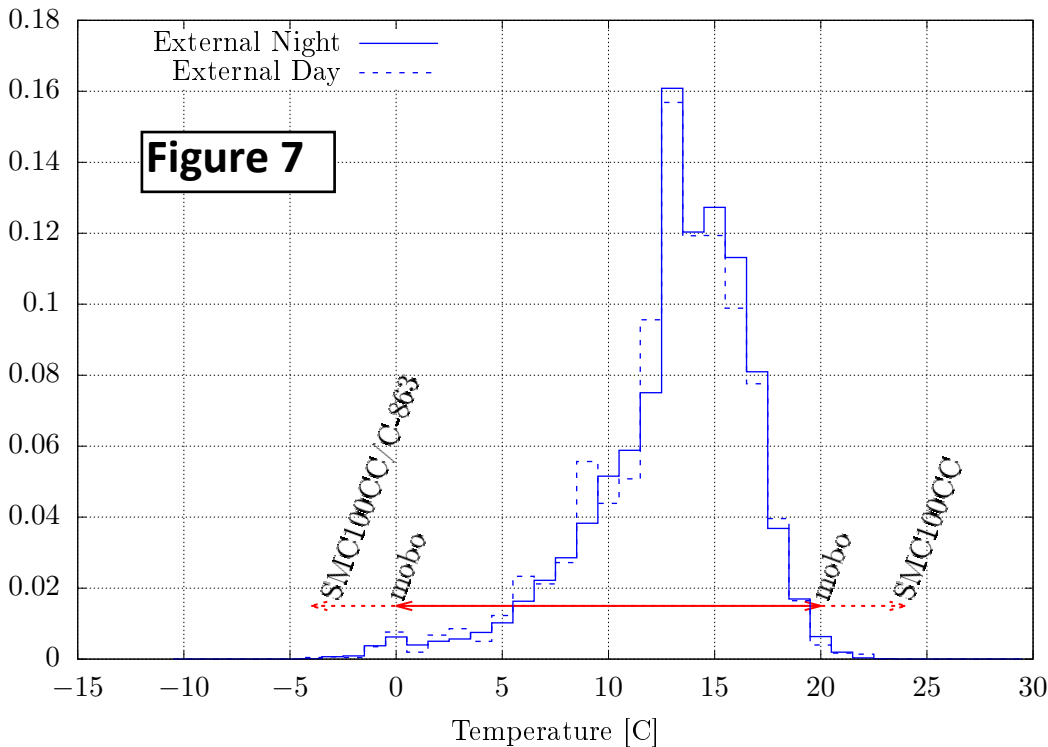
Table 1

Component	Operating temperature (°C)		Max allowable temperature (°C)	Margin	
	@ 25°C	@ 20°C		@ 25°C	@ 20°C
PCIe PSU	37	32	50	13	18
ioLogik	37	32	75	38	43
12/24 VDC PS	37	32	40	3	8
TS-16	37	32	50	13	18
1 GB Switch	37	32	40	3	8
10 GB Switch	37	32	50	13	18
PDU	37	32	50	13	18
HODM	37	32	40	3	8
LODM	40	35	50	10	15
ICC PSU	40	35	50	10	15
ICC Motherboard	40	35	35	-5	0
RTC PSU	40	35	50	10	15
RTC Motherboard	40	35	35	-5	0
PI Driver	43	38	50	7	12
OCAM2K	28	23	35	7	12
Andor 897	25	20	30	5	10
Andor 888	25	20	30	5	10
RTC GPU (chip)	43	38	94	51	56
RTC CPU (chip)	67	62	80	13	18
ICC CPU (chip)	68	63	80	12	17
PCIe GPU (chip)	51	46	94	43	48
E-861	41	36	50	9	14
C-863	41	36	50	9	14
Vicor Flatpac	41	36	85	44	49
SMC100CC	41	36	40	-1	4
MCBL	41	36	85	44	49

Table 2

Component	Operating temperature (°C)		Min allowable temperature (°C)	Margin	
	@ -5°C	@ 0°C		@ -5°C	@ 0°C
PCIe PSU	3	8	0	3	8
ioLogik	3	8	-40	43	48
12/24 VDC PS	3	8	-10	13	18
TS-16	3	8	0	3	8
1 GB Switch	3	8	0	3	8
10 GB Switch	3	8	0	3	8
PDU	3	8	-15	18	23
HODM	3	8	0	3	8
LODM	5	10	0	5	10
ICC PSU	5	10	0	5	10
ICC Motherboard	5	10	10	-5	0
RTC PSU	5	10	0	5	10
RTC Motherboard	5	10	10	-5	0
PI Driver	7	11	5	2	6
OCAM2K	-4	1	--	--	--
Andor 897	-5	0	0	-5	0
Andor 888	-5	0	0	-5	0
RTC GPU (chip)	9	14	0	9	14
RTC CPU (chip)	33	38	0	33	38
ICC CPU (chip)	33	38	0	33	38
PCIe GPU (chip)	9	14	0	9	14
E-861	4	9	0	4	9
C-863	4	9	5	-1	4
Vicor Flatpac	4	9	0	4	9
SMC100CC	4	9	5	-1	4
MCBL	4	9	0	4	9

Relative Frequency





3.2 Computers and Data Management

Jared Males
Nirav Merchant, Eric Lyons



Overview

- This describes our computer system design and the closely related data management plan.
- Requirements:
 - Computer-system:
 - Perform real-time calculations with minimum latency, no more than 1/4 frame (125 microseconds)
 - Perform near-real-time loop maintenance (gain optimization, filter determination)
 - Instrument control: stages, filter wheels, camera readouts
 - Support user interfaces: AO operations and Science control
 - Data Management Plan
 - Minimum requirement: save all science camera images, along with appropriate metadata
 - Goal: save ALL data, including AO system telemetry at full rate.



FLOPS Budget

- Main Loop: matrix-vector-multiply (MVM) reconstruction:
 - $(2*MN - M)$ FLOPS per calculation
 - $M = 14400$ (max pixels assuming no-slope calculation*)^{*Note: Slope calculation consumes FLOPS too}
 - $N = 2048 + 97$ (total actuators being controlled)
 - 3700 Hz $\Rightarrow 0.23$ TFLOPS
 - This gives 1 frame delay due to calculation
 - 1 TFLOP capacity = 1/4 frame delay
 - All of this is highly naive, we won't achieve these rates
 - NVIDIA GTX 1080 Ti: 11 TFLOPS
 - 1/48 frame delay due to calc. (naive)
 - ~\$700 each --> we can meet the MVM requirement with minimum possible delay due to reconstruction
- Other Main Loop Tasks:
 - PyWFS image processing
 - Integration and Filtering (control law)
 - DM safety checks, applying commands, etc.

Other FLOPS Heavy Tasks

- Gain Optimization:
 - Need PSDs of each mode (~2200)
 - Optimum technique: 30 FFTs of 3700 points (1 sec), averaged
 - Probably need rolling average with frequent updates => basically 2200 FFTs calculate each sec
 - Gain optimization includes numerical minimization
- LQG
 - Kalman filter system determination (line identification)
- Predictive Control:
 - Poyneer Method: layer identification and filter determination
 - EOF method: SVDs of size ~10k X 2200
 - LP method: efficient Levinson Recursion with gain opt
 - Both EOF and LP result in large filters (time history)
- Other loops
 - LOWFS (same tasks, just fewer pixels and actuators)
 - FPWFS (similar tasks)
 - Pupil alignment, PyWFS pupil stabilization



Computer Inventory

- Computer Needs:
 - Real-Time control Computer (RTC)
 - PyWFS reconstruction, HODM and LODEM control
 - Various gain optimization and filter calculation tasks
 - Real-time telemetry
 - Instrument Control Computer (ICC)
 - LOWFS reconstruction and LOWFS-DM control
 - Science camera acquisition (2 cameras)
 - Motion control (> 26 DOF)
 - TCS Telemetry monitoring
 - AO Operations Computer (AOC)
 - In control room, custom workstation for AO operations
 - AO operator workstation
 - Server for Astronomer User Interface
- FLOPS Requirement
 - Main loop requires 1 1080 Ti class GPU
 - SCExAO Experience: ~4x 1080 Ti GPUs can handle everything, but Pred. Con. may require more
 - Managing real-time processes is easier with more GPUs, even if each one not 100% loaded



Data Management Requirements

- Goal: save everything for later use
 - Long term system analysis (e.g. see Bailey+, SPIE 2016)
 - Data reduction

Table 1:: RTC Data Rate and Capacity Requirements.

Source	Name	Type	Bits /pix	Size [pixels]	Rate [frames/sec]	Rate [B/sec]	Notes
PyWFS	WFS Images	ushort	14	14400	3700	93247400	Assumed stored @14 bits
LODM	LODM Commands	single	32	97	2000	780000	
HODM	HODM Commands	single	32	2048	3700	30317800	
Misc.	Various	uchar	8	10485760	1	52428810	A 50 MB/sec margin.
			MB/sec	TB/hr	TB/night	TB/run	
			Total:	168.6	0.58	5.79	17.4
							10 hr/night x 3/run

Table 2:: ICC Data Rate and Capacity Requirements.

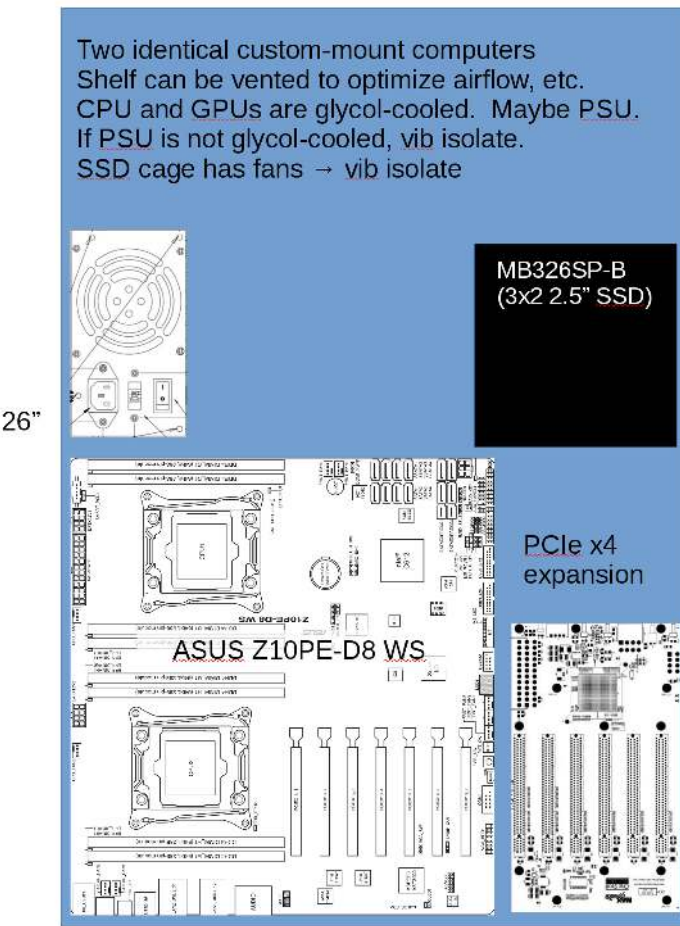
Source	Name	Type	Bits /pix	Size [pixels]	Rate [frames/sec]	Rate [B/sec]	Notes
SCI-1	Science image	ushort	16	1048576	26	54526004	
SCI-2	Science image	ushort	16	1048576	26	54526004	
TCS Telem	Various	uchar	8	1	261.9	383.9	Avg rate, see App. C.
Pupil Alignment	Pupil Images	ushort	16	4096	1	8194	
LOWFS	LOWFS Images	ushort	16	262144	56	29360240	
LOWFSDM	LOWFS Commands	single	32	97	2000	780000	
Misc.	Various	uchar	8	10485760	1	52428810	50 MB/sec margin.
			MB/sec	TB/hr	TB/night	TB/run	
			Total:	130.8	0.45	4.49	13.47
							10 hr/night X 3/run



Data Management Requirements

- Requirements:
 - Write speeds: > 170 MB/sec (mostly sequential write)
 - Nightly Capacity: > 6 TB each for RTC and ICC (10 hr night)
 - Run Capacity: > 31 TB total (3 nights)
 - Must get this back to UA, store, and make it accessible.
- Following design uses today's technology and prices
 - Shows we can achieve it
 - But... we won't buy anything until we need it (1-2 years)
 - That means it will be cheaper and/or easier to achieve

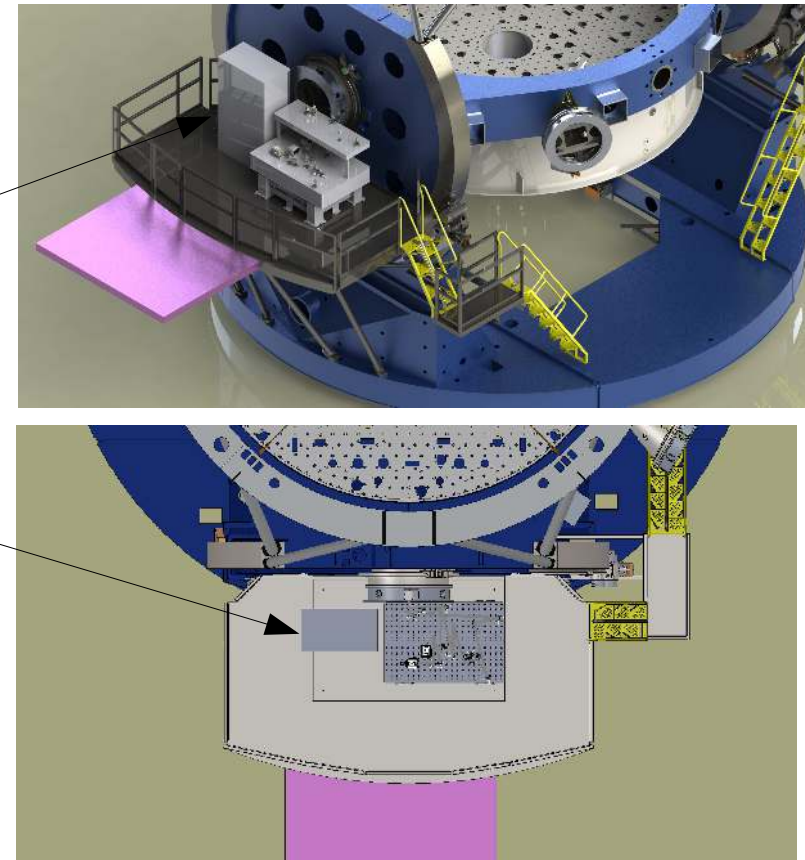
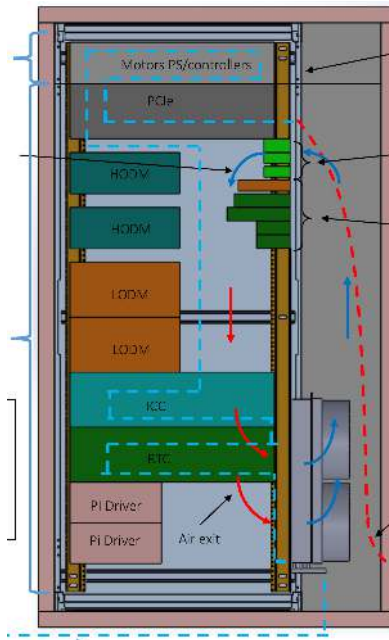
Custom Rack Mount Computers



- RTC and ICC will be on platform next to instrument
- No case, we will drill our own ATX hole pattern (etc) in an Aluminum plate (a rack shelf)
 - Max space and airflow and ease of cabling
 - What we did for VisAO and it works great
- Specs on following slides
- PCIe expansion card gives extra slots
- CPU and GPUs are direct liquid cooled
 - See thermal design by Dan Alfred

Electronics Rack

Electronics rack on platform contains RTC, ICC, and PCIe expansion, plus many other controllers and drivers.



For details see part 3.1



RTC Specs

Component		Manuf.	Part No.	No.	Cost Each.	Total Cost	Notes
ATX 12"x13"	Motherboard	ASUS	Z10PE-D8 WS	1	\$554.08	\$554.08	
	Processor (x2)	Intel	i7 6950x (10 core)	2	\$1,649	\$3,298.00	Liquid Cooled, 20 cores total
ATX	PS	Quiet Power	Quiet 1050W PC ATX PSU	1	\$89.99	\$89.99	Fan--> vibration isolated mount
	RAM	G.Skill	8x16 GB DDR 2400	1	\$759	\$759.00	128 GB total
	HDD Cage		MB326SP-B	1	\$80.00	\$80.00	Holds 6 2.5" SSDs
OS	HDD	Crucial	CT525MX300SSD1	2	\$149.90	\$299.80	525GB ea, RAID-1, 525GB total
Storage	HDD	Samsung	MZ-75E4T0B/AM	4	\$1,480	\$5,918.20	4TB ea, 4 RAID-5, 12TB total

PCIe Slots:

PCIe Slot 1 (x16 3.0 CPU-1)	GPU	NVIDIA	1080 Ti	1	\$699.99	\$699.99	Liquid Cooled. If expanded, this is HIC slot
PCIe Slot 2 (x8 3.0 CPU-1)							
PCIe Slot 3 (x16 3.0 CPU-1)	GPU	NVIDIA	1080 Ti	1	\$699.99	\$699.99	Liquid Cooled. If expanded, this is HIC slot
PCIe Slot 4 (x8 3.0 CPU-1)							
PCIe Slot 5 (x16 3.0 CPU-2)	GPU	NVIDIA	1080 Ti	1	\$699.99	\$699.99	Liquid Cooled
PCIe Slot 6 (x8 3.0 CPU-2)							
PCIe Slot 7 (x16 CPU-2)	Expansion Card	Cyclone Microsystems	PCIe2-437	1	\$709	\$709.00	

PCIe Expansion:

PCIe Slot 1 (x4 2.0)	HOWFS F.G. (x4)	Matrox	Solios eV-CLF	1	\$0	\$0	Part of OCAM purchase
PCIe Slot 2 (x4 2.0)	HODM (x1)	BMC	HVA Interface Card	1	\$0	\$0	Included in BMC DM cost
PCIe Slot 3 (x4 2.0)	LODM	Alpao	DM Interface Card	1	\$0	\$0.00	Included in Alpao DM cost
PCIe Slot 4 (x4 2.0)	10 GBs Net	Small Tree	P2E10G-2-T	1	\$599	\$599.00	

Total \$14,407.04 Assumes no overhead

RTC PCIe Expansion

- COTS solution gives 6 more double-wide GTX slots
 - CUBIX Xpander 8 (have to use 2 slots to connect)



Component	Manuf.	Part No.	No.	Cost Each.	Total Cost	Notes
Rack Module	5U	Cubix Xpander	Rackmount 8 Gen 3	1	\$8,799	\$8,799 Possible upgrade, thermal is sized for this
Slot 1	GPU	NVIDIA	1080 Ti	1	\$0	\$0 Moved from Slot 1
Slot 2	GPU	NVIDIA	1080 Ti	1	\$0	\$0 Moved from Slot 2
Slot 3	GPU	NVIDIA	1080 Ti	1	\$700	\$700 Liquid Cooled
Slot 4	GPU	NVIDIA	1080 Ti	1	\$700	\$700 Liquid Cooled
Slot 5	GPU	NVIDIA	1080 Ti	1	\$700	\$700 Liquid Cooled
Slot 6	GPU	NVIDIA	1080 Ti	1	\$700	\$700 Liquid Cooled
Slot 7	GPU	NVIDIA	1080 Ti	1	\$700	\$700 Liquid Cooled
Slot 8	GPU	NVIDIA	1080 Ti	1	\$700	\$700 Liquid Cooled
				Total:	\$12,999	

We have budgeted for this (financially, thermally, and spatially), but it is an upgrade we do not plan to start with.



ICC Specs

Component	Manuf.	Part No.	No.	Cost Each.	Total Cost	Notes
ATX 12"x13"	Motherboard	ASUS	Z10PE-D8 WS	1	\$554.08	\$554.08
	Processor (x2)	Intel	i7 6950x (10 core)	2	\$1,649	\$3,298.00
ATX	PS	Quiet Power	Quiet 1050W PC ATX PSU	1	\$89.99	\$89.99
	RAM	G.Skill	8x16 GB DDR 2400	1	\$759	\$759.00
	HDD Cage		MB326SP-B	1	\$80.00	\$80.00
	OS	Crucial	CT525MX300SSD1	2	\$149.90	\$299.80
Storage	HDD	Samsung	MZ-75E4T0B/AM	4	\$1,480	\$5,918.20
4TB ea, RAID-5, 12TB total						

PCIe Slots:

PCIe Slot 1 (x16 3.0 CPU-1)	GPU	NVIDIA	1080 Ti	1	\$699.99	\$699.99	For LOWFS Recon.
PCIe Slot 2 (x8 3.0 CPU-1)							
PCIe Slot 3 (x16 3.0 CPU-1)	SCI-1 F.G. (x4)	Matrox	Solios eV-CLB	1	\$925.00	\$925.00	Andor 888
PCIe Slot 4 (x8 3.0 CPU-1)	SCI-2 F.G. (x4)	Matrox	Solios eV-CLB	1	\$925.00	\$925.00	Andor 888
PCIe Slot 5 (x16 3.0 CPU-2)	LOWFS F.G. (x4)	Matrox	Solios eV-CLB	1	\$925.00	\$925.00	Andor 897
PCIe Slot 6 (x8 3.0 CPU-2)							
PCIe Slot 7 (x16 CPU-2)	Expansion Card	Cyclone Microsystems	PCIe2-437	1	\$709	\$709.00	

PCIe Expansion:

PCIe Slot 1 (x4 2.0)							
PCIe Slot 2 (x4 2.0)							
PCIe Slot 3 (x4 2.0)	LODM	Alpao	DM Interface Card	1	\$0	\$0.00	Included in Alpao DM cost
PCIe Slot 4 (x4 2.0)	10 GBs Net	Small Tree	P2E10G-2-T	1	\$599	\$599.00	

Total \$15,782.06 Assumes no overhead



AOC Specs

Component	Manuf.	Part No.	No.	Cost Each.	Total Cost	Notes
ATX 12"x13"	Motherboard	ASUS	Z10PE-D8 WS	1	\$554.08	\$554.08
	Processor (x2)	Intel	i7 6950x (10 core)	2	\$1,649	\$3,298.00 Liquid Cooled, 20 cores total
ATX	PS	Quiet Power	Quiet 1050W PC ATX PSU	1	\$89.99	\$89.99 Fan--> vibration isolated mount
	RAM	G.Skill	8x16 GB DDR 2400	1	\$759	\$759.00 128 GB total
	HDD Cage		MB326SP-B	1	\$80.00	\$80.00 Holds 6 2.5" SSDs
OS	HDD	Crucial	CT525MX300SSD1	2	\$149.90	\$299.80 525GB ea, RAID-1, 525GB total
Storage	HDD	Samsung	MZ-75E1T0B/AM	4	\$355	\$1,419.80 1TB ea, RAID-5, 3TB total
PCIe Slots:						
PCIe Slot 1 (x16 3.0 CPU-1)	GPU	NVIDIA	1080 Ti	1	\$699.99	\$699.99 For display purposes, 2 monitors
PCIe Slot 2 (x8 3.0 CPU-1)						
PCIe Slot 3 (x16 3.0 CPU-1)	GPU	NVIDIA	1080 Ti	1	\$699.99	\$699.99 For display purposes, 2 monitors
PCIe Slot 4 (x8 3.0 CPU-1)						
PCIe Slot 5 (x16 3.0 CPU-2)	10 GBs Net	Small Tree	P2E10G-2-T	1	\$599	\$599.00
PCIe Slot 6 (x8 3.0 CPU-2)						
PCIe Slot 7 (x16 CPU-2)						
					Total	\$8,499.65 Assumes no overhead

- This will be in the control room, so in a workstation case with 4 monitors, keyboard, mouse, etc.



Specification Summary

- Using SSD Drives:
 - 4x 4TB in RAID 5 in RTC and ICC each:
 - $(1-1/N) = 12$ TB capacity on each of RTC and ICC
 - Single drive sequential write speed: 520 MB/sec (only need 32% of this)
 - This meets the nightly data management spec
- 20 true CPU cores per machine, 128 GB RAM
- On platform: 10 NVIDIA 1080 Ti
 - 113 TFLOPS from 35,840 CUDA cores

How Do We Get It Home?

- Extensive network transfer testing from LCO to Tucson with existing MagAO data shows that we can't do it.
 - Can be as low as ~100 GB a day (depends on load)
 - So it could take 310 days to transfer a 31 TB run's worth
- Solution: we pack it home in 2 of these:



5x 8TB RAID Array. 8.5" X 4.6" X 6.8".

Just drives, no computer

RAID 5: 32 TB

- enough for 1 run
- Unload RTC and ICC to this each day.

\$2395 each, 2x for redundancy

- Alternative to shipment: with collaborators Merchant and Lyons (UA/CyVerse) we are exploring using a host in Chile for these units
 - Instead of transporting all the way home, they could be delivered to a site in La Serena or Santiago where network transfer will be possible

How Do We Store It At UA?

- We buy a 136 TB RAID machine, which will be hosted by CyVerse (not in Steward)
- Connected to CyVerse iRODS. Interface through CyVerse
 - Currently stores and manages 2.5 peta-bytes of data
- Automagically gives us distribution to users, with access rights, can enforce proprietary periods, etc.
- ~ \$20 K each
 - 1 at UA, 1 at TACC for offsite backup
- Can hold 4 runs worth
 - We may only save non-science telemetry for a set period of time
- Ongoing hosting/management cost: 10 hrs, ~\$720/year.





Computing Budget

- Main Components:
 - RTC: \$14,407
 - PCIe Xpansion: \$12,999
 - ICC: \$15,782
 - AOC: \$8450
 - Transport: 2x \$2395 = \$4790
 - Storage: 2x \$20k = \$40k
 - Various Spares: ~\$5k
- Total: \$101,428



Reality

- It is unlikely that we will operate at full-rate 10 hours/night
 - With pointing overheads, etc, this probably has ~2.5 hr margin.
- Data specs assumed full-frame and full-rate for all cameras. LOWFS, especially, will use small windows and therefore much smaller rates most of the time
- Someday, runs might be longer than 3 nights
 - But space and speed will continue to get cheaper
- **This design can meet our needs today, and has capacity margin**
 - PCIe expansion may not be needed (GPU capacity is ever expanding)
 - More space will be available for same money in the future.
 - Can cut off-site backup if space needed at UA

Can We Reduce This Much Data?

- We have developed a cloud-based data reduction system through our collaboration with Nirav Merchant, Eric Lyons, and Asher Haug-Baltzell (CyVerse / BIO5)
 - Distributed computing solution to image processing / reduction problem: Findr
 - See: <http://adsabs.harvard.edu/abs/2016SPIE.9913E..0FH> and <http://adsabs.harvard.edu/abs/2017ApJ...836..223W>
 - We recently obtained 10^6 CPU hours on NSF Jetstream: [resources are available](#).

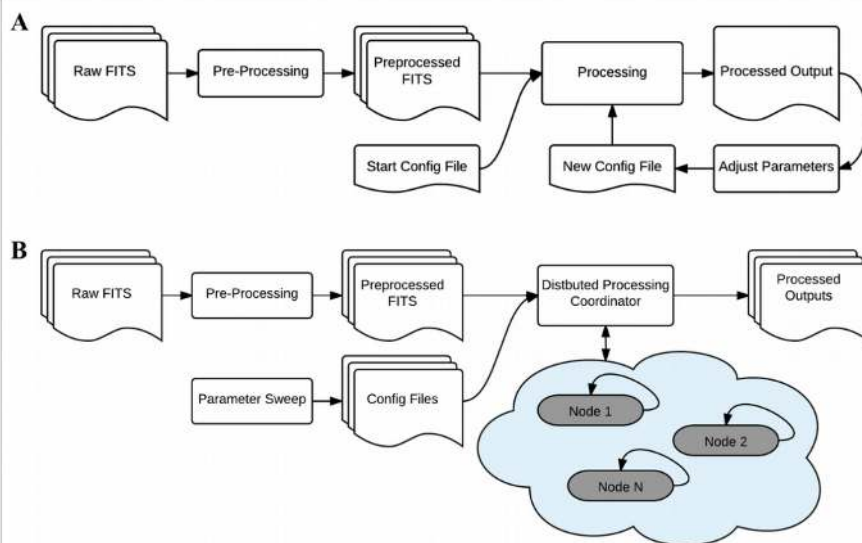
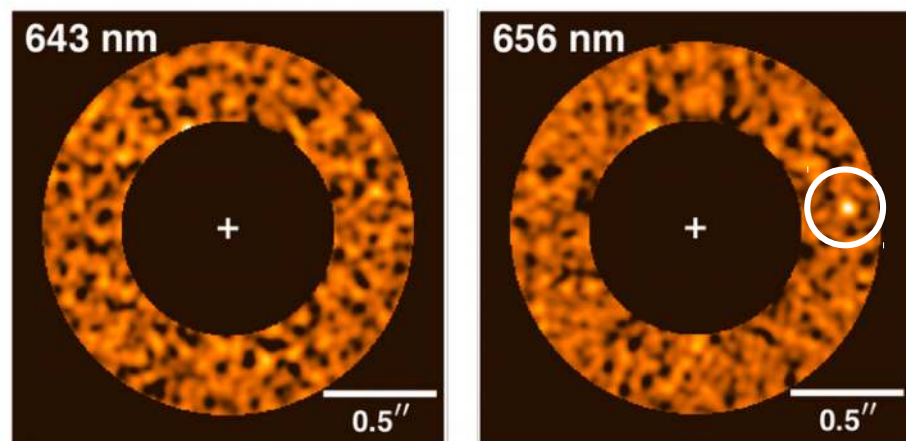


Figure 1. PSF subtraction workflows before (A) and after (B) cloud distribution. (A) Before cloud distribution, determining optimum parameters for KLIP reduction was a slow, manually intensive process. After each reduction, parameters would be adjusted and results compared until a high signal-to-noise ratio was achieved. (B) Distribution of the reduction process to cloud computing resources leads to a simplified workflow and enables full sweeps investigating all parameter combinations. This workflow is faster, less prone to bias, requires less manual input, and leads to statistically sound conclusions.



Images of GQ Lup B reduced with Findr on the NSF Chameleon cloud system. See Haug-Baltzell+ (2016) for details, and Wu+ (2017) for the interpretation.



Detailed Data Management Plan

Here we describe in detail how the data collected by the MagAO-X project will be managed.

1. Products of the Research

The following data products will be generated from MagAO-X related laboratory testing: (1) deformable mirror (DM) influence functions; (2) DM flat measurements; (3) pyramid wavefront sensor (PyWFS) characterization; and (4) detector characterization. On-sky engineering data will include: (1) PyWFS pupil images; (2) adaptive optics (AO) system telemetry; and (3) science camera images (for Strehl ratio measurements, etc.). These data will be made available using the NSF-funded CyVerse (formerly iPlant) infrastructure described below. All developed techniques and engineering results for the MagAO-X project will be made publicly available through one (or more) PASP papers and SPIE conference papers. These will be made publicly available on arxiv.org, and we will make pre-prints available directly from the project website (<https://visao.as.arizona.edu>).

Science observations enabled by this project will produce raw images and spectra, as well as AO system telemetry. These will be analyzed and used to produce scientific publications by the responsible astronomer. All scientific publications based on MagAO-X data will be made publicly available on arxiv.org, and we will make pre-prints available directly from the project website (<https://visao.as.arizona.edu>).

2. Data and Metadata Quantity and Format

All raw data will be saved in HDF5 files, including science images. This is a departure from the norm in astronomy, however the standard FITS (Pence et al., 2010) format is quite outdated and has limited metadata description capabilities. Furthermore, we expect HDF5 to provide better performance in terms of access speed (reading and writing). To support legacy data processing systems, we will follow the HDFITS standard (Price et al, 2015). This standard is designed for converting from HDF5 to FITS and provides python code to do so. This includes generation of FITS header metadata.

We will follow the same standards used for VisAO for our metadata collection and storage. Metadata describing the AO system configuration, weather, science camera configuration, and other details relevant to observations will be stored in appropriate HDF5 attributes, and published in FITS headers when converted.

3. Access to Data and Data Sharing Practices and Policies

Laboratory and Engineering Data: All laboratory and on-telescope-engineering data (whether daytime testing or night-time observations) generated for this project will be made publicly available after a three-month period. This is primarily to give the team time to analyze the data and perform quality control. Access to the data will be provided using the NSF-funded CyVerse infrastructure. CyVerse provides several resources for scalable data management with connections to large-scale and distributed computing resources, namely:

	MagAO-X Preliminary Design 3.2 Computers and Data Management	Doc #: MagAOX-001 Date: 2017-Apr-X Status: Rev. 0.0 Page: 21
---	---	---

- **The Data Store (iDS):** The iDS is the foundation for data management, and is built on the integrated rule-oriented data system (iRODS) and delivers cloud data storage/transfer accessible through command line, software (iDrop), and web-based systems. Advantages of iDS include: (1) scalable, distributed, and redundant storage; (2) the appearance of a single file system to the user that nonetheless consists of easily expanded distributed data servers; (3) parallel file transfers of up to 1 Gb per second; and (4) strong support for metadata. All data generated by this project will be made publicly available through the iDS.
- **CyVerse’s Authentication Service (iAS):** iAS, built on the secure identity system Shibboleth, validates researchers on CyVerse’s systems, allows researchers to move among CyVerse’s resources, and permits other systems to validate users. Systems federated with CyVerse’s Authentication Service can then retrieve data from iDS, analyze them, and then send the analytical results back for downstream visualization.
- **CyVerse Atmosphere:** This is CyVerse’s cloud computing platform and is based on OpenStack for managing virtual machines (VM) images and instances. Any complicated software stack developed in this project that cannot be integrated in CyVerse’s Discovery Environment will be made available on a VM for other researchers to use.
- **CyVerse Discovery Environment (DE):** This is CyVerse’s rich web-based system that allows users to manage their data in the iDS and run analyses on CyVerse’s computing grid. All command-line driven workflows will be integrated in the DE for other researchers to use.
- **Powered by CyVerse:** This program offers technical assistance to analytical software systems that wish to utilize CyVerse’s CI to power their bioinformatics platforms.
- **CyVerse Science APIs:** This service will be a gateway for CyVerse and third-party platforms to register web-based APIs for data exchange and services.

Science Observations: Prior to publication, by default the raw data from science observations enabled by this project will be subject to a 24-month proprietary period during which the responsible astronomer will have exclusive access. The CyVerse system will automatically enforce this proprietary period by leveraging “rules” used by the Data Store (part of the iRODS architecture). Exceptions to this policy will be made based on astronomer requests and the policies of the Magellan partner institutions. Published data will be made available upon request, with approval by the responsible astronomer, using the CyVerse infrastructure.

4. Policies and provision for re-use, re-distribution and products of derivatives

Raw data access will come with a simple request to cite the relevant MagAO-X-based publication if used in a public product. Reproductions of published images made available on the MagAO-X project website will always include citations to the primary source, with standard academic citation practices applied. All software generated by this project will be released under the MIT license for use without restriction, and integrated in the appropriate CyVerse resource for ease of reuse by the scientific community. No reach-through rights or intellectual property rights will be claimed on the outcomes of this research, including associated data, software, and hardware designs.

5. Archiving of Data

We will utilize the CyVerse infrastructure at the University of Arizona (UA) to store data for the life of the MagAO-X system and beyond. All data will be saved in FITS format, preserving all

	MagAO-X Preliminary Design 3.2 Computers and Data Management	Doc #: MagAOX-001 Date: 2017-Apr-X Status: Rev. 0.0 Page: 22
---	---	---

relevant metadata in the headers. Management of data at UA will be coordinated through three phases; initial, near term, and long term. The specific practices will depend on several factors, especially the available technology and associated costs, data quantity, and long-term public access. **Initial** data management will facilitate robust storage and later analysis phases. At least two copies of all data files will reside on redundant disk systems; a working copy will be backed up by at least one archive copy. All analyses will occur using the working copy. The primary goal of these considerations is to preserve raw data in case of catastrophic hardware failure.

Near-term data management will support the project's computational analyses and facilitate public access. Once data are made public, they will be made available for public anonymous access through a specific area of the CyVerse Data Store. **Long-term** the data will be safely stored for later use. The Data Store replicates data between computers at UA and the Texas Advanced Computing Center (TACC). Currently, each site has at least 2 petabytes storage.

Access permissions will be managed automatically. Metadata recording the owning astronomer will be used to assign user permissions and provide a searchable database. Data will automatically become public at the end of the proprietary period.

6. Documentation

All data sets and software generated by this project will be documented and linked to using a wiki provided by UA, CyVerse, or another publicly available online documentation site. This site will also serve as a coordination hub between groups for documenting how data were handled, pre-processed, post-processed, published, and made publicly available.

References

Pence, W. D., Chiappetti, L., Page, C. G., Shaw, R. A.; Stobie, E. "Definition of the Flexible Image Transport System (FITS), version 3.0", *Astronomy and Astrophysics*, Volume 524, id.A42, 40 pp.
<http://adsabs.harvard.edu/abs/2010A<sup>%26lt;/sup>524A..42P>

Price, D. C., Barsdell, B. R., Greenhill, L. J. "HDFITS: Porting the FITS data model to HDF5", *Astronomy and Computing*, Volume 12, p. 212-220.
<http://adsabs.harvard.edu/abs/2015A<sup>%26lt;/sup>12..212P>

	MagAO-X Preliminary Design Computers & Software	Doc #: MagAOX-001 Date: 2017-04-23 Status: Rev. 0.0 Page: 1 of 14
---	--	--

3.3 Software design

Jared R. Males

1 Introduction

The MagAO project was constructed around a working AO system, that of the LBT. We re-used the real-time control software as-is, and adapted the AO control software developed by Arcetri (hereafter the AdOpt system) to the Magellan computing environment. In addition, we developed a major extension to the LBTAO baseline by adding the VisAO camera which works seamlessly as part of the MagAO system and routinely and reliably takes science data on the 6.5 m Clay telescope. We also developed an interface for the Clio camera to work as part of MagAO without rewriting the Clio control software itself.

The overall philosophy of MagAO-X software development will closely follow that used for MagAO: we will base it on a working AO control architecture (in this case SCExAO) and adapt it for our use, minimizing truly new software development. We will save significant development time through our use of the same components which are already in use at SCExAO or on the existing MagAO system. These components include:

1. The BMC 2k Deformable Mirror
2. The OCAM-2k EMCCD PWFS detector
3. The PI TTM head
4. Filter wheel motors
5. Tip/tilt stage actuators
6. PI stages

In Section 3.2 we presented the preliminary design of the MagAO-X compute system. This includes the real-time computer (RTC), the instrument control computer (ICC), and the AO operations computer (AOC), as well as workstations in the Clay control room. Here we describe the software preliminary design.

2 Software Management

2.1 Version Control: git will be used for version control, with a repository hosted on github. The standard “centralized workflow” will be used, where development occurs on local copies, with changes committed to the central repository.

The git SHA-1 hash (essentially the version number) will be used as a reproducibility tracer. The SHA-1 of the git repo at the time data or calibrations are taken will be traceable, either via timestamps or (when appropriate) by writing the SHA-1 to metadata. To facilitate this, all processes will have the SHA-1 embedded at compile time

	MagAO-X Preliminary Design Computers & Software	Doc #: MagAOX-001 Date: 2017-04-23 Status: Rev. 0.0 Page: 2 of 14
---	--	--

and will record this in their log at startup¹. This ensures that at any time the state of the software system can be recovered if needed to understand data recorded in the past.

Configuration files will also be kept under version control with `git`, and similarly the SHA-1 will be tracked and traceable.

Note: for this system to work, it will be policy that in general no data will be taken with uncommitted changes in the local repository. The user interface will warn when this is occurring (including compiler warnings). This will be strictly enforced on the telescope. Common sense will be allowed during development and lab testing².

2.2 Coding Standards and Documentation: The main language used for MagAO-X development will be c++. This is mainly driven by performance, and the PI/Software-lead is proficient in modern c++. The SCExAO real-time code is written in c, so adaptation of that code base for our use will be straightforward. The AdOpt low-level code is also primarily in c, so re-use of various motion control code will be straightforward. The INDI library is also provided in c++.

Python will also be used for scripting and other tasks.

All new code will be documented for processing with doxygen. Doxygen is a well known and maintained code-documentation system. It allows for programmers to document code as they go, with the addition of a few markup symbols. The result is nicely formatted html documentation, with browseable source code, indices, etc, all automatically generated from source. We will also use this to document application interfaces (command line options and configuration file parameters). The VisAO camera control software demonstrates this, https://visao.as.arizona.edu/software_files/visao/html/annotated.html, though we expect to improve on the application interface documentation significantly over what is shown there.

A minimum coding standard will be adhered to, which defines such things as header layouts, declare/define standards, documentation conventions, etc. We provide a draft version of this in Appendix A.

3 Computer Design

The MagAO-X computing system includes three custom computers: the Real-Time Computer (RTC), the Instrument Control Computer (ICC), AO Operations Computer (AOC). The specifications and mechanical design of these three computers is presented in Section 3.2. MagAO-X will also make use of the existing workstations in the Magellan Clay control room for science operations (zorro and guanaco).

3.1 Operating System: MagAO-X will standardize on 64-bit CentOS 7, chosen for long term stability. The expected lifetime for CentOS 7 is³

- Full Updates: through the end of 2020
- Maintenance Updates: through 2024-June-30.

This will ensure a stable computing environment throughout the development, commissioning, and first four operating years of the instrument.

¹We already use this technique in data reduction, see this script which creates a header to accomplish it: <https://bitbucket.org/jaredmales/mxlib/src/6aec98c12c7fded062bcff3b7c58402e9ab62cb0/gengithead.sh?at=master&fileviewer=file-view-default>

²SHA-1s are free

³see <https://wiki.centos.org/About/Product>



CentOS 7 also has the advantage that up-to-date real-time (RT) kernel packages are readily available from the CERN⁴ repositories. The RT kernel is used in the existing MagAO system on the VisAO computer, where priorities were optimized for low-latency in several critical processes. The RT kernel will be employed on the RTC and the ICC, and the AOC if needed.

4 Instrument Control

Here we describe our preliminary design for the instrument control software system (ICSS). This encompasses control of the various stages and motors, the science cameras, and high level AO loop control (stop/start, status monitoring etc).

4.1 INDI: We will employ the Instrument Neutral Distributed Interface (INDI) protocol (Downey, 2007) for communication between the various components of the ICSS. INDI is now the de-facto standard within the Center for Astronomical Adaptive Optics (CAAO), where it is used for the LBTI control software and is an integral part of the planned MMTAO upgrade (Milton, 2017). Using it has the advantage that one of the main developers of INDI is a member of CAAO making support readily available.

INDI essentially replaces the real-time-database (RTDB) and message daemon (MsgD) middle-ware in the AdOpt architecture. The basic architecture is that INDI devices communicate with a simple protocol via an INDI server on the host machine, see Figure 1, left. INDI servers are connected over the network, providing communications between machines. A very nice CGI interface is possible, which will provide a light-weight interface for astronomers to use, see Figure 1, right.

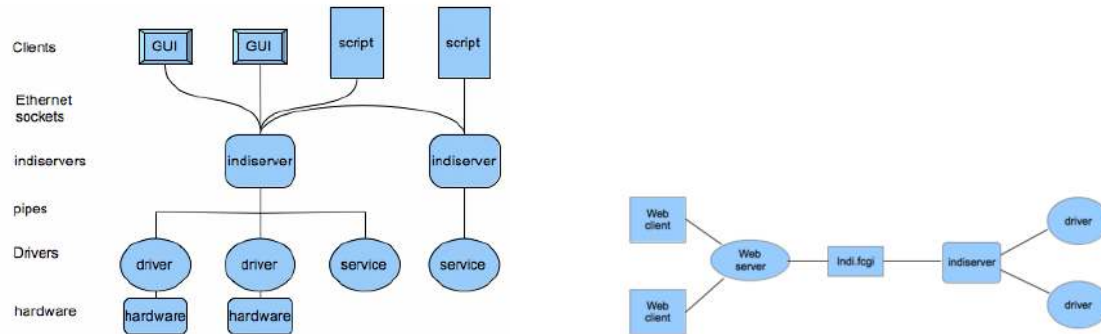


Figure 1: The INDI architecture. Source: the INDI wiki.

For MagAO-X, each of the RTC, ICC, and AOC will have an INDI server running and communicating with the others. On RTC INDI will provide for monitoring the status of the AO loop, high level AO control (start/pause/stop, etc), and show component status (PWFS camera, DMs). On the ICC INDI will be used to control the various stages, motors, and mechanisms, control and interact with the science cameras, and monitor the status of the LOWFS loop. On the AOC, an INDI device will interface to the TCS. The AOC INDI server will support the AO Operations Interface, and through the fast-CGI capability and a web server provide the astronomer's interface. The MagAO-X INDI architecture is shown in Figure 2.

⁴<http://linux.web.cern.ch/linux/rt/>

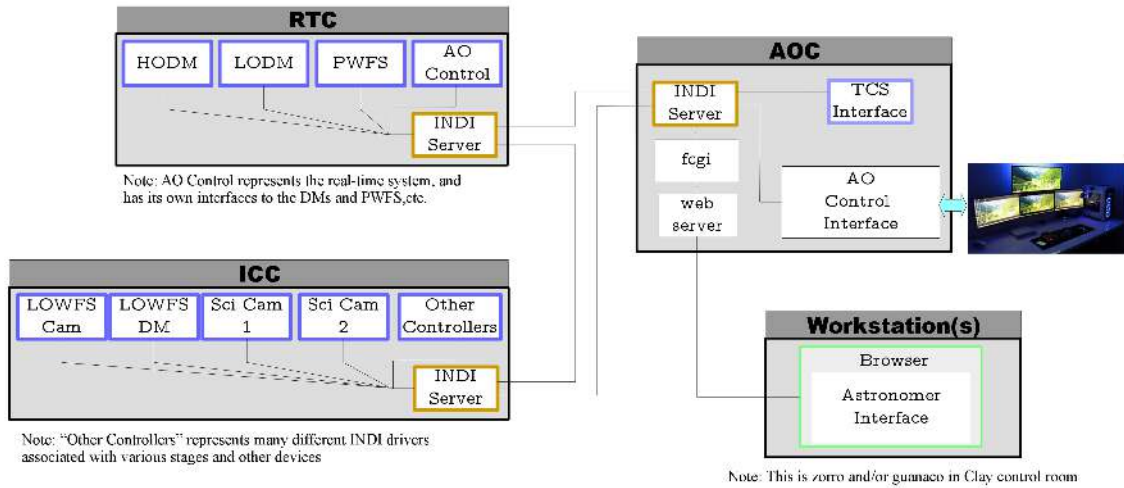


Figure 2: The MagAO-X INDI architecture. Purple borders indicate INDI device, gold borders are INDI servers. Note that several drivers are not shown on each machine, such as housekeeping and telemetry drivers which will publish properties.

4.2 MagAOXApp: The class defining an application in the MagAO-X ICSS will be derived from a standard class called MagAOXApp. Similar to the AOApp and VisAOApp base class in the AdOpt and VisAO systems, this will provide a standard set of functionality. This will include the INDI driver and client facilities, configuration, logging, and management of real-time priority.

4.3 Configuration: For MagAO-X we will use ini-style configuration files. This a standard format using key=value pairs and allows sections. For example

```
[basic]
name=The Name
rt_priority=0

[section2]
avector=0,3,5,6,3
```

Each derived class is responsible for knowing the intended type of each value. A template-based configuration parsing system will be used for ease of coding.

The MagAOXApp will employ a cascaded configuration system. At startup, the application will configure itself using the following sources in order

1. Default configuration [compiled in]
2. System Global configuration [set by environment variable, common to all MagAOXApp processes]
3. App global configuration [location set by environment variable, name compiled in]
4. Command line specified configuration file.

	MagAO-X Preliminary Design Computers & Software	Doc #: MagAOX-001 Date: 2017-04-23 Status: Rev. 0.0 Page: 5 of 14
---	--	--

Only the default configuration needs to exist. Each level overrides the previous. By specifying the location of configuration files via environment variables, we will have a straightforward way to maintain several configurations (e.g. for lab, cleanroom, and telescope).

4.4 Interprocess Communication: Non-real-time interprocess communication will generally take place via the INDI protocol. Any process which needs the status of another will subscribe to the appropriate property. An example is a focus stage which may need to know the position of several filter wheels in order to go to the correct position. This will also suffice for such things as AO setup (i.e. which reconstructor to load could depend on beamsplitter selection, among other things).

Real-time IPC on the ICC will make use of shared memory and semaphores. For instance, the science camera controllers will notify the framegrabber process for that camera when the format has changed via a semaphore, causing the framegrabber process to read the shared memory buffer containing the configuration details. The framegrabber in turn notifies the frame-writer process every time a new image is ready to write to disk.

The main AO control real-time software is described below.

4.5 Logging: Event logging is a crucial facility for a system such as MagAO-X. Here we include recording specific events (“loop closed”) as well as telemetry such as WFS images and telescope position. These data will be used for system performance analysis and diagnosis, and perhaps more importantly for data reduction. Given our goal of recording all system data for future use in data reduction, we want to have a very efficient log system.

A lesson learned from the AdOpt system is that ASCII logs can use a great deal of disk space over time — especially when things going wrong causes frequent logging, the time when we least want to be managing disk space. Furthermore, having a somewhat rigid log structure should be more efficient for later analysis. In MagAO-X we will address these issues by logging only an event code and a time-stamp, along with data of known format based on the event code, all in binary. That is log files will not be easily human-readable as stored on disk.

The event code is a 32-bit fixed width unsigned integer, `uint32_t`. This gives 4,294,967,296 independent event codes, which we assess is more than enough.

The time-stamp will be stored as two fixed-width integers, where the first `int64_t` holds the whole seconds since the Unix epoch and the second `int32_t` holds the nanosecond. This is the `timespec` structure, except we are explicit about the integer width (another lesson learned from AdOpt, where the `timeval` structure was a source of 32/64 compatibility problems, though we are unlikely to use 32-bit systems).

So a time stamp consists of a minimum of 12 bytes. For comparison logging to nanosecond precision with ASCII requires a string of the form YYYYMMDDHHMMSSNNNNNNNN, which is 23 bytes. This could be hex encoded, say, reducing it to 12 bytes. We could use a 32-bit unsigned integer for the seconds field, but this would reduce compatibility with the standard library on 64-bit linux⁵. Consider, though, that MagAO-X has a maximum operating frequency of 3700 Hz. Assume that an average of 10 events are logged each timestep (a conservatively high number). The extra 4 bytes then amounts to $3700*10*4 = 16$ kB/sec = 5 GB/10-hrs. This is a relatively small overhead compared to the several TB of image data we will record in the same time and so we consider it negligible.

Human readable logs in ASCII would take the form:

```
YYYY-MM-DDTHH:MM:SS.SSSSSSSS INF loop closed\n [ 46 bytes ]
```

⁵and place us at risk of the Unix millenium bug in 2038, or 2106 if we used unsigned integers. We may not operate for that long though, so this is of minor concern.

	MagAO-X Preliminary Design Computers & Software	Doc #: MagAOX-001 Date: 2017-04-23 Status: Rev. 0.0 Page: 6 of 14
---	--	--

YYYY-MM-DDTHH:MM:SS.SSSSSSSS ERR unable to connect\n [52 bytes]
YYYY-MM-DDTHH:MM:SS.SSSSSSSS INF telra 12:00:00.00\n [52 bytes]

In contrast, these three log entries will take 16, 16, and 24 bytes respectively, or 37% of the disk space.

Logs will then be saved as binary records in HDF5 files on a per-process basis. For efficient access, these records will have a maximum length (to be optimized) and have the timestamp of the first entry recorded as an attribute in the file. Parsing each record will require determining the type from the event code and calling an appropriate function (with a pointer to the entry as argument) to read the data.

Simple utilities will display logs in human-readable format as needed (i.e. a replacement for tools like cat).

Using c++ templates we will provide a very simple logging interface within the code. A sketch of how this will work is shown in Appendix B.

A drawback to this system will be the overhead of creating a new event code. This overhead will be paid during development, every time a new log entry is needed. The minimum steps to create a new log entry will include:

1. declare log entry structure containing the event code
2. define `length()` member of the struct
3. declare and define a specialized `log<>()` function to do the work of logging.

In general this will also necessitate updating the log parsing facility to handle this new event type. A database of event codes will also be maintained automatically with a code analyzer minimizing effort to safely generate a new one.

4.6 RT Priority: MagAOXApp based processes will have the ability to set their real-time (RT) priority. This will be determined by a configuration setting, allowing for optimization. This requires installing processes with mode 4755. Upon startup, processes will immediately decrease privileges to the lowest setting, and only increase privileges to set RT priority. The MagAOXApp will do this by default during construction⁶.

5 TCS Interface

The instrument-TCS interface at Magellan is well documented in Eychaner (2015). Instruments connect via a TCP/IP socket and send and receive formatted ASCII. We have already implemented a process called the MagAOI (for MagAO Interface) which handles TCS queries at 1 Hz. This retrieves all data available from the TCS which is relevant to the MagAO system. We will adapt this code to work as an MagAOXApp (and INDI Driver and Client) and use it to manage interfacing with the TCS. In Appendix C we list all the TCS parameters which will be used.

As part of the MagAO test system, we developed a software TCS simulator which will be used for MagAO-X software development and lab testing.

6 User Interfaces

Based on long experience using it on the MagAO project, we plan to avoid running GUIs via x-forwarding on ssh. There are two main GUIs to be provided.

⁶See `VisAO_base()` at https://visao.as.arizona.edu/software_files/visao/html/VisAOApp_base_8cpp_source.html for a working example



6.1 The Astronomer Interface: Following typical practice in CAAO INDI implementations (such as at the LBTI), astronomers will interact with the instrument using a GUI implemented using the jQuery UI framework, and running on a web browser. This will be served by a web server running on the AOC, connected to the AOC INDI server via the W3 fcgi protocol. This will be very flexible, allowing astronomers to use the workstations in the Clay control room with minimal fuss.

We will also provide support for observation scripting through this interface.

6.2 The AO Operator Interface: Experience on MagAO has shown that reliable high-speed display of AO status, including PWFS images and DM commands and positions, is extremely helpful in optimizing AO performance. To that end, we will implement a custom AO interface served on the AOC. It will make use of 4 monitors, and its organization will be optimized for ease of use. For instance, all buttons needed to operate the AO system will be located on a single pane – it will not be necessary to switch tabs or windows while operating the loop. Where appropriate, this may also make use of a web-browser interface (likely re-using code from the Astronomer Interface). Where needed, compiled Qt will be used for high performance.

To support the reliable high-speed AO updates, we will send telemetry and diagnostic data from the RTC and ICC to the AOC on an *as-displayable* basis. For instance, it is typically only possible to display PWFS images at ~ 30 Hz. In this case, a decimator process on the RTC will send frames on only 30 fps to the AOC. This will minimize network traffic, and processing time devoted to sending telemetry.

7 Real-time Software

For the real-time control of the AO loops we will use the RT software (RTS) developed by MagAO-X Co-PI Olivier Guyon for the Subaru SCExAO instrument. It is Linux-based, open-source C code along with high-level scripts. It uses publicly available libraries, including CUDA and MAGMA (for GPU computing), FFTW, FISIO, GSL. The source code is available at <https://github.com/oguyon/AdaptiveOpticsControl>.

Because we are using essentially identical hardware to SCExAO (BMC 2k MEMS and OCAM-2K EMCCD) we save significant development time in implementing our RTS. Here we provide a very brief overview of the highlights of this system. More details are given in Appendix D to this Section.

7.1 Performance on Hardware: The RTS runs on a single multi-core computer. Minimum 15 cores system, 128GB ram (heavy use of shared memory and shielded processes running on single core). Supports NVIDIA hardware (CUDA lib). Interfaces to hardware through shared memory structure. Hardware already coupled with RTS: BMC deformable mirror, Ocam2k camera, SAPHIRA camera (with UH readout electronics), OwlCam In-GaAs Raptor Photonics camera, Andor sCMOS.

7.2 Speed: Largely limited by hardware. Fully system timing stable at 10us level, and RTS latency due to IPC, TCP transfers between computers, and GPU transfers is $< 100 \mu\text{s}$ total, so it can drive a ~ 10 kHz loop on multi-computer system, and ~ 20 kHz loop on single computer. SCExAO implementation drives 2000-actuator, 14,400-sensor loop at 3.5kHz, limited by camera readout speed.

7.3 Flexible architecture: All input, output and intermediate data is stored as shared memory. A common format for all shared memory data streams facilitates software development. Multiple processes run simultaneously to perform operations on shared memory streams. Additional processes can be deployed (for example, real-time

	MagAO-X Preliminary Design Computers & Software	Doc #: MagAOX-001 Date: 2017-04-23 Status: Rev. 0.0 Page: 8 of 14
---	--	--

analysis of an intermediate data stream) without impacting existing processed.

IPC is built in the shared memory structure which contains POSIX semaphores (default of 10 semaphores, more if needed): 10 different processes can run on the same input. Each process waits on input stream(s), and posts output stream(s) semaphore(s), so real-time operations can be chained, with multiple branches.

References

Downey, E. C. 2007, 755, L28

Eychaner, G. 2015, Instrument Communication with the Magellan Telescopes, Tech. rep.

Milton, M. 2017, MMT AO ASM Upgrade Software Architecture, Tech. rep.

	MagAO-X Preliminary Design Computers & Software	Doc #: MagAOX-001 Date: 2017-04-23 Status: Rev. 0.0 Page: 9 of 14
---	--	--

A Coding Standards

Here we show some sketches of our standard coding practices, including use of doxygen comments.

```

///Brief description for one parameter function
/** Long description
 *
 * \returns functions should return 0 on success, and a negative integer to
 * indicate error.
 *
 * \tparam T document the type here.
 */
template<typename T>
int aFunction( T & param /**< [in/out] documentation for param*/ )
{
    //code goes here.

    return 0; ///\retval 0 on success.
}

///Brief description for two or more parameter function
/** Long description
 *
 * \returns functions should return 0 on success, and a negative integer to
 * indicate error.
 *
 * \tparam T1 document the type of param1 here.
 * \tparam T2 document the type of param2 here.
 */
template<typename T1, typename T2>
int aFunction( T1 & param1 //< [out] documentation for param1, an output
              T2 & param2 //< [in] documentation for param2, an input
            )
{
    //code goes here.

    return 0; ///\retval 0 on success.
}

///Brief description for a class
/** Long description
 *
 * \tparam _T document type _T/T here.
 */
template<typename _T>
class aClass

```



```
{  
public:  
    typedef _T T; //;< public typedefs first, with documentation. All template  
                    parameters typdef-ed as shown.  
  
    aClass(); //;<Default c'tor  
  
    ~aClass(); //;<Destructor.  
  
protected:  
    typeT member1; //;<Document protected members.  
  
public:  
  
    int actionFoo( T & inPlace /*< [in/out] parameter documentation*/ );  
  
    int actionfoo( T & after, //;< [out] parameter documentation  
                  T & before //;< [in] parameter documenation  
                );  
}
```

	MagAO-X Preliminary Design Computers & Software	Doc #: MagAOX-001 Date: 2017-04-23 Status: Rev. 0.0 Page: 11 of 14
---	--	---

B Logging Code Sketch

Here we sketch the logging framework.

```

namespace logger
{
    struct timespecX
    {
        int64_t time_s;
        int32_t time_ns;
    };

    //Logger events are declared:
    struct loop_closed
    {
        const uint32_t eventCode = 1000;

        void length( uint32_t * logPtr /*< A pointer to a log entry, in this case not
                                       used */ )
        {
            return 12;
        }
    };

    struct tel_pos
    {
        const uint32_t eventCode = 103458;

        void length( uint32_t * logPtr /*< A pointer to a log entry, in this case not
                                       used */ )
        {
            return 12 + 8 + 7 + 6 + 6 + 4 + 7; // the size of the TCS responses, after
                                              // '.' is removed.
        }
    };

    struct user_log
    {
        const uint32_t eventCode = 38958;
    };
}

//etc...

//And template specializations of the log function:
template<typename logT>

```



```
void log();

///Log specialization for the loop closed event
template<>
inline void log<loop_closed>()
{
    // Step 1: get timestamp
    // Step 2: format and store log
}

///Log specialization for telescope position
template<>
inline void log<tel_pos>( char[8] telra, ///< Telescope RA as returned by TCS,
    with '.' removed
        char[7] teldc, ///< Telescope Dec as returned by TCS, with '.'
        removed
        char[6] telep, ///< Telescope Equinox as returned by TCS, with
        '.' removed
        char[6] telha, ///< Telescope HA as returned by TCS, with '.'
        removed
        char[4] telam, ///< Telescope Airmass as returned by TCS, with
        '.' removed
        char[7] rotangle ///< Telescope rotator angle as returned by
        TCS, with '.' removed
)
{
    // Step 1: get timestamp
    // Step 2: format and store log
}

///Log specialization for the loop closed event
template<>
inline void log<user_log>( const std::string & fromUser )
{
    // Step 1: get timestamp
    // Step 2: format and store log
    // Note: here the format must include a string length.
}

//etc...

}; //namespace logger
```

And then within the code itself entries such as

```
using namespace logger;
```



```
log< loop_closed >();  
  
log< tel_pos >( telra, teldc, telep, telha, telam, rotangle );  
  
//User enters a log from a GUI:  
// std::string fromUser <--- "Photometric conditions"  
  
log< user_log >( fromUser );
```

	MagAO-X Preliminary Design Computers & Software	Doc #: MagAOX-001 Date: 2017-04-23 Status: Rev. 0.0 Page: 14 of 14
---	--	---

C TCS Parameters

Here we collect the various telescope and environment parameters which will be queried and logged.

Table 1: Telescope and Environment Parameters

TCS Name	TCS Format	Stored As	Size [Bytes]	Rate [Hz]	Notes
Telescope Position					
dateobs	YYYY-MM-DD	char[8]	8	0.1	UT date in year month day format.
ut	HH:MM:SS	char[6]	6	1	UT time in hours minutes and seconds.
st	HH:MM:SS	char[6]	6	1	Sidereal time in hours minutes and seconds.
ra	HH:MM:SS.SS	char[8]	8	1	Right ascension in hours, minutes, and seconds.
dec	DD:MM:SS.S	char[7]	7	1	Declination in degrees, minutes, and seconds.
epoch	YYYY.YY	char[6]	6	1	Equinox of current telescope coordinates.
ha	HH:MM:SS	char[6]	6	1	Hour angle in hours, minutes, and seconds.
airmass	A.AAA	char[4]	4	1	Observational airmass.
telaz	AAA.AAAA	char[7]	7	1	Azimuth angle, in degrees.
telel	EE.EEEE	char[6]	6	1	Elevation angle, in degrees.
zd	ZZ.ZZZZ	char[6]	6	1	Zenith angle, in degrees.
telpa	PPP.PPPP	char[7]	7	1	Parallactic angle, in degrees.
teldm	DDD	char[3]	3	1	Dome azimuth angle, in degrees.
dinstat	DD	char[2]	2	1	Dome status (0 = closed; 1 = open; -1 = unknown)
telguide	ab	char[2]	2	1	a: 0 = not tracking, 1 = tracking; b: guider number of active guider, or 0 if not guiding
gdmountmv	abc	char[3]	3	1	Telescope and rotator motion status (see below)
mountmv	abcd	char[4]	4	1	Telescope and rotator motion status flags (see below)
telfocus	FFFFFF	char[6]	6	1	Secondary mirror focus (Z axis) set (instrument) offset, in microns.
vefocus	FFFFFF	char[6]	6	1	Secondary mirror focus (Z axis) encoder reading, in microns.
vezima	FFFFFF	char[6]	6	1	Secondary mirror Z axis ima (Shack-Hartmann) offset, in microns .
vezpsn	FFFFFF	char[6]	6	1	Secondary mirror Z axis psn (flexure) offset, in microns.
vexset	FFFFFF	char[6]	6	1	Secondary mirror X axis set (instrument) offset, in microns.
vexenc	FFFFFF	char[6]	6	1	Secondary mirror X axis encoder reading, in microns.
vxexima	FFFFFF	char[6]	6	1	Secondary mirror X axis ima (Shack-Hartmann) offset, in microns
. vexpsn	FFFFFF	char[6]	6	1	Secondary mirror X axis psn (flexure) offset, in microns.
vexset	FFFFFF	char[6]	6	1	Secondary mirror Y axis set (instrument) offset, in microns.
veyenc	FFFFFF	char[6]	6	1	Secondary mirror Y axis encoder reading, in microns.
veyima	FFFFFF	char[6]	6	1	Secondary mirror Y axis ima (Shack-Hartmann) offset, in microns.
veypsn	FFFFFF	char[6]	6	1	Secondary mirror Y axis psn (flexure) offset, in microns.
vehset	FFFFFF.FFF	char[9]	9	1	Secondary mirror H axis (rotation) set (instrument) offset, in arcseconds.
vehenc	FFFFFF.FFF	char[9]	9	1	Secondary mirror H axis (rotation) encoder reading, in arcseconds.
vehima	FFFFFF.FFF	char[9]	9	1	Secondary mirror H axis (rotation) ima (Shack-Hartmann) offset, in arcseconds.
vehpsn	FFFFFF.FFF	char[9]	9	1	Secondary mirror H axis (rotation) psn (flexure) offset, in arcseconds.
vevset	FFFFFF.FFF	char[9]	9	1	Secondary mirror V axis (rotation) set (instrument) offset, in arcseconds.
vevenc	FFFFFF.FFF	char[9]	9	1	Secondary mirror V axis (rotation) encoder reading, in arcseconds.
vevima	FFFFFF.FFF	char[9]	9	1	Secondary mirror V axis (rotation) ima (Shack-Hartmann) offset, in arcseconds.
vevpsn	FFFFFF.FFF	char[9]	9	1	Secondary mirror V axis (rotation) psn (flexure) offset, in arcseconds.
telroi	R	char[1]	1	0.1	Rotator of interest (0 to 5 are NASW, NASE, CASS, AUX1, AUX2, and AUX3 respectively).
rotmode	R	char[1]	1	0.1	Rotator tracking mode; normally either 0 (OFF; no tracking) or 2 (EQU; equatorial tracking, rotator tracks sky).
rotangle	RRR.RRRR	char[7]	7	1	Current rotator offset angle, in degrees.
nrotoff	RRR.RRRR	char[7]	7	1	Angle between rotator zero and sky north for input coordinates and rotator offset, in degrees.
rotatore	RRR.RRRR	char[7]	7	1	Current rotator encoder angle, in degrees.
User Catalog Input					
catra	HH:MM:SS.SS	char[8]	8	0.1	Current catalog object right ascension.
catdc	DD:MM:SS.S	char[7]	7	0.1	Current catalog object declination.
catep	YYYY.YY	char[6]	6	0.1	Current catalog object equinox.
catro	RRR.RRRR	char[7]	7	0.1	Current catalog object rotator offset angle, in degrees.
catrm	TTT	char[3]	3	0.1	Current catalog object rotator offset mode; one of OFF, EQU, GRV, or HRZ.
catobj	string	char[30]	30	0.1	Current catalog object name (up to 30 characters, containing no spaces).
Environment					
fwhm	FFF.F	char[4]	4	0.1	30-second average FWHM value from the active guider.
dimmfw	FFF.F	char[4]	4	0.1	DIMM seeing, available from wx database, not TCS.
mag1fw	FFF.F	char[4]	4	0.1	Baade seeing, available from wx database, not TCS.
wxtemp	TTT.TT	char[5]	5	0.1	Outside temperature (degress Celcius).
wxpres	PPPP.PP	char[6]	6	0.1	Outside pressure (millibars).
wxhumid	HHH.LHH	char[5]	5	0.1	Outside humidity (percent).
wxwind	VVV.VVV	char[5]	5	0.1	Outside wind intensity (mph).
wxwdir	DDD.DD	char[5]	5	0.1	Outside wind direction (degrees).
wx dewpt	TTT.TT	char[5]	5	0.1	Outside dewpoint (degress Celcius).
truss	TTT.TTT	char[5]	5	0.1	Telescope truss temperature (degress Celcius).
tcell	TT.TTT	char[5]	5	0.1	mirror cell temperature (degress Celcius).
tseccell	TT.TTT	char[5]	5	0.1	Secondary mirror cell temperature, skyward side (degress Celcius).
tambient	TT.TTT	char[5]	5	0.1	Dome air temperature (degress Celcius).
tair	TT.TTT	char[5]	5	0.1	Primary mirror air temperature (degress Celcius).



3.3 Software Appendix D

SCExAO Real-Time Architecture

AO Loop Control Software

Overview

Linux-based

Open-source, no closed library

C code (~100k lines) + high-level scripts (baseline control interface using bash scripts provided)

Uses libraries: CUDA & MAGMA (GPU computing, optional), FFTW, FITSIO, GNU scientific library, readline

Source code + example simulated AO system:

<https://github.com/oguyon/AdaptiveOpticsControl>

Hardware

Hardware Requirements / compatibility:

RTS runs on a single multi-core computer. Minimum ~15 cores system, 128GB ram (heavy use of shared memory and shielded processes running on single core)

CPU only or CPU+GPU computing engine. Requires GPU(s) for high speed / high actuator count. Supports NVIDIA hardware (CUDA lib).

Can span multiple computers (for example, camera or DM driven by computer other than main RTS). Software uses and configures fast private low-latency TCP link (eg. 10GbE or 40GbE fibers) for transfers.

Interfaces to hardware through shared memory structure. Hardware already coupled with RTS: BMC deformable mirror, Ocam2k camera, SAPHIRA camera (with UH readout electronics), OwlCam InGaAs Raptor Photonics camera, Andor sCMOS.

Capabilities

Speed

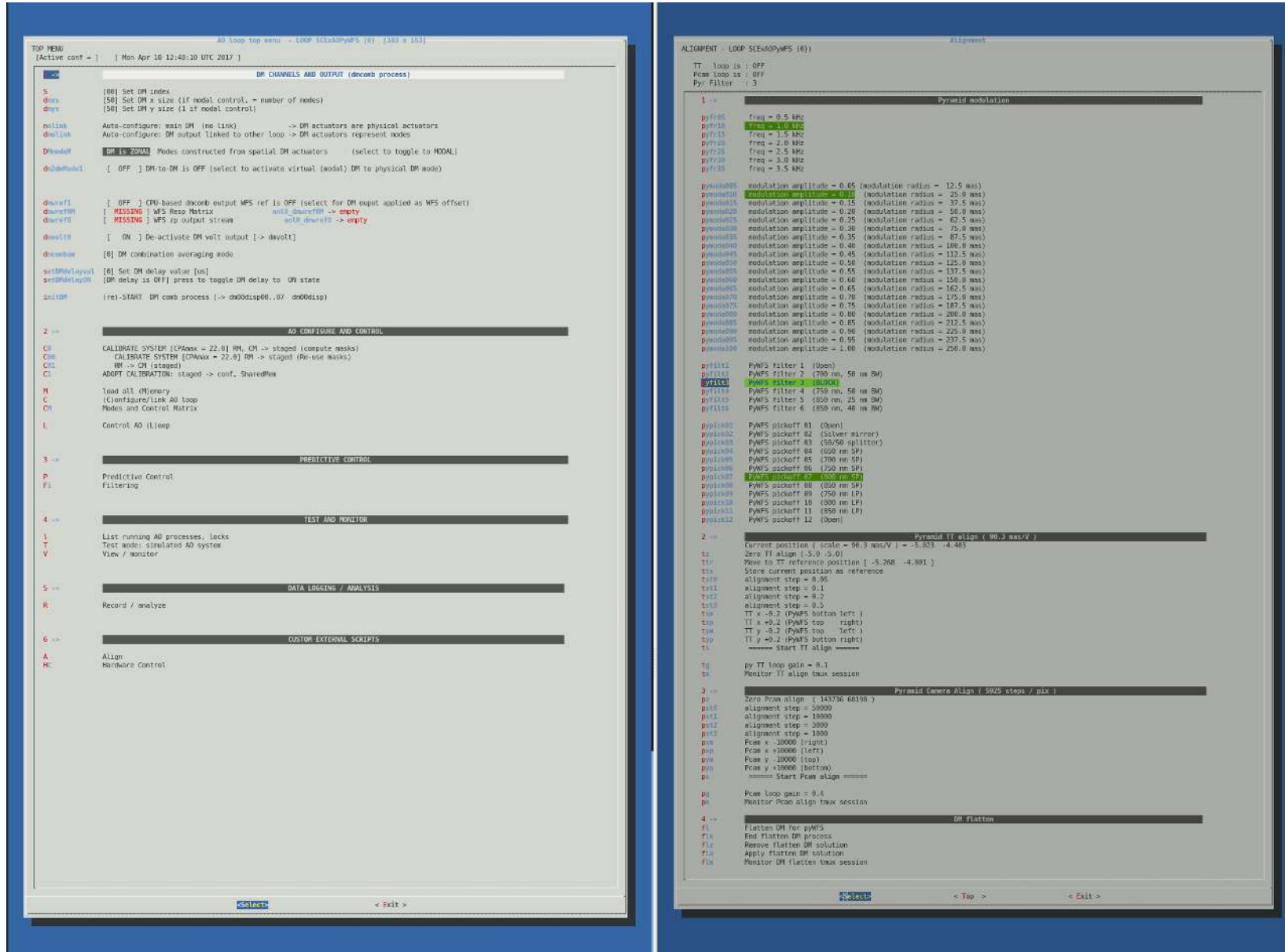
Largely limited by hardware. Fully system timing stable at 10us level, and RTS latency due to IPC, TCP transfers between computers, and GPU transfers is <100us total → can drive ~10 kHz loop on multi-computer system, and ~20 kHz loop on single computer. SCExAO implementation drives 2000-actuator, 14,400-sensor loop at 3.5kHz, limited by camera readout speed.

Flexible architecture

All input, output and intermediate data is stored as shared memory. A common format for all shared memory data streams facilitates software development. Multiple processes run simultaneously to perform operations on shared memory streams. Additional processes can be deployed (for example, real-time analysis of an intermediate data stream) without impacting existing processed.

IPC is built in the shared memory structure which contains POSIX semaphores (default of 10 semaphores, more if needed): 10 different processes can run on the same input. Each process waits on input stream(s), and posts output stream(s) semaphore(s) → Real-time operations can be chained, with multiple branches

Example control GUI (bash scripts)



For each file:
conf_<name>_name.txt points to archived file location

conf/conf_<name>_name.txt are read by function ReadConfFile for
loading into shared memory and FITS copy to
./conf/aol#_<name>.fits

Calibration Work Flow

Conventions :

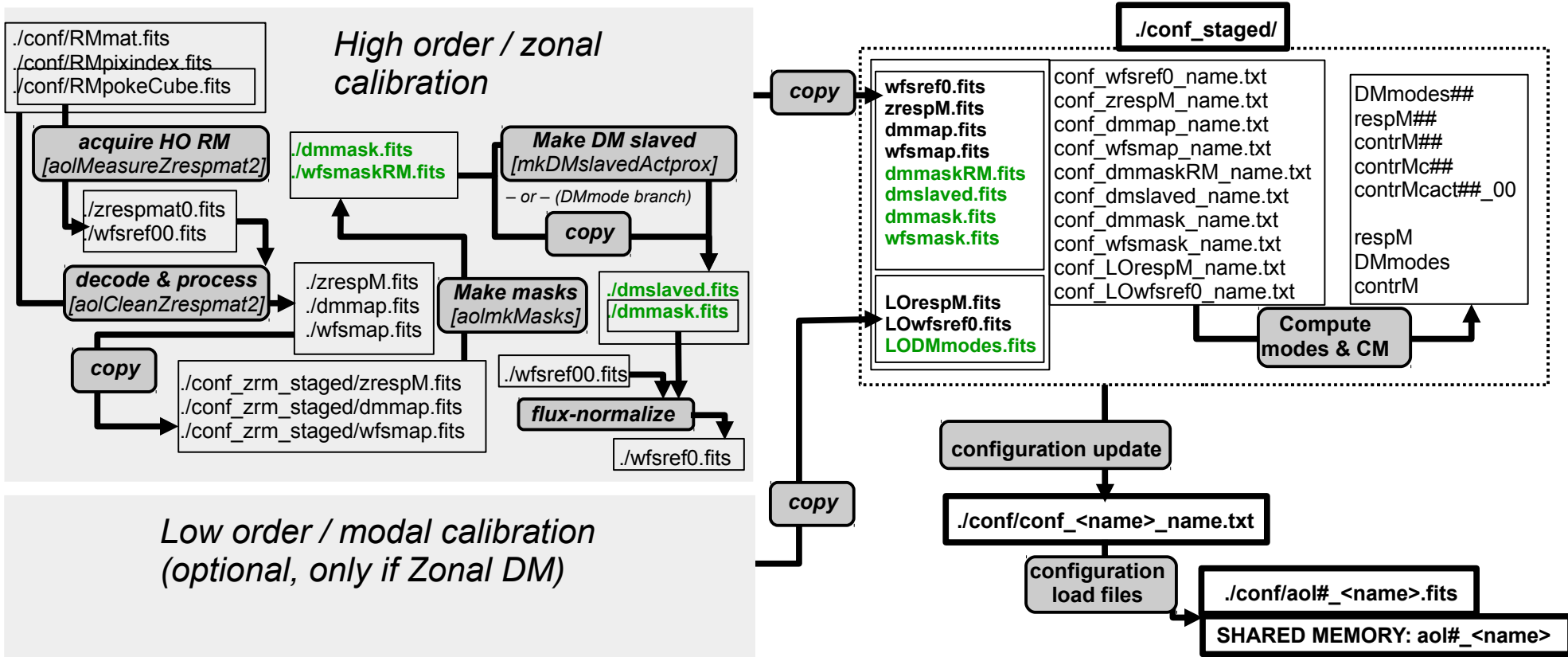
Modal DM: “actuators” indices have no spatial meaning

- No spatial filtering options
- “Direct write” CM and “Modal” CM are the same (1 mode = 1 actuator)

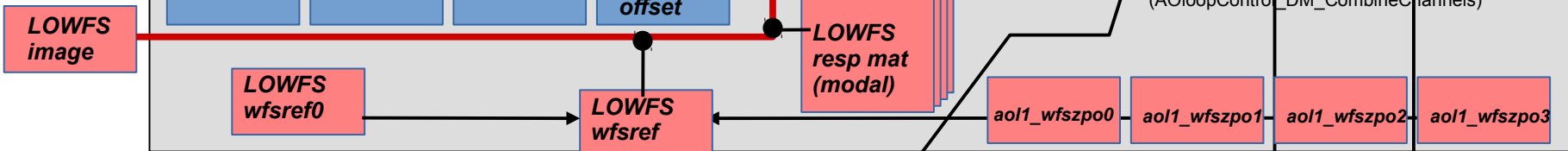
Zonal DM: actuator indices correspond to spatial coordinates

- Need linear transformation between mode coefficients and actuators

If re-using masks,
keep from previous
calibration

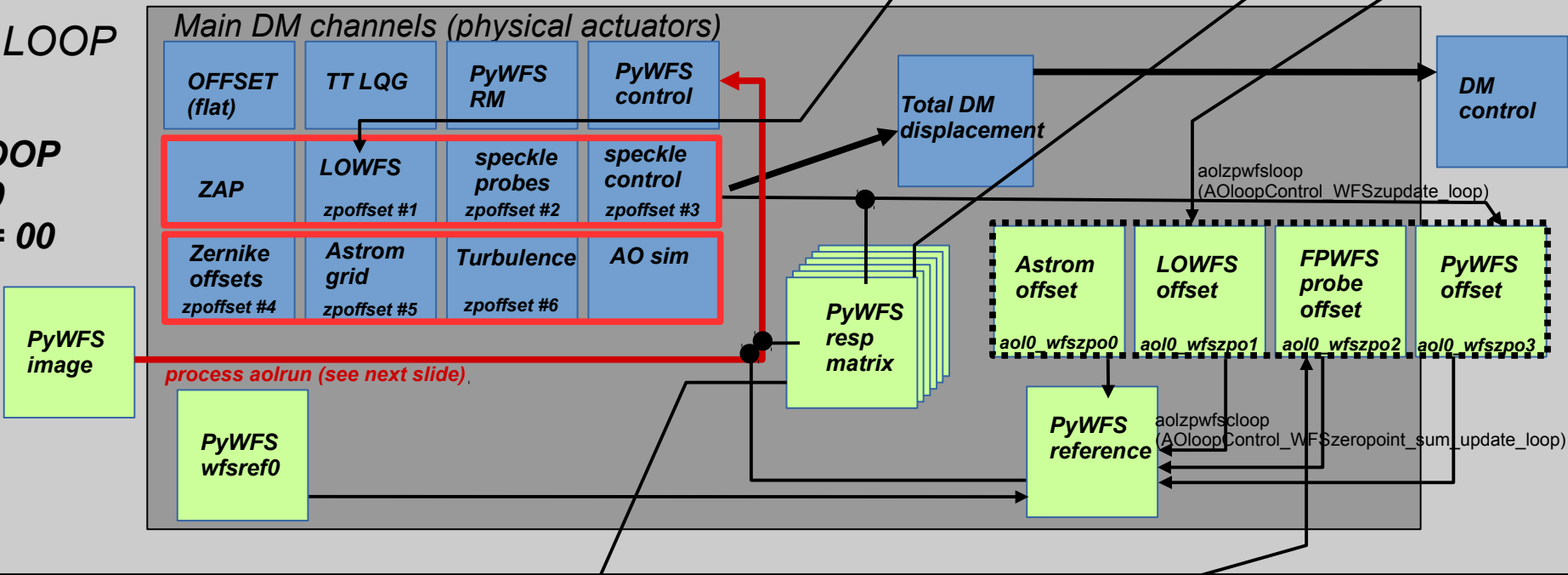


LOWFS LOOP
 $loopnb = 1$
 $DMindex = 01$

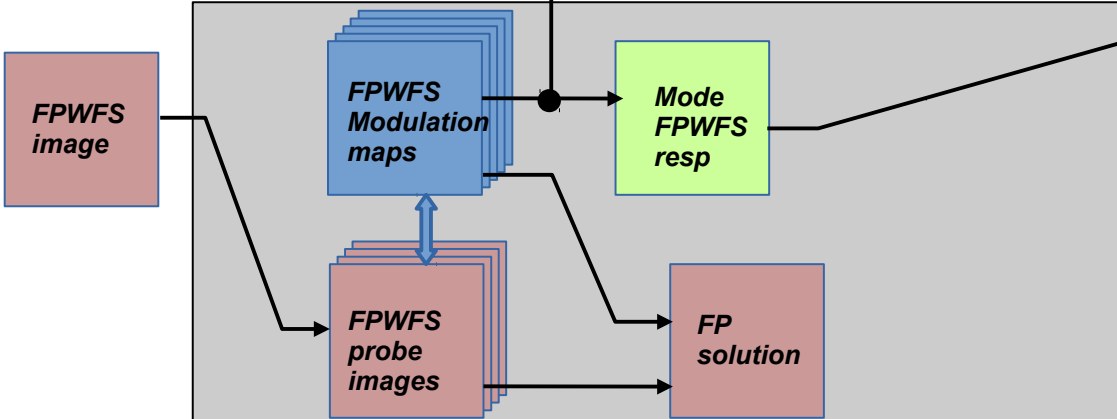


MASTER LOOP

PyWFS LOOP
 $loopnb = 0$
 $DMindex = 00$



FPWFS LOOP
 $loopnb = 2$



LOWFS + HOWFS + FPWFS
wavefront control
architecture

Control Matrix Computation Modes

WFSnorm (../conf/conf_WFSnormalize.txt) ***WFS normalization mode*** C code: [AOconf\[loop\].WFSnormalize](#)
0: Do not normalize WFS images
1: Normalize WFS images

WFSnorm should be left unchanged between RM acquisition and Loop control

DMprimaryWrite (../conf/conf_DMprimWriteON.txt) ***DM primary write*** C code: [DMprimaryWrite_ON](#)
0: DM primary write is off
1: DM primary write is on

CMmode (../conf/conf_CMmode.txt) ***Combined Control matrix mode*** C code: [MATRIX_COMPUTATION_MODE](#)
0: not combined: control matrix is WFS pixels → modes
→ Linking aol#_DMmode_meas ↔ aol#_modeval
→ modesextractwfs reads from aol_DMmode_meas instead of computing
1: combined: control matrix is WFS pixels → DM actuators

DMMODE (../conf/conf_DMMODE.txt) ***DM mode (zonal vs. modal)*** Bash script only, only affects bash scripts and options
ZONAL: pixel coordinates correspond to DM actuators physical location
→ spatial filtering enabled for DM modes creation
→ blocks built by spatial frequencies, user can set independent gain values for mode blocks
MODAL: DM pixels correspond to abstract modes
→ no spatial filtering, setting 1 block only

Note: **DMMODE**=ZONAL → **CMMODE**=MODAL (CPA-splitting of modes into blocks)

GPUmode (../conf/conf_GPUmode.txt) ***# of GPUs to use for CM multiplication*** C code: [AOconf\[loop\].GPU](#)
0: use CPU
>0: number of GPUs

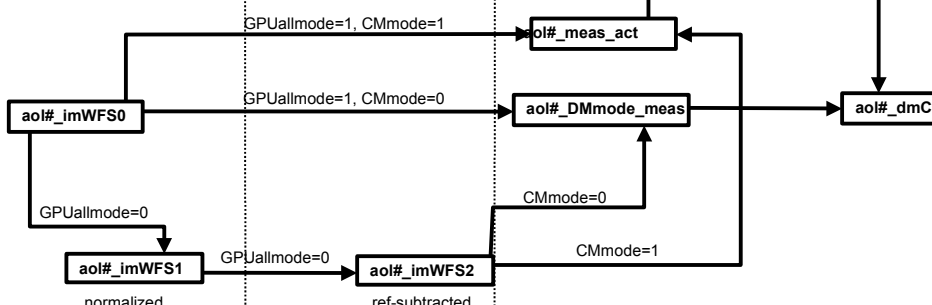
if CMmode=1 and GPUmode>0:

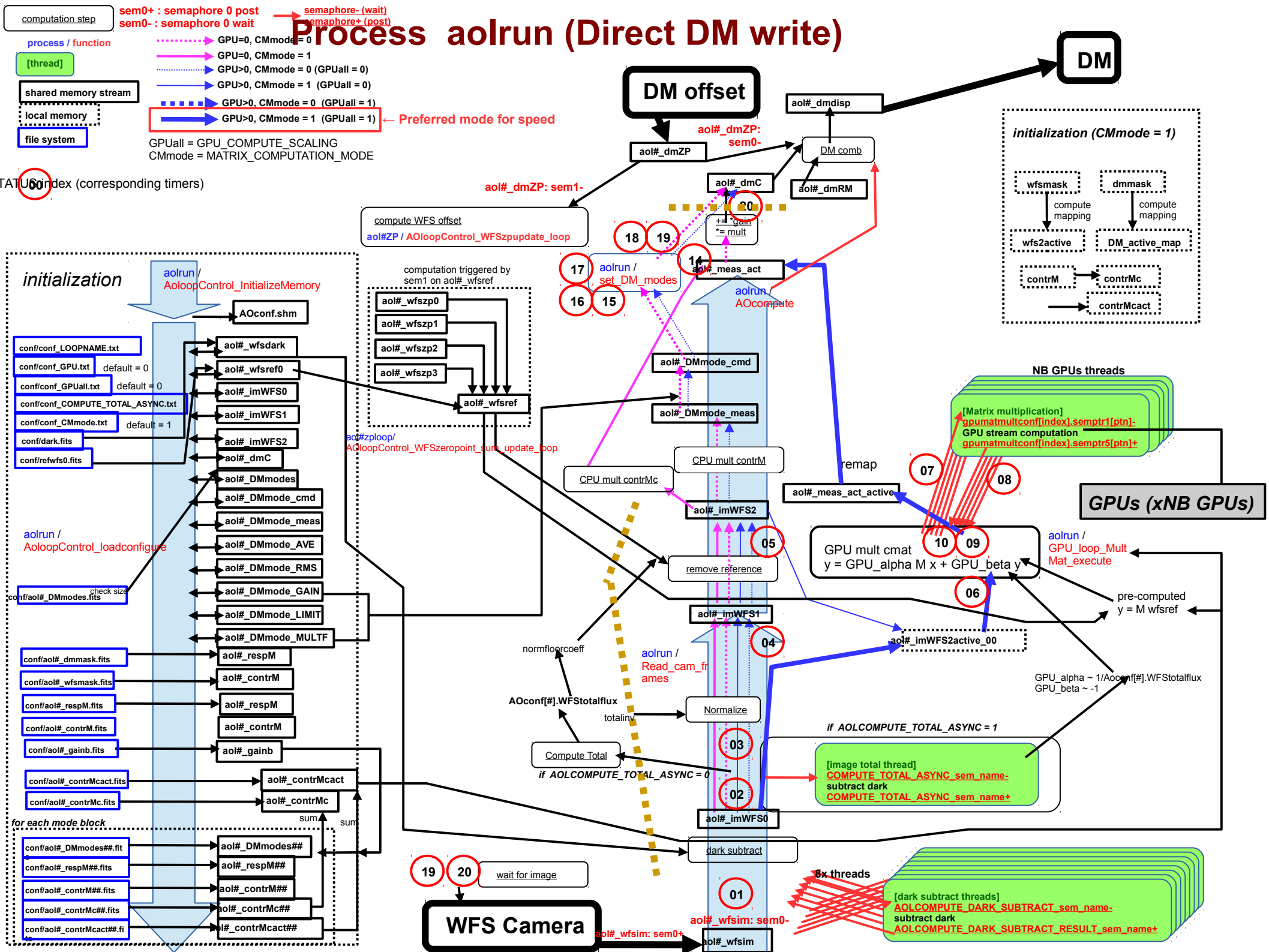
GPUallmode (../conf/conf_GPUall.txt) ***Use GPU for all computations*** C code: [AOconf\[loop\].GPUall = COMPUTE_GPU_SCALING](#)
0: Use CPU for WFS reference subtraction and normalization
→ WFS reference subtraction and normalization done by CPU (imWFS0→ imWFS1→ imWFS2)
→ CM multiplication input is imWFS2 (GPU or CPU)
1: Use GPU for all computation
→ WFS reference subtraction and normalization done by GPU
→ GPU-based CM multiplication input is imWFS0

Control Matrices

Matrix	Description	Input → output	Gain control (primary write)	Notes
contrM (CMmode=0)	Full modal control matrix Split in multi-GPU	WFSpix → DMmodes	0.0 < loopgain < 1.0 0.0 < DMmodes_GAIN[m] < 1.0	gainMB has no effect and will not update contrM
contrMc (CMmode=1, GPUmode=0)	Full combined control matrix Split in multi-GPU	WFSpix → DMactuators	0.0 < gainMB[k] < 1.0 0.0 < loopgain < 1.0	contrMc re-built for each change of gainMB If DM is MODAL: gainMB has no effect and will not update contrM
contrMcact (CMmode=1, GPUmode=1)	Combined control matrix, only active pixels Split in multi-GPU	Active WFS pixels → Active DM actuators	0.0 < gainMB[k] < 1.0 0.0 < loopgain < 1.0	contrMcact re-built for each change of gainMB If DM is MODAL: gainMB has no effect and will not update contrM

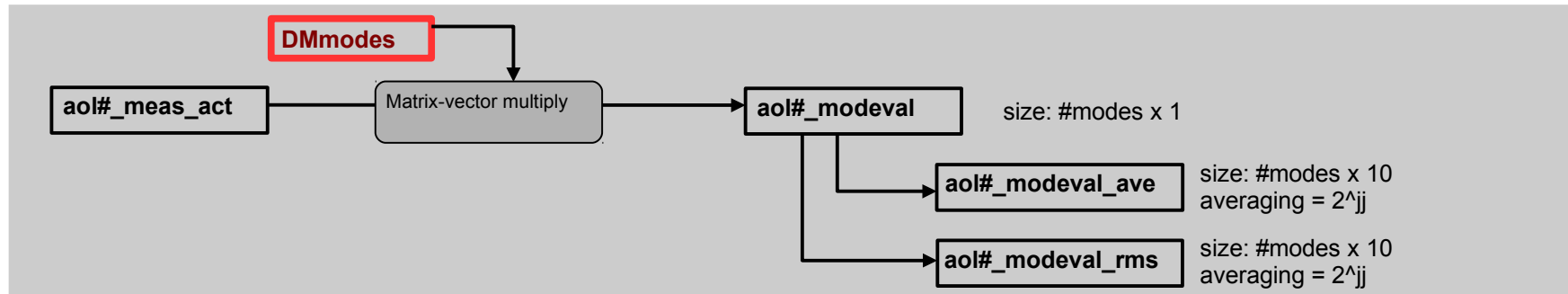
CMmode <u>MATRIX COMPUTATION MODE</u>	GPUmode	GPUallmode <u>COMPUTE GPU SCALING</u>	Camera read output (Read_cam_frame)	WFS reference subtraction	Control Matrix operation(s)
0	0	0	→ imWFS1	CPU subtraction → imWFS2	contrM x imWFS2 → DMmode_meas [CPU] DMmode_meas → cmd_modes [CPU] DMmodes x cmd_modes → dmC [CPU]
0	>0	0	→ imWFS1	CPU subtraction → imWFS2	contrM x imWFS2 → DMmode_meas [GPU] DMmode_meas → cmd_modes [CPU] DMmodes x cmd_modes → dmC [GPU]
0 [to be done]	>0	1	→ imWFS0 / GPU_alpha, GPU_beta	done in GPU as part as CM mult	contrM x imWFS0 → DMmode_meas [GPU] DMmode_meas → cmd_modes [CPU] DMmodes x cmd_modes → dmC [GPU]
1	0	0	→ imWFS1	CPU subtraction → imWFS2	contrMc x imWFS2 → meas_act [CPU] meas_act → dmC [CPU]
1	>0	0	→ imWFS1	CPU subtraction → imWFS2	contrMcact x imWFS2_active → meas_act_active [GPU] meas_act → dmC [CPU]
1	>0	1	→ imWFS0 / GPU_alpha, GPU_beta	done in GPU as part as CM mult	contrMcact x imWFS0_active → meas_act_active [GPU] meas_act → dmC [CPU]



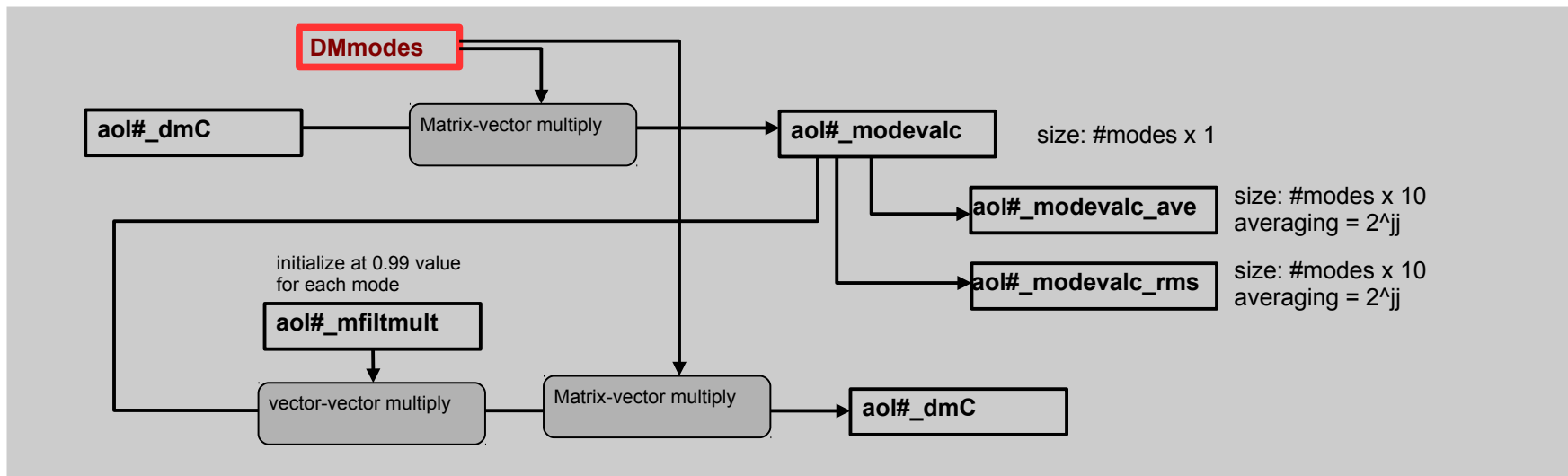


Auxillary processes

Decompose WFS measurements in modes

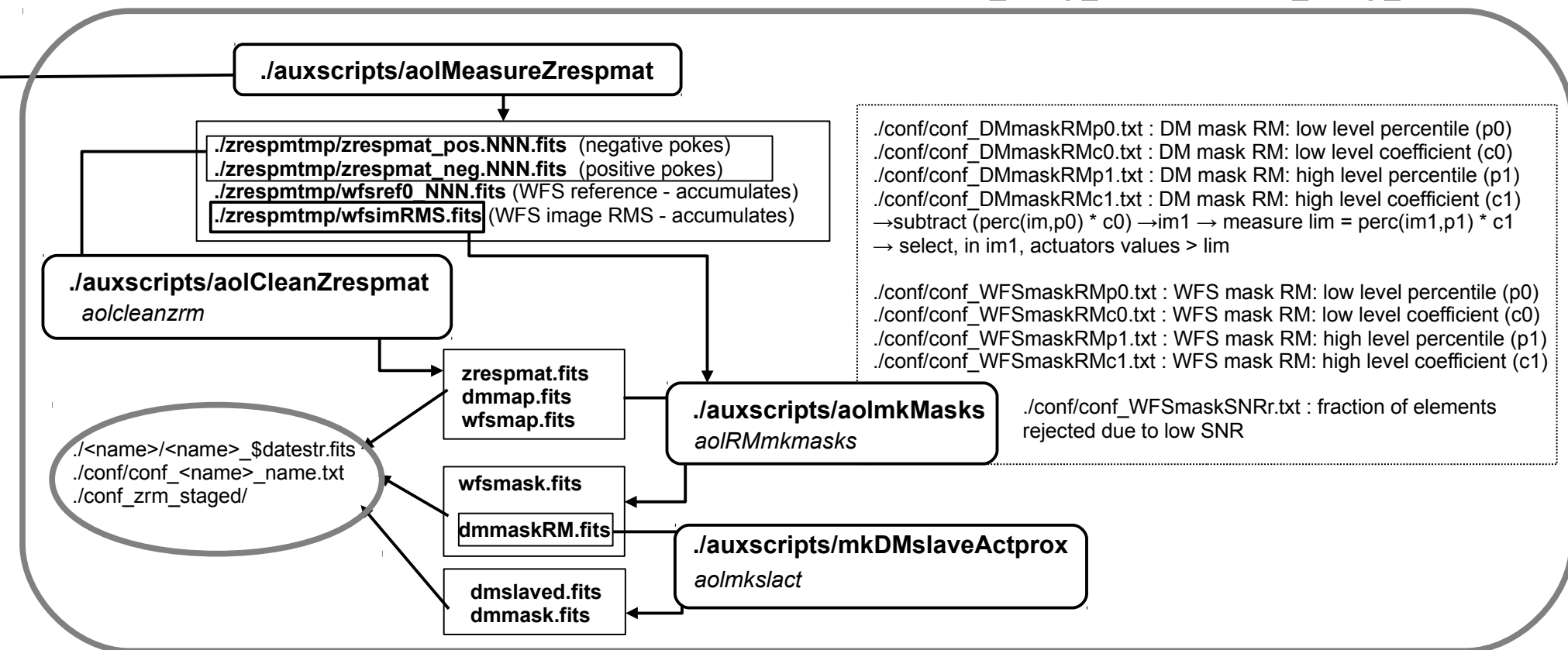


Decompose DM commands in modes + apply modal mult gains

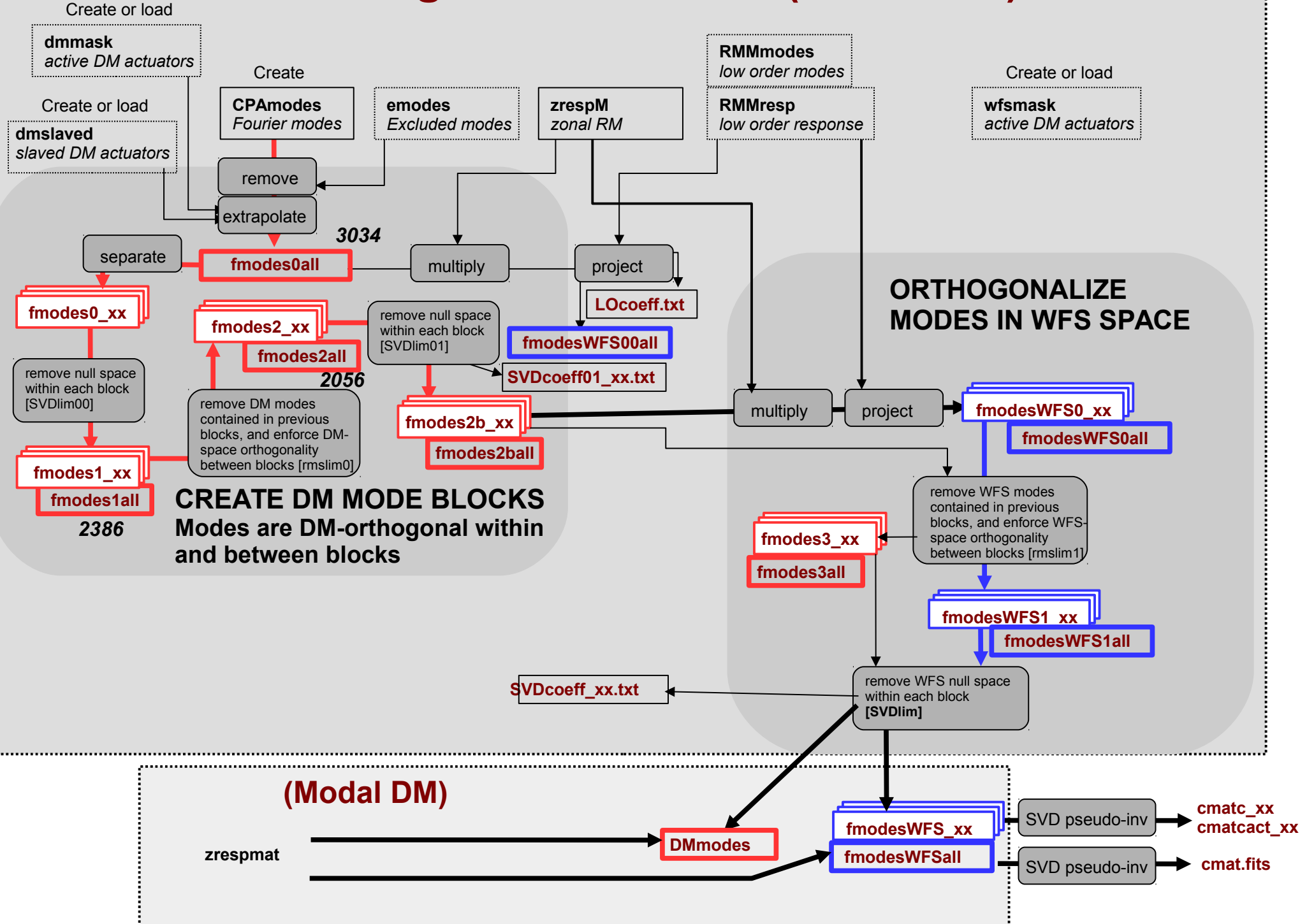


Zonal response matrix acquisition → masks

function_zresp_on → function_zresp_off



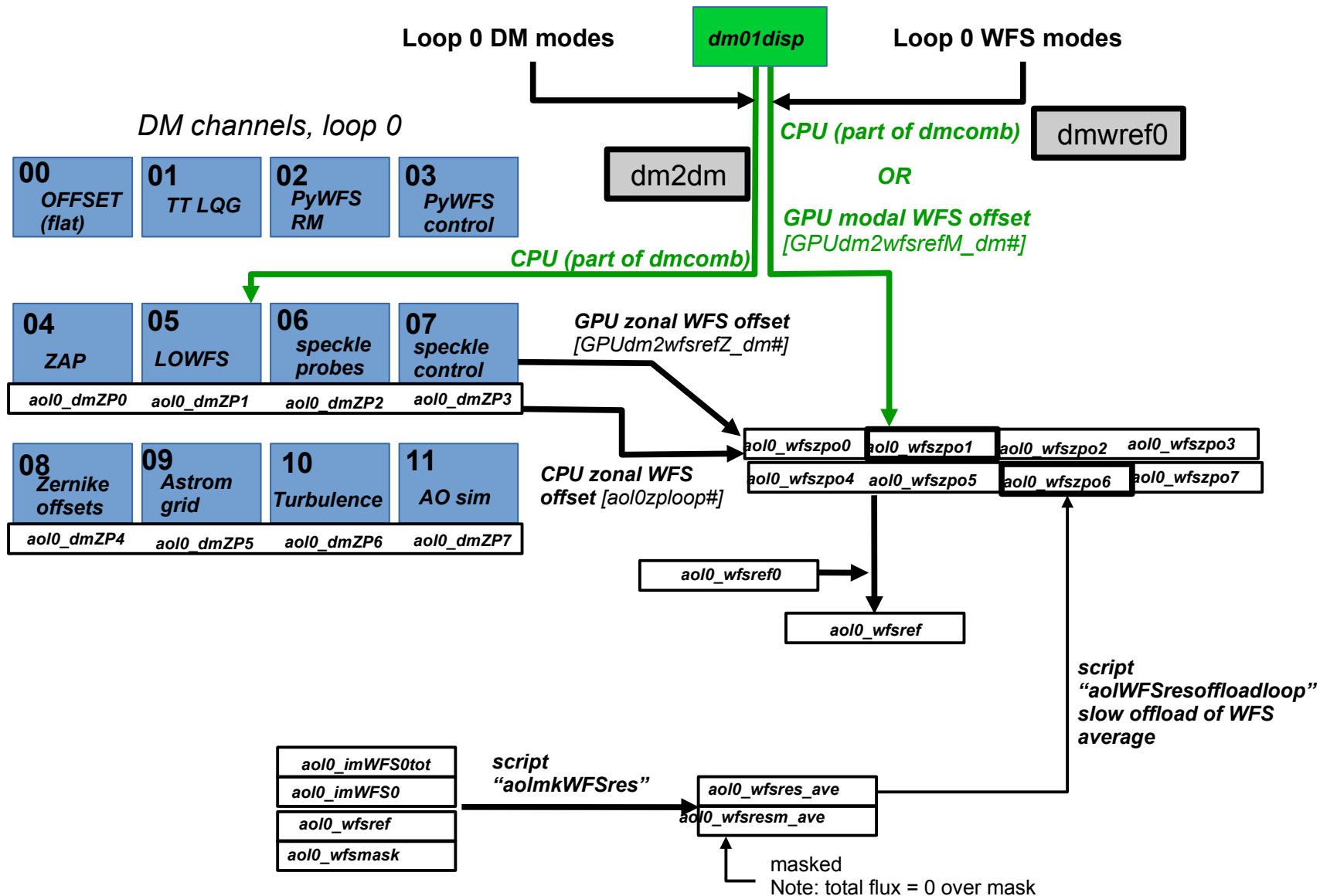
Making control modes (Zonal DM)



OFFSETTING

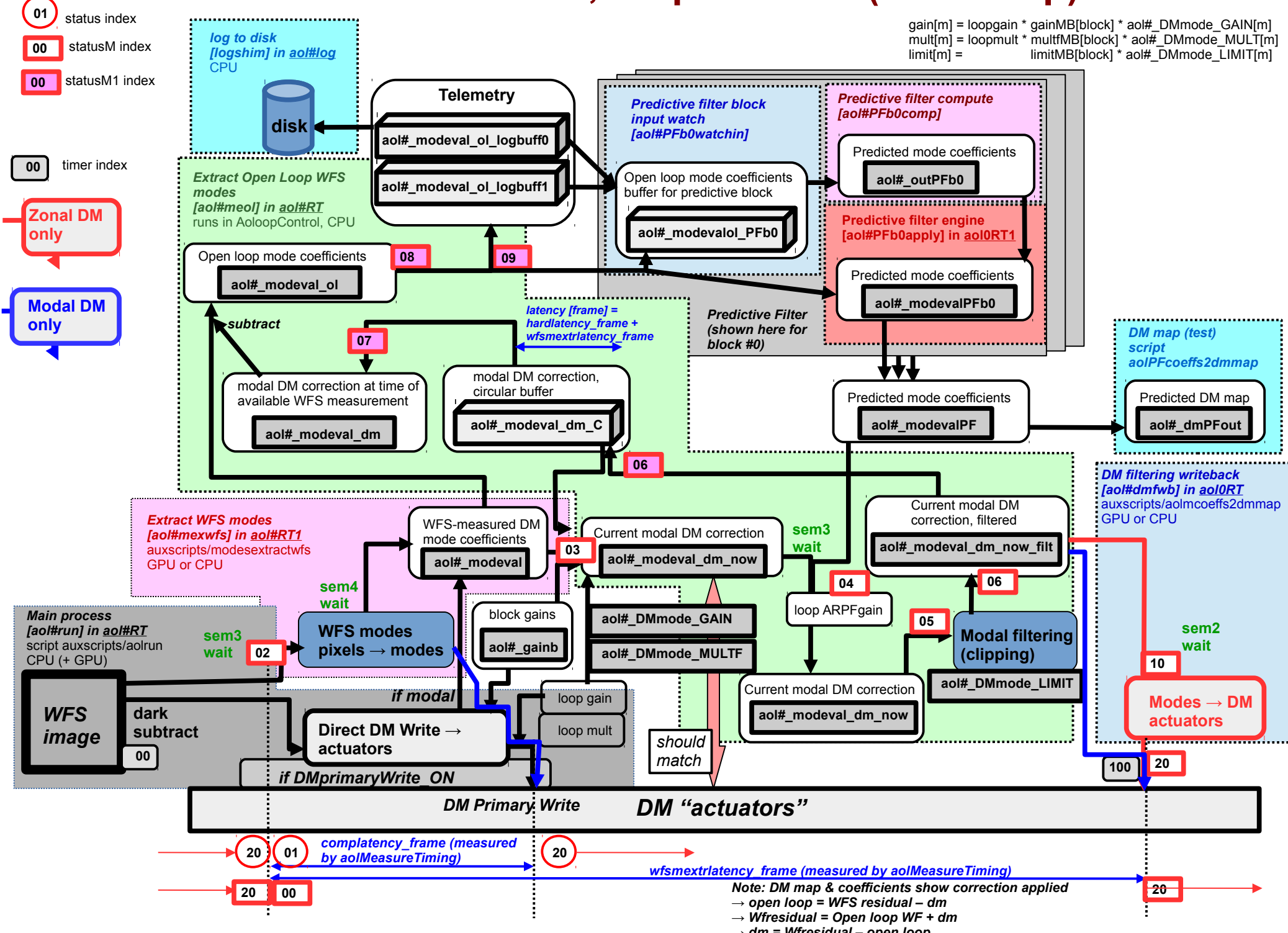
LOWFS (loop #1, dm01) → PyWFS (loop #0, dm00)

Green color: process is part of loop #1



[process name] (same name as tmux session)
 aol0RT : CPU set

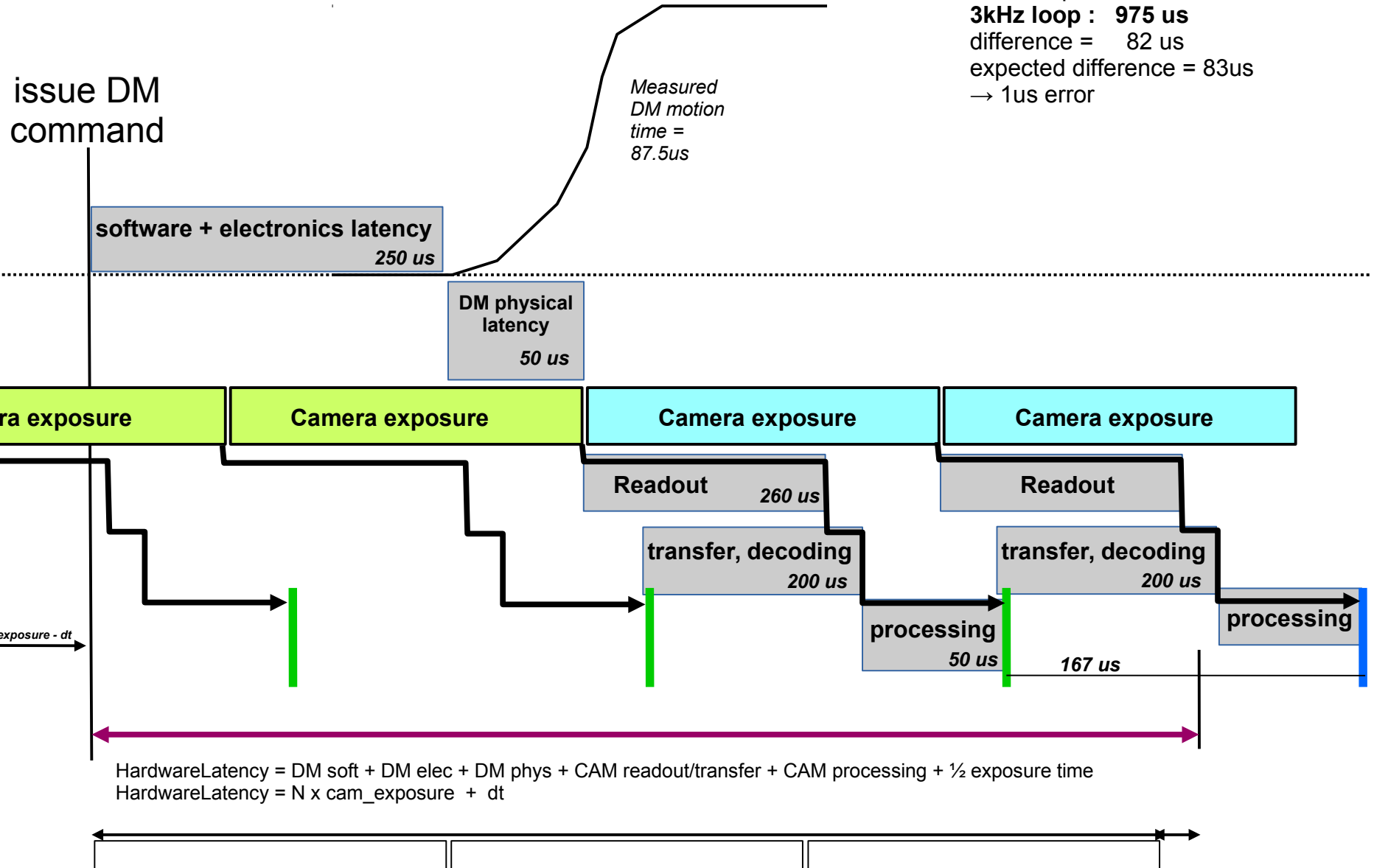
Processes, output to DM (main loop)



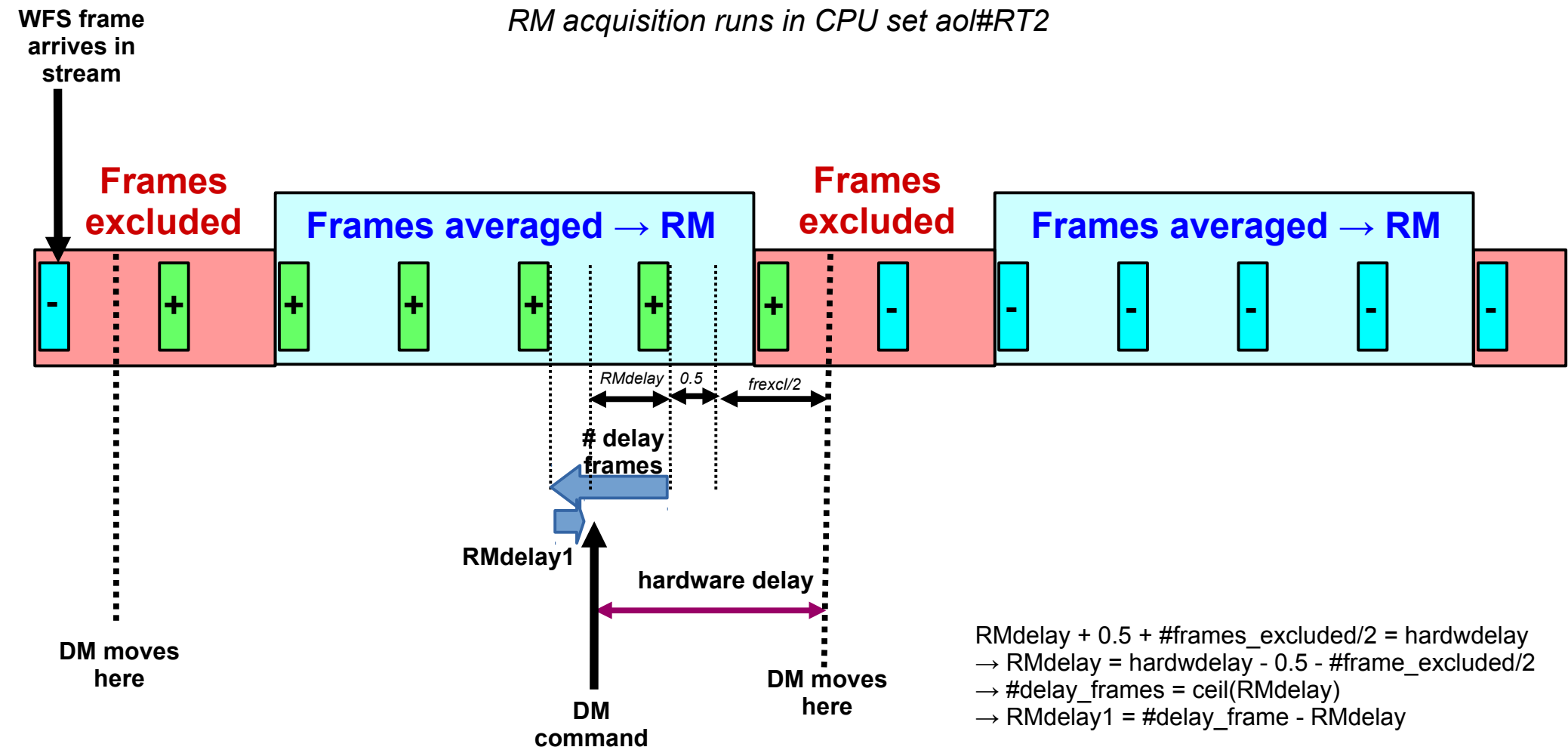
Hardware Latency

Definition:

*Time offset between DM command issued, and mid-point
between 2 consecutive WFS frames with largest difference*



RM acquisition - Timing



Loop:

Wait on and read WFS frame → allocate WFS frame to appropriate frame block
 If poke required: wait RMdelay1, then poke



4.1 AO Control and Simulations

Jared R. Males

1 Introduction

Here we describe our end-to-end simulations of MagAO-X. The requirement for these simulations is to demonstrate that the overall MagAO-X architecture and components can control atmospheric turbulence well enough to deliver the contrast and Strehl required for MaXProtoPlanets. This includes evaluation of the options we are considering for woofer-tweeter control and showing that they are each viable.

2 Wavefront Control Strategies

We are considering several different control strategies, each with pros and cons.

2.1 Phase I: In Phase I no new high-order wavefront control will be added. The existing MagAO system, with 585 actuators running at up 2kHz, will provide the correction. A beamsplitter at the input to MagAO-X will send some fraction of the light to the MagAO PWFS, and the rest will enter MagAO-X. The vAPP coronagraph will be used, and low-order wavefront sensing and control will occur using the coronagraph channel LOWFS-DM. Figure 1 shows a block diagram of the major components of this phase.

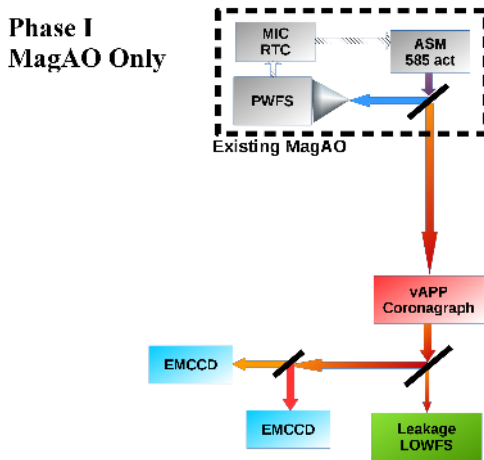


Figure 1: Phase I: all high order wavefront correction is by the existing MagAO system.

2.2 Phase II: In Phase II we will implement high-order wavefront control using the MEMS 2k with 2048 actuators total. Assuming a $1.5 \mu\text{m}$ stroke device is used, we will augment it with either a first stage or a woofer. There are three possible strategies:

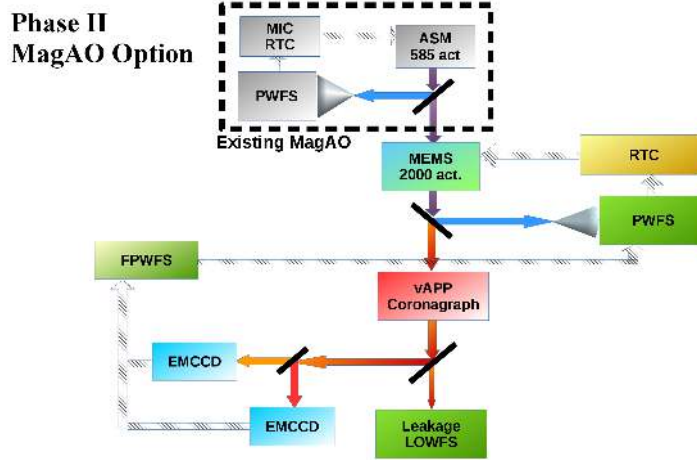


Figure 2: Phase II MagAO Option: Existing MagAO is used as an independent first stage (as is done with AO 188 at SCExAO).

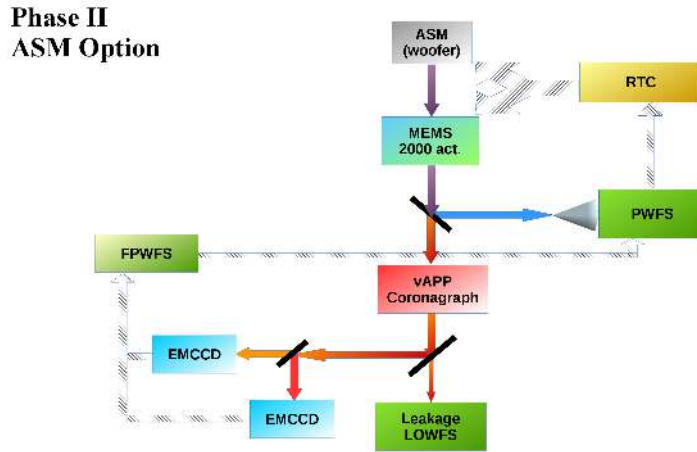


Figure 3: Phase II ASM Option: The MagAO ASM is used as a woofer, with all wavefront sensing by the MagAO-X PWFS.

- The existing MagAO system could be used as an independent first stage. This is what is currently done at Subaru with SCExAO and AO188. Some fraction of the incoming light would be sent to the MagAO PWFS, and the rest used in MagAO-X. The main benefit is the simplicity: only the MEMS needs to be controlled by our new system. The drawbacks are that few photons are available for MagAO-X PWFS, and the dynamics are sub-optimal in that the overshoot of existing MagAOs control will be in the temporal bandwidth of MagAO-X for low spatial-frequencies. This is shown schematically in Figure 2.
- The MagAO ASM could be used as a woofer. Here the new MagAO-X PWFS gets all the photons in the WFS band, and control is split between the ASM (low orders) and MEMS (high orders). The benefits are

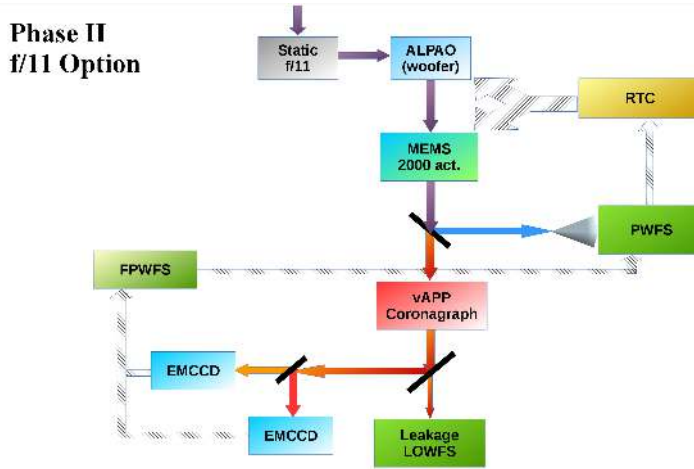


Figure 4: Phase II f/11 Option: The static f/11 secondary is used, all wavefront sensing is by the MagAO-X PWFS, and an on-board woofer is used.

efficient use of photons. The major drawback is that system calibration requires access to the ASM on the telescope. This is shown schematically in Figure 3.

- A further option we are considering (and the one we prefer) is to use the static f/11 secondary, and add a woofer to MagAO-X. The benefits are in the efficient use of photons for WFS, and this significantly improves the concept of operations due to being able to do nearly all AO calibrations off the telescope, and the relative ease of scheduling observing runs. The drawback is an additional 4 optics to relay onto the woofer. This is likely mitigated by the much fresher coating on the f/11 compared to the ASM, meaning we expect only a minor throughput loss. This is shown schematically in Figure 4.
- A final possibility is that BMC is successful in delivering a $3.5 \mu\text{m}$ stroke device, largely obviating the need for a woofer. Here we would use the f/11, and would likely still relay to the Alpa DM to offload the lowest orders from the MEMS (i.e. minimize stroke use to flatten) and to handle large non-Kolmogorov disturbances, e.g. from telescope vibrations.

The opto-mechanical design admits all of the above options to be used, and we have not yet committed to a single one. Our current preference is for the static f/11 with woofer option, due to the great simplification in the concept of operations. We intend to keep all of the above options open for some time as we implement the system and determine which one provides the best performance.

3 Simulations

We have conducted extensive end-to-end simulations to quantify the performance of MagAO-X and allow evaluation of the various control possibilities. Here we give details of the simulations. In the simulations all propagation is performed using the Fraunhofer approximation.

3.1 Pyramid Sensor: We simulate the pyramid using a fully diffractive model, which includes interference between the quadrants. Each quadrant has a tip OPD applied, calculated to place the subsequent pupil images in



Table 1: MagAO PyWFS Specifications

Parameter	Value	Notes
Readout Noise	$3\text{-}25 e^-$	depends on readout rate
Max frame rate	2000 fps	Max rate
λ_0	$0.842 \mu m$	See throughput document
$\Delta\lambda$	$0.261 \mu m$	See throughput document
Throughput	0.112	See throughput document
Modulation Radius	$3.0 \lambda/D$	
Pupil Diameter	30 pixels	can be binned

Table 2: MagAO-X PyWFS Specifications

Parameter	Value	Notes
Readout Noise	$150 e^-$	
EM Gain	500	
Effective RON	$0.3 e^-$	
Dark Current	$20 e^-/\text{pix/sec}$	Upper limit at 2000 fps
Clock Induced Charge	0	Assumed negligible
Max frame rate	3630 fps	Max stable rate at SCExAO
λ_0	$0.851 \mu m$	See throughput document
$\Delta\lambda$	$0.257 \mu m$	See throughput document
Throughput	0.227	See throughput document
Modulation Radius	0.0 - 3.0 λ/D	
Pupil Diameter	56 pixels	See lens design

the correct location. The images are binned to 120x120, such that the pupil images are 56 pixels in diameter. The binning preserves flux.

Modulation is simulated by applying tilts in the pupil plane prior to the pyramid. We use a number of discrete modulation steps so that there are at least 2 per λ/D along the circular modulation path. The MagAO pyramid is simulated using its nominal parameters, including the CCD-39. See Table 1. The MagAO-X pyramid simulation is based on the optical design and the specifications for the OCAM-2K EMCCD. See Table 2 and Figure 5.

3.2 Deformable Mirrors:

3.2.1 Tweeter: MagAO-X will use a Boston Micromachines 2k MEMS deformable mirror as the tweeter. The specifications of this device are summarized in Table 3. In the simulator we model this device using Gaussian influence functions, which are a very good match to a BMC DM. BMC specifies a coupling, which is the height of the influence function at the position of a neighboring actuators. The coupling specified is $15\pm3\%$. We generated a simulated mirror with actuators assigned an influence function with width drawn from a uniform distribution to produce coupling across this range. The pseudo-inverse of the influence function map is calculated, which is then projected on to the desired modal basis set to generate the “modes-to-commands” (M2C) matrix. This allows us to go from modal amplitudes (determined by the PyWFS and controller, described below) to a mirror command in physical units.



MagAO-X Preliminary Design

4.1 AO Control and Simulations

Doc #: MagAOX-001
Date: 2017-04-24
Status: Rev. 0.0
Page: 5 of 14

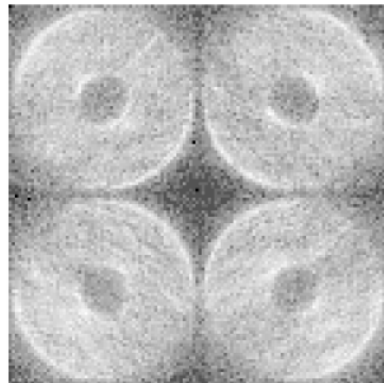


Figure 5: Simulated MagAO-X PWFS Image. This is for an 8th magnitude star, with a log stretch to illustrate the noise simulation.

Table 3: BMC 2k Tweeter Specifications

Parameter	Value	Notes
Total Actuators	2048	
Actuators Across	50	
Coupling	15%	
Settling Time	0.06 ms	
Max Frequency	\sim 10 kHz	
Interactutor Stroke	$0.85 \mu\text{m}$	Surface
Row-up/down Stroke	$1.1 \mu\text{m}$	Surface
4x4 Stroke	$2.1 \mu\text{m}$	Surface

Table 4: Alpa DM97-15 Woofer Specifications . These are from the test report for the as-delivered device.

Parameter	Value	Notes
Total Actuators	97	
Actuators Across	11	
Coupling	40%	
Settling Time	0.33 ms	
Max Frequency	2196 Hz	
Interactutor Stroke	$2.24 \mu\text{m}$	Surface
3x3 Stroke	$4.5 \mu\text{m}$	Surface
Tip/Tilt Stroke	$15 \mu\text{m}$	Surface, reduced for high speed
Focus Stroke	$12.5 \mu\text{m}$	Surface
Astig. Stroke	$12.5 \mu\text{m}$	Surface
Coma Stroke	$9 \mu\text{m}$	Surface

3.2.2 Woofer: When using the f/16 ASM option, the existing MagAO system serves as the woofer. To model the ASM we simply use the Karhunen Loeve modal basis measured interferometrically, that is we do not simulate



individual actuators.

For the f/11 option, we will need a woofer on the MagAO-X bench. We have chosen the Alpa DM97-15 with high speed option to serve as the woofer. We have procured a DM97 (using startup funds) to begin testing it to verify that it is suitable for this purpose. Its characteristics are summarized in table 4.

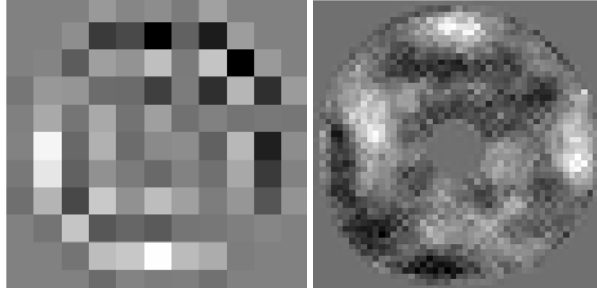


Figure 6: Actuator commands during simulation. At left for the DM97 woofer, and at right the 2k tweeter.

3.2.3 Modeling DM Stroke Limits: The BMC and Alpa mirrors have well documented stroke limits, as listed in the tables. The various limits have complicated relationships, and we do not simulate the physics of the facesheet so it is difficult to capture this. However, the inter-actuator stroke limits are the most limiting and so we enforce them in our simulations. If any two actuators reach the inter-actuator stroke limit for the device the commands for those actuators are reduced proportionally to the limit. We know this is working in our code since the limits occasionally engage when gains are too high causing the loop to diverge or a poorly constructed basis set is used.

We also monitor the overall peak-to-valley stroke of the BMC and Alpa mirrors in our simulations. The BMC is typically less than $1 \mu\text{m}$ P2V, and the Alpa is typically less than $3 \mu\text{m}$ P2V. These are well within the limits of the chosen DMs as well.

The key conclusion we have reached from our simulations is that the inter-actuator strokes of the devices are sufficient for Kolmogorov turbulence at LCO. We have already procured an Alpa DM97-15 which will allow us to develop a suitable slaving model for its un-illuminated actuators and validate our model of it.

3.3 Basis Sets: When simulating the MagAO-as-1st-stage option, the MagAO system is simulated using the KL basis used on sky. For MagAO-X we construct a basis set from a 40x40 square grid of Fourier modes which is augmented with the first 10 Zernike polynomials.

The basis set for MagAO-X with a woofer is constructed in the following steps:

- A custom KL basis is constructed as a decomposition of a 10x10 grid of Fourier modes for the von Karman spectrum with tip and tilt subtracted. Using the Fourier basis instead of the usual Zernike polynomials allows us to control the spatial frequency content of this basis and avoid the high derivatives at the edge of the pupil that occur with the Zernikes. We keep the first 48 modes of this basis.
- the KL basis is then augmented with pure tip and tilt modes. This forms a 50-mode low-order basis used for the woofer.
- For the tweeter, we use an NxN grid of Fourier modes, where the N used depends on star brightness. N ranges from 22 to 42 depending on star brightness.



So far we do not explicitly orthogonalize the woofer-tweeter bases. Rather, we depend on the SVD in the reconstructor pseudo-inverse to find an orthogonal projection. In simulations this works and we have stable loops. We recognize that this may not be optimal, and we are investigating various orthogonalization strategies as well.

3.4 Control Law: For MagAO we calculate slopes from the CCD-39 simulated detector and use a pure-integrator control law as is standard. MagAO loop parameters (speed, gains, WFS binning) were adjusted to optimize the performance of MagAO-X. A key point is that the control-loop dynamics of these cascaded loops were fully simulated.

For MagAO-X we calculate slopes from the OCAM-2K simulated images. Here we use a leaky integrator control law and find that it performs better than the pure integrator. Modal gains were optimized using PSDs (Smith & Véran, 2003; Poyneer & Véran, 2005) for various star magnitudes. When the woofer-tweeter system is simulated, the Alpaq woofer is given a longer settling time (0.5 ms) than the BMC (0.25 ms, minimum time-step in simulation). This simulates the different dynamics of the two devices.

3.5 Turbulence Simulation: We used a model of the LCO atmosphere based on the GMT site survey Prieto et al. (2010) and LCO seeing statistics and outer scale $L_0 = 25$ mFloyd et al. (2010). We use only DIMM seeing to have a valid measure of r_0 independent of L_0 . In our end-to-end simulations we include the outer scale (von Kármán statistics) and the median C_n^2 profile. We simulated multiple layers using the C_n^2 profile from site testing Prieto et al. (2010), propagating with characteristic wind velocities.

We normally have little knowledge of wind speed at altitude. We incorporate our own experience at LCO (*many* nights on-sky with MagAO) to estimate typical winds. As a baseline we use the GMT survey wind layers, which have a C_n^2 weighted mean of $\bar{v} = 18.7$ m/s. To model good conditions, we use winds 50% slower.

We summarize our atmosphere model in Table 5. For this analysis we use 2 distinct models, intended to represent “excellent”, and “good” conditions. The “25%” model corresponds to first quartile DIMM seeing, and low winds. The “50%” model corresponds to median DIMM seeing, and the GMT atmosphere winds. We also show our “75%” model, which includes third quartile DIMM seeing, and higher winds. Wind and seeing are not necessarily coupled, so various combinations of these parameters are possible.

Table 5: Summary of MagAO Atmosphere Models

Quartile	\bar{v} [m/s]	@ V (0.5 μm)		
		FWHM ["]	r_0 [m]	τ_0 [msec]
25%	9.4	0.51	0.20	7.4
50%	18.7	0.65	0.16	2.9
75%	23.4	0.81	0.13	1.9

4 Results

Simulations were run over a range of guide star magnitudes for median and 25%-ile conditions. The Strehl ratio results are shown in Figure 7 for the typical MEMS surface quality, and Figure 8 for the worst case MEMS surface quality. See Section 5.1 for the static and NCP error budget.

Next we show unocculted PSFs as well as coronagraphic PSFs using the vAPP (design described in 5.2 below) for 30 second exposures. We also show contrast profiles through the dark hole. In the contrast profile plots, photon noise limits are shown which take into account the Strehl both due to AO performance and the vAPP Strehl, as

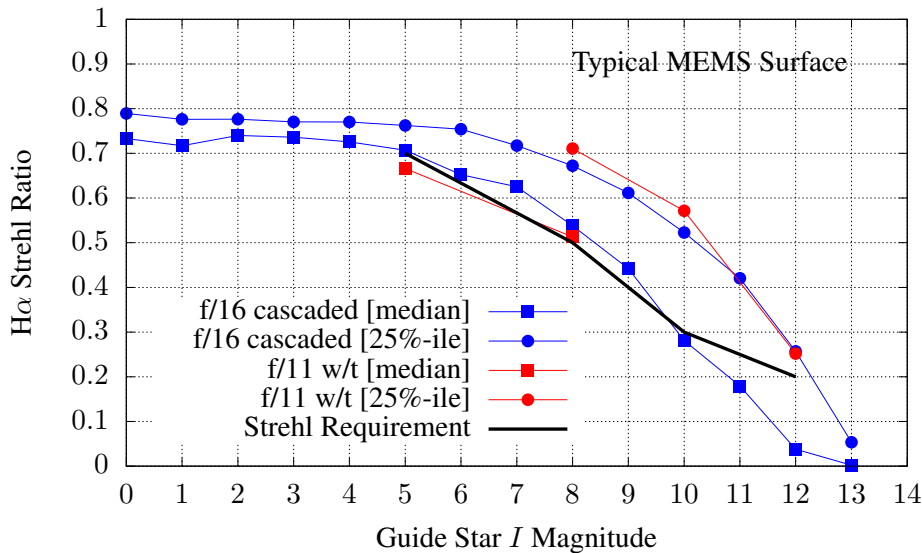


Figure 7: Strehl vs guide magnitude from simulations. The static and NCP error budget from Section 5.1 is include for the typical MEMS surface quality. The Strehl requirement is met for 25%-ile conditions. We are close to the Strehl goal for stars brighter than I=10mag, meaning that median conditions can be used for MaXProtoPlanets.

well as the typical MEMS case static and NCP. The photon noise is calculated for the custom designed H_α filter presented in 2.1, with throughputs a shown in 5.4 below.

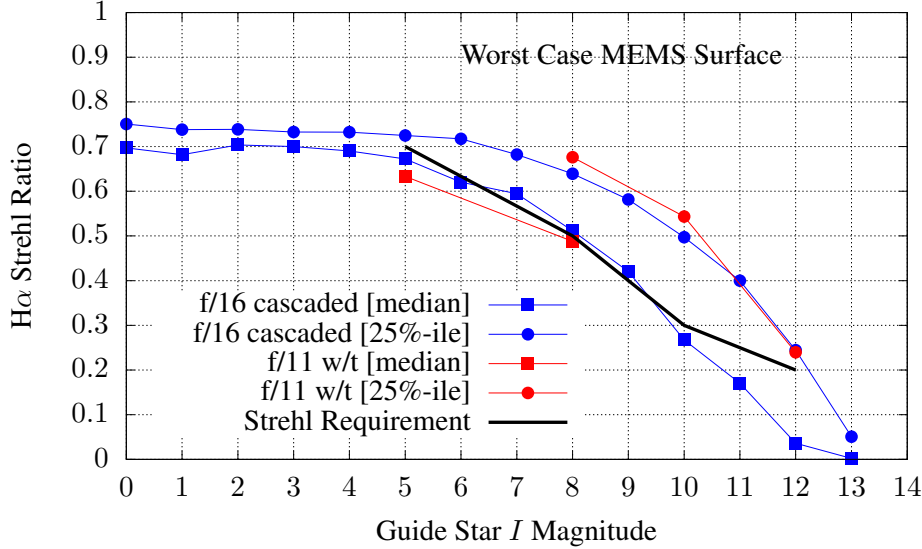


Figure 8: Strehl vs guide magnitude from simulations. The static and NCP error budget from Section 5.1 is included for the worst case MEMS surface quality. The Strehl requirement is met for 25%-ile conditions. For bright stars, we are limited by static and NCP dominated by the worst case DM. We are still close enough to the Strehl goal for stars brighter than $I=10\text{mag}$, that we expect median conditions can be used for MaXProtoPlanets here as well.

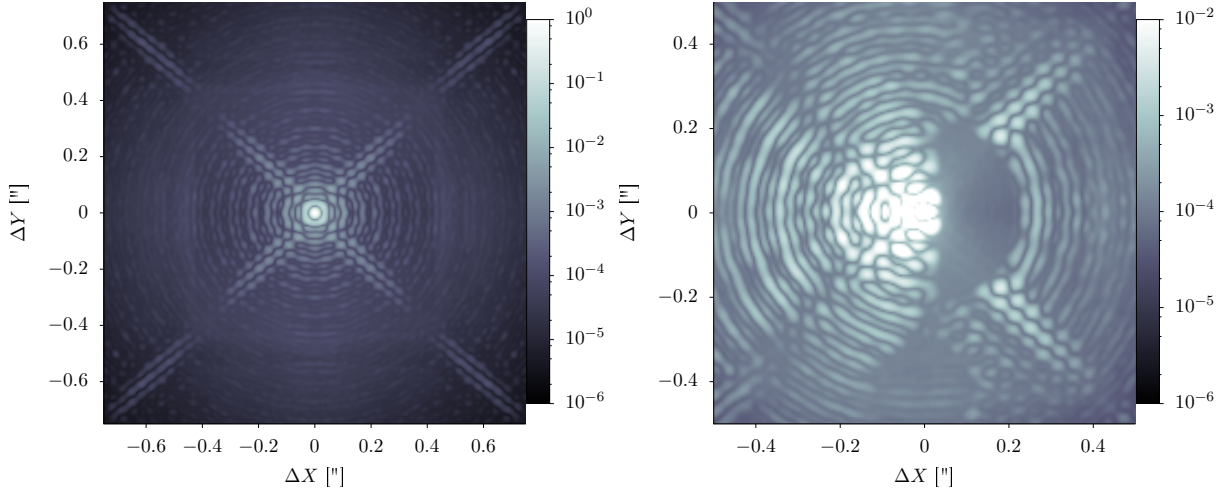


Figure 9: PSF for an 8th magnitude star in 25%-ile conditions.

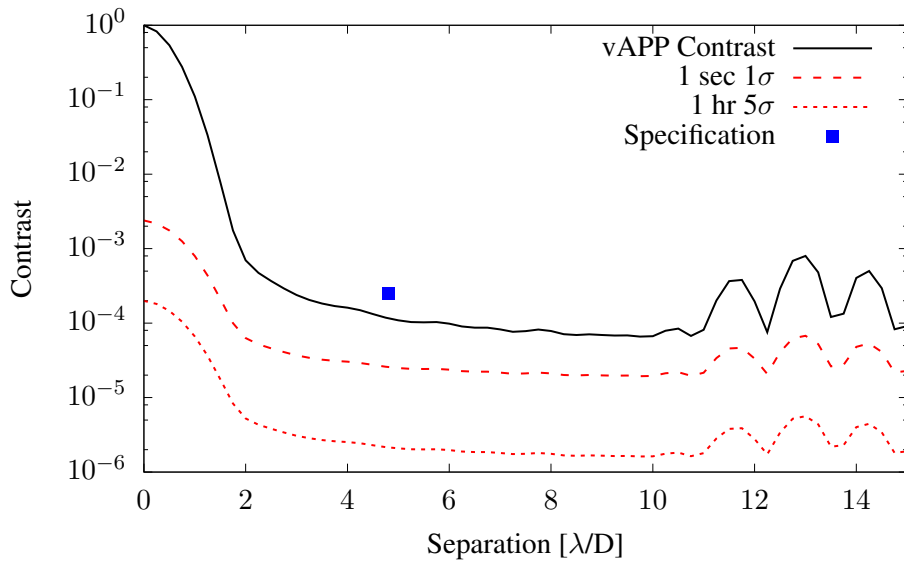


Figure 10: Contrast for an 8th magnitude star in 25%-ile conditions. The contrast at 100 mas ($5 \lambda/D$) meets the specification of 2.5×10^{-4} .

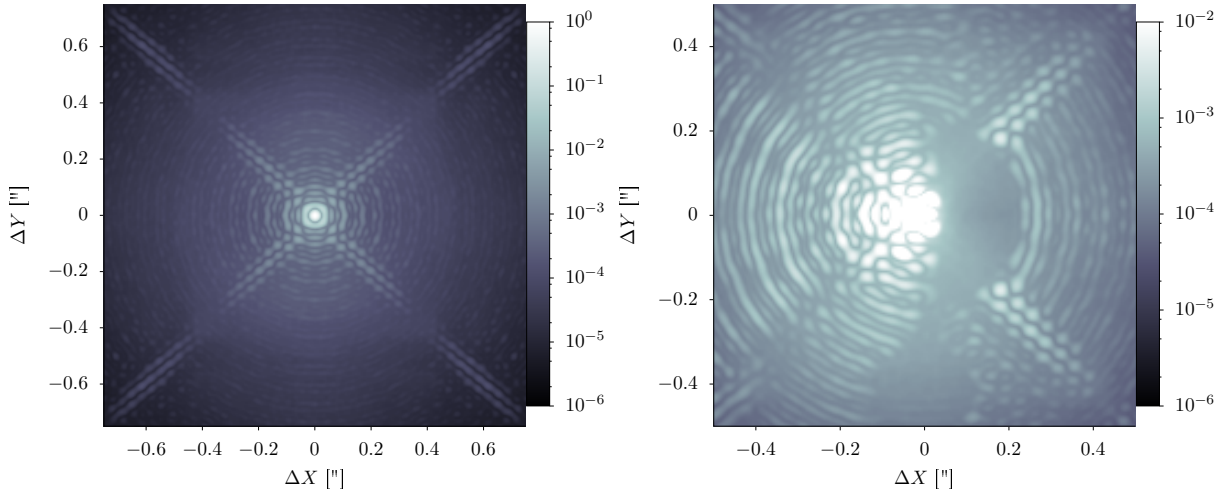


Figure 11: PSF for a 10th magnitude star in 25%-ile conditions.

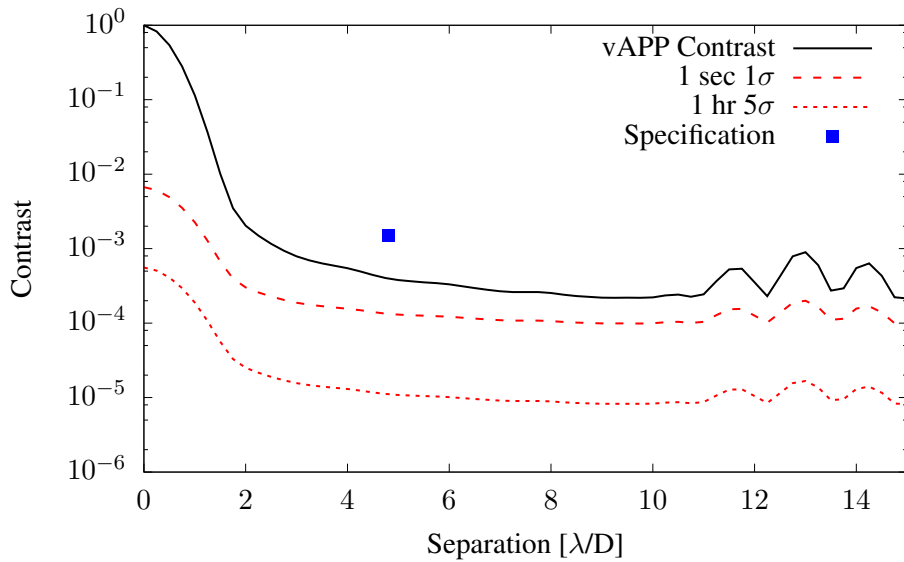


Figure 12: Contrast for a 10th magnitude star in 25%-ile conditions. The contrast at 100 mas ($5 \lambda/D$) meets the specification of 1.5×10^{-3}

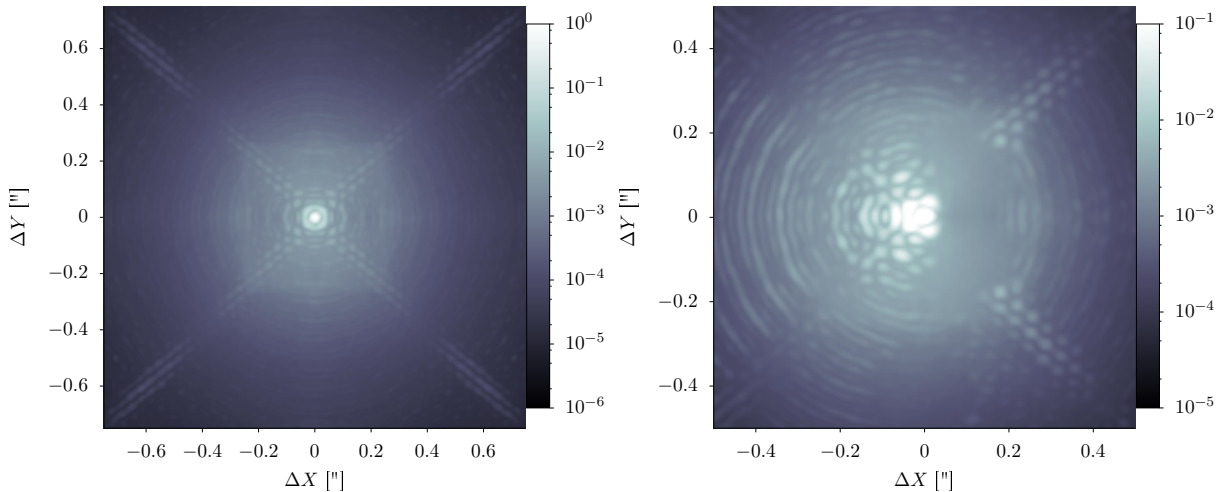


Figure 13: PSF for a 12th magnitude star in 25%-ile conditions.

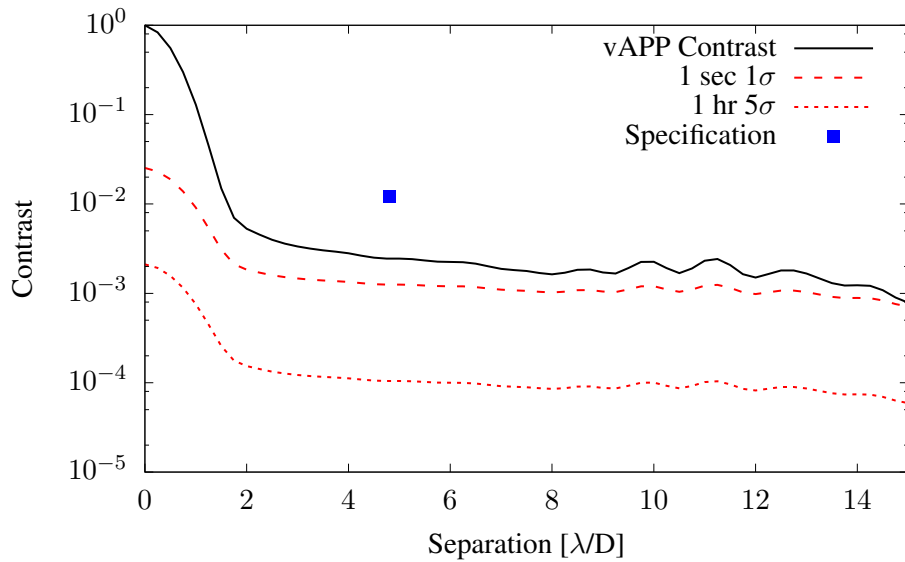


Figure 14: Contrast for an 12th magnitude star in 25%-ile conditions. The contrast at 100 mas ($5 \lambda/D$) meets the specification of 1.0×10^{-2}

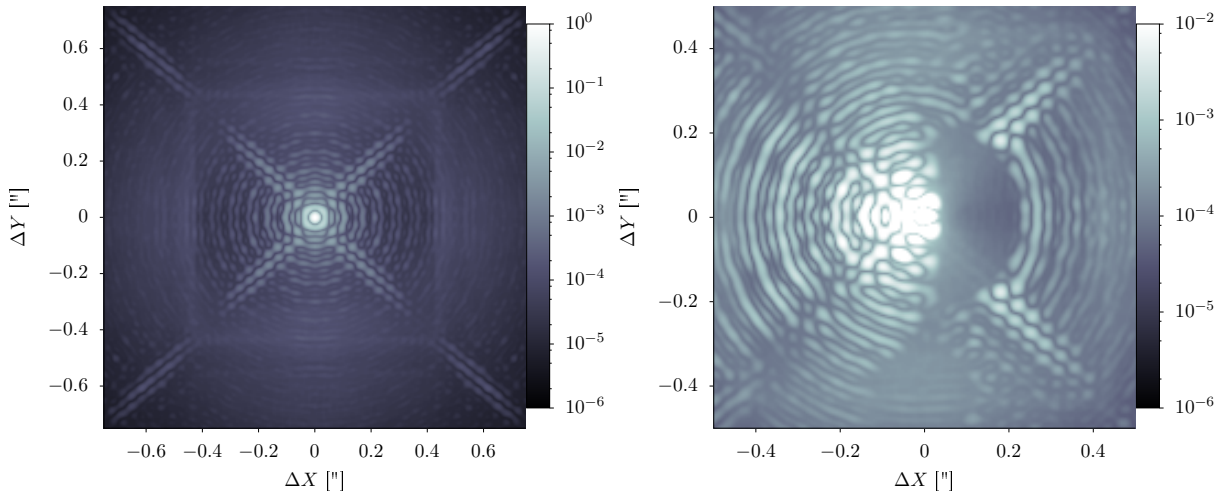


Figure 15: PSF for a 5th magnitude star in 50%-ile conditions.

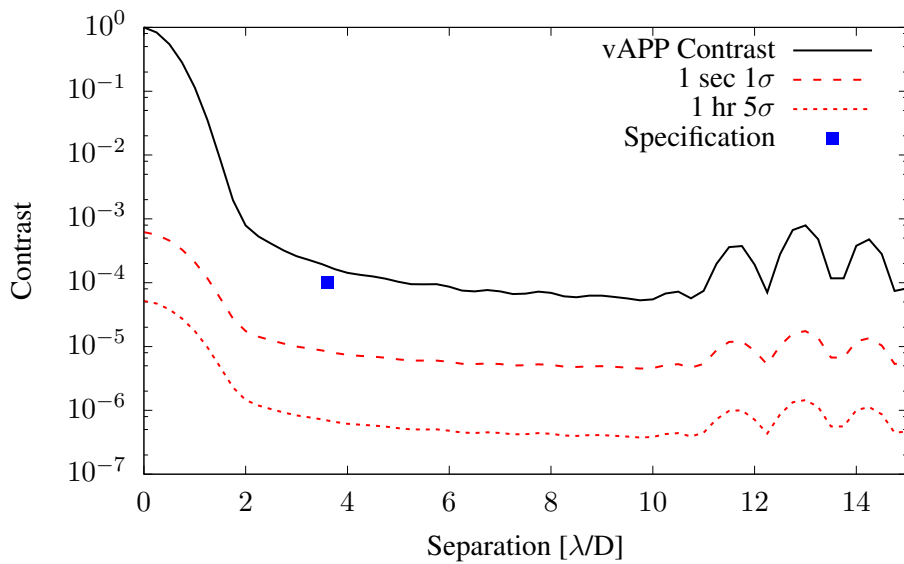


Figure 16: Contrast for a 5th magnitude star in 50%-ile conditions. This is our most demanding requirement. The raw contrast at 75 mas ($3.5 \lambda/D$) is below the specification, however the photon noise limits are well below. This means that we will be able to sense (using LOWFS and FPWFS) and calibrate (using SDI) the residuals to meet the detection requirement of 1.0×10^{-4} even in median conditions.



5 Conclusion

End-to-end simulations have shown that the MagAO-X design can deliver the wavefront quality needed for MaXProtoPlanets. Strehl ratio (a soft requirement), is met in 25%-ile conditions with margin, and we reach or come close to the goal of working in median conditions. Most importantly, we meet the contrast requirements. The raw turbulence limited contrast, as well as the photon noise from the residual, is below the spec in 25% conditions. Even in median conditions, the 5th mag star case shows that we can meet our most demanding specification with SDI and LOWFS and FPWFS techniques.

References

- Floyd, D. J. E., Thomas-Osip, J., & Prieto, G. 2010, PASP, 122, 731
Poyneer, L. A., & Véran, J.-P. 2005, Journal of the Optical Society of America A, 22, 1515
Prieto, G., Thomas-Osip, J. E., Phillips, M. M., McCarthy, P., & Johns, M. 2010, Proc. SPIE, 7733, 773340
Smith, M. J., & Véran, J.-P. 2003, Proc. SPIE, 4839, 964



4.2 Low-Order & Focal Plane Wavefront Sensing and Control

Kelsey Miller

1 Low-Order Wavefront Sensing (LOWFS)

1.1 LOWFS theory: Low-order wavefront sensing (LOWFS) is a coronagraphic wavefront sensing technique designed to sense pointing errors and other low-order wavefront aberrations using starlight that would normally just be rejected by the coronagraph. In a Lyot coronagraph, a mask is placed at the focal plane which diffracts starlight outside the geometrical pupil into a downstream pupil plane at which a Lyot mask, an undersized replica of the entrance pupil, is placed. In traditional coronagraphs, starlight is simply blocked by both of these masks, but for LOWFS, that rejected starlight from either the focal plane and the reimaged pupil plane is reflected, respectively, by a reflective focal plane mask (FPM) as well as a reflective Lyot stop, each toward a reimaged focal plane. The resulting PSFs from the starlight rejected by both masks are imaged by separate detectors and used to measure the low-order aberrations. LOWFS is a linear wavefront reconstructor that fits post-AO wavefront residuals to a command matrix built by registering the response of these rejected starlight PSFs to aberrations injected into the system by a deformable mirror (DM). This technique relies on the assumption that if the post-AO wavefront residuals are $\ll 1$ radian rms then the intensity variations in the reflected light are a linear combination of the low-order aberrations occurring upstream of the focal plane mask. LOWFS has been successfully deployed on-sky by the Subaru Coronagraphic Extreme AO (SCExAO) team, who are contributors to the MagAO-X effort. (1)

1.2 LOWFS for MagAO-X: In the MagAO-X system, a separate LOWFS arm has been designed to sense and correct pointing, tip/tilt, and other low-order modes. Slightly different from the original technique described above, the MagAO-X LOWFS system will use the stellar light leakage term from the vAPP coronagraph (see Section 5.5 Vector apodizing phase plate coronagraph for MagAO-X) as the LOWFS signal. To build the LOWFS control loop around this signal, an ALPAO deformable mirror (DM) with 97 actuators has been selected to be the wavefront corrector to compensate these low-order errors. The MagAO-X instrument will take full advantage of the ability to do wavefront correction with all 97 accessible modes. To do this, LOWFS must be sensitive to all 97 modes; this is accomplished in part by defocusing the LOWFS PSF which broadens the area on the detector over which the modes can be sensed. Due to their smaller uncompensated residual wavefront fitting error (as compared to Zernike modes), atmospheric Karhunen-Loeve (KL) modes were chosen to build a 97 mode reconstruction matrix. The following document demonstrates the MagAO-X LOWFS ability to sense and control 97 KL modes individually and in random combinations, and its ability to use a KL modal basis set to sense and correct random Kolmogorov phase errors. The reflective Lyot stop PSF was defocused by $0.1 \mu\text{m}$ for these demonstrations.

1.3 LOWFS elements:

1.3.1 Stellar signal: As previously mentioned, the MagAO-X system will rely on the signal from the stellar light leakage term from the vAPP coronagraph (Fig 1). In terms of spatial frequency sensitivity, the LOWFS control loop built around the response of the light leakage PSF will be similar to both the reflected FPM and reflected Lyot



mask cases described previously. This is because the signal from the light leakage term in the vAPP case is not diffracted or blocked by any masks; instead, the stellar leakage PSF is passed directly to a detector, thereby containing both the low and the high spatial frequency content that would be seen by the reflective FPM and Lyot mask cases. The reflective Lyot mask case was chosen to for the following demonstrations of LOWFS on MagAO-X as it was under development for use with the PIAACMC, and the underlying principle is the same. The reflective Lyot mask used for these simulations is shown in Fig 2. The signal from this reflected starlight contains the low, mid, and high spatial frequency content (see Section 1.4 for verification) that will be seen with the vAPP stellar leakage PSF.

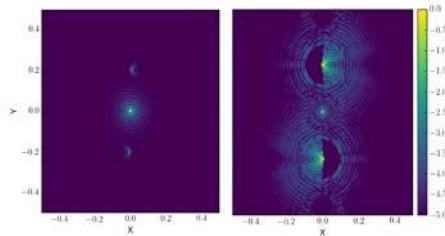


Figure 1: LOWFS signal from the vAPP stellar light leakage term (center PSF) shown between the two coronagraphic PSFs. See Section 5.5 Vector apodizing phase plate coronagraph for MagAO-X for details.

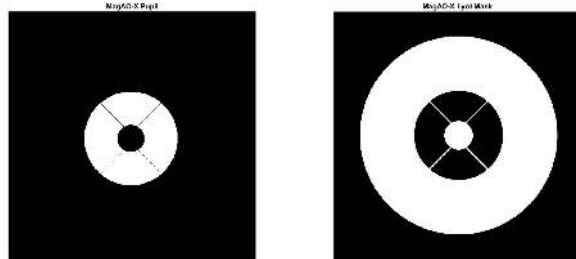


Figure 2: MagAO-X masks: Entrance pupil mask (left) and the reflective Lyot stop used for the following LOWFS simulations (right)

1.3.2 Deformable mirror: In the MagAO-X LOWFS arm, the low-order aberrations sensed using the starlight reflected by the Lyot mask will be corrected using an ALPAO DM 97-15 (see full spec sheet for this DM below in Figure 3.). The ALPAO DM is circular and 13.5 mm in diameter and has 97 actuators across the full pupil. This will allow for LOWFS correction with up to 97 individual modes. This DM has been modeled using the mirror's gaussian influence functions for use in the following simulation work demonstrating the MagAO-X LOWFS ability to sense and correct 97 modes.



MagAO-X Preliminary Design

4.2: LO/FP WFS&C

Doc #: MagAOX-PDR-001
Date: 2017-04-22
Status: Rev. 0.0
Page: 3 of 16



	DM 69	DM 88	DM 97-08	DM 97-15	DM 241	DM 277	DM 468	DM 820
Number of actuators	69	88	97	97	241	277	468	820
Pupil diameter (mm)	10.5	20.0	7.2	13.5	37.5	24.5	33.0	45.0
Pitch (mm)	1.5	2.5	0.8	1.5	2.5		1.5	
Mirror best flat in close loop	7.0nm RMS (no print through)							
Wavefront tip/tilt stroke (PV)	60μm	40μm	80μm	60μm	40μm		15μm	
Settling time (at +/-10%)	800μs		1.6ms	800μs	1.6ms		500μs	

Figure 3: ALPAO DM 97-15 with specifications (2)

1.4 Sensitivity and correction with 97 Karhunen-Loeve modes: To demonstrate the MagAO-X LOWFS ability to sense and correct 97 modes, a Karhunen-Loeve (KL) modal basis set was derived using Fourier modes. (All 97 KL modes can be seen in Figure 4.)

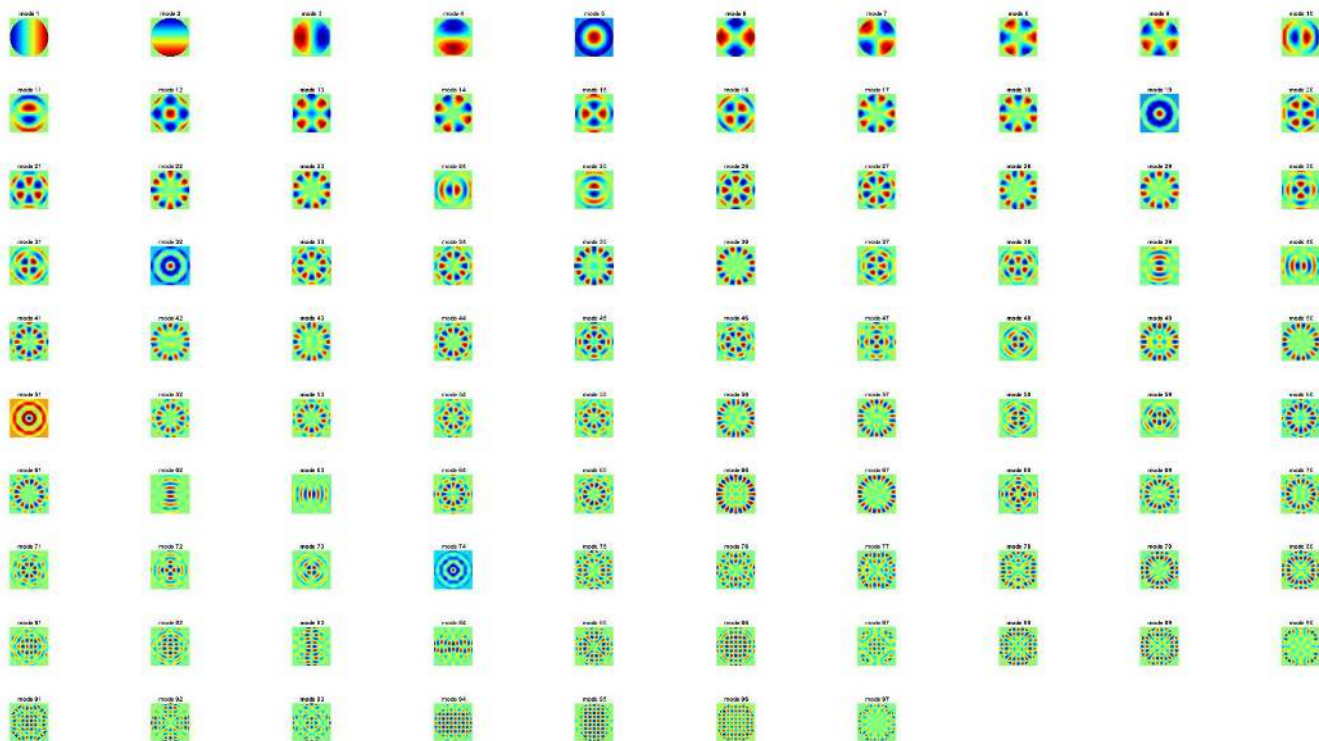


Figure 4: 97 KL modes sensed in the following section

The LOWFS response matrix used in the LOWFS control loop was then constructed using these 97 KL modes. To build the LOWFS response matrix, each of these individual modes was then applied to the model ALPAO DM, and the PSF formed by the light reflected by the Lyot mask was recorded for each mode. (All 97 PSFs can be seen in Figure 5)



MagAO-X Preliminary Design 4.2: LO/FP WFS&C

Doc #: MagAOX-PDR-001
Date: 2017-04-22
Status: Rev. 0.0
Page: 4 of 16

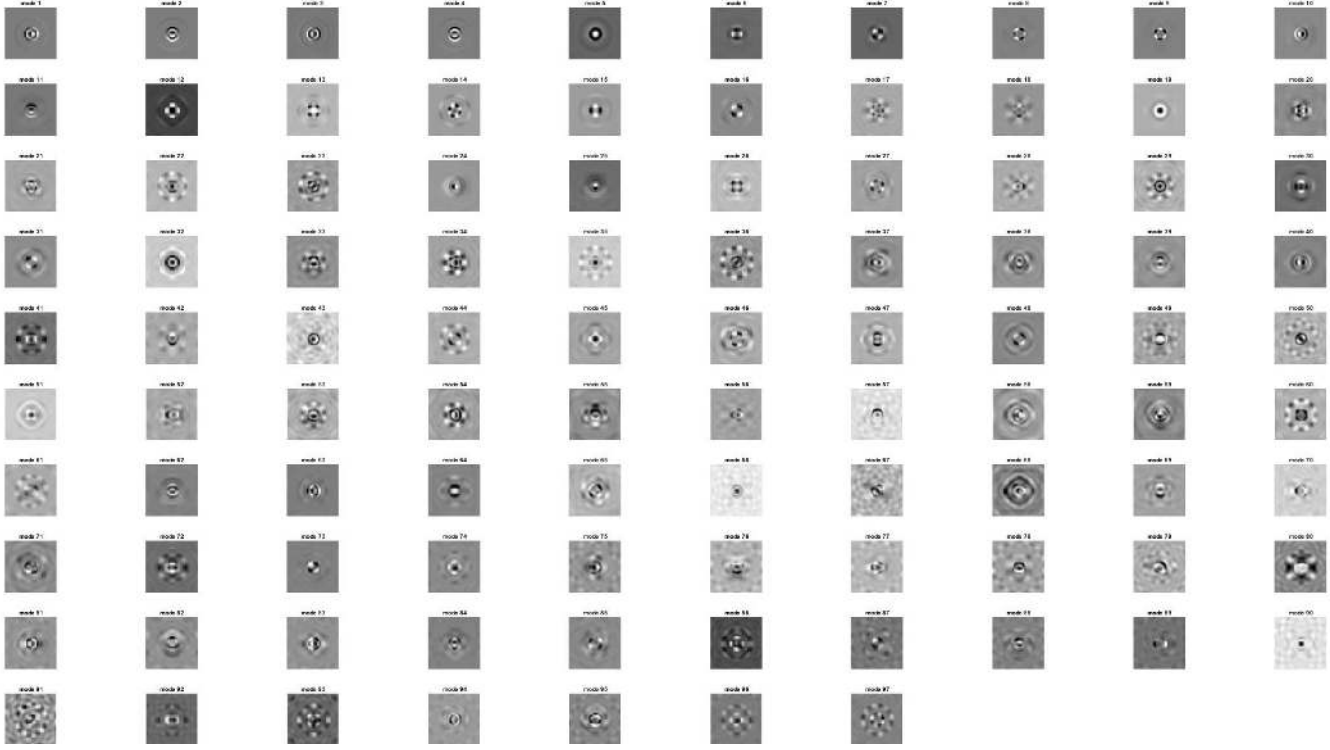


Figure 5: The LOWFS PSF for all 97 KL modes

Each of these PSFs is then reshaped into a single column vector in the LOWFS response matrix. The command matrix used in the LOWFS control loop is then the pseudo-inverse of this response matrix. This command matrix was then used in the following simulations to show the MagAO-X LOWFS ability to sense and control these modes.

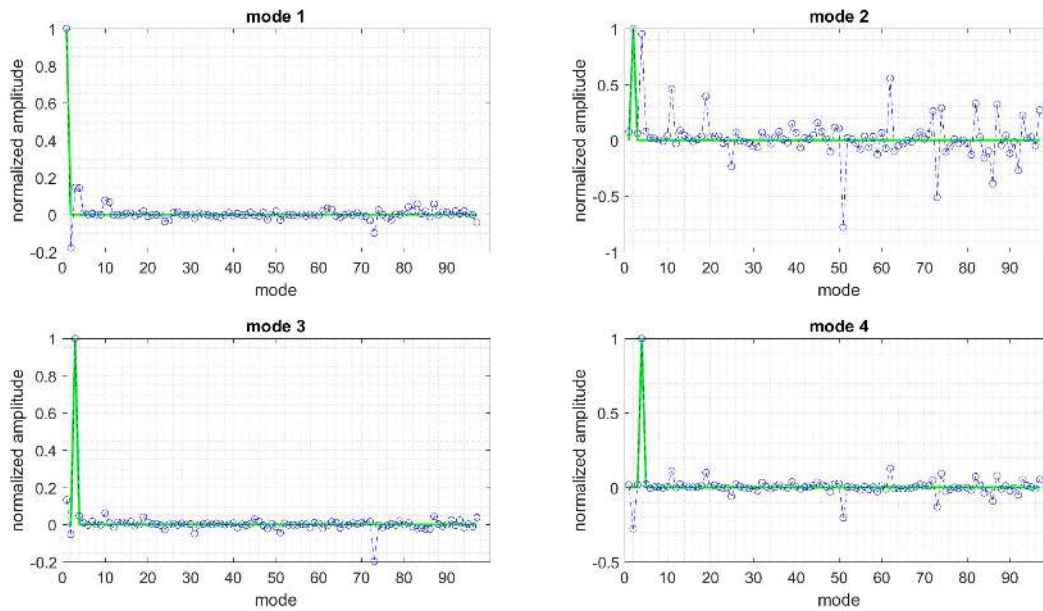
1.4.1 Sensing and correcting individual KL modes: In the following section, each of the 97 KL modes shown in Figure 4 was applied individually to the ALPAO DM model and sensed using the model MagAO-X LOWFS system. Each plot shows the normalized amplitude of the single KL mode that was applied (in green) and the normalized amplitude of each KL mode in the LOWFS response (in blue). For this simulation, the LOWFS PSF was defocused by $0.1 \mu\text{m}$. It should be noted that the LOWFS response to certain modes is noisier than others. This is due to the fact that, for mid-spatial frequencies, there is a tradeoff between coronagraph inner working angle (IWA), transmission at small angles and LOWFS sensitivity. With a low-IWA coronagraph with good throughput outside of the IWA, LOWFS can only measure a few modes with good sensitivity.



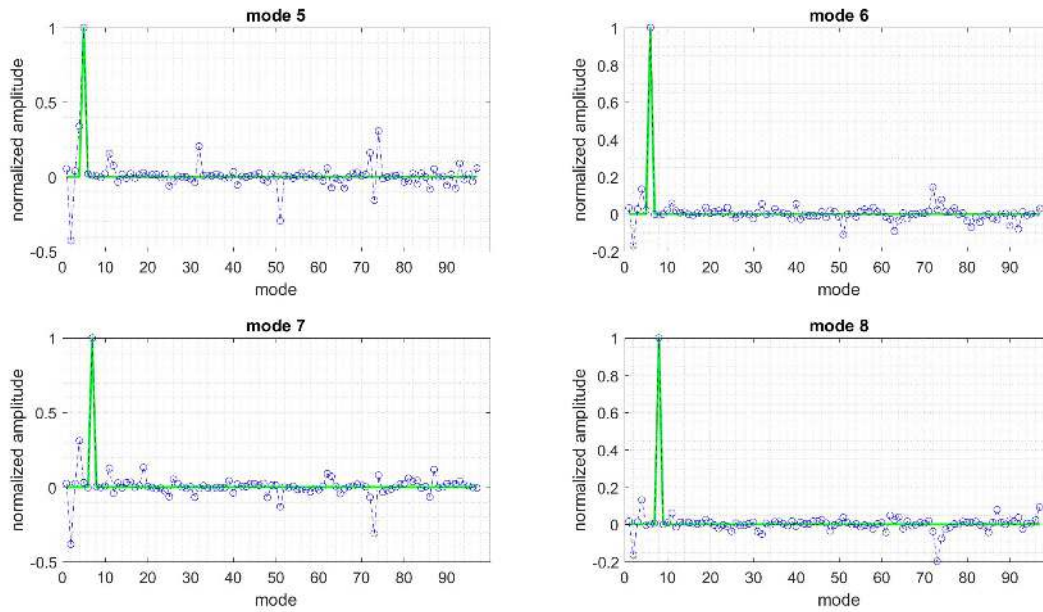
MagAO-X Preliminary Design

4.2: LO/FP WFS&C

Doc #: MagAOX-PDR-001
Date: 2017-04-22
Status: Rev. 0.0
Page: 5 of 16



(a) Sensitivity to KL modes 1 - 4



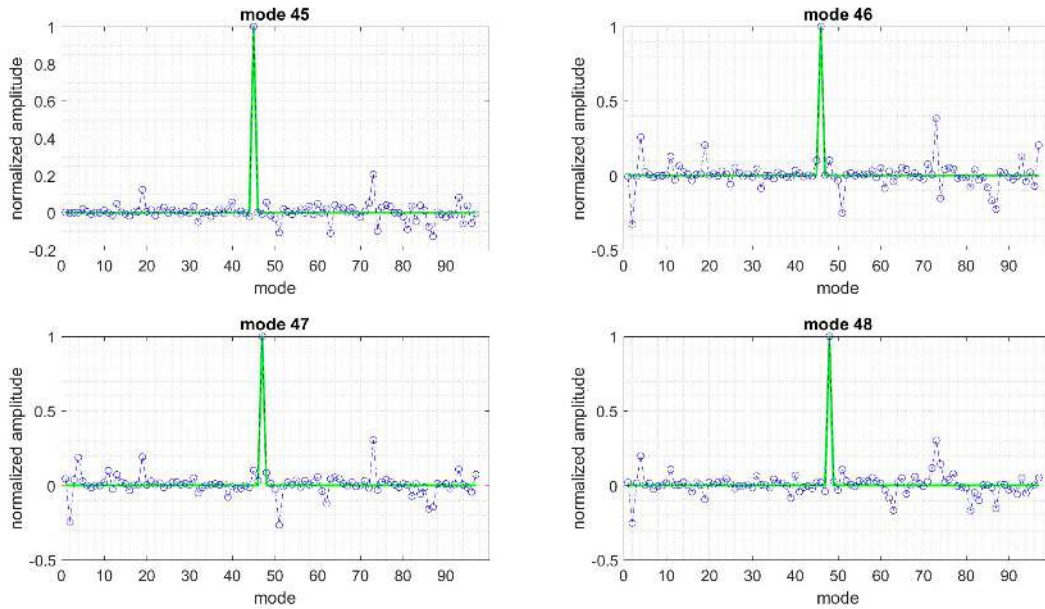
(b) Sensitivity to KL modes 5 - 8

Figure 6: LOWFS response to low-order KL modes with low spatial frequency content

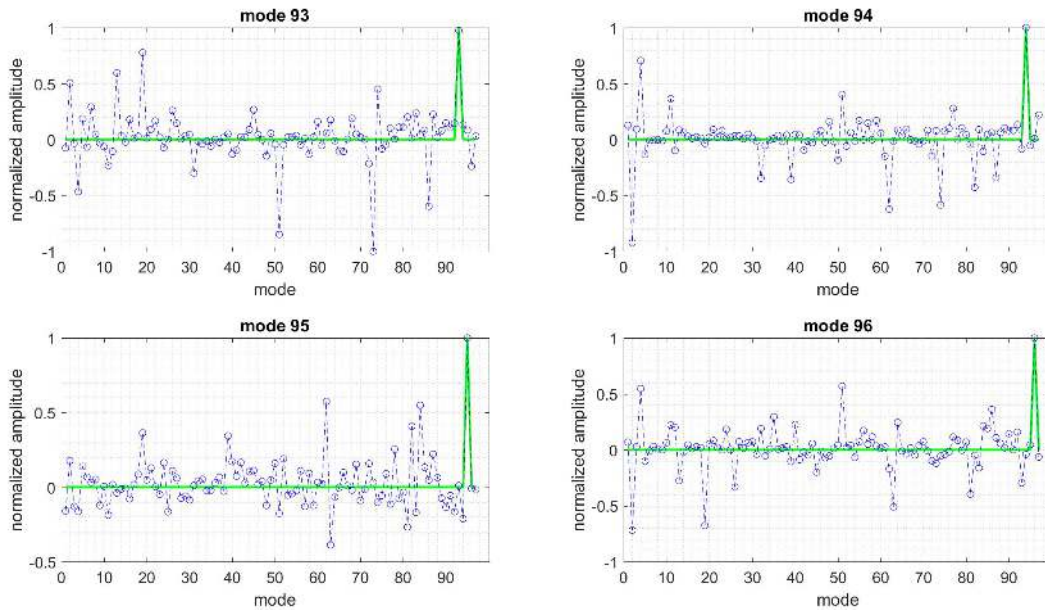


MagAO-X Preliminary Design
4.2: LO/FP WFS&C

Doc #: MagAOX-PDR-001
Date: 2017-04-22
Status: Rev. 0.0
Page: 6 of 16



(a) Sensitivity to KL modes 45 - 48



(b) Sensitivity to KL modes 93 - 96

Figure 7: LOWFS response to mid- and high-order KL modes with mid and high spatial frequency content



1.4.2 Sensing and correcting a combination of KL modes: LOWFS is capable of correcting low-order aberrations within spatial frequency bands to which the technique is sensitive. One demonstration of this ability is shown below. The MagAO-X PSF was aberrated by a random combination of 10 of the 97 KL modes injected into the pupil and then corrected by LOWFS using the full 97 KL mode command matrix. In Figure 8, this 10 KL mode aberration is shown to the left. The LOWFS response to cancel this aberration is applied to the model ALPAO DM in the center image, and the residual wavefront error after the LOWFS correction is shown to the right.

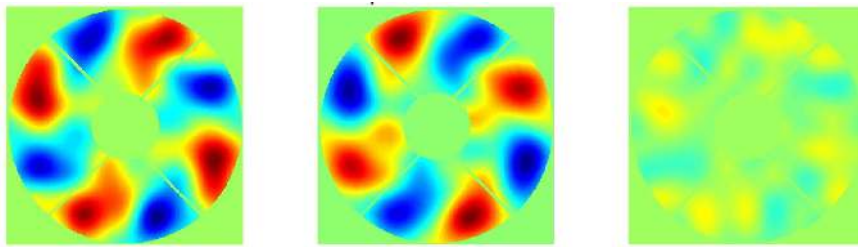


Figure 8: Injected 10 KL mode aberration (left). Applied LOWFS correction (center). Residual phase error after LOWFS (right).

The results from this test are visualized in Figure 9 by showing the LOWFS PSFs and the PSFs seen at the science detector. In the top row, the $0.1 \mu\text{m}$ defocused LOWFS PSF used for sensing the aberration in the pupil is shown. The PSF to the left is aberrated by the random 10 KL mode phase aberration injected into the pupil shown in the left panel of Figure 8. The PSF to the right is the final LOWFS-corrected PSF after the DM has compensated the injected aberration by applying the shape seen in the center panel of Figure 8. In the bottom row, the aberrated PSF at the science detector is shown to the left, and the LOWFS-corrected science PSF is shown to the right. The center PSF in the top and bottom rows of Figure 9 are the differences between the corrected and aberrated LOWFS and science PSFs respectively.



MagAO-X Preliminary Design

4.2: LO/FP WFS&C

Doc #: MagAOX-PDR-001
Date: 2017-04-22
Status: Rev. 0.0
Page: 8 of 16

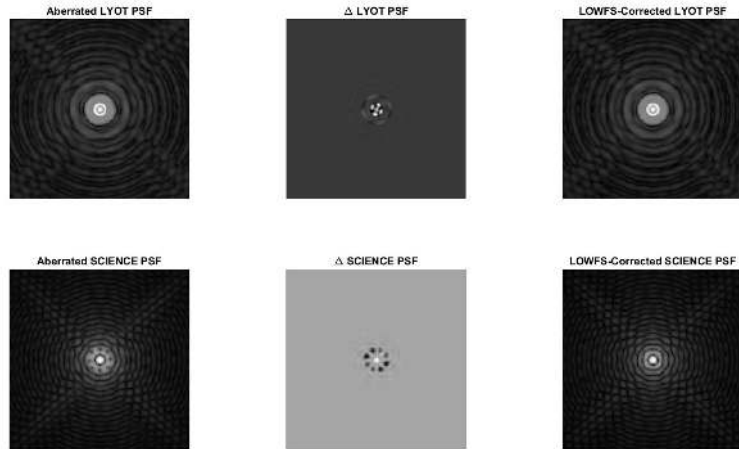


Figure 9: Correction of 10 applied random KL modes using full 97 mode response matrix. Shows the aberrated and corrected LOWFS PSF (top row), and the the aberrated and corrected science PSF (bottom row)

Figure 8 shows the normalized amplitudes of the 10 KL modes in the injected aberration (in green) and the normalized amplitudes of all 97 KL modes in the LOWFS response to this aberration.

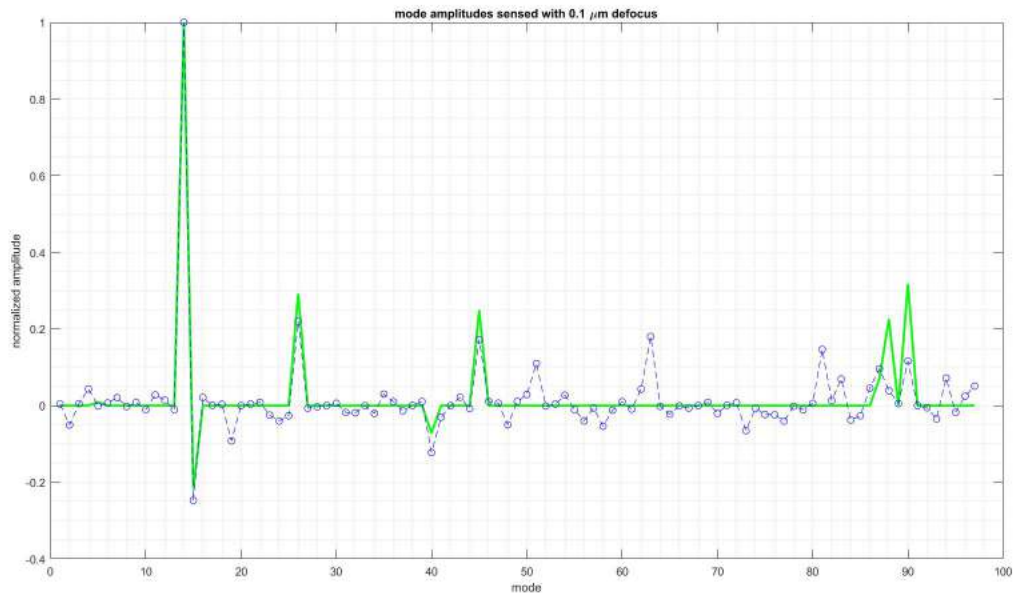


Figure 10: The amplitudes of the 10 applied random KL modes (green) and the amplitude of each mode in the LOWFS response (blue).



1.4.3 Sensing and correcting random Kolmogorov phase: In Section 5.1 Optics Specifications, subsection 5.3 Spec comparison, the PSDs for all of the optics in the LOWFS arm of MagAO-X were summed to determine the total power that will be added by the optical surfaces of these noncommon path (NCP) optics. This added power must be actively sensed and corrected by the LOWFS system. To ensure that the correction of this added power due to static and noncommon path (NCP) does not saturate the ALPAO DM, the stroke required to impose these corrections was analyzed (see Section 5.1 Optics Specifications, subsection 5.4 DM stroke). For the highest precision optics with a surface quality of $\lambda/200$, the RMS surface error that must be sensed and corrected by the LOWFS system is 9.6 nm. To prove that the MagAO-X LOWFS system is capable of removing this power, a modified Kolmogorov phase screen with a $\frac{\beta}{k^\alpha}$ PSD was simulated in the system pupil plane to model the combined NCP optics PSD. (In this PSD, k is the spatial frequency, β is a normalization constant, and α is the PSD index.) To model the optical surface PSD, α was chosen to be 2, and the surface precision of the phase screen was set to be 9.6 nm RMS. Using this model, it was then shown that, in the presence of photon noise, the MagAO-X LOWFS system will be capable of sensing and correcting this 9.6 nm RMS optical surface error for multiple stellar magnitudes.

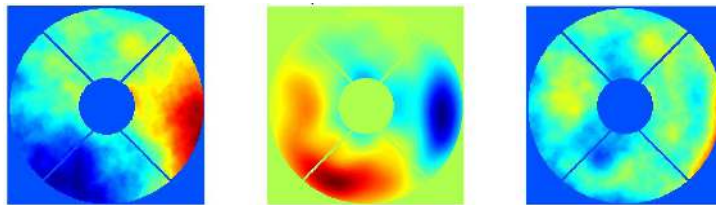
The LOWFS response and correction of the 9.6 nm RMS optical surface error was run for stellar magnitudes 0, 5, 8, 10, and 12 and the frequency at which the LOWFS loop must run to obtain this correction for each stellar magnitude. The LOWFS response matrix was built using the first 20 KL modes. Results from these tests are shown below.



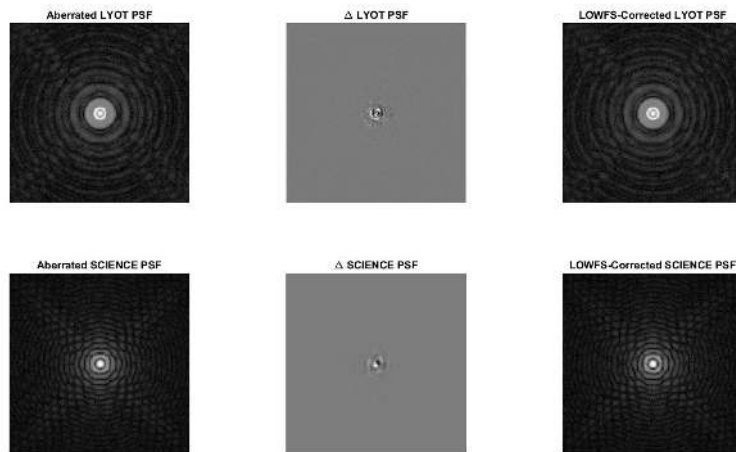
MagAO-X Preliminary Design

4.2: LO/FP WFS&C

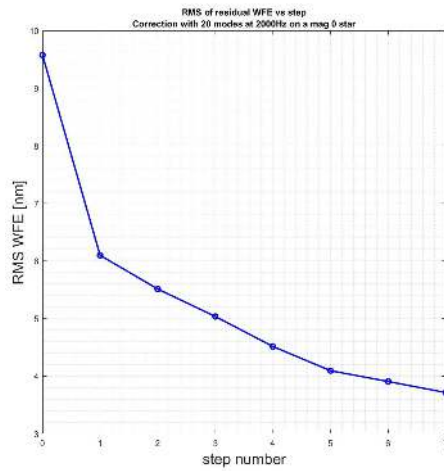
Doc #: MagAOX-PDR-001
Date: 2017-04-22
Status: Rev. 0.0
Page: 10 of 16



(a) (Left) 9.6 nm RMS optical surface (Center) LOWFS correction applied on ALPAO DM (Right) Residual error after LOWFS correction



(b) (Top row) LOWFS PSF before and after correction. (Bottom row) Science PSF before and after correction.



(c) Residual RMS error after LOWFS correction step in nm.

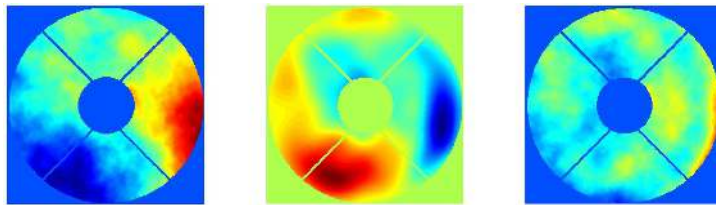
Figure 11: LOWFS correction running at 2 kHz on a 0 magnitude star. Residual error is less than 3.8 nm RMS.



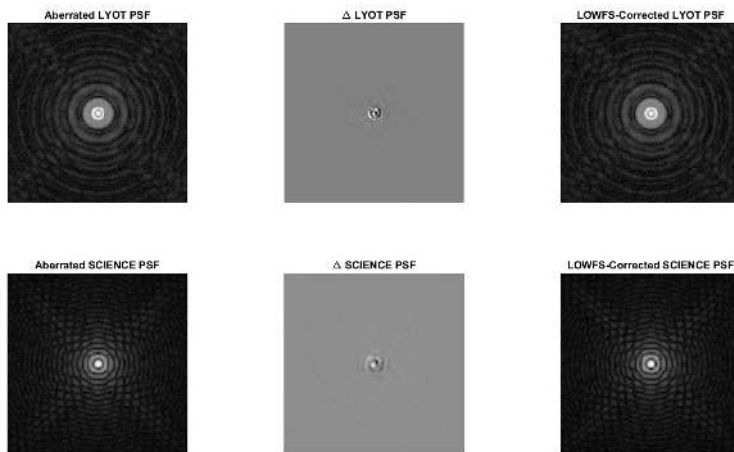
MagAO-X Preliminary Design

4.2: LO/FP WFS&C

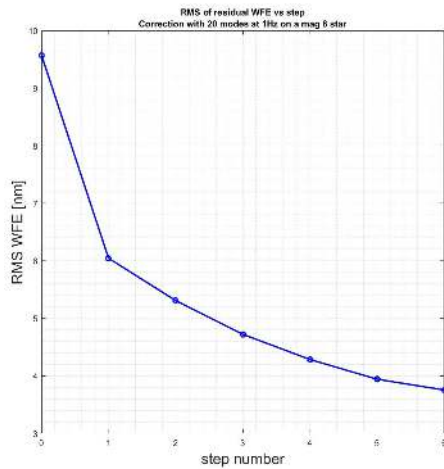
Doc #: MagAOX-PDR-001
Date: 2017-04-22
Status: Rev. 0.0
Page: 11 of 16



(a) (Left) 9.6 nm RMS optical surface (Center) LOWFS correction applied on ALPAO DM (Right) Residual error after LOWFS correction



(b) (Top row) LOWFS PSF before and after correction. (Bottom row) Science PSF before and after correction.



(c) Residual RMS error after LOWFS correction step in nm.

Figure 12: LOWFS correction running at 1 Hz on an 8 magnitude star. Residual error is less than 3.8 nm RMS.



Figure 13 shows the maximum frequency at which the LOWFS loop can be run for stellar magnitudes 0, 5, 8, 10, and 12 while correcting the 9.6 nm RMS surface error.

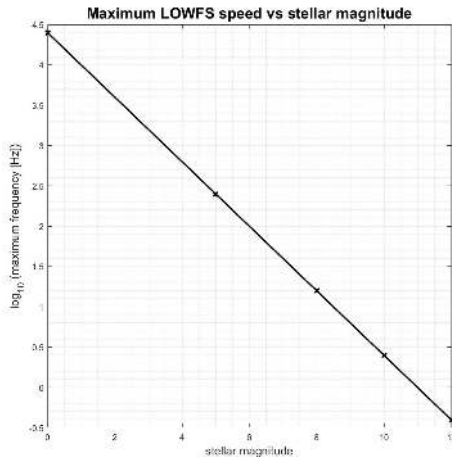


Figure 13: Stellar magnitude vs the \log_{10} scale maximum LOWFS frequency for sensing and correcting 9.6 nm RMS surface error

This plot shows that, for a magnitude 0 star, the maximum frequency at which LOWFS can be run is 25 kHz. For a magnitude 12 start this decreases to 0.4 Hz. For all five stellar magnitudes, LOWFS is capable of sensing and correcting the required 9.6 nm RMS error induced by the NCP optics surface PSD.

1.5 Sensing and correcting quadrant piston error: A common problem that has been seen on-sky by multiple observatories is phase-wrapping error that appears as a piston term in wavefront sensor correction. This piston term appears across entire sectors within the entrance pupil that are defined by the projection of the support structures known as 'spiders' in the pupil plane. This piston error is not sensed by the wavefront sensor and causes the correction to walk-off. MagAO-X intends to sense and correct this error using LOWFS. In the section below, a 50 nm piston error was induced in each of the four MagAO pupil quadrants. LOWFS was then used to sense this piston and suppress it. The injected piston and LOWFS response in each quadrant can be seen in Figure 14.



MagAO-X Preliminary Design

4.2: LO/FP WFS&C

Doc #: MagAOX-PDR-001
Date: 2017-04-22
Status: Rev. 0.0
Page: 13 of 16

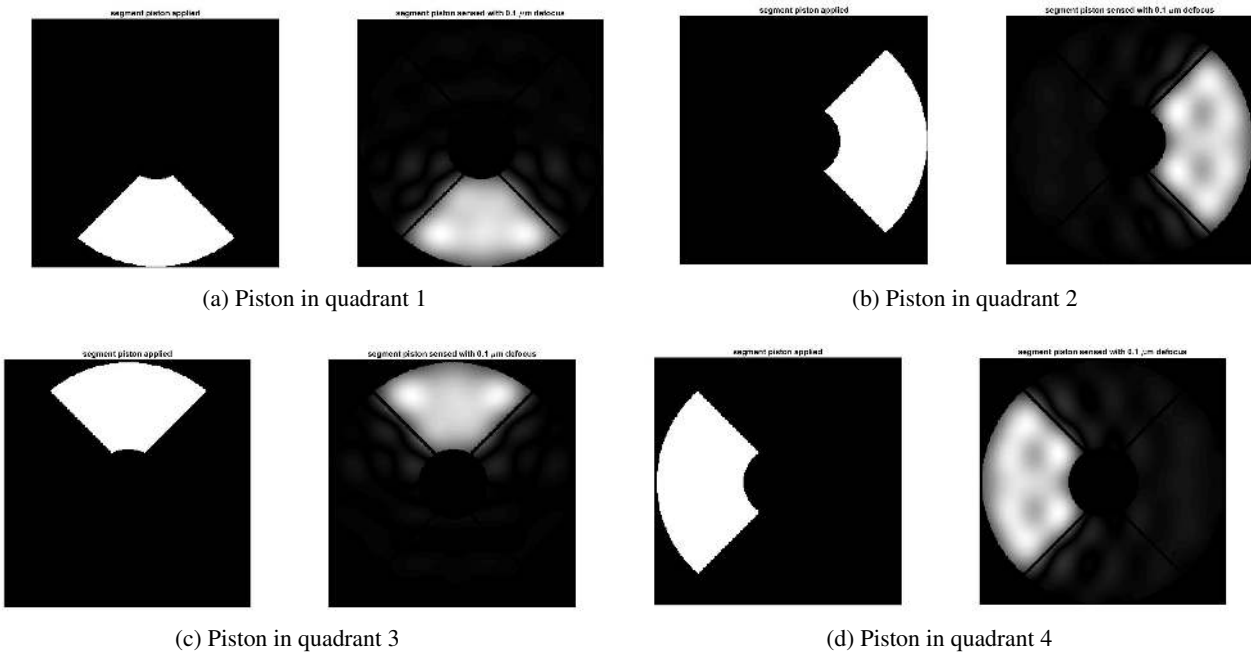


Figure 14: The applied piston error in each quadrant (left images) and the resulting piston error sensed by LOWFS (right images)

The normalized amplitude of the applied piston (in green) and the normalized amplitude of the LOWFS response to the injected piston (in blue) are shown in Figure 15.

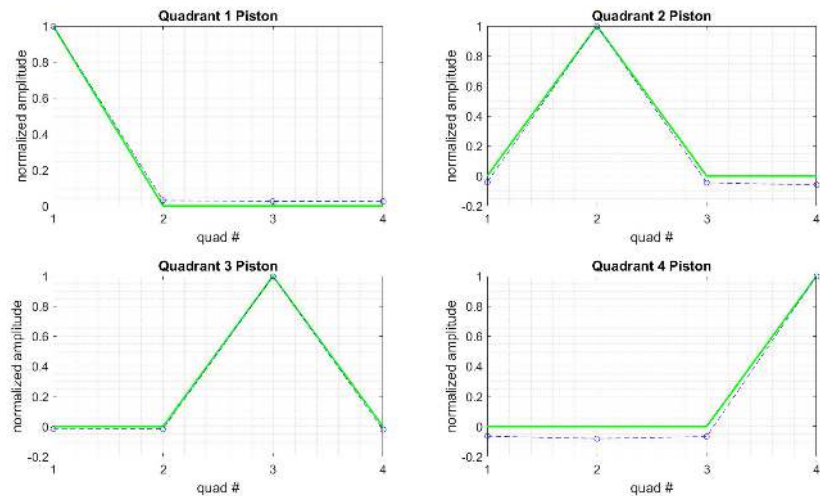


Figure 15: The applied piston error in each quadrant (green) and the piston error sensed by LOWFS (blue) for each of the four quadrants



For quadrant 4, the effect of the piston error on the LOWFS PSF (top row) and science PSF (bottom row) can be seen in Figure 16. The images to the left show the aberration induced in the LOWFS and science PSFs by the piston error, and the right images show the resulting LOWFS corrections.

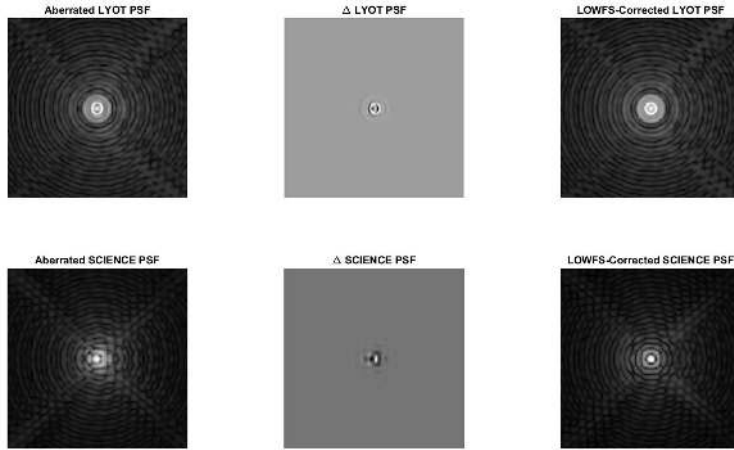


Figure 16: Correction of piston in quadrant 4. Shows the aberrated and corrected LOWFS PSF (top row), and the the aberrated and corrected science PSF (bottom row)

These results are a promising indicator that MagAO-X will be capable of sensing and canceling this known piston error using LOWFS.

2 Focal Plane Wavefront Sensing (FPWFS)

2.1 FPWFS theory: To directly image exoplanets, high-precision wavefront control is required. This required precision cannot be obtained by wavefront sensor systems like LOWFS that branch off from the main science beam since, in doing so, they introduce optics to the seen by the wavefront sensor that are not seen by the science detector. The resulting differences between the wavefront sensor (WFS) and science detector caused by these optics in the separate wavefront sensor arm are known as non-common path (NCP) errors. NCP errors limit the ability of the wavefront sensor to achieve the wavefront control precision required for techniques such as electric field conjugation (EFC) that are essential for exoplanet direct imaging.(3)

Focal plane wavefront sensing (FPWFS) is capable of achieving the necessary high precision by using the science detector as the WFS, thereby avoiding NCP errors. The FPWFS control loop consists of the science camera/WFS and the deformable mirror (DM) which modulates the field at the science camera.

2.2 FPWFS for direct exoplanet imaging: The MagAO-X instrument will feature a Boston Micromachine 2K DM as its main wavefront corrector. This DM will allow for FPWFS with access to high spatial frequencies. With this DM, MagAO-X will be capable of creating regions of deep contrast (a dark hole) within which an orbiting



MagAO-X Preliminary Design
4.2: LO/FP WFS&C

Doc #: MagAOX-PDR-001
Date: 2017-04-22
Status: Rev. 0.0
Page: 15 of 16

exoplanet can be directly imaged.

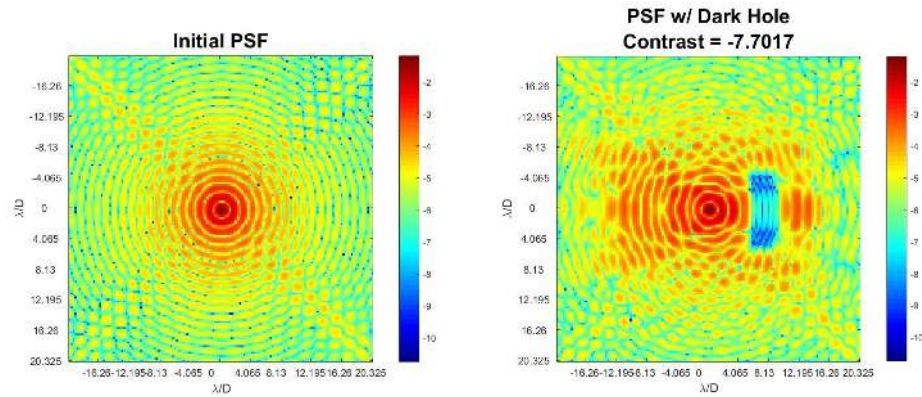


Figure 17: Dark hole with $10^{-7.7}$ contrast that has been created within the stellar PSF using EFC.



**MagAO-X Preliminary Design
4.2: LO/FP WFS&C**

Doc #: MagAOX-PDR-001
Date: 2017-04-22
Status: Rev. 0.0
Page: 16 of 16

References

- [1] G. Singh, J. Lozi, O. Guyon, P. Baudoz, N. Jovanovic, F. Martinache, T. Kudo, E. Serabyn, and J. Kuhn, “On-sky demonstration of low-order wavefront sensing and control with focal plane phase mask coronagraphs,” *Publications of the Astronomical Society of the Pacific* **127**(955), p. 857, 2015.
- [2] ALPAO, “Deformable mirrors,” tech. rep., 2017.
- [3] T. D. Groff, A. J. Eldorado Riggs, B. Kern, and N. Jeremy Kasdin, “Methods and limitations of focal plane sensing, estimation, and control in high-contrast imaging,” *Journal of Astronomical Telescopes, Instruments, and Systems* **2**(1), p. 011009, 2015.



5.1 Optics Specifications

Jared R. Males

1 Introduction

This document describes the specifications for the optical components of MagAO-X, including surface quality and coatings. We include our knowledge of the existing telescope optics, and the expected performance of the wavefront control systems.

In this analysis we assume polished optics follow a von Kàrmàn-like PSD of the following form

$$\mathcal{P}(\vec{k}) = \frac{\beta}{\left((1/L_0)^2 + |\vec{k}|^2\right)^{\alpha/2}} e^{-(|\vec{k}|l_0)^2} + \beta_{sr}. \quad (1)$$

where \vec{k} is the spatial frequency, β is a normalization constant, α is the PSD index, L_0 is an outer scale (low frequency flattening), and l_0 is the inner scale (high frequency roll-off), and β_{sr} is the surface roughness (the floor reached at high spatial frequency). See Appendix A for a detailed justification of this model using representative PSDs, as well as the methods we use to project the PSDs of various optics onto the primary mirror.

The wavefront error (WFE) analysis presented here does not take into account diffraction, rather our goal is to quickly compare trades in the various possible specifications. See the Fresnel model of the system for a diffraction-based analysis.

2 Requirements

This analysis is concerned primarily with the static and non-common path (NCP) wavefront errors (WFEs). These sources of WFE affect the Strehl ratio and the contrast. The requirements on the optical surface quality are derived from the high-level science requirements, in conjunction with the performance simulations and error budget. They are

- Requirement: Static/NCP WFE < 45 nm rms. At H α this multiplies Strehl ratio by 0.83. This specification ensures that the bright star Strehl ratio requirement of 70% can be met.
- Goal: Static/NCP WFE < 35 nm rms. Strehl ratio (S) due to static/NCP impacts exposure time as $t \propto S^3$. Hence we should seek maximum possible performance.
- Requirement: Static/NCP WFE contribution to contrast should be $< 1 \times 10^{-3}$ from 0 to 24 λ/D . This is after the effects of low-order WFS (LOWFS) and/or focal-plane WFS (FPWFS) are taken into account.

All of these requirements are derived for the science channel. The WFS channel requirement is simply that it should not be worse, as it has fewer optics.



3 The Clay Telescope

MagAO-X is designed for the 6.5 m Magellan Clay telescope. Here we present analysis of the primary mirror (M1), the f/11 fixed secondary (M2), and the tertiary mirror (M3).

3.1 M1: The Magellan Clay primary mirror was cast and polished at the Steward Observatory Mirror Lab (SOML). The post-polishing test data were analyzed (see Appendix B). The surface map is shown in Figure 1. The surface height has 12.52 nm rms across all spatial frequencies sampled by the map. Figure 2 shows the surface map with 29% central obscuration (defined by the secondary baffle) and with the outer edge masked by 4.4% to mask the jagged edge. This also has a 12.52 nm rms, only negligibly reduced from the unmasked map.

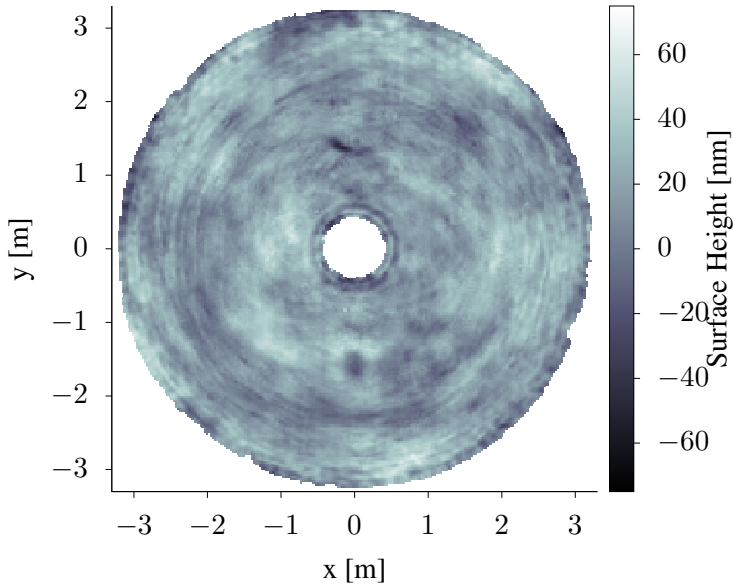


Figure 1: M1 surface unmasked

Using the un-masked surface map we calculated the 2D PSD of the masked surface. An annular Hann window was applied before the FFT, and the resultant PSD was renormalized to have total variance corresponding to 12.52 nm rms. Figure 3 shows the median radial profile of the PSD. The best fit (in log space) has slope $\alpha = -2.8$, a very steep power law.

See Appendix B for additional analysis of the M1 surface.

3.2 Pupil Definition : The Magellan Clay telescope secondary mirror baffle forms a 29% central obscuration. The secondary is supported by 4 supports, called vane ends at Magellan, a.k.a. spiders. Using a 3D model of the telescope (provided by Charlie Hull), we found the spiders to be offset by 0.34 m from the center, and running at 45°. The vane end struts are nominally 0.75" wide. On two of them the MagAO cable-trays, used to route power and cooling to the ASM, increase the width to 1.5". These are thin relative to other observatories (e.g. Subaru is reported to have 20 cm wide spiders).

For analysis and simulations pupil masks were made informed by the above specifications. Two masks were

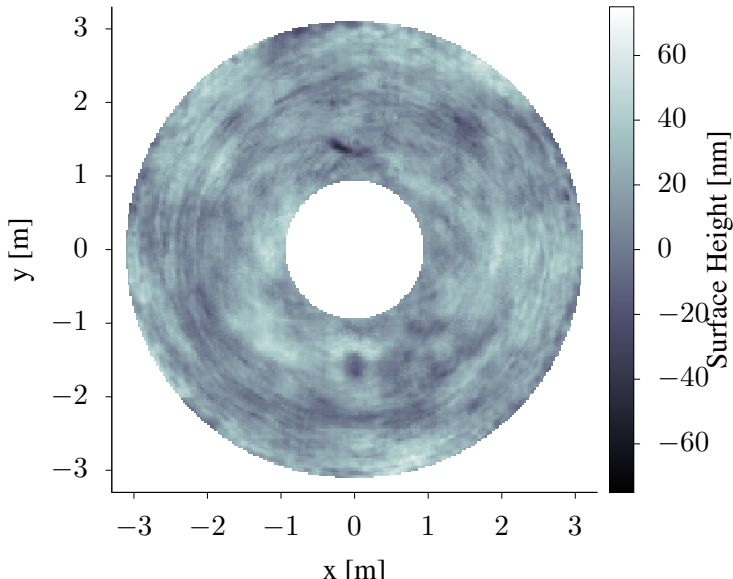


Figure 2: M1 surface masked with a 95.6% outer radius and 29% central obscuration.

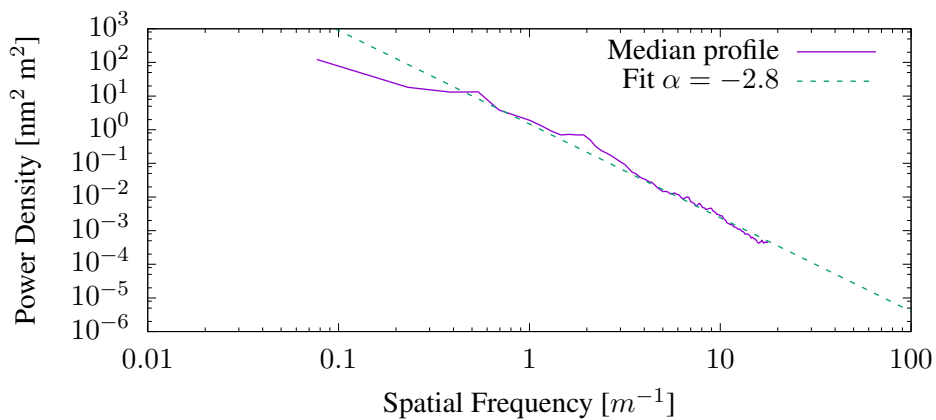


Figure 3: Median radial profile of the PSD of M1 surface.

made:

1. Input Pupil. This is 6.5m wide, with a 29% central obscuration. Grayscale is used for the spiders to account for their width relative to the pixel scale in the mask (calculated by re-binning larger arrays). This is used as the input for end-to-end simulations, etc.



2. Coronagraph Pupil. This mask is intended for use in the coronagraph arm. The goal of this mask is to oversize the various features (undersize the pupil overall) to ensure that coronagraph designs are feasible and alignment tolerances can be met. The outer diameter is undersized to 95.6% (6.21 m projected) to mask out the rough outer edge identified above. The central obscuration is oversized to 31% of the undersized diameter, which corresponds to 1/2 an actuator projected onto the high-order (MEMS) DM. The spider masks are binary and oversize to 68 mm. For scale, this corresponds to a 0.3° tolerance in the pupil rotation alignment.

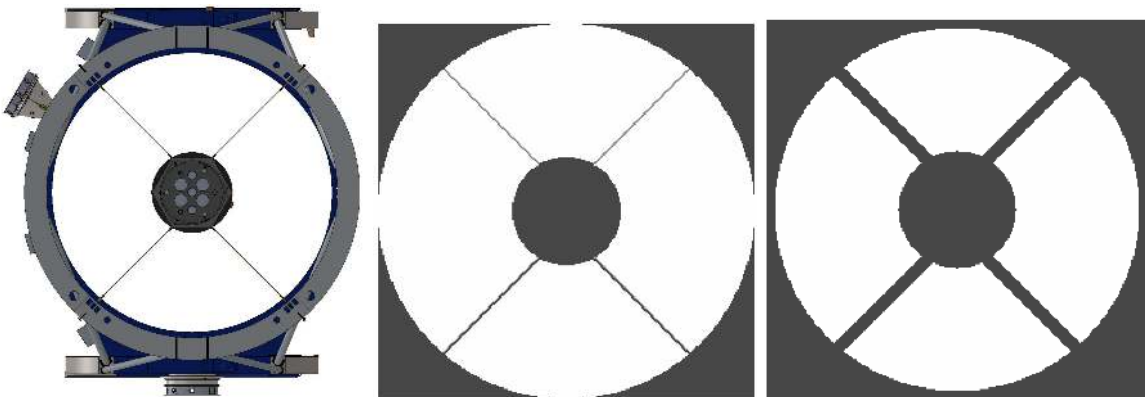


Figure 4: Defining the MagAO-X pupil. Left: solid model of the telescope showing. Middle: input pupil mask. Right: coronagraph channel mask.

3.3 M2: A post-fabrication measurement of the surface structure function of the Clay f/11 static secondary is shown in Figure 5. We fit this to a power law with index $\alpha - 2$, where α is the index of the spatial PSD as in Equation (1) (Noll, 1976). The measurements indicate that the surface of M2 has 12.7 nm rms.

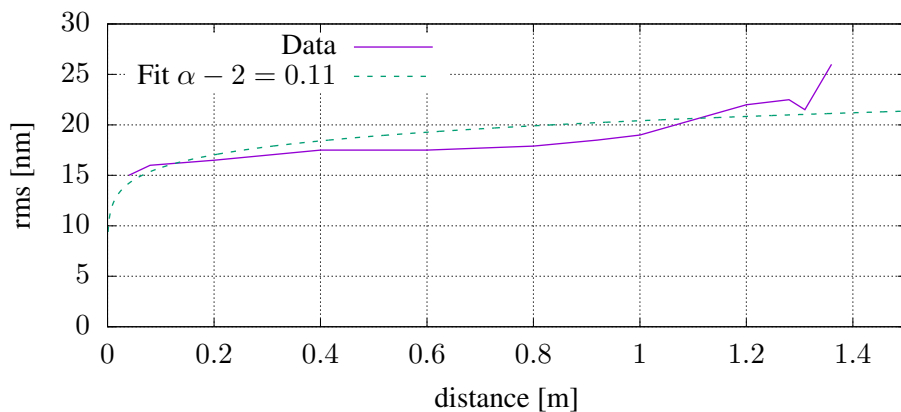


Figure 5: Measured structure function of the static f/11 (M2) and our power-law fit.



3.4 M3: From the manufacturer's test report for the (now re-coated) tertiary mirror, we have the surface map shown in Figure 6. We analyzed this map using the same procedure as for M1, and found the PSD shown in Figure 7. M3 has a reported surface finish of 13.8 nm rms, with a best fit PSD having $\alpha = 3.28$.

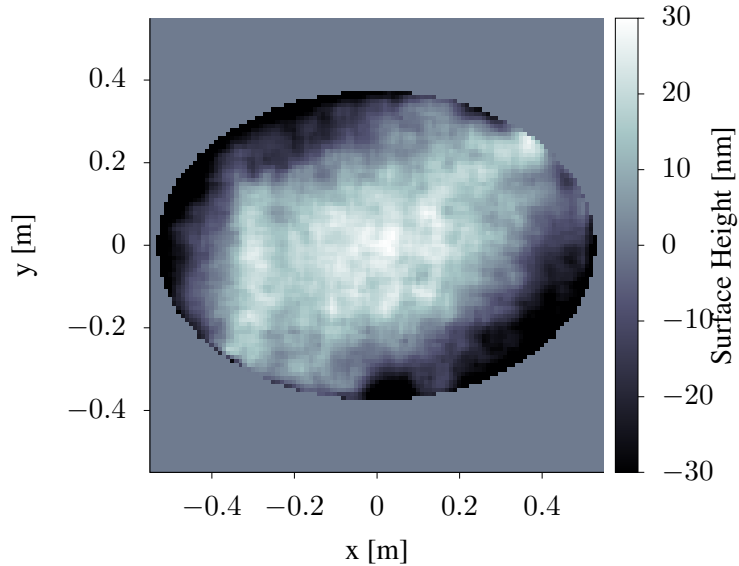


Figure 6: M3 surface.

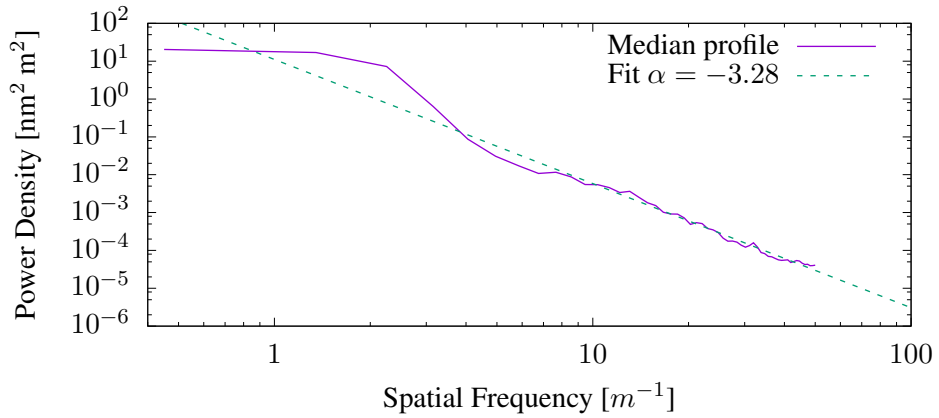


Figure 7: M3 PSD from a circular aperture.



4 Deformable Mirrors

Here we describe the specifications of the deformable mirrors we will use for wavefront correction. For this analysis, in all cases we assume that the flat surface quality is perfect within the device's spatial control bandwidth, so the given surface quality is for the remaining higher spatial frequencies. We assume a PSD with $\alpha = 2$ for these surfaces.

4.1 High Order DM: The high order DM, or tweeter, is a Boston Micromachines Corp. MEMS 2k. This is a 2048 actuator device, with 50 actuators across a circular aperture. BMC has guaranteed a 100% yield device within the clear aperture described by pupil (allowing for a limited number of bad actuators under a spider). The main optical characteristics are summarized in Table 1.

The nominal device we have specified is a $1.5 \mu\text{m}$ P-V stroke DM. BMC has begun working to determine if they have a $3.5 \mu\text{m}$ stroke 2k DM already fabricated which meets our yield needs. If they do, we have the option of taking this device. In this case, all other specifications (other than stroke) remain the same. Actuator stroke requirements are addressed in the simulation section.

Table 1: Boston Micromachines 2k Specifications.

	Total Act.	Linear Act.	Pitch [mm]	CA mm	Flat surface Max Spec	[nm rms] Typical
Value:	2048	50	0.4	19.7	20	13

4.2 Low Order DM: We plan to use the Alpao DM97-15 for our low order DMs. We have designed in two of these. The first serves as the woofer to minimize the stroke requirements on the BMC 2k tweeter. The second will be used in the science channel (after the HOWFS beamsplitter), under control by the LOWFS. This allows for correction of non-common path errors sensed by the LOWFS.

The main optical characteristics are summarized in Table 2.

Table 2: Alpao DM97-15 Specifications.

	Total Act.	Linear Act.	Pitch [mm]	CA mm	Flat surface Max Spec	[nm rms] Typical
Value:	97	11	1.5	13.5	7	4

5 WFE of the MagAO-X Design

Now we proceed to analyze the specifications needed in the remaining optics of the system.

5.1 Available Optics: Quotations from two vendors have been obtained for off-axis parabolas. Their parameters are summarized in Table 3. We have not yet obtained detailed quotes for flats, but flats of high quality are readily available from various vendors so we use specifications typical for such optics.

5.2 Optical Design: The detailed opto-mechanical design is presented in section 2.1. Tables 4 and 5 list the optical surfaces in the MagAO-X design which are considered here.



MagAO-X Preliminary Design

5.1 Optics Specifications

Doc #: MagAOX-001
 Date: 2017-04-19
 Status: Rev. 0.0
 Page: 7 of 18

Table 3: Possible optic specifications

Type	Manufacturer & Description	D_{CA} [mm]	Specified				PSD		Notes
			λ_t [nm]	PV [nm rms]	σ [nm rms]	d [mm]	α	β^4 [nm ²]	
OAP	Vend. 1 Standard	40.0 ¹	—	—	63.3	5.0	1.55	94.98	Spec'd in refl. WFE
OAP	Vend. 1 Precision	40.0 ¹	—	—	31.7	0.5	1.55	5.23	Spec'd in refl. WFE
OAP	Vend. 1 High Prec.	40.0 ¹	—	—	12.7	0.5	1.55	0.84	Spec'd in refl. WFE
OAP	Vend. 2 $\lambda/8$	41.1 ²	633	79.1	—	—	1.55	85.46	Spec'd in surf. error
OAP	Vend. 2 $\lambda/20$	43.4 ²	633	31.7	—	—	1.55	13.97	Spec'd in surf. error
FLAT ³	$\lambda/20$	50.8	—	31.7	—	—	2.0	63.63	Spec'd in surf. error
FLAT ³	$\lambda/50$	50.8	—	12.7	—	—	2.0	10.18	Spec'd in surf. error
FLAT ³	$\lambda/100$	50.8	—	6.33	—	—	2.0	2.55	Spec'd in surf. error
FLAT ³	$\lambda/200$	50.8	—	3.16	—	—	2.0	2.55	Spec'd in surf. error

¹ CA for Vendor 1 could be 35-40 mm for the 50 mm OAPs.

² CA varies in Vendor 2 quote.

³ Quotes for flats not yet obtained.

⁴ β specified for reflected wavefront error.

Table 4: MagAO-X Optical Surfaces – Common Path.

No.	Type	Name	D_{beam}	θ_i	Coating	Notes
Common Path						
1	Primary	M-1	6.5	0.0	Al	
2	F/11	M-2	1.36	0.0	Al	
3	Tertiary	M-3	1.1	45.0	Custom	
4	Flat	F-1	2.9	45.0	P-Ag	
5	Flat	F-2	2.9	45.0	P-Ag	
6	OAP	O-0	13.7	32.5	P-Ag	
7	Flat	K-1	13.4	60.0	P-Ag	
8	Flat	K-2	13.2	30.0	P-Ag	
9	Flat	K-3	13.5	60.0	P-Ag	
10	Woofer	LODM	13.5	15.0	P-Ag	Alpao DM-97
11	OAP	O-1	14.1	26.5	P-Ag	
12	Flat	F-3	13.0	17.5	P-Ag	
13	OAP	O-2	20.41	10.0	P-Ag	
14	Tweeter	HODM	19.41	8.4	UnP-Au	BMC 2K
15	OAP	O-3	22.97	7.5	P-Ag	
16	Flat	F-4	20.0	45.0	P-Ag	Down to lower level
17	Flat	F-5	6.4	45.0	P-Ag	From upper level
18	OAP	O-4	12.56	7.5	P-Ag	
20	Flat	F-6	10.8	48.5	P-Ag	Possible DM
21	ADC	ADC-1			AR	
22	ADC	ADC-2			AR	
23	ADC	ADC-3			AR	
24	ADC	ADC-4			AR	



MagAO-X Preliminary Design

5.1 Optics Specifications

Doc #: MagAOX-001
Date: 2017-04-19
Status: Rev. 0.0
Page: 8 of 18

Table 5: MagAO-X Optical Surfaces – Non-Common Path.

WFS						
W-25	Beamsplitter	BS-1-T	—			Transmission to WFS
W-26	Flat	TTM	9.0	42.0	P-Ag	PYWFS Modulator
W-27	OAP	O-5	13.31	7.5	P-Ag	Same optic as C-28, different footprint
W-28	Flat	F7	10.7	30.0	P-Ag	
W-29	Pyramid	PYR-1	—			
W-30	Pyramid	PYR-2	—			
W-31	Pyramid	PYR-3	—			
W-32	Pyramid	PYR-4	—			
W-33	Zoom lens	PZL-1	—		AR	For pupil magnification and positioning.
W-34	Zoom lens	PZL-2	—		—	For pupil magnification and positioning.
W-35	Zoom lens	PZL-3	—		—	For pupil magnification and positioning.
W-36	Zoom lens	PZL-4	—		AR	For pupil magnification and positioning.
Coronagraph						
C-25	Beamsplitter	BS-1-R	10.3	42.0	—	Reflection
C-26	Flat	F-8	9.3	42.0	P-Ag	
C-27	Flat	F-9	10.3	42.0	P-Ag	
C-28	OAP	O-5	13.31	7.5	P-Ag	Same optic as W-27, different footprint
C-29	Fold	F-10	7.2	7.5	P-Ag	
C-30	FPM	FPM	—			
C-31	OAP	O-6	13.3	7.5	P-Ag	
Coronagraph focal plane						
C-32	Lyot Stop	LS-T	—			
C-33	Fold	F-11	10.2	7.5	P-Ag	
C-34	OAP	O-7	13.3	7.5	P-Ag	
C-35	Fold	F-12	—		P-Ag	
C-36	SDI	—	—			multiple surfaces
Coronagraph Lyot plane						
L-32	Lyot Stop (flat)	LS-R	9.0			
L-33	Lens	L-L-1	9.0		AR	



5.3 Spec Comparison: PSDs for each of the optics were constructed according to the specifications in Table 3. These were added, grouped as common path (CP), non-common path (NCP) in the WFS and science channels. The CP optics had all power up to $1/(2d_{ho})$ removed, assuming that the WFS and LODM and HODM remove these aberrations. The NCP optics had all power removed up to $1/(2d_{lo})$, assuming that the LOWFS and LOWFS-DM remove this power.

The resultant rms WFE for each grouping are given in the tables below, for different combinations of the OAP and flat specifications. Here we assume $D/d_{lo} = 11$, that is ~ 97 modes are corrected by the LLOWFS using the LLOWFS-DM.

Table 6: Uncorrectable Common Path WFE (nm rms waveform)

OAPS	Flats:	No BMC				BMC 20 nm rms flat				BMC 13 nm rms flat			
		$\lambda/20$	$\lambda/50$	$\lambda/100$	$\lambda/200$	$\lambda/20$	$\lambda/50$	$\lambda/100$	$\lambda/200$	$\lambda/20$	$\lambda/50$	$\lambda/100$	$\lambda/200$
Vend. 1 Standard		229.1	218.7	217.1	216.7	231.2	220.8	219.3	218.9	230.0	219.6	218.1	217.7
Vend. 2 $\lambda/8$		219.2	208.2	206.6	206.2	221.4	210.5	208.9	208.5	220.1	209.2	207.6	207.2
Vend. 2 $\lambda/20$		113.1	90.1	86.3	85.3	117.3	95.2	91.7	90.7	114.9	92.3	88.6	87.6
Vend. 1 Precision		90.9	59.8	53.9	52.3	96.0	67.3	62.1	60.7	93.1	63.0	57.5	56.0
Vend. 1 High Prec.		79.2	39.8	30.2	27.3	85.0	50.4	43.2	41.2	81.7	44.5	36.3	33.9

Table 7: Non-Common Path WFE (nm rms waveform)

OAPS	Flats:	WFS Channel				Science Channel			
		$\lambda/20$	$\lambda/50$	$\lambda/100$	$\lambda/200$	$\lambda/20$	$\lambda/50$	$\lambda/100$	$\lambda/200$
Vend. 1 Standard		183.7	169.2	167.1	166.5	188.9	180.5	179.2	178.9
Vend. 2 $\lambda/8$		176.4	161.3	159.0	158.4	180.6	171.8	170.5	170.2
Vend. 2 $\lambda/20$		100.9	71.2	65.9	64.5	91.8	73.0	69.9	69.1
Vend. 1 Precision		86.5	48.8	40.6	38.3	72.9	47.1	42.1	40.8
Vend. 1 High Prec.		79.3	34.6	21.6	16.9	62.8	29.1	20.2	17.2

5.4 DM Stroke: To ensure that the static and NCP corrections do not saturate the DMs, we also analyzed the stroke requirement these corrections impose. These are shown in Tables 8 and 9. The BMC HOWFS has a minimum interactuator stroke of 855 nm, and the Alpa DM has a minimum interactuator stroke of 2500 nm. We conclude that DM stroke is more than sufficient to handle the static and NCP errors (dynamic stroke requirements are addressed in the simulation section).

Table 8: Stroke Used By HOWFS (nm rms).

OAPS	Flats:	Woofer				Tweeter			
		$\lambda/20$	$\lambda/50$	$\lambda/100$	$\lambda/200$	$\lambda/20$	$\lambda/50$	$\lambda/100$	$\lambda/200$
Vend. 1 Standard		177.7	154.7	151.1	150.2	185.8	171.5	169.4	168.8
Vend. 2 $\lambda/8$		172.8	149.1	145.4	144.4	178.8	163.8	161.6	161.0
Vend. 2 $\lambda/20$		127.8	93.2	87.1	85.6	108.0	80.8	76.2	75.0
Vend. 1 Precision		120.8	83.3	76.5	74.7	95.1	62.6	56.5	54.8
Vend. 1 High Prec.		117.6	78.6	71.3	69.4	88.8	52.6	45.2	43.1



Table 9: Stroke Used By LOWFS (nm rms).

OAPS	Flats:	LOWFS-DM			
		$\lambda/20$	$\lambda/50$	$\lambda/100$	$\lambda/200$
Vend. 1 Standard		103.3	90.8	88.9	88.4
Vend. 2 $\lambda/8$		99.6	86.6	84.6	84.1
Vend. 2 $\lambda/20$		63.5	40.2	35.6	34.4
Vend. 1 Precision		57.2	29.3	22.6	20.6
Vend. 1 High Prec.		54.2	22.9	13.4	9.6

6 Contrast

Finally, we consider the effect of static/NCP aberrations on the contrast. The raw PSF-profile contrast at a given separation is given by the variance of the WFE in radians in the Fourier mode corresponding to that separation. Using this fact, and the PSDs calculated for the system, we present variance vs. separation profiles in Figure 8 to characterize the contrast degradation of the optical surfaces. We included the effects of LOWFS, but not FPWFS.

We compare the static/NCP variance to the dynamic variance expected from atmospheric turbulence. This is calculated using an update version of the method in Guyon (2005). This is also shown for 5th and 10th magnitude stars.

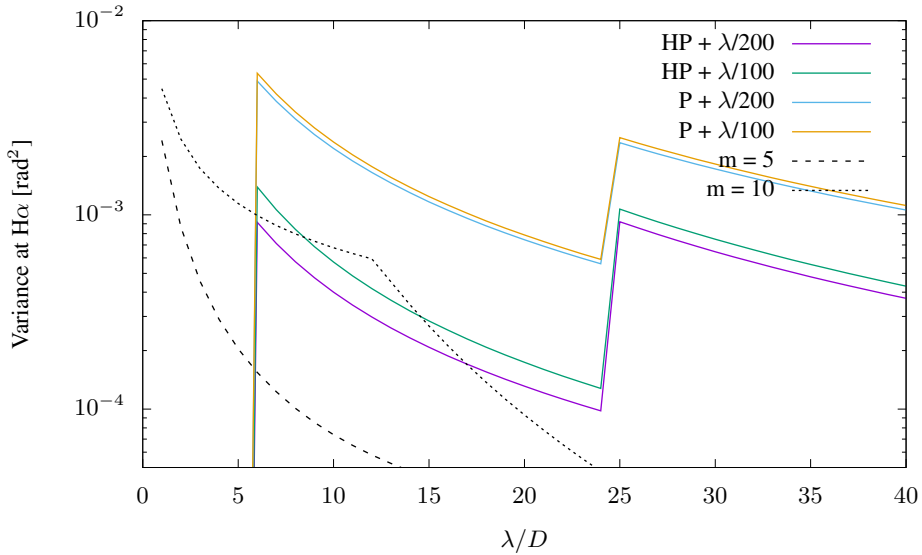


Figure 8: Variance profiles due to the optics of MagAO-X.

7 Conclusions

From this analysis we draw the following conclusions:

1. OAPs with Vendor #1's High Precision specification are required to reach the static/NCP WFE specification (45 nm rms).



2. OAPs with Vendor #1's High Precision specification are required to reach the 1×10^{-3} contrast specification.
3. The requirement on flat surface quality depends strongly on the surface quality of the BMC DM. If that is worst case 20 nm rms, then $\lambda/200$ flats are needed to meet the WFE spec. $\lambda/100$ flats are sufficient if the BMC DM is delivered with a typical 13 nm rms post-flat surface.
4. The flat specifications only weakly affect the contrast profile.
5. With the BMC DM, we are unlikely to reach the goal of 35 nm rms static/NCP WFE. This analysis shows that we can reach 38 nm rms.

We have shown that our design can meet the static/NCP WFE and contrast specifications with available optics.



A Power Spectral Densities

To understand the impact of the surface quality on both Strehl ratio and contrast, we need to know the power spectral density (PSD) of the surface. To begin with we will assume a PSD of the form

$$\mathcal{P}(\vec{k}) = \frac{\beta}{|\vec{k}|^\alpha}.$$

As we will show, this basic form is well justified in the literature. The two parameters, α and β must be determined.

A.1 PSD Normalization: The PSD can be normalized by the root-mean-square, or rms, of the departure of the optical surface from the design shape. This can be calculated as the integral of the PSD over a limited spatial-frequency band:

$$\sigma^2 = \int_{k_{min}}^{k_{max}} \frac{\beta}{|\vec{k}|^\alpha} k dk d\phi$$

This leads to the following expression for β :

$$\beta = \sigma^2 \times \begin{cases} \frac{\alpha-2}{2\pi(k_{min}^{-\alpha+2} - k_{max}^{-\alpha+2})} & \alpha \neq 2 \\ \frac{1}{2\pi \ln(\frac{k_{max}}{k_{min}})} & \alpha = 2 \end{cases} \quad (2)$$

Optical manufacturers seldom specify any of σ , k_{min} or k_{max} . In the case of one vendor, σ over a certain spatial scale, which we will refer to as l_{min} , is specified, and $k_{max} = 1/l_{min}$. Equivalently, we can specify this in terms of sampling length d , such that $l_{min} = 2d$ which gives the usual $k_{max} = 1/(2d)$.

We can safely assume that $k_{min} = 1/D_{CA}$, where D_{CA} is the diameter of the clear aperture (CA) of the optic being specified.

In cases where only a peak-to-valley (PV) figure error is specified, usually as λ_t/N where λ_t is the test wavelength, we have to make some assumptions. Depending on the low-order Zernike being considered, the ratio of PV/σ ranges from 3-6 (Evans, 2009; Schwertz, 2010). We adopt $PV/\sigma = 4$ as recommended by Schwertz (2010) as a conservative compromise which will not underestimate the WFE.

The number of Zernike modes, or equivalently the value of d , over which the PV specification is determined is almost never specified in any way. From the statements of equivalence given in Vendor 1's quote, we can infer that $D/d \approx 4-5$. We assume that the number of Zernikes (or degrees of freedom (DOF)) is $\pi/4(D/d)^2$, so this corresponds to 13–20 Zernike modes being considered in the Figure error. In Evans (2009) 36 Zernike modes are used to develop the PVr metric, corresponding to $D/d \sim 7$. A presentation by several optical engineers¹ recommends that the cutoff for Figure error be 5 – 10 cycles per aperture, or $D/d = 10 – 20$. This is quite a range. For this analysis we adopt $D/d = 7$.

So when given only the PV metric we assume $\sigma = PV/4$, and $k_{max} = 7/(2D)$.

A.2 Surface vs. Reflected WFE: When a surface specification is given, we have to convert it to the total reflected wavefront error. This means that the rms will be a factor of 2 larger due to double pass in reflection, and we must also account for angle of incidence, which makes the surface error larger for anything other than 90°. So we use

$$\sigma_{refl} = 2\sigma_{surf}/\cos(\theta_i). \quad (3)$$

Note that this is an overestimate, as only one axis of the beam is subject to the $\cos(\theta_i)$ correction.

¹http://www.savvyoptics.com/files/MSF_ripple_presentationSep_26-3.pdf



MagAO-X Preliminary Design 5.1 Optics Specifications

Doc #: MagAOX-001
 Date: 2017-04-19
 Status: Rev. 0.0
 Page: 13 of 18

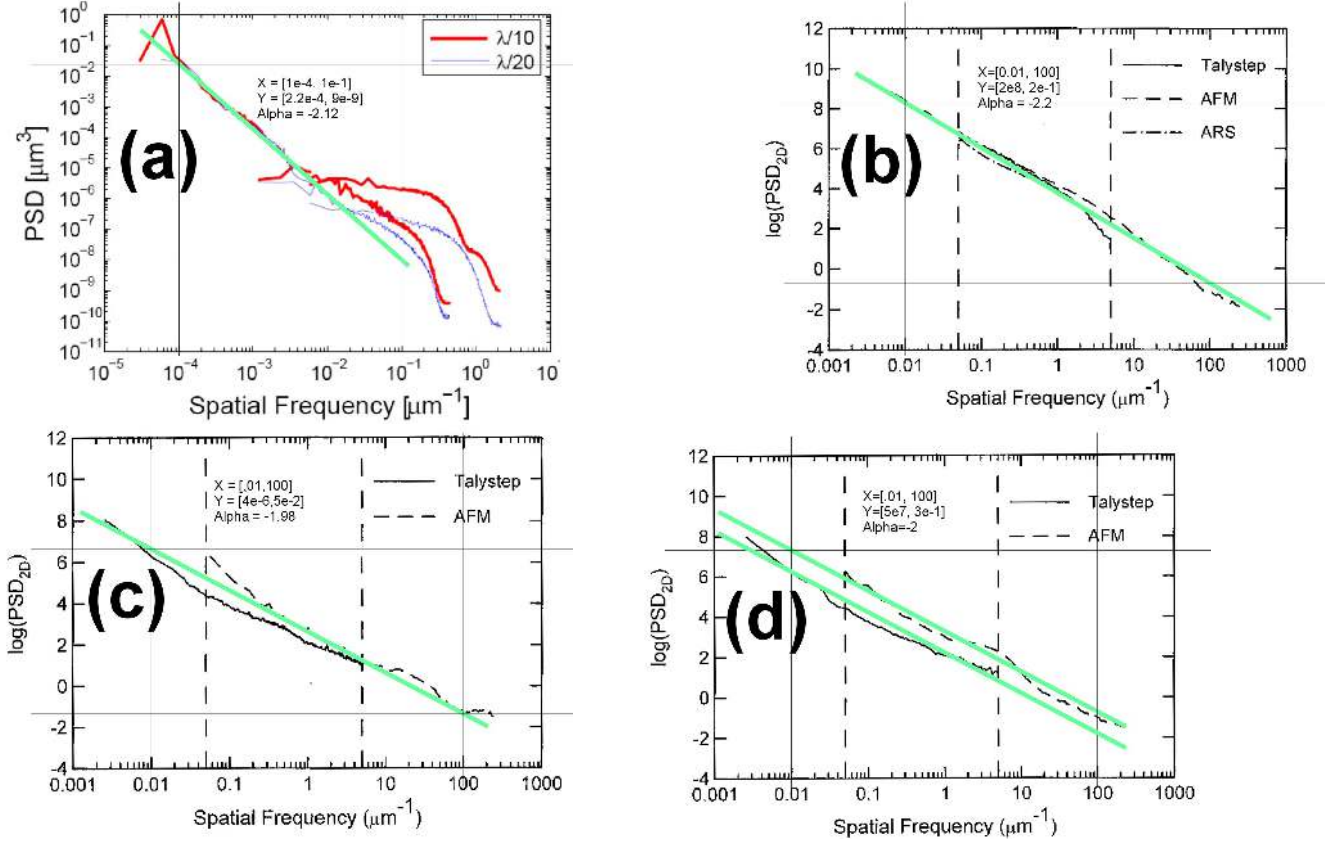


Figure 9: Measured PSDs of flats. (a) is for 25 mm Al coated BK7 with $\lambda/10$ and $\lambda/20$ P-V from Alcock et al. (2010). (b)-(d) are from Duparré et al. (2002). (b) is a polished fused-silica flat, (c) is a polished fused-silica flat, and (d) is polished Zerodur 665. Based on these results we adopt $\alpha = 2.0$ for flats.

A.3 PSD Index: The value of α for a selection of flats was determined by “fit-by-eye” to PSDs presented in Alcock et al. (2010) and Duparré et al. (2002). The fits are illustrated in Figure 9. We adopt $\alpha = 2$ based on these results.

PSDs for aspheric optics are difficult to find in the literature. The one example located so far is by Tinker & Xin (2013). Examples for 2 optics are shown in Figure 10. These results imply $\alpha \approx 1.6$ for OAPs. In a report provided by a vendor for a single optic, they found $\alpha = 1.55$ by fitting PSD data. We will use 1.55 for all OAPs.

A.4 Surface Roughness: According to ISO-10110-8, the surface roughness is specified over length scales of 85 μm to 2.5 μm . Based on the plots from Tinker & Xin (2013) shown in Figure 10 we will assume the PSD is white in this range. That is

$$\mathcal{P}_{sr} = \beta_{sr} \quad (4)$$

with β_{sr} constant. The normalization for the PSD in this range is

$$\beta_{sr} = \frac{\sigma_{sr}^2}{\pi(k_{max}^2 - k_{min}^2)} \quad (5)$$



MagAO-X Preliminary Design

5.1 Optics Specifications

Doc #: MagAOX-001
Date: 2017-04-19
Status:
Page:

Rev. 0.0
14 of 18

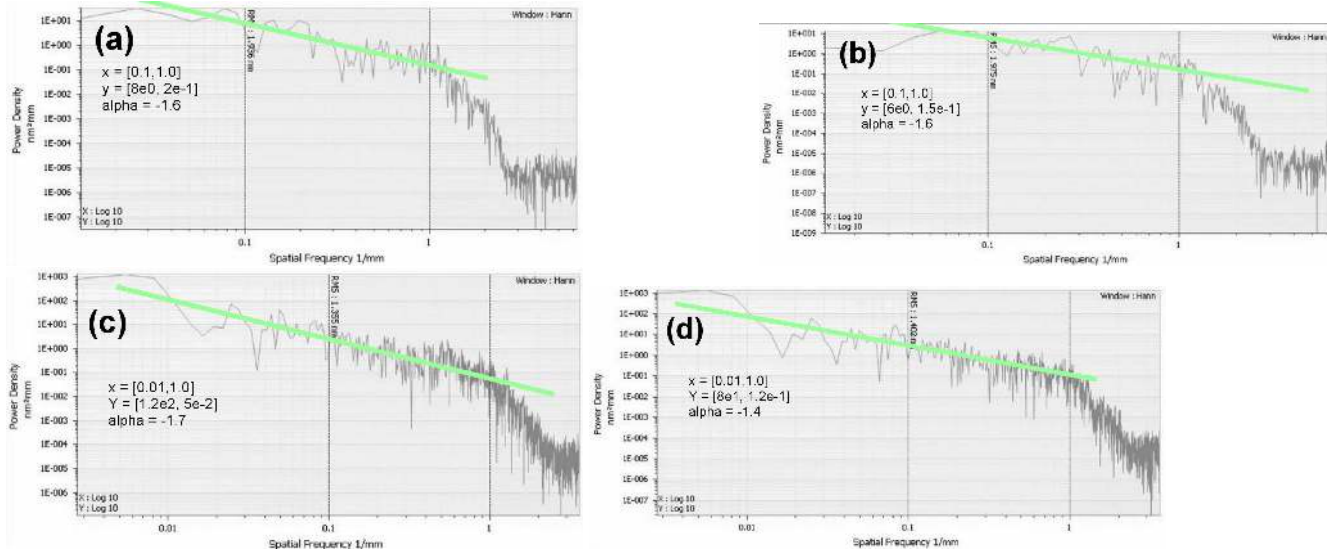


Figure 10: PSDs of manufactured SiC OAPs from Tinker & Xin (2013). (a) and (b) are cuts from the PSD of 58 mm f/1.4 OAP. (c) and (d) are cuts from a 150 mm f/1.7 OAP. The green lines show a rough “fit-by-eye” to the data.

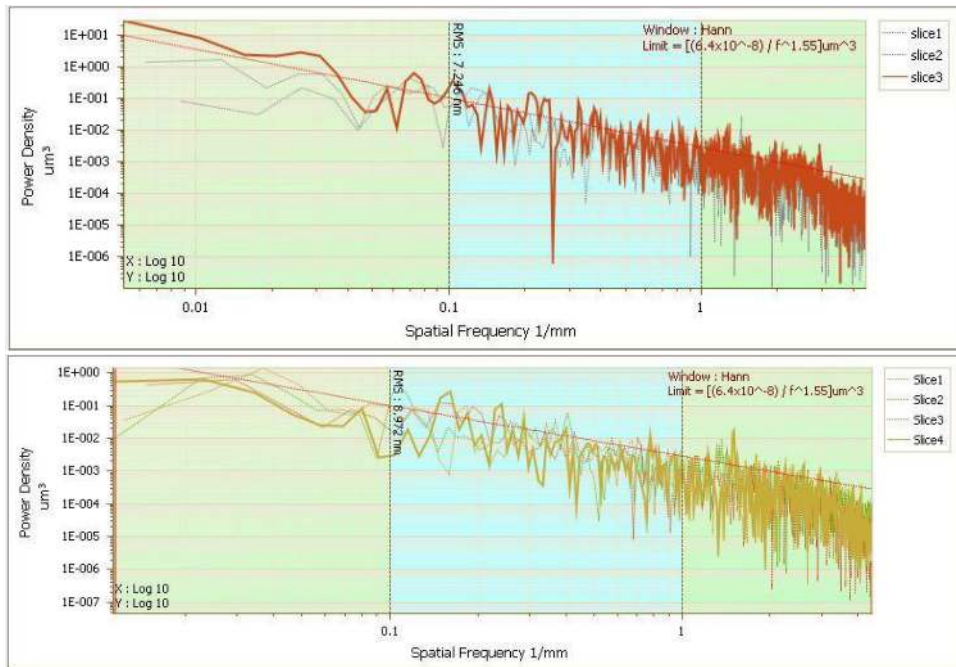


Figure 11

	MagAO-X Preliminary Design 5.1 Optics Specifications	Doc #: MagAOX-001 Date: 2017-04-19 Status: Rev. 0.0 Page: 15 of 18
---	---	---

where σ_{sr} is the surface roughness RMS, $k_{max} = 1/2.5 \mu\text{m}$, and $k_{min} = 1/85 \mu\text{m}$.

A.5 Inner Scale: Note the fall-off in the PSDs at higher spatial frequencies. In Alcock et al. (2010) it is claimed that these are due to instrument and measurement artifacts. However, the roll-off in the PSD evident in the OAP results seems to be real. This is confirmed by considering the surface roughness of these optics as we just did, since the simple power-law can not extend to infinitely high spatial frequencies and still produce the surface roughness. As is evident in Figure 10 there must be a roll-off in order to meet the surface roughness specification. This roll-off evidently has the form of an inner-scale, which can be modeled with a PSD of the form

$$\mathcal{P}(\vec{k}) = \frac{\beta}{|\vec{k}|^\alpha} e^{-(kl_0)^2} \quad (6)$$

where l_0 is the inner scale. This is illustrated in Figure 12. For the OAPs shown in 10 we estimate $l_0 \sim 0.3$. The PSDs for flats are measured at much higher spatial frequencies and do not show the same behavior, so we do not apply an inner scale to the flats.

A.6 Outer Scale: There is also a flattening at low spatial frequencies in some of the PSDs, pointing to an outer scale effect. We model this in the usual way with parameter L_0 . $L_0 = 15 \text{ mm}$ gives a reasonable match to typical OAP PSDs.

A.7 Complete PSD: Taking all of the above into account we have the final complete PSD

$$\mathcal{P}(\vec{k}) = \frac{\beta}{\left((1/L_0)^2 + |\vec{k}|^2\right)^{\alpha/2}} e^{-(|\vec{k}|l_0)^2} + \beta_{sr}. \quad (7)$$

A.8 Projections: The above characteristics apply to the entire CA. In general, the beam will be smaller than this, and be of different size on each optic in the instrument. To compensate, we project each PSD back to the primary mirror. To start with, the variance on the entire optic is

$$\sigma_{CA} = \beta_{CA} \int_{1/D_{CA}}^{k_{max}} \frac{1}{k^\alpha} k dk d\phi$$

and across the beam we have

$$\sigma_{beam} = \beta_{CA} \int_{1/D_{beam}}^{1/2d} \frac{1}{k^\alpha} k dk d\phi.$$

Now we assert that

$$\sigma_{pri} = \sigma_{beam}$$

and that

$$\frac{D}{d} = n = \text{constant}$$

for both the beam and the primary mirror. We then have

$$\beta_{pri} = \left(\frac{D_{pri}}{D_{beam}} \right)^{-\alpha+2} \beta_{CA} \quad (8)$$

for normalizing the PSD projected onto the primary mirror.

Both L_0 and l_0 scale linearly as D_{pri}/D_{CA} .

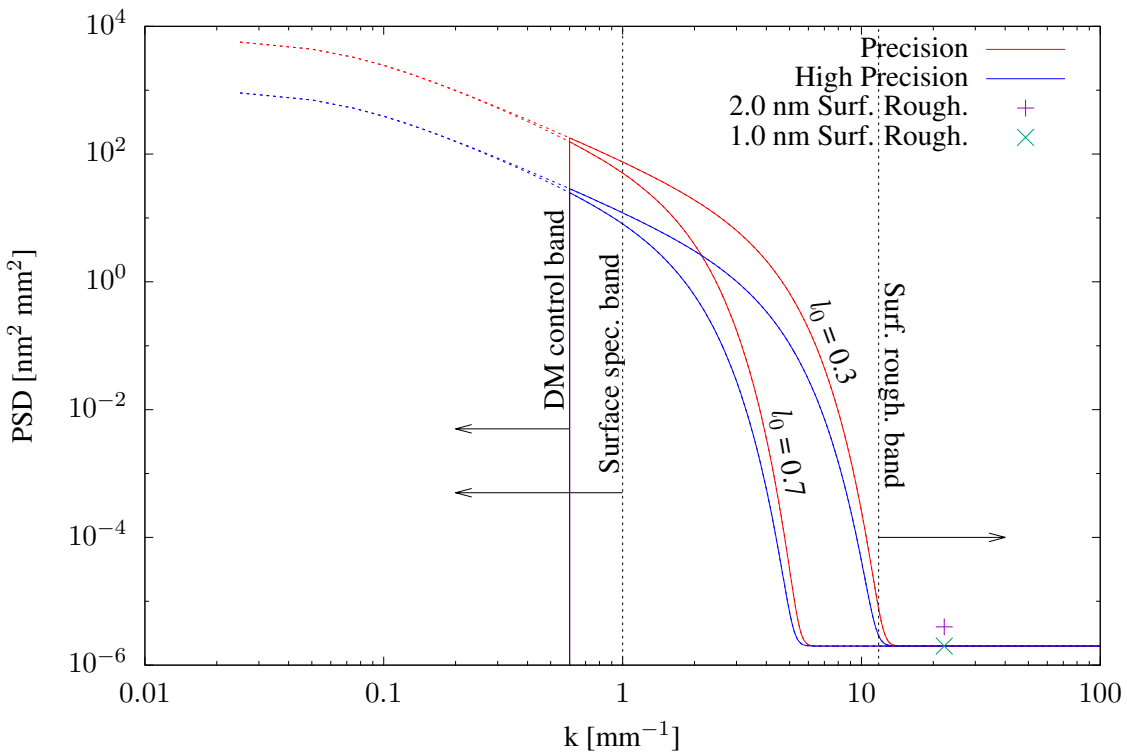


Figure 12: The complete PSD as modeled by Equation 7. Here we show PSDs for an OAP vendor's specifications, with $\alpha = 1.55$, $L_0 = 15$ mm, two choices for l_0 , and 1 nm surface roughness. Various spatial frequency bands of interest are noted.

B Clay M1

Buddy Martin of SOML provided the post-polishing measurements of the surface. The data file was processed using the C code provided by him. The header of the file contained

```
! Diffraction International conversion from Durango to Code V
! ACQ S/N: 0003-992161670
! Part #:
! Serial #:
! Surface:
! Data: 1:1]
! Subtractions: PST TLT PWR AST CMA SA3 MOR
! ROI is pixels X=11 thru X=243, Y=17 thru Y=249
```

GRD 233 233 WFR WVL 0.632820 SSZ 65536 NDA 32767

The short data values were scaled by the indicated value to be in nm of surface height in single precision. The



following plots show the results of a PSD analysis. Figure 1 shows the raw map as extracted from the data file.

Figure 13 shows the 2D PSD of the masked surface. An annular Hann window was applied, and the PSD was renormalized to have total variance corresponding to 12.52 nm rms.

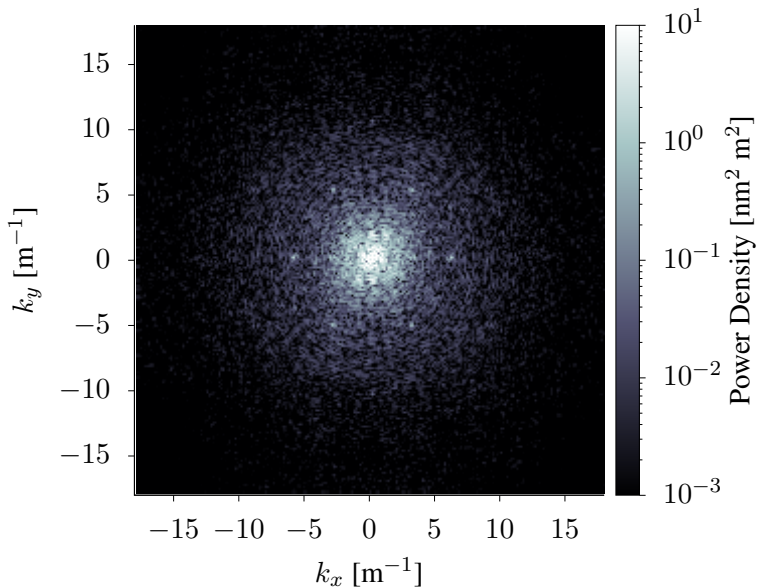


Figure 13: PSD of M1 surface.

Figure 14 shows the PSF of an image formed by using the masked surface as a pupil plane phase aberration in reflection (multiplied by 2) at 656 nm (H α).

Figure 15 shows the image formed assuming an ideal coronagraph.

References

- Alcock, S. G., Ludbrook, G. D., Owen, T., & Dockree, R. 2010, in Proc. SPIE, Vol. 7801, Advances in Metrology for X-Ray and EUV Optics III, 780108
- Duparré, A., Ferre-Borrull, J., Gleich, S., et al. 2002, Applied Optics, 41, 154
- Evans, C. J. 2009, Optical Engineering, 48, 043605
- Noll, R. J. 1976, Journal of the Optical Society of America (1917-1983), 66, 207
- Schwartz, K. 2010, Master's thesis, The University of Arizona, Tucson, AZ
- Tinker, F., & Xin, K. 2013, in Proc. SPIE, Vol. 8837, Material Technologies and Applications to Optics, Structures, Components, and Sub-Systems, 88370M

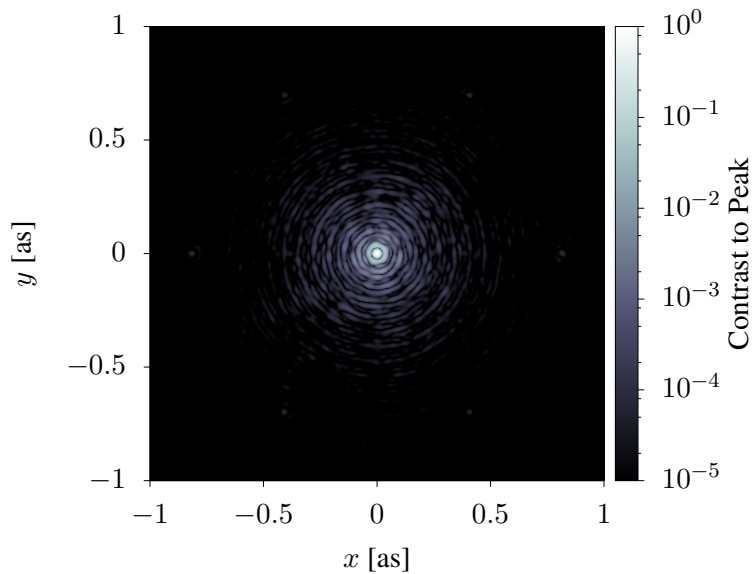


Figure 14: PSF of M1 at H α .

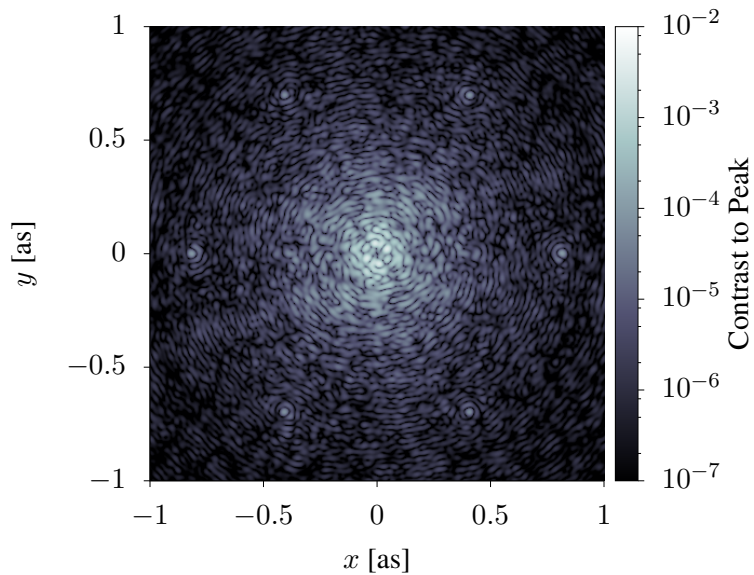


Figure 15: PSF of M1 at H α with ideal coronagraph. The 6 spots are due to print-through of the hexagonal honeycomb structure, and are observed in MagAO+VisAO diffraction-limited images.

  Universiteit Leiden European Research Council	MagAO-X Preliminary Design 5.2 Vector Apodizing phase plate coronagraph for MagAO-X	Doc #: MagAOX-001 Date: 2017-Apr-24 Status: Rev. 1.0 Page: 1 of 8
--	--	--

5.2 Vector Apodizing phase plate coronagraph for MagAO-X

David Doelman, Mike Wilby, Emiel Por, Frans Snik, Matthew Kenworthy, Christoph Keller (Leiden Observatory)

1. Requirements

1. The vector Apodizing Phase Plate (vAPP) shall operate close to the Halpha-wavelength, between 650 nm and 675 nm.
2. The pupil diameter shall be undersized from 9mm of the incoming beam by a factor of 0.956, to 8.6 mm.
3. The vAPP shall define the pupil for downstream optics. This can be implemented using a high-frequency polarization grating outside of the pupil, scattering the light outside the pupil outside of the FOV.
4. The coronagraph shall be on a 1 inch diameter $\lambda/20$ substrate with AR coating and a wedge.
5. The dark zone shall have an inner working angle of $2.1 \lambda/D$.
6. The dark zone shall have an outer working angle of $10 \lambda/D$.
7. The dark zone shall have a design contrast of 10^{-5} .
8. The dark zoned shall have a D-shape, displaced from the PSF core by the inner working angle with an outer radius of the outer working angle.
9. The design Strehl ratio of the coronagraphic PSF shall be higher than 50%.
10. The transmission of the vAPP device shall be higher than 70% in the specified wavelength range.
11. The vAPP shall produce coronagraphic PSFs within the inner 3"x3" FOV of the 6"x6" FOV on the detector.

2. Goals

1. The first additional goal w.r.t. the baseline requirements above integrates focal plane wavefront sensing to measure at least 9 Zernike modes from Zernike mode 4 up, with a maximum of 36 modes. This can be implemented with the holographic modal wavefront sensor, which is implemented by adding a phase pattern on top of the vAPP pattern.
2. A second upgrade of the vAPP is to develop a version of the vAPP with requirements listed above, and additionally consists of a first step to make the vAPP broadband. This is achieved by producing an “achromatic” retarder by stacking three liquid-crystal layers. This device can then be operated in narrow band filters between 550 nm and 1100 nm.
3. A different implementation of low-order wavefront sensing with of the vAPP can be achieved by producing a “wavelength-selective” device, where the transmission into the coronagraphic PSFs is close to 100% around H-alpha and transmission into the regular leakage-term PSF is close to 100% at surrounding wavelength. By physically separating the leakage term into a different optical path this light can be used for low-order wavefront sensing.
4. An ultimate broadband vAPP device would consist of a regular polarizing beam-splitter (i.e. not a grating), in combination with an achromatic quarter-wave retarder. The leakage terms then overlap with the coronagraphic PSFs and need to be minimized by design of both the half-wave retarder structures of the liquid crystals and the properties of the quarter-wave plate.

  Universiteit Leiden <small>Universität Leiden</small> European Research Council	MagAO-X Preliminary Design 5.2 Vector Apodizing phase plate coronagraph for MagAO-X	Doc #: MagAOX-001 Date: 2017-Apr-24 Status: Rev. 1.0 Page: 2 of 8
--	--	--

3. The vector apodizing phase plate coronagraph

The vector apodizing phase plate (vAPP) is a pupil-plane coronagraph that modifies the phase of the incoming wavefront. This modification allows for redistribution of the light in the point spread function (PSF) to create an area where the star light is suppressed, i.e. a dark zone. In this dark zone, the decrease in stellar light allows for the detection of faint companions. By splitting both circular polarizations we obtain two coronagraphic PSFs with dark zones on either side of the PSF.

3.1 Benefits of the vAPP

- Insensitive to tip-tilt errors
- Insensitive to partially resolved star
- Small inner working angle
- Single optic
- Easy alignment
- High contrast (for ground-based purposes)
- Close to full coverage around star
- Inherently achromatic
- Extreme phase patterns possible
- Opportunities for implementing (focal-plane) wavefront sensing
- Natural combination with polarimetry

3.2 Technical details of the vAPP

The vAPP coronagraph (Snik et al. 2012, Otten et al 2014, 2017) can be described by a half-wave retarder where the fast axis orientation is a function of the pupil-plane coordinates. For left-handed circular polarization input, the output will be right-handed circular polarization, with a phase pattern depending on the orientation pattern of the fast-axis. Similar, right-handed circular polarization switches to left-handed circular polarization, now with opposite phase. The applied phase is \pm twice the angle of the fast-axis orientation and is pure geometric phase, inherently independent of wavelength.

While geometric phase is achromatic, the retardance is a function of wavelength. A leakage terms appears when the retardance is not perfectly half-wave. There is no phase induced to the leakage term, other than aberrations caused by imperfections in the optic itself. For the unpolarized light of the star, the vAPP generates three PSFs, two PSFs with a dark zone on opposite sides and a leakage PSF.

The orientation of the fast-axis can be controlled with high precision using a liquid-crystal alignment layer in combination with a direct-write technique (Miskiewicz, Escuti 2014). The vAPP can be written with pixel-sizes down to 5 micron. The wavelength-dependent retardance is controlled with multiple twisted self-aligning liquid-crystal layers on top of the alignment layer. The layered retarder structures are called multi-twist retarders (MTRs) (Komanduri 2013).

4. Vector Apodizing Phase Plate for MagAO-X

4.1 Baseline phase pattern

The vAPP for MagAO-X was created using a global linear optimization algorithm from Emiel Por (Por et al. in prep) to calculate the phase pattern that creates a dark zone at the specified location with a maximized Strehl ratio. For MagAO-X, the inner working angle is $2 \lambda/D$, the outer working angle is $10 \lambda/D$, the dark zone has a contrast better than 10^{-5} and the Strehl ratio of this design is 60%. The design is shown in Fig. 1.

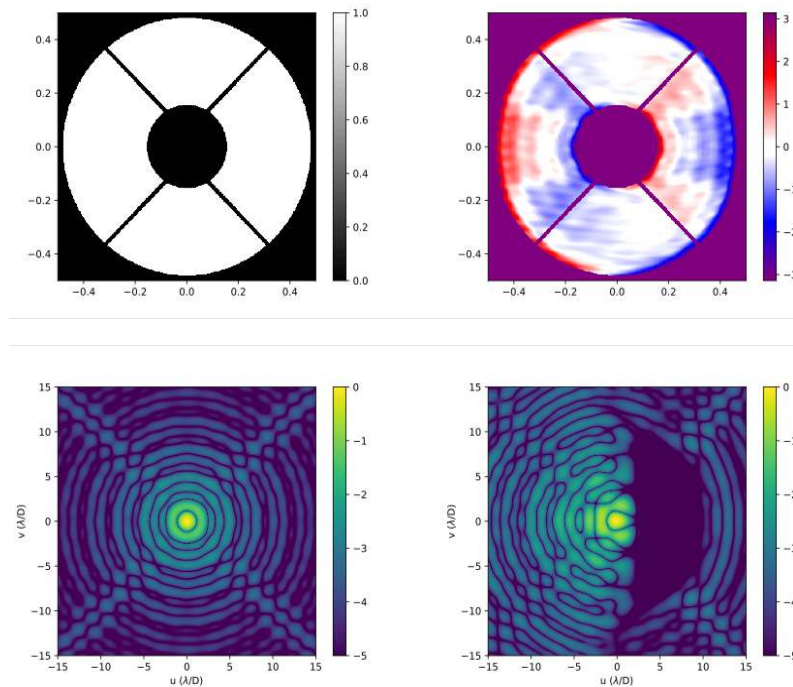


Figure 1: **Top left:** Aperture of MagAO-X. **Top right:** Phase pattern of the vAPP. **Bottom left:** PSF of the aperture with constant phase. **Bottom right:** PSF of the vAPP with a D-shaped dark zone from $2-10 \lambda/D$ and contrast better than 10^{-5} .

As mentioned in the section 3.2, the vAPP coronagraph will create three PSFs: two coronagraphic PSFs with dark zones on opposite sides and a leakage term PSF. To separate these on the detector, a “polarization grating” is added on top of the phase pattern, which imposes a linear phase ramp which changes sign for the two polarization states, i.e. the two coronagraphic PSFs. This polarization grating will thus split the left- and right-circular polarization PSFs, shifting them on the detector. The amount of splitting depends linearly on wavelength because it is imposed by a grating, but this is not an issue given the narrow spectral bandwidth of this setup. The leakage term goes through unaffected and ends up at the center of the detector. The combined PSF (right) for unpolarized light going through the grating vAPP (left) is shown in Fig. 2 as it would be on the MagAO-X detector for H-alpha wavelength. The phase pattern was reoptimized using Gerchberg-Saxton to remove crosstalk between the two coronagraphic PSFs and the leakage-term PSF.

To further simplify the vAPP and also integrate the amplitude mask in the actual phase pattern, we will write a very high frequency grating in the white area of Fig. 2. This effectively diffracts all the unwanted light outside of the pupil (as defined by this optic) outside of the beam/FOV. The exact angle and direction of this diffractive light, and how it is kept away from the focal plane is TBD.

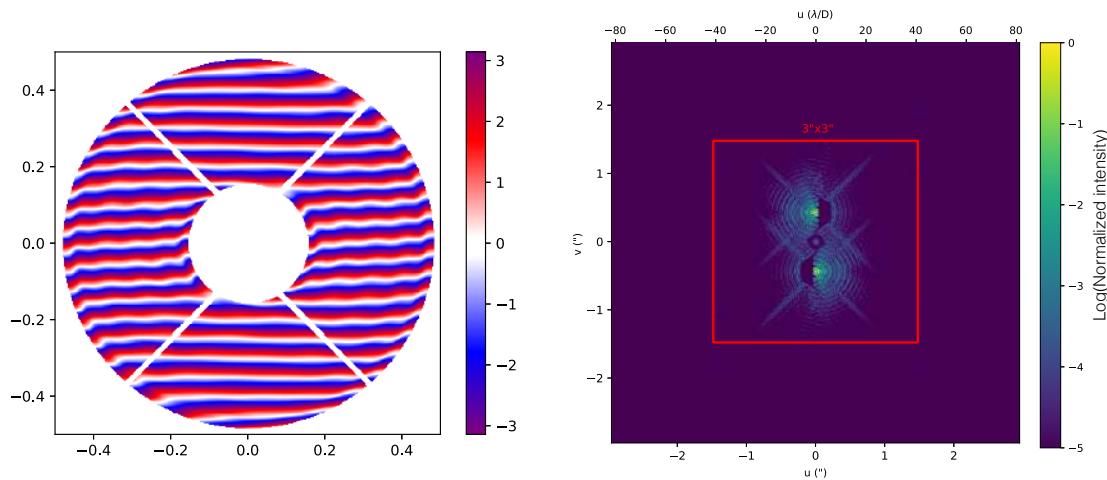


Figure 2: Left: The phase of the grating vAPP with a grating added in the vertical direction.
Right: The combined PSF of the vAPP for $\lambda=656 \text{ nm}$. The top and bottom PSFs are separated on the detector by the polarization grating. The center PSF is the leakage PSF with 1% leakage at $\lambda=656 \text{ nm}$.

4.2 Additional features

With the baseline design for the phase described in section 4.1, additional features can be added for increased functionality. These features come at little cost and include alterations to the phase pattern and different optimizations for the liquid crystal structure. In total, four options can be provided and these will be explained in further detail in the different sections below. The options are:

- 1) The vAPP with broadband 3-layer liquid-crystal design with the baseline phase pattern.
- 2) The vAPP with broadband 3-layer liquid-crystal design with a holographic modal wavefront sensor on top of the baseline phase pattern.
- 3) The vAPP with a wavelength selective 3-layer liquid-crystal design with the baseline phase pattern.
- 4) The vAPP with a wavelength selective 3-layer liquid-crystal design with a holographic modal wavefront sensor on top of the baseline phase pattern.

Both the broadband (1-2) and wavelength selective (3-4) liquid-crystal designs have their advantages and disadvantages and are mutually exclusive. The option to add the holographic modal wavefront sensor is independent of the choice of liquid-crystal designs.

The first vAPP device will have the extra features of option 2, with the broadband 3-layer liquid-crystal design and a holographic modal wavefront sensor on top of the baseline phase pattern.

4.2.1 Goal #1: Focal plane wavefront sensing with holograms

A great advantage of the liquid crystal technology is that it allows the flexibility to add almost any phase pattern. Here, we exploit this freedom to add holograms with Zernike modes to sense wavefront aberrations up to the detector. The holographic modal wavefront sensor (Wilby et al. 2017), creates two copies per

mode of the central PSF on opposite sides of the PSF, aberrated by \pm mode that we want to sense. When this wavefront error mode is present in the optical system, one spot will be less aberrated, while the other spot is even more aberrated. Comparing the relative amplitude of the two spots gives the sign and the amount of aberration in the system.

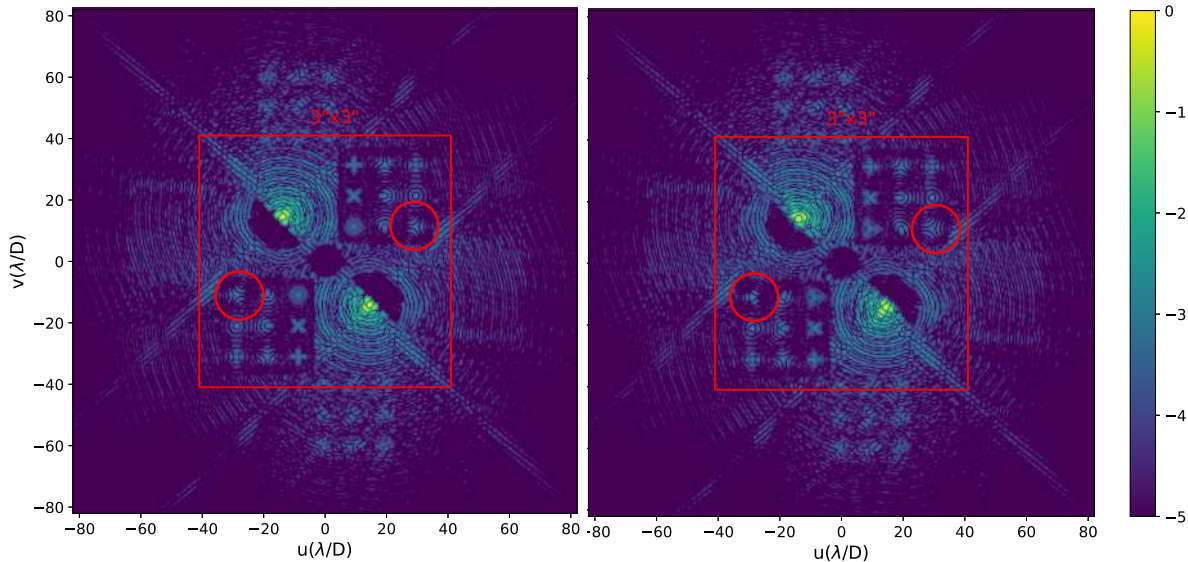


Figure 4: PSF of the focal plane holographic modal wavefront sensor (with 0% leakage assumed). The polarization grating orientation is rotated to create more space for the holograms. **Left:** The PSF without aberration. **Right:** The PSF with trefoil (Z_9). The hologram in the left circle has higher intensity than the hologram on the right. The applied aberration can be constructed from this information.

For MagAO-X, a preliminary design contains 9 spots that fit in the 3''x3'' FOV for increased readout speed. The ideal PSF is shown on the left in Fig. 4; the PSFs are aberrated with trefoil (Z_9) on the right.

For every mode four copies are generated, two for every polarization. The amount of light in the modes has to be sufficient to be detected for (slow) closed-loop control of the non-common path aberrations, which is estimated to be 1% per mode. Therefore, there is a trade-off between adding more modes and the amount of light in the coronagraphic PSFs. There is room for more modes on the detector outside of the 3''x3'' FOV, however, the trade-off study still has to be done.

4.2.2 Goal #2: Broadband liquid-crystal design

The twist and thickness of the liquid crystal stack is optimized to reduce the leakage as much as possible around H-alpha. For observations around H-alpha i.e. from 650 nm to 675 nm, one layer (1TR) of liquid crystals allows for a leakage below 2%. To increase the bandwidth, a stack with three layers (3TR) is necessary. For this MTR, the leakage is below 1% from 550 nm to 1.1 μ m, as shown in Fig. 3.

To fulfill goal #1, a vAPP device can be produced with a 3TR liquid crystal structure. The cost of 1TR vs 3TR are the added layers of only a few microns thick. This does almost nothing to the transmission of the device in the selected wavelength range. The cost increases slightly.

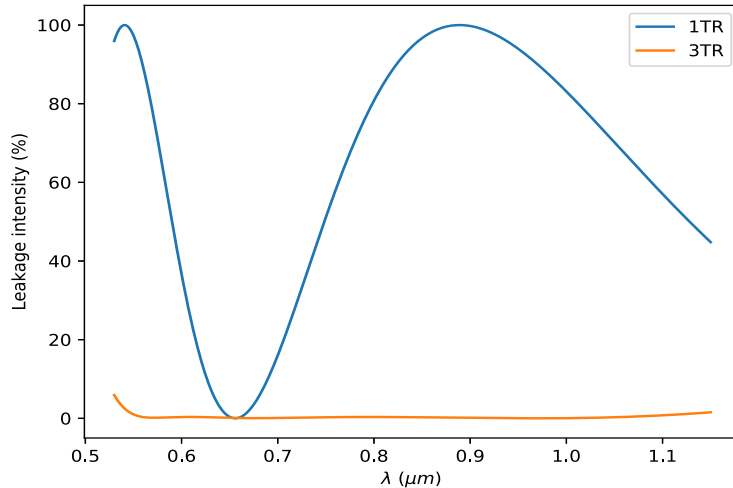


Figure 3: Leakage intensity vs. wavelength for one layer of liquid crystals (1TR) and three layers of liquid crystals (3TR) with different twist and thickness. For the 1TR, the leakage is sub 2% between 650nm and 675 nm. The 3TR design has a leakage below 1% from 550 nm to 1.1 μm .

4.2.3 Goal #3: Low-order wavefront sensing with a wavelength-selective vAPP

The half-wave retardance profile of the liquid crystal layers can be optimized to any profile by changing the twist and thickness of the layers. This freedom allows for a different way of low-order wavefront sensing. The retardance is optimized to increase the leakage term intensity (transmittance) to close to 100% outside of the scientific wavelength range, as shown in Fig. 5. On the left, we show the leakage intensity (transmittance) as function of wavelength. The leakage-term intensity is a few % around H-alpha and mostly above 80% outside of this band. The PSF in the middle panel corresponds to location 1 in the left panel of Fig. 5, with close to 100% leakage-term intensity at 580 nm. Location 2 in Fig. 5 corresponds to the PSF in the right panel, with close to 100% intensity in the coronagraphic PSFs at the H-alpha wavelength.

The leakage term can be separated in the focal plane, e.g. with a slightly rotated glass plate with a small mirror at the location of the leakage term. The reflected light of the leakage-term can be used in a low-order wavefront sensor.

The leakage term of the wavelength-selective vAPP is inherently broadband. To make good use of all the light in this leakage term, a broadband wavefront sensor is necessary. One option would be a vector-zernike WFS (Doelman et al. in prep 1), that uses a liquid crystal Zernike focal plane mask. For opposite polarization states, the Zernike mask applies a $\pm\pi/2$ geometric phase to part of the core of the PSF in a subsequent focal plane. By splitting the opposite polarization states with a quarter-wave plate and a Wollaston prism, two pupil images are created that can be used not only for achromatic phase aberration measurements, but also for achromatic amplitude aberration measurements.

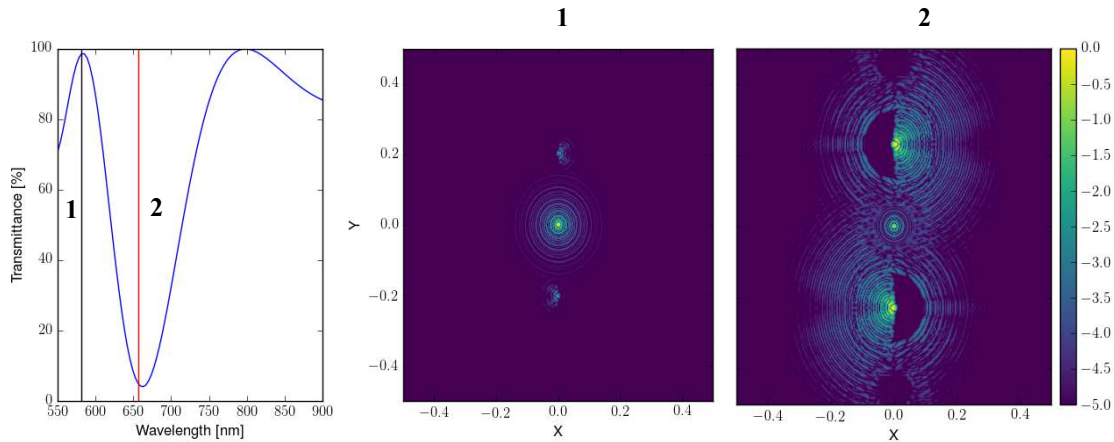


Figure 5: **Left:** Leakage-term intensity (transmittance) as function of wavelength. The leakage term intensity is lowest around H-alpha and mostly above 80% outside of the scientific band. **Center:** The PSF corresponding to 580 nm (black line left panel), with a leakage term of close to 100%, and almost no light in the coronagraphic PSFs. **Right:** The PSF corresponding to the H-alpha wavelength (656 nm, red line left panel). Most of the light is in the coronagraphic PSF and almost none in the leakage PSF.

5. Goal #4: A truly broadband vAPP coronagraph

To combine the high-contrast imaging (HCI), as enabled by the vAPP at MagAO-X, with high-resolution spectroscopy (HRS) with e.g. RHEA (Feger et al. 2014) or an integrated HCI+HRS approach as is currently being developed in Leiden (Por et al. in prep; Haffert et al. in prep), the vAPP needs to deliver achromatic splitting in addition to achromatized retardance performance. Achromatic splitting of linear polarization is easily implemented by replacing the dichroic splitter in front of the two science cameras with a polarizing beam-splitter cube (either based on a dielectric coating or a wiregrid structure). An additional quarter-wave plate (QWP) is then required to convert the two opposite circular polarization states of the two coronagraphic PSFs to the linear polarization states that the beam-splitter splits. This QWP can be positioned directly after the vAPP optic, as the two relevant linear polarization states are eigenvectors of the optical system in between the vAPP pupil and the beam-splitter (they correspond to the S and P directions on all mirrors). The vAPP itself then consists of the phase pattern as depicted in Fig. 1, with a broadband 3TR liquid-crystal structure design as presented in Fig. 3.

The main challenge of this implementation is to sufficiently suppress the leakage terms that emerge due to offsets from half-wave retardance of the vAPP and from quarter-wave retardance of the QWP. As there is no longer a grating to inherently separate the coronagraphic PSFs from the leakage PSF, the retardance profile of the vAPP needs to be <1% over the entire bandwidth to suppress the first Airy ring of the regular leakage-term PSF in the dark holes to <3E-4. Even then this term would still dominate the intensity error budget inside the dark hole. And because for a combination with a fiber-feed to a hi-res spectrograph it is unlikely that a "rotation-subtraction" technique (see Otten et al. 2017) can be applied to enhance the contrast during data-reduction, this leakage term needs to be suppressed in a different way. Fortunately, we have already introduced the "double-grating-vAPP" (Doelman et al. in prep 2), which combines a grating-

  Universiteit Leiden European Research Council	MagAO-X Preliminary Design 5.2 Vector Apodizing phase plate coronagraph for MagAO-X	Doc #: MagAOX-001 Date: 2017-Apr-24 Status: Rev. 1.0 Page: 8 of 8
--	--	--

vAPP with a regular polarization grating, which effectively delivers the desired phase pattern without any splitting. However, it diffracts out the leakage terms of both liquid-crystals patterns, effectively suppressing the leakage terms by a factor of ~ 100 to $1\text{E}-4$, leading to a print-through of the first Airy ring of only $\sim 3\text{E}-6$.

Such a diffraction trick cannot be implemented for the QWP, and thus we will need to procure a "achromatic" or even a "superachromatic" QWP. An achromatic QWP consists of a quartz and a MgF₂ plate with their fast axes crossed, such that their retardance dispersions largely cancel out. Over a 40% bandwidth, the retardance is typically constrained within 0.24–0.26 waves¹. The offset from quarter-wave retardance causes a mixing of the two coronagraphic PSFs, that scales with $\sin^2(\Delta\delta)$, so the 0.01 wave retardance offsets cause a typical leakage of 0.4%. But the first "Airy ring" on the bright side of the coronagraphic PSF has a relative intensity of 0.26, leading to an untolerable intensity in both dark holes of $\sim 1\text{E}-3$. So, it will be necessary to use a so-called "superachromatic" QWP, that consists of a stack of 3 quartz+MgF₂ combinations at different angles. Such plates can have a maximum retardance offset of 0.001², and thus suppress the leakage to $<1\text{E}-4$. However, the fast axis orientation of this type of QWP necessarily varies with wavelength, leading to additional leakage terms. In addition, the large number of crystal plates can cause significant amounts of WFE and "polarization aberrations" (Breckinridge et al. 2015). A better option may in the end be found by optimizing a thin (unpatterned!) liquid-crystal stack. The design trade-off and tolerance analysis on this is all still TBD.

Another alternative solution would be based on the production of a fully rotationally symmetric PSF that does not need to be split, and is optimized to deliver high contrast when feeding a multi-fiber system (Por et al. in prep; Haffert et al. in prep). A double-grating implementation then suppresses all pertinent leakage terms.

¹ http://www.b-halle.de/EN/Catalog/Retarders/Achromatic_Quartz_and_MgF2_Retarders.php

² http://www.b-halle.de/EN/Catalog/Retarders/Superachromatic_Quartz_and_MgF2_Retarders.php



5.3 Fresnel Analysis

Jennifer Lumbres, Ewan Douglas, Jared Males

1 Introduction

This section will show the Fresnel propagation analysis of the MagAO-X optical system design. The Fresnel analysis will show the diffraction generated by each optical element in the MagAO-X optical system. This section will describe the software used, how the system is built, and an analysis describing an aberrated and unaberrated version of the MagAO-X system.

2 Software Description: POPPY

The software used for Fresnel analysis is named POPPY, which stands for Physical Optics Propagation in PYthon. The POPPY source code may be obtained here (1) . The POPPY framework allows users to build an optical system composed of multiple planes (pupils, images) from a flexible library of optical element classes. POPPY can model both Fraunhofer and Fresnel diffraction for wavefront propagation through an optical system, and has PSF formation capabilities. Unlike raytrace software, POPPY uses the paraxial approximation and assumes perfectly focusing optics.

3 Building MagAO-X in POPPY

In POPPY, the MagAO-X optical system is built by inserting an optical element and propagating the field generated from the optical element to a certain distance until the next optical element. The field propagation is calculated using Fresnel approximation and angular spectrums (2). This process is repeated throughout the entire system, until the science detection plane. The MagAO-X design optical elements used in POPPY can be found in Section 5.1 and the distances between each optic were pulled from the MagAO-X Zemax model (see Section 2.1, pages 20-24). The MagAO-X POPPY model may be found here (3).

3.1 Optical Elements: Since POPPY assumes that all optics inserted in the system will focus perfectly, many otherwise complex optical elements are represented in simple form. Parabolic mirrors (M-1, M-2, all OAPs) are treated as quadratic lenses with a focal length parameter. Detection planes (focal planes, cameras) and deformable mirrors are represented as scalar transmission locations. Flat mirrors are also set as scalar transmission, but only in the unaberrated case. Flat mirrors have a PSD surface applied in the aberrated case.

POPPY also allows the user to insert custom amplitude transmissive or OPD phase optical elements into the system, thereby letting the user induce aberration at their discretion. This custom optical element feature has been used throughout the MagAO-X design analysis for custom pupils, optical surface quality, and the vAPP coronagraph mask. These surfaces are applied when the optical element is declared in POPPY.

The optics specifications described in Section 5.1 were used to generate representative surfaces for the various optics in MagAO-X. The actual surface map of M1 was used. For the other optics, PSDs were generated with the appropriate parameters and normalization. See Fig. 1 for sample PSDs generated. M2 and M3 are based on the known as-built surface specifications. For the new optics we used Vendor 1 High Precision for the OAPs, and



assumed lambda/100 (PV) flats. See 5.1 for a complete description. The PSDs were used to generate surface maps by using standard Fourier convolution with Gaussian white noise.

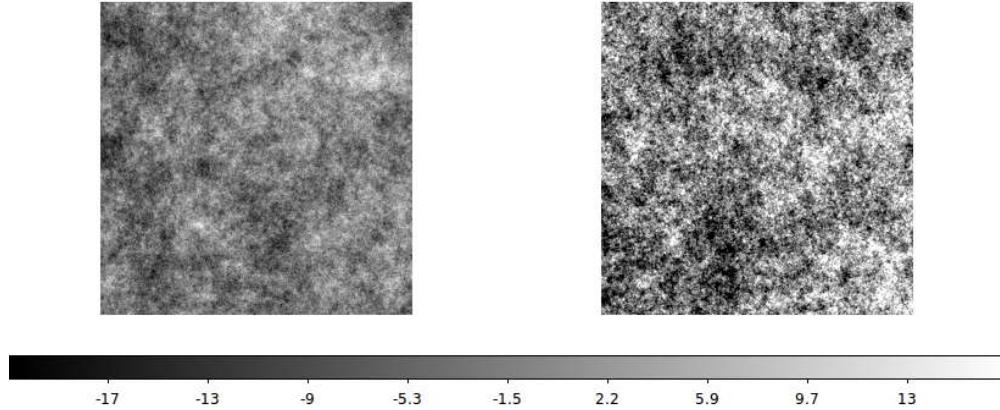


Figure 1: Sample MagAO-X optical surfaces used in POPPY (left: F-0 flat mirror; right: O-0 OAP mirror)

3.2 System Build: There are two different MagAO-X system builds analyzed in POPPY: an unaberrated case (POPPY's default perfect optics case) and an aberrated case (includes a surface PSD at each optical element). Both systems use the same unmasked pupil and vAPP coronagraph mask and are tested at 656 nm. More information about the POPPY modeling can be found in the A section. Once an optical system has been built into POPPY, it is possible to calculate the wavefront amplitude, phase, and intensity at each optical element. The aberrated and unaberrated cases are examined for both with and without the vAPP coronagraph present.

3.2.1 MagAO-X without vAPP coronagraph: To show the MagAO-X design performance, Figs. 2 - 6 present PSFs generated at each focal plane, both aberrated and unaberrated, without the vAPP coronagraph present. As the beam propagates through the system, the aberrated case shows the PSF rings gradually losing shape as more optics are encountered.

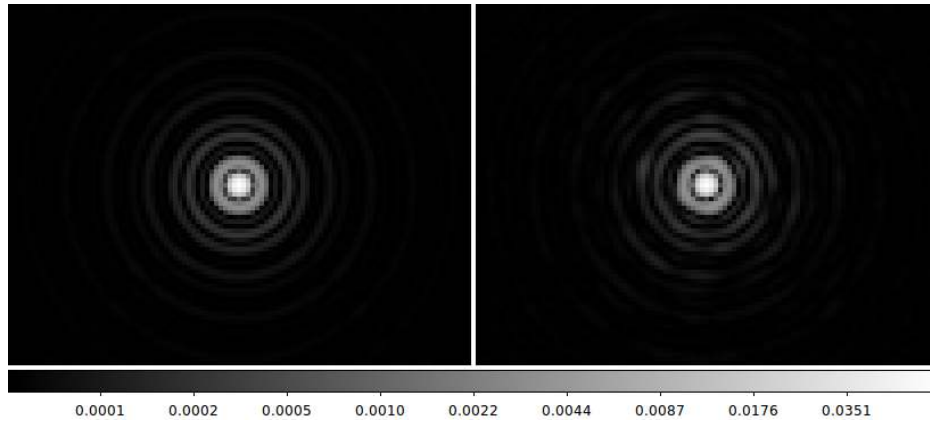


Figure 2: MagAO-X F/11 PSFs for unaberrated (left) and aberrated (right) systems



MagAO-X Preliminary Design
5.3: Fresnel Analysis

Doc #: MagAOX-001
Date: 2017-04-23
Status: Rev. 0.0
Page: 3 of 6

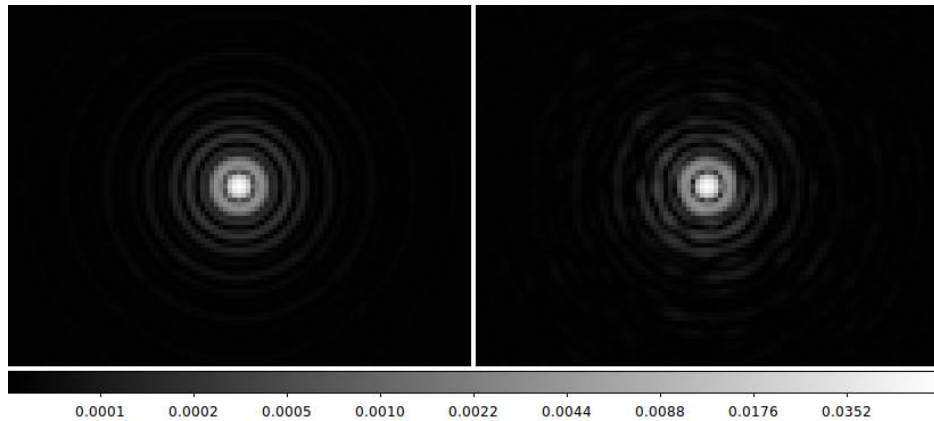


Figure 3: MagAO-X F/16 PSFs for unaberrated (left) and aberrated (right) systems

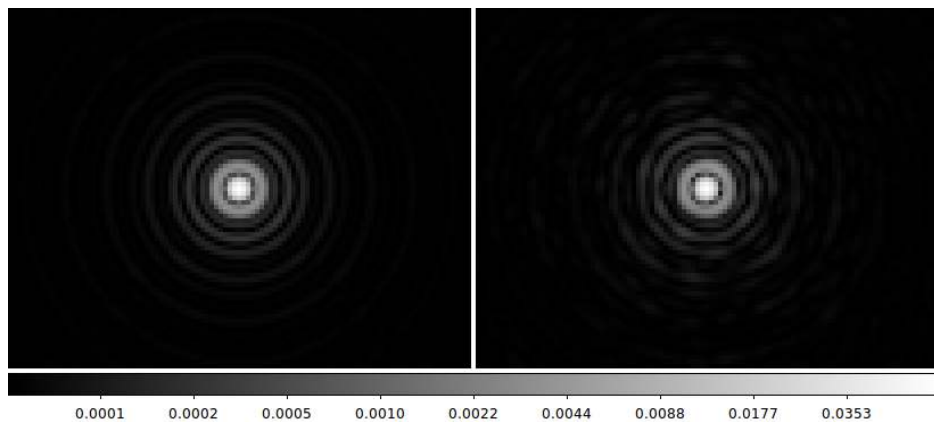


Figure 4: MagAO-X F/57 PSFs for unaberrated (left) and aberrated (right) systems

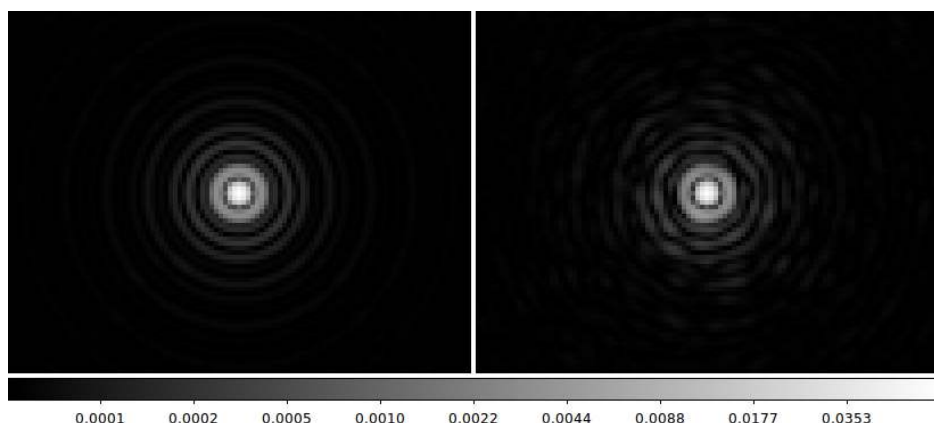


Figure 5: MagAO-X F/69 PSFs for unaberrated (left) and aberrated (right) systems

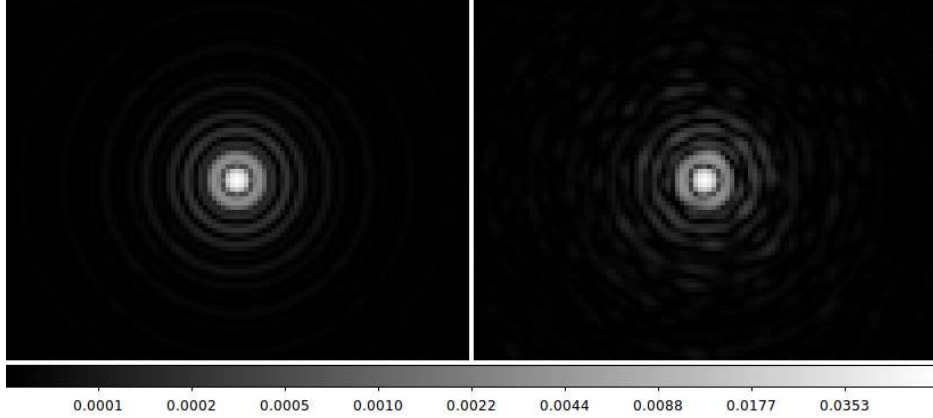


Figure 6: MagAO-X F/69 Science plane PSFs for unaberrated (left) and aberrated (right) systems

3.2.2 MagAO-X with vAPP coronagraph: The MagAO-X system was tested with the vAPP coronagraph present. The vAPP coronagraph used in POPPY is the phase pattern version (see Section 5.2 for more information regarding the vAPP coronagraph design). The intermediary focal planes will not be shown, as the performance remains the same from earlier. Fig. 7 compares the vAPP coronagraph F/69 science plane PSF performance between the unaberrated and aberrated cases. Both cases generate a dark hole on the left, however the aberrated case displays less contrast. This reduced contrast is caused by Fresnel effects generated from the optical elements post-coronagraph.

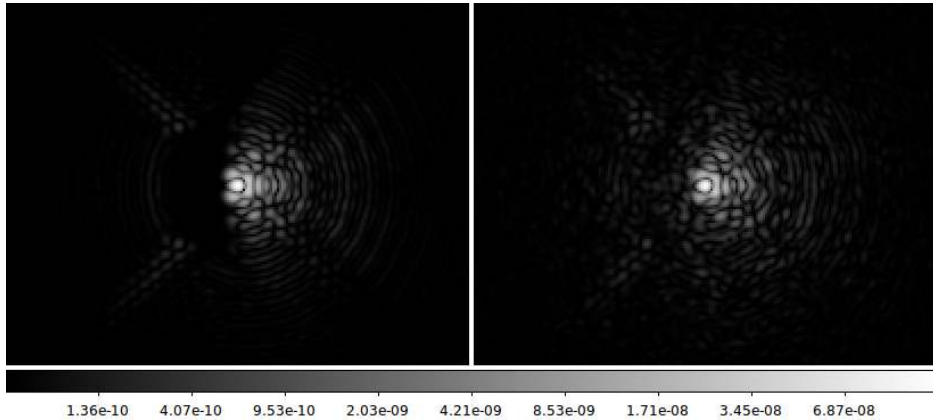


Figure 7: MagAO-X F/69 Science plane PSFs with vAPP coronagraph implemented, for unaberrated (left) and aberrated (right) systems

4 vAPP Performance

Fig. 8 compares the vAPP contrast with and without the expected optical imperfections in the MagAO-X system. The black and red dashed lines show the design contrast of the vAPP phase mask, presented in section 5.2. The black dashed line is for simple Fraunhofer propagation through the vAPP, and the red dashed line is the output of our POPPY simulation with no aberrations. The solid red line is the vAPP contrast with the aberrations included



in the MagAO-X optics. The dot-dashed red line shows the case where Fresnel propagation through the aberrated optics is performed to the vAPP pupil plane, but Fraunhofer propagation is performed thereafter. This indicates that the optics downstream of the coronagraph apodizer plane are having a strong effect on post-coronagraph contrast due to Fresnel effects. Finally, we show in blue the residual halo from atmospheric turbulence in our end-to-end (E2E) simulations.

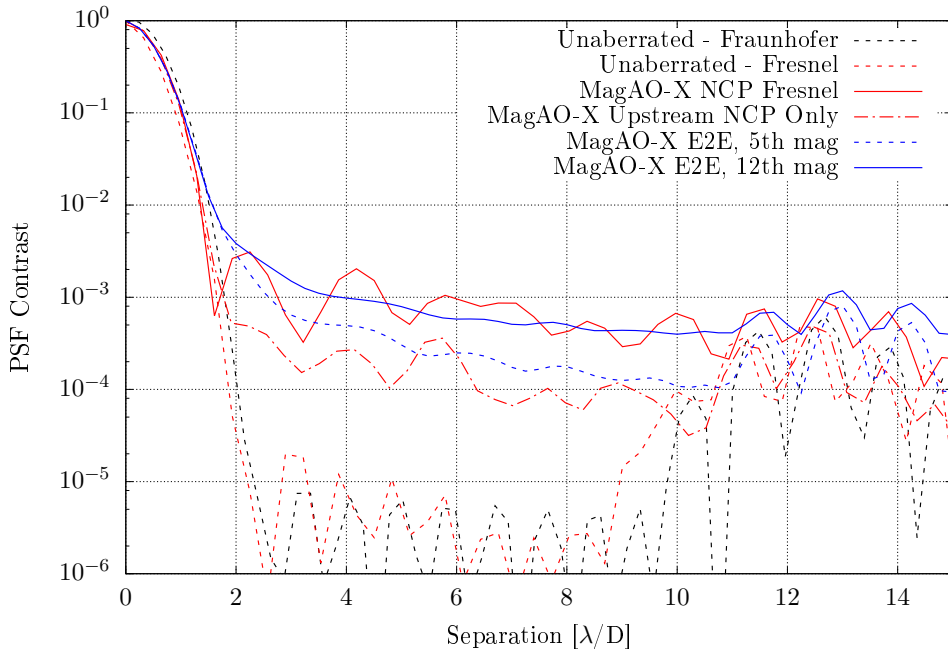


Figure 8: vAPP Performance in MagAO-X

A POPPY program parameters

The POPPY project is a work in progress, so different versions may affect how the MagAO-X POPPY Fresnel analysis gets rendered. Here we will list various details and assumptions made in the analysis.

The following optical element assumptions were implemented in POPPY for both aberrated and unaberrated cases:

- No wavefront sensing feedback
- Perfect DM surfaces
- Perfect wavefront sensor at each intermediary focal plane and at F/69 science focal plane
- No amplitude alteration from optical surface PSD implemented

The following is a list of version control details regarding the MagAO-X POPPY Fresnel analysis used here:

- POPPY version: 0.6.0rc



- Date of POPPY download: January 17, 2017
- Git hash for MagAO-X aberrated model in POPPY: eb594df
- Git hash for MagAO-X unaberrated model in POPPY: 6be492b

References

- [1] M. Perrin, J. Long, E. Douglas, N. Zimmerman, A. Sivaramakrishnan, K. Douglass, and M. Grochowicz, “Physical optics propagation in python,” 2017.
- [2] G. Lawrence, “Optical modeling,” Applied Optics and Optical Engineering XI, p. 125, 1992.
- [3] J. Lumbres, “Magao-x poppy source,” 2017.



5.4 System Throughputs

Jared R. Males

1 Introduction

This section documents our analysis of the system throughputs of the as-designed system. The key quantity is the photon rate (photons/sec) delivered to each of the detector planes in the system. These are the high-order wavefront sensor (HOWFS), the low-order WFS (LOWFS), and the two SDI science cameras.

The requirements to be met by this analysis are that it is complete (considers all main sources of throughput loss) and that it is realistic. This ensures that we can adequately analyze and simulate system performance. There are no required values on the final system throughput.

2 Coatings

The following coatings were considered:

- Primary and Secondary: protected Aluminum
- Tertiary: a custom coating with enhanced reflectivity near $0.8 \mu\text{m}$.
- OAPs and Flats: protected Silver, using a curve provided by Thor Labs.
- Alpaq DMs: same protected Silver curve.
- BMC MEMS DM: unprotected gold
- Transmissive surfaces: a standard anti-reflective coating.

The coating reflectance and transmission profiles are shown in Figure 1.

3 Cameras

The quantum efficiency (QE) curves for the First Light Imaging OCAM-2K (HOWFS detector) and the Andor iXon 897 (LOWFS detector) and 888 (Science detectors) were digitized from the manufacturer specification sheets. These are shown in Figure 2.

4 Filters

The following filters were designed for the H α configuration

- A dichroic beamsplitter which divides the light between the HOWFS and Science channels. Cuts-on at $0.68 \mu\text{m}$, with T and R both 95%.
- A LOWFS filter which selects only in-band light of the vAPP leakage term, including the 5% leakage term.
- An H α SDI filter set, as quoted by a vendor (see Opto-Mechanical design for details).

These curves are shown in Figure 3.

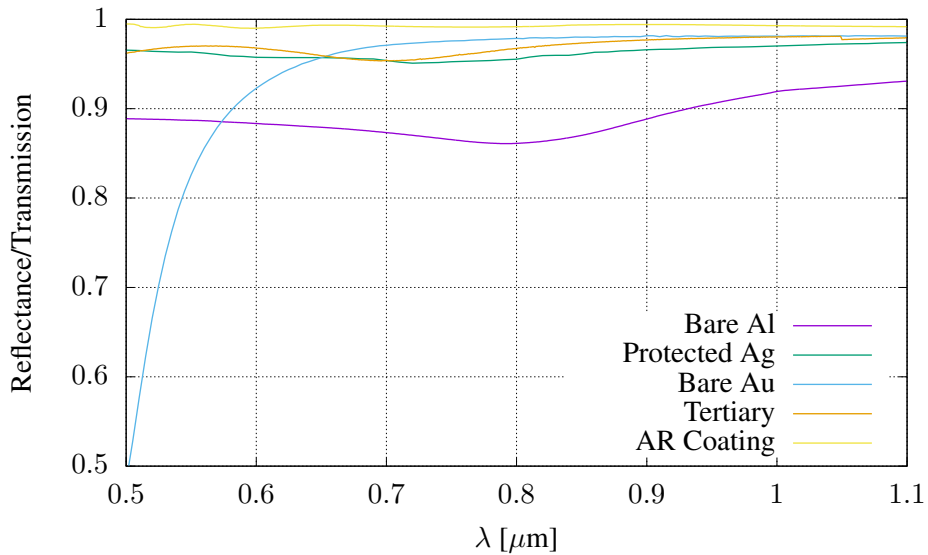


Figure 1: Reflectance and transmission profiles of coatings assumed.

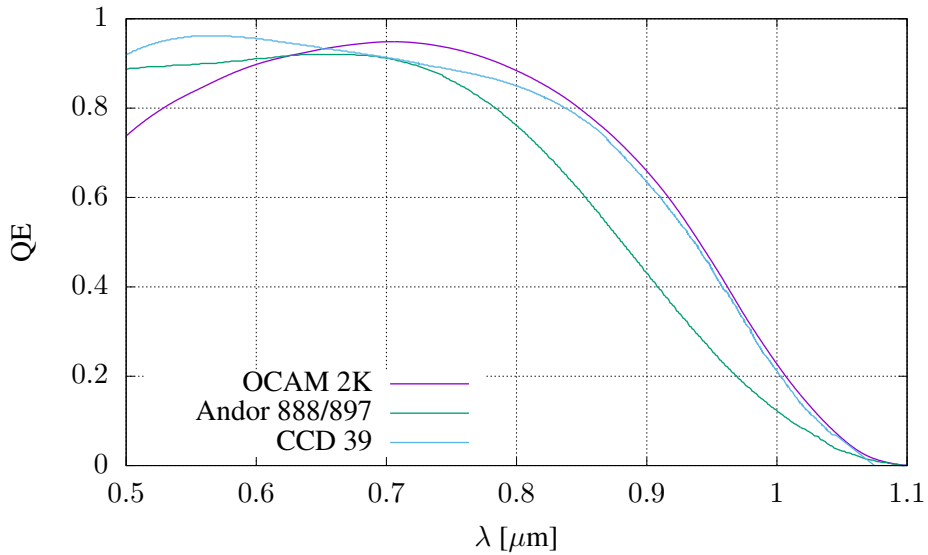


Figure 2: QE curves of the cameras to be used in MagAO-X.

5 Atmosphere

We include atmospheric transmission calculated using the BTRAM IDL code. We assumed 5.0 mm precipitable water vapor (PWV), and observing at zenith distance 30° , or airmass 1.15. The calculated telluric transmission is



MagAO-X Preliminary Design

5.4 System Throughputs

Doc #: MagAOX-001
Date: 2017-04-23
Status: Rev. 0.2
Page: 3 of 6

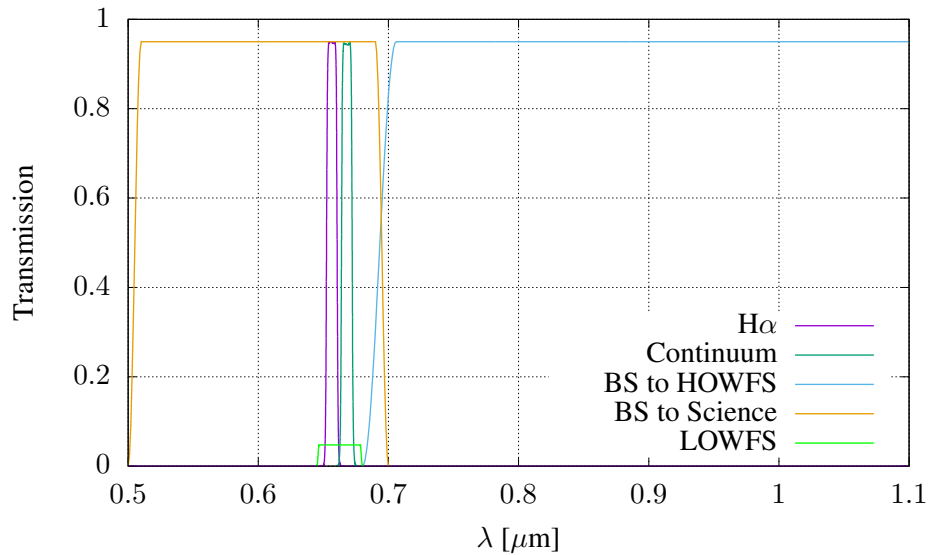


Figure 3: Filter curves designed for MagAO-X.

shown in Figure 4.

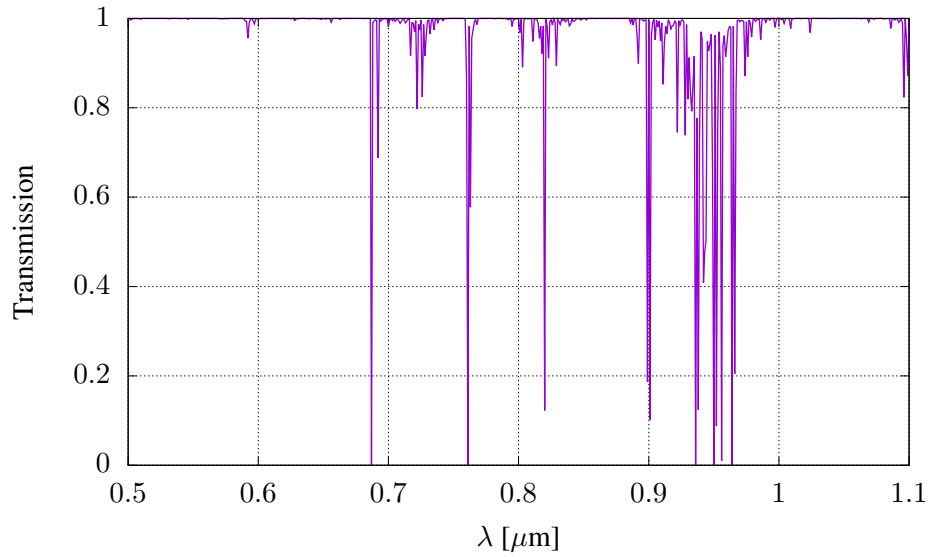


Figure 4: Atmospheric transmission for LCO calculated with BTRAM. Assumed 5.0 mm PWV and 30° zenith distance (airmass 1.15).



6 Transmission Characteristics and Throughputs

Finally, the complete transmission curves for each of the planes in the H α configuration was calculated by multiplying the above curves. This the reflectance or transmittance for each optic in the system, the atmosphere, the detector QE, and the appropriate filter curves. We also included a 10% loss due to diffraction derived from the Fresnel propagation analysis. These final transmission curves are shown in Figure 5.

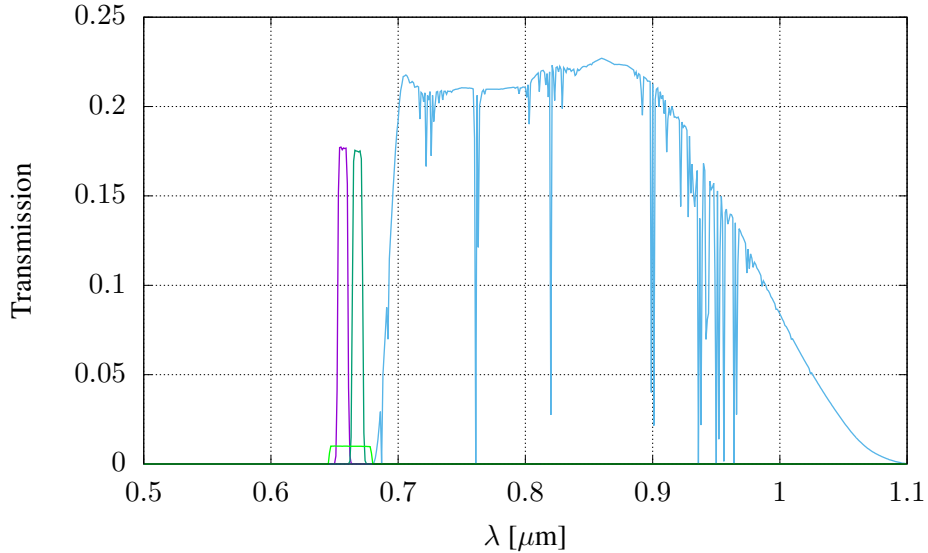


Figure 5: The final transmission curves for MagAO-X at each of the detector planes.

We then characterized each filter. We declare the throughput η of each filter to be the peak of the curve shown in Figure X. For each final filter curve, we converted to photon-weighted “relative spectral response” following Bessell (2000):

$$T(\lambda) = \frac{1}{hc} \lambda T_0(\lambda)$$

where T_0 is the raw energy-weighted profile. We also normalized these curves have a peak of 1. The central wavelength is

$$\lambda_0 = \frac{\int_0^\infty \lambda T(\lambda) d\lambda}{\int_0^\infty T(\lambda) d\lambda}$$

Using the Vega spectrum of Bohlin (2007), we determine the photon flux-density of a 0 magnitude star at 100% in each filter from

$$F_\lambda(\lambda_0) = \frac{\int_0^\infty F_\lambda(\lambda) T(\lambda) d\lambda}{\int_0^\infty T(\lambda) d\lambda}$$

and the effective width $\Delta\lambda$ from

$$\Delta\lambda = \int_0^\infty T(\lambda) d\lambda$$



such that the total photon flux in the filter is

$$F_\lambda(\lambda_0)\Delta\lambda = \int_0^\infty F_\lambda(\lambda)T(\lambda)d\lambda.$$

Finally, we have the total 0-magnitude photon rate at a given plane in the MagAO-X system

$$F_\gamma(0) = F_\lambda(\lambda_0)\Delta\lambda A\eta$$

where A is the collecting area of the telescope. We included the central obscuration, and for the planes downstream of the coronagraph we took into account the undersized mask.

The resultant filter characteristics are shown in Table 1.

Table 1: Final filter characteristics for the H α configuration.

Plane	Throughput	λ_0 μm	$\Delta\lambda$ μm	$F_\gamma(0)$ Photons/sec	Notes
Science H α	0.177	0.657	0.0082	2.3×10^9	
Science Cont.	0.176	0.668	0.0083	2.6×10^9	
LOWFS	0.010	0.662	0.033	5.9×10^8	5% vAPP leakage
HOWFS	0.227	0.851	0.257	7.6×10^{10}	

7 Throughputs for the f/16 ASM feed

The operation of MagAO-X with the f/16 ASM will require splitting photons between the MagAO WFS and the MagAO-X WFS. We plan to employ a set of selectable dichroic beamsplitters. These will reflect some fraction of photons into the existing MagAO system (as Clio2's entrance window does now) and transmit the remaining photons to MagAO-X. Here we analyze the $H\alpha$ science case. Here, 100% of the light short of 680 nm will be transmitted into MagAO-X. Longer than 680, 25% is reflected to MagAO, and 75% is transmitted to MagAO-X. These red photons will be used for wavefront sensing.

We also consider the transmissions and reflections in the optical train for each system, as above. For MagAO, we include the various surfaces after the dichroic, assume no beamsplitter is used internal to the MagAO WFS, and use the CCD 39 detector QE.

The resultant transmission curves for each system are shown in Figure 6. These curves were then integrated over the spectrum of Vega to determine the 0-magnitude photon rate for each part of the MagAO+MagAO-X system. These are given in Table 2.

References

Bessell, M. S. 2000, PASP, 112, 961

Bohlin, R. C. 2007, in Astronomical Society of the Pacific Conference Series, Vol. 364, The Future of Photometric, Spectrophotometric and Polarimetric Standardization, ed. C. Sterken, 315



MagAO-X Preliminary Design

5.4 System Throughputs

Doc #: MagAOX-001
Date: 2017-04-23
Status: Rev. 0.2
Page: 6 of 6

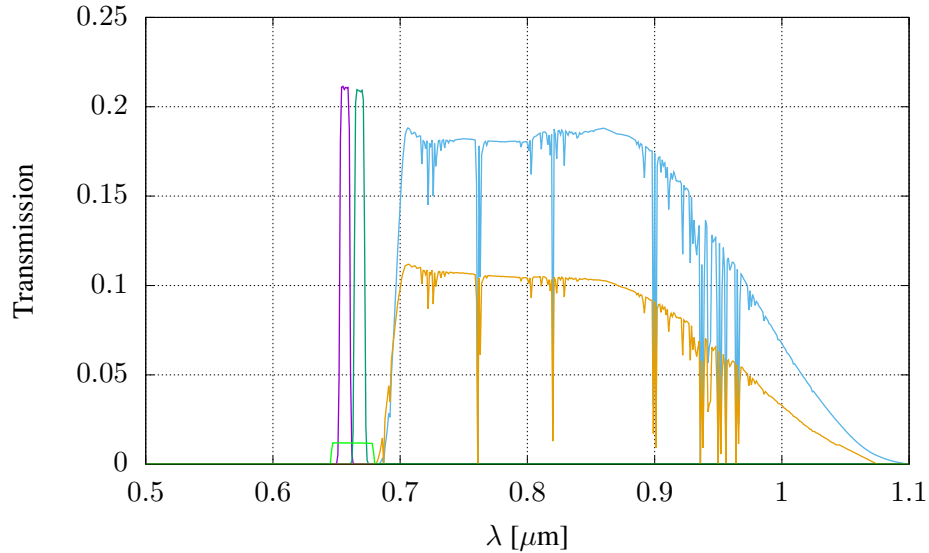


Figure 6: The final transmission curves for MagAO-X+f/16 at each of the detector planes. The gold curve corresponds to the MagAO WFS.

Table 2: Zero-magnitude fluxes for MagAO and MagAO-X for the $H\alpha$ science case

Plane	Throughput	λ_0 μm	$\Delta\lambda$ μm	$F_\gamma(0)$ Photons/sec	Notes
Science $H\alpha$	0.211	0.657	0.0082	2.8×10^9	
Science Cont.	0.21	0.668	0.0083	3.2×10^9	
LOWFS	0.012	0.663	0.033	7.0×10^8	
HOWFS	0.188	0.85	0.258	6.3×10^{10}	
MagAO-WFS	0.112	0.842	0.261	3.9×10^{10}	



6.0 Management Plan, Schedule and Budget

6.1 Project Organization: The PI of MagAO-X is Dr. Jared Males, Steward Observatory Assistant Astronomer. The PI will direct the project in coordination with the Project Manager (PM) for MagAO-X. The PI will derive the system-level requirements and will confirm that the technical definitions for the project are sufficient to achieve the scientific goals for MagAO-X. The PM will work in conjunction with Team Leads to establish the requirements and technical specifications corresponding to the top-level scientific requirements. Each Team Leader will be responsible for a respective sub system and the execution of tasks to meet the milestones associated with the subsystem. Specific personnel at UA with the experience and skills required for this project have been identified and are included in the budget and schedule. Coordination between individual engineering teams will be the PM's responsibility along with the schedule, budget, external reporting to NSF, quality assurance, and configuration control. The MagAO-X project organization is shown in Fig. 6.1.

6.2 Project Management: The PM will assign tasks to Team leads, oversee the subcontract, and coordinate delivery, tests, and shipping. Weekly meetings will be held as necessary with all relevant personnel. Scheduling of installation, off-line testing, and on-sky testing will be under the direction of the PI. The project has been organized into a design phase and three subsequent development phases, and a WBS developed to organize the work and to assess progress. A high level summary of the project WBS and schedule is shown in Fig. 6.2 and detailed a WBS is shown in section 6.5.

Conceptual Design: This proposal is based on the MagAO-X conceptual design. A conceptual design review (CoDR) was held during the AO4ELT conference at Lake Arrowhead, CA, in Oct 2015 with a panel of three highly qualified external reviewers. After completing several actions to address concerns, the CoDR was passed.

Design Phase: The preliminary design process will commence immediately following the MRI award. Here we will layout and model the system and create the various interfaces to the telescope and existing MagAO system. An outside panel of reviewers are being convened for the PDR to be held on 02 May 2017. Post PDR, the project will move on to the final design process that will address the issues identified at the PDR stage. The layout will be finalized and we will create fabrication drawings for mounts and interfaces. This process culminates with the internal final design review (FDR) targeted for June 14, 2017. Deliverables for the design phase include the PDR/FDR reports published on our website and at least one SPIE paper describing the design of the instrument.

After passing design reviews, component procurement will continue (long lead items such as the BMC

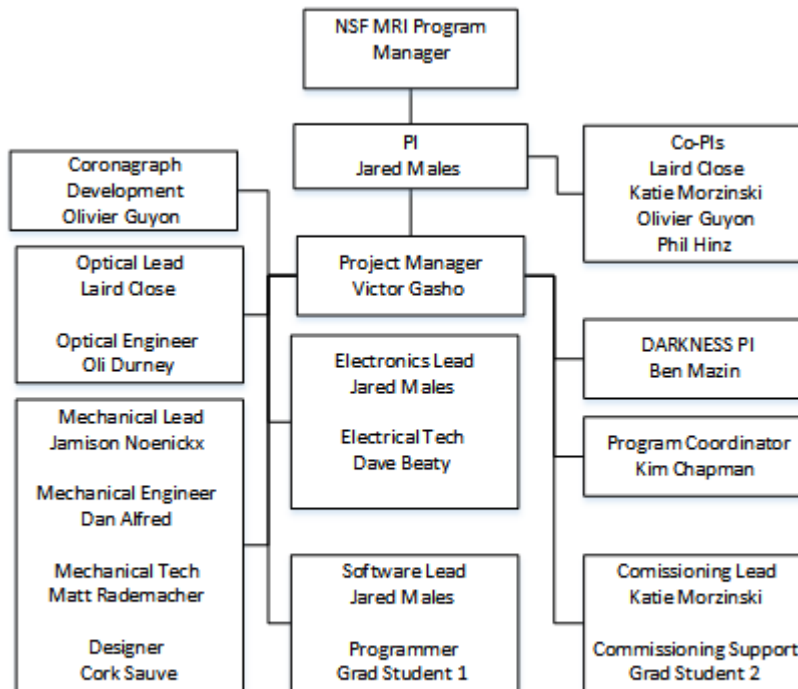


Figure 6.1: MagAO-X Project Organization



DM have already been procured), instrument construction, laboratory testing, and on-sky testing, will proceed and will be organized in three phases. We have budgeted for shipping the needed components between LCO and UA between telescope runs to continue development and testing. ***Phase I: Development of visible vAPP and LOWFS.*** Components will be populated on the floating bench, aligned, tested and then shipped to LCO for integration and one, three-day commissioning run. ***Pre-ship Review (PSR):*** Prior to shipping Phase I, we will provide an end-to-end demonstration of the instrument working in the lab to a panel of external experts, a Magellan Observatory requirement. Estimated deliverables for this phase include at least one SPIE paper documenting performance of the instrument and at least two refereed science papers utilizing the instrument.

Phase II: Development of visible Ex-AO. Phase II begins after Phase I testing, which allows parallel work in the lab on various improvements to the instrument to be developed for Phase II while phase I work is still ongoing. This enables the lab table to become a staging area for components to be tested and then implemented for the following stage of work. Phase II work integrates and aligns the PyWFS and science camera on the floating bench. After testing, the system will be shipped to LCO for integration and two, three-day commissioning runs spaced three months apart to address any issues. Estimated deliverables: at least one SPIE paper documenting performance of the instrument and at least two refereed science papers utilizing the instrument.

Phase III: Development of visible PIAACMC. Phase III will commence after Phase II commissioning run #1. The Lyot-based LOWFS and PIAACMC will be installed, aligned, and tested. The complete system will undergo final acceptance testing, then be shipped for re-installation at the LCO site. DARKNESS will be shipped to LCO. MagAO-X will be commissioned in two, three-day runs with a four-month spacing between them to resolve issues. Estimated deliverables of this phase include: at least one SPIE paper documenting performance of the instrument, a refereed paper (PASP) documenting system performance, and at least two refereed science papers utilizing the instrument.

DARKNESS Subaward: Funds for a subaward to collaborator Prof. Ben Mazin at UCSB was secured to support bringing the DARKNESS spectrograph to MagAO-X. Specifically, these funds will support a graduate student at UCSB who will coordinate interfacing DARKNESS to MagAO-X, develop FPWFS speckle control techniques, and perform post-processing of data under the direction of Prof. Mazin.



MagAO-X Preliminary Design

6.0 Management Plan, Schedule and Budget

Doc #: MagAOX-001
Date: 2017-Apr-18
Status: Rev. 1.0
Page: 3 of 10

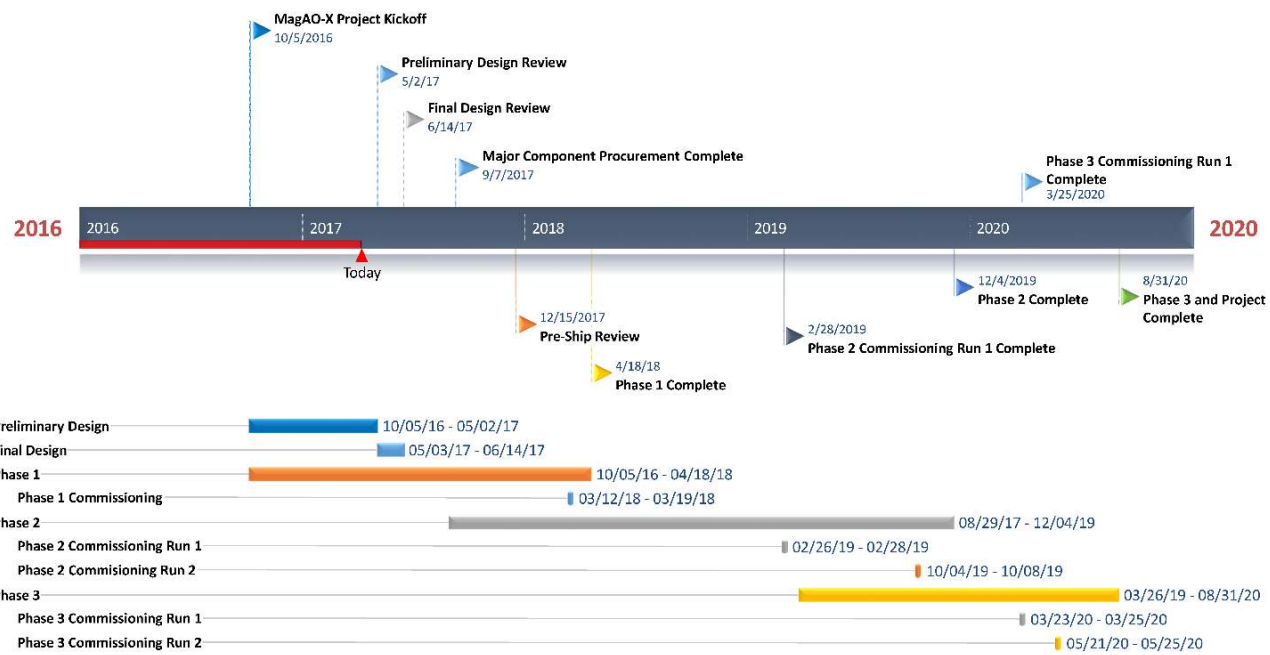


Figure 6.2: MagAO-X Project rolled-up work breakdown structure (WBS) and schedule

6.3 Risk Assessment: We have carefully structured the project plan and schedule to manage the risk associated with our aggressive goals. Our three-phased approach will allow us to develop, test, and deploy the instrument in manageable modules progressing from very low-risk in Phase I, to moderate-risk in Phase III. At each step, we have ensured the evolving instrument will be capable of producing ground breaking science. This phased approach allows a natural capability to de-scope the project if a technical or scheduling challenge prevents 100% completion, while still producing a scientifically capable instrument. Table 6.1 lists our assessment of some of the important risks of this project and their mitigation.

6.4 Design Availability: The MagAO-X instrument design will be made available through publications and through the project public website.



MagAO-X Preliminary Design

6.0 Management Plan, Schedule and Budget

Doc #: MagAOX-001
Date: 2017-Apr-18
Status: Rev. 1.0
Page: 4 of 10

Table 6.1: Key Challenges and Risks

Risk	Likelihood Severity	Comment/Mitigation
Existing MagAO doesn't work	very low	MagAO required for stroke requirement on MagAO-X DM.
	high	MagAO has <5% downtime to-date. Ability to use F/11 feed mitigates this risk
Unable to obtain telescope time for commissioning	very low	Commitment of time from the Director of Steward Observatory mitigates this risk.
	high	
Weather/seeing unsuitable for MagAO-X on commissioning runs	very low	Design based on median conditions. From extensive site characterization: very unlikely that a commissioning period is complete loss. Testing can be done in sub-standard conditions, mitigating overall schedule risk.
	low	
Poor yield on DM (too many bad actuators)	low	We have budgeted for a 100% yield (inside illuminated pupil) with quote from BMC. A small number (1-2) of bad actuators can be masked.
	moderate	
Unable to obtain Pyramid of sufficient quality.	very low	Pyramid of visible-AO quality (< 5 micron tip) already in possession (it is a spare component from MagAO construction) and tested successfully on-sky.
	high	
Unable to meet servo-loop time delay requirement.	low	Re-use of SCExAO software, with upgraded COTS GPUs means that we have a on-sky tested solution.
	moderate	
PIAACMC does not perform as designed	moderate	Affects only most aggressive $1\lambda/D$ science cases. Significant science still achieved with on-sky proven vAPP coronagraph at $>2\lambda/D$. Optical design easily accommodates alternatives, such as vector vortex, apodized Lyot.
	low	
Unable to obtain optical quality spec. on OAP relays	low	Two experienced OAP vendors will meet our spec. Our low, mid, and high freq. specs will produce ~ 12 nm rms (even before DM correction) see Table 1.
	low	
Unable to meet NCP aberration specifications	low	The LOWFS is common path after the Lyot stop: <i>all</i> low orders (LO) will be sensed and removed at DM. HO NCP will be <30 nm rms using 4D interferometer for acceptance & alignment.
	low	
Unable to control vibrations on MagAO-X bench	low	Vibration environment well understood from MagAO. Most severe for PIAACMC near $1\lambda/D$. vAPP coronagraph essentially impervious to vibrations (pupil-plane optic).
	moderate	
Coronagraphic LOWFS does not work.	low	The LOWFS technique has been demonstrated on-sky at SCExAO (Singh et al., 2015).
	moderate	
Focal plane WFS speckle control does not perform well enough.	moderate	Speckle nulling demonstrated on-sky (Martinache et al., 2014). Most science possible without FPWFS, i.e., raw PSF contrast is sufficient combined with SDI and ADI techniques.
	low	

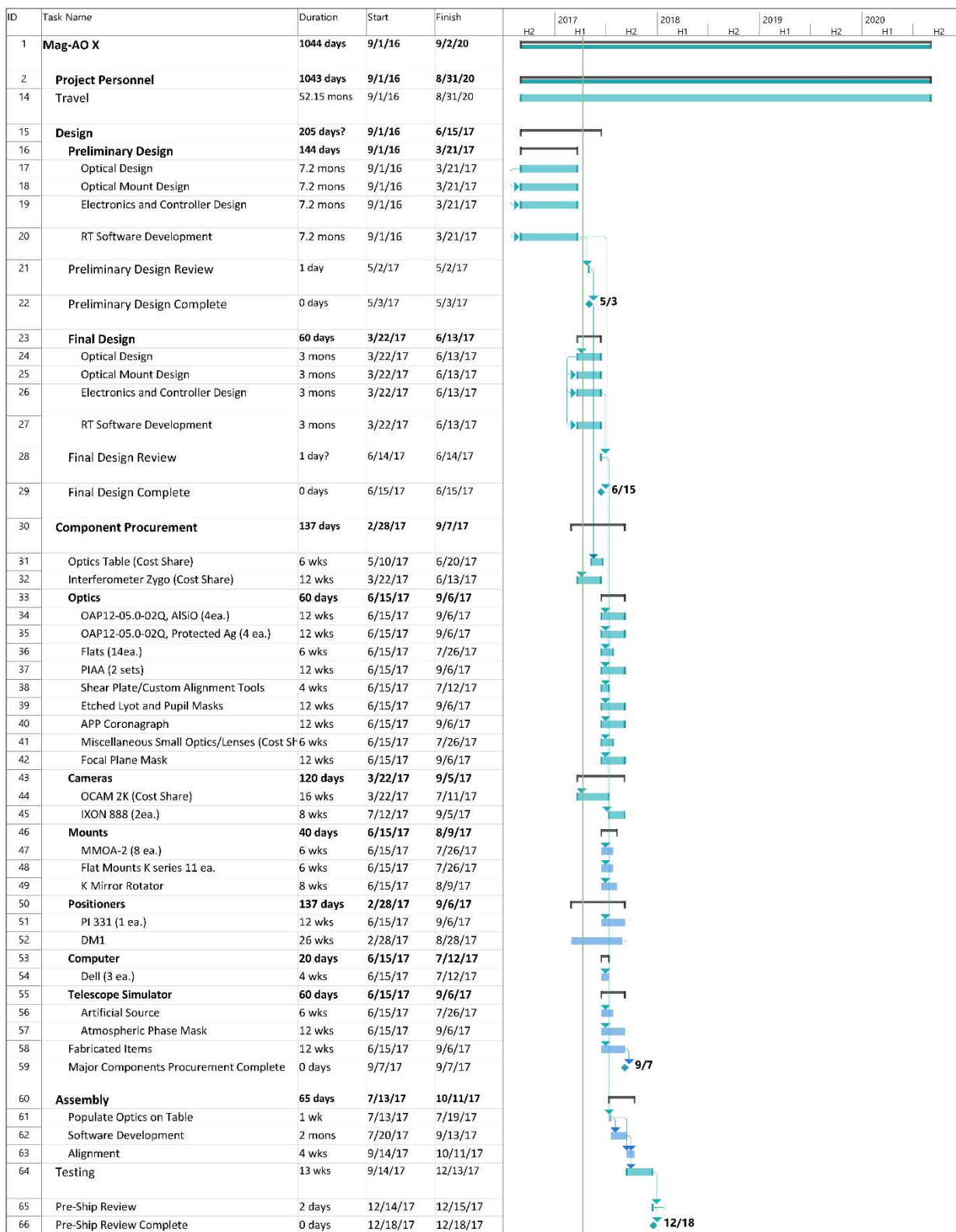


MagAO-X Preliminary Design

6.0 Management Plan, Schedule and Budget

Doc #: MagAOX-001
Date: 2017-Apr-18
Status: Rev. 1.0
Page: 5 of 10

6.5 Detailed Schedule and WBS





MagAO-X Preliminary Design

6.0 Management Plan, Schedule and Budget

Doc #: MagAOX-001
Date: 2017-Apr-18
Status: Rev. 1.0
Page: 6 of 10

ID	Task Name	Duration	Start	Finish		2017	H1	H2	2018	H1	H2	2019	H1	H2	2020	H1	H2
67	Shipping	1 mon	1/29/18	2/23/18													
68	Integrate at Telescope	2 wks	2/26/18	3/9/18													
69	System Checkout on Telescope	3 days	3/12/18	3/14/18													
70	Commissioning	3 days	3/15/18	3/19/18													
71	Return Shipment	1 mon	3/15/18	4/11/18													
72	Contingency	1 wk	4/12/18	4/18/18													
73	Phase 1 Complete	0 days	4/18/18	4/18/18													
74	Phase 2	591 days	8/29/17	12/4/19													
75	Assembly	260 days	8/29/17	8/27/18													
76	Populate Optics on Floating Bench	2 wks	8/29/17	9/11/17													
77	Alignment	2 mons	8/29/17	10/23/17													
78	Software Development	13 mons	8/29/17	8/27/18													
79	Testing	70 days	8/28/18	12/4/18													
80	End to End Tests	2 mons	8/28/18	10/22/18													
81	Final Acceptance Tests	2 wks	10/23/18	11/5/18													
82	Package and Ship System	1 mon	11/6/18	12/3/18													
83	Phase 2 Testing Complete	0 days	12/4/18	12/4/18													
84	Shipping	1 mon	12/4/18	12/31/18													
85	Integrate at Telescope	2 wks	2/5/19	2/18/19													
86	System Checkout on Telescope	1 wk	2/19/19	2/25/19													
87	Commissioning Run 1	3 days	2/26/19	2/28/19													
88	Commissioning Run 1 Complete	0 days	3/1/19	3/1/19													
89	Return Shipment	1 mon	3/1/19	3/28/19													
90	Shipping to Telescope	1 mon	9/1/19	9/26/19													
91	Commissioning Run 2	3 days	10/4/19	10/8/19													
92	Contingency	1 mon	10/9/19	11/5/19													
93	Return Shipment	1 mon	11/6/19	12/3/19													
94	Phase 2 Complete	0 days	12/4/19	12/4/19													
95	Phase 3	374 days	3/26/19	8/31/20													
96	Assembly	204 days	3/26/19	1/3/20													
97	Populate Optics on Floating Bench	2 mons	3/26/19	5/20/19													
98	Alignment	2 mons	3/26/19	5/20/19													
99	Software Development	4 mons	5/21/19	9/9/19													
100	Software Development Complete	0 days	9/10/19	9/10/19													
101	Testing	70 days	9/10/19	12/16/19													
102	End to End Tests	2 mons	9/10/19	11/4/19													
103	Final Acceptance Tests	2 wks	11/5/19	11/18/19													
104	Package and Ship System	1 mon	11/19/19	12/16/19													
105	Shipping	1 mon	2/3/20	2/28/20													
106	Integrate at Telescope	2 wks	3/2/20	3/13/20													
107	System Checkout on Telescope	1 wk	3/16/20	3/20/20													
108	Commissioning Run 1	3 days	3/23/20	3/25/20													
109	Commissioning Run 1 Complete	0 days	3/26/20	3/26/20													
110	Commissioning Run 2	3 days	5/21/20	5/25/20													
111	Contingency	69 days	5/26/20	8/28/20													
112	Phase 3 Complete	0 days	8/31/20	8/31/20													



MagAO-X Preliminary Design

6.0 Management Plan, Schedule and Budget

Doc #: MagAOX-001
Date: 2017-Apr-18
Status: Rev. 1.0
Page: 7 of 10

6.6 Budget

The total project cost is \$3.280M. The total cost includes \$2.296M of direct costs from NSF and \$984K of cost share from non-federal sources. The estimate included all labor costs, operations, capital expenses, travel, and indirect (F&A) charges. We have revised these cost based on developments during the preliminary design phase. Fig. 6.3 contains the current “MagAO-X Burn Chart”, showing the total costs for the project, current actual expenditures (as of March 31, 2017), planned cost share and planned direct costs over time.

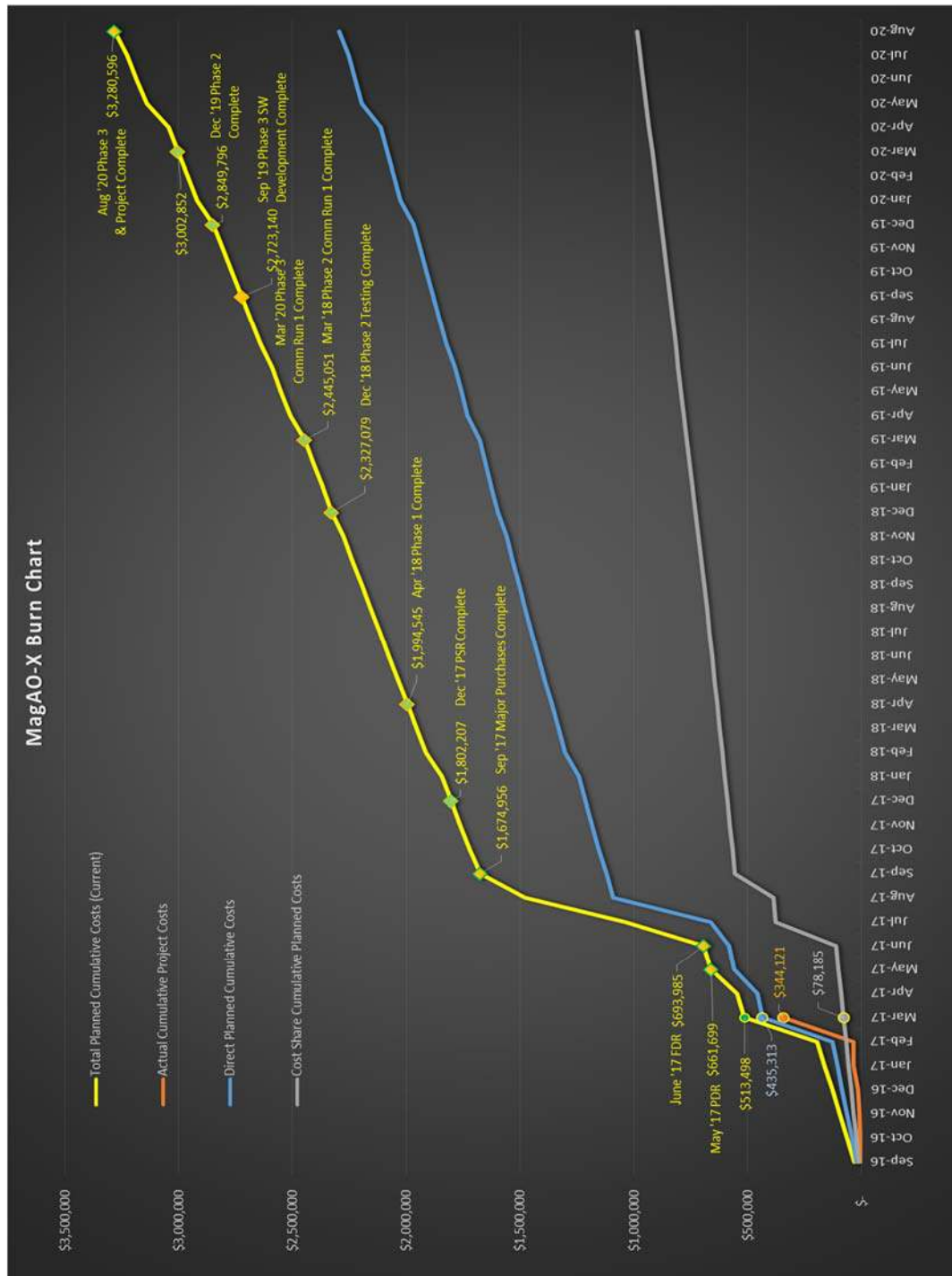


Figure 6.3: MagAO-X Burn



6.6.1 Labor and Personnel

Table 6.2 contains the project personnel and description of their assigned tasks and/or past experience. Figure 6.3 shows how the labor hours and labor costs are distributed over time. The labor hours for senior personnel slowly ramp up as the project progresses. This is mainly due to more expertise needed during phase two and three commissioning occurring in years 3 and 4. The other personnel such as the engineers and technicians are primarily required in year 1 and tapering off in year 2. The relatively low hours for the engineers and technicians is due to the experimental nature of the project using off the shelf equipment that requires very little custom designs and fabrication. Graduate student help ramps up in year 2 as the instrument readies for commissioning in phase 1 and tapers off in years 3 and 4 as more senior personnel take on more of the commissioning tasks.

Table 6.2: Project personnel.

Project Title	Name	Project Role
Sr. Personnel		
Principal Investigator	Dr. Jared Males	Will oversee the technical direction of the entire project and will lead the software and electronics group.
Co-PI	Dr. Laird Close	Dr. Close is the overall MagAO system PI and optics team lead.
Co-PI	Dr. Phil Hinz	Dr. Hinz is the PI of the CLIO Infrared Camera.
Co-PI	Dr. Olivier Guyon	Dr. Guyon is the world leader in coronagraph design.
Co-PI	Dr. Katie Morzinski	Dr. Morzinski has many years of experience in AO science, which will be valuable for the instrument testing and commissioning.
Other Personnel		
Project Manager	Mr. Victor Gasho	Mr. Gasho has managed several complex telescope instrument/system builds including Mag-AO He will be responsible for project cost, schedule, configuration management and task assignment.
Optical Engineer	Mr. Oli Durney	Mr. Durney was the principal optical engineer for LBTI and has designed the optics for MagAO-X
Mechanical Engineer	Mr. Jamison Noenickx	Mr. Noenickx was involved with the MagAO development. Mechanical team lead.
Mechanical Engineer	Mr. Daniel Alfred	Mr. Alfred is in charge of the thermal analysis of the electronics rack and table environment. He was formerly on the Osiris-Rex project in that role.
Designer	Mr. Cork Sauve	Mr. Fern will be responsible for the engineering/shop drawings for the system under the direction of Mr. Noenickx.
Electrical Technician	Mr. Dave Beaty	Mr. Beaty will be responsible for the electrical interconnects for the system under the direction of Dr. Males.
Mechanical Technician	Mr. Matt Rademacher	Mr. Rademacher will be responsible for mechanical assembly of the system under the direction of Mr. Noenickx.
Program Coordinator	Ms. Kim Chapman	Ms. Chapman will be responsible for arranging travel, tracking account expenditures, effort reporting, and purchasing.
Students		
Graduate Student 1	Ms. Kelsey Miller	Ms. Miller will assist in the design, build and phase 1-2 commissioning of the instrument.
Graduate Student 2	Ms. Lauren Schatz	Ms. Schatz will be tasked with the design, build and phase 1-2 commissioning of the instrument.
Graduate Student 3	Mr. Joseph Long	Mr. Long will assist with phase 2 - 3 build and commissioning.



Figure 6.3: Project personnel labor hours and costs over time.

6.7 Equipment, Shipping, Subcontracts, Travel and Indirect

Table 6.3 contains the rollup costs for the equipment, shipping and travel costs. Table 6.4 shows the current rolled-up costs for major capital equipment and quotes for purchased items (some purchased items are estimated costs were quotes were not available or where called out as miscellaneous items). Please note that the capital equipment quotes are confidential and can be provided upon request. The air-freight and ground shipping is based on fresh quotes from WJ Byrnes and Co. for the Tucson to Santiago leg and actuals from the FIRE instrument shipping for the Santiago to LCO leg. A quote for the return shipments of the table and electronics rack crates were also received from W.J. Byrnes. There will be five round-trip shipments of the table and electronics rack, with the final shipment being a one-way to the site for commissioning run 2 in phase 3. The table legs and shipping fixture will be shipped one time, one-way to the site in phase 1. A subcontract will be let to University of California Santa Barbara (UCSB) to provide the DARKNESS instrument to be used on the MagAO-X system. The funds will be used to support a graduate student at UCSB under the supervision of PI Dr. Ben Mazin. Travel costs are based on previous travel for the MagAO runs and includes air fare from Tucson to La Serena and lodging at LCO. Indirect costs are charged on labor, non-capital equipment, travel, shipping and on the first \$25K of subcontracts at the rate of 53.5%. The total indirect cost of the project are \$495K (Note that the cost share portion of the project do not incur indirect charges).



MagAO-X Preliminary Design
6.0 Management Plan, Schedule and Budget

Doc #: MagAOX-001
 Date: 2017-Apr-18
 Status: Rev. 1.0
 Page: 10 of 10

Table 6.3: Rolled-up costs for the equipment, travel, shipping and subcontracts.

		Year 1	Year 2	Year 3	Year 4	Total
1	Equipment	\$ 476,872	\$ 1,751	\$ 1,804	\$ 1,858	\$ 482,284
2	Travel	\$ -	\$ 24,637	\$ 25,376	\$ 52,274	\$ 102,287
3	Shipping	\$ 12,740	\$ 12,600	\$ 25,200	\$ 39,000	\$ 89,540
4	Subcontracts	\$ -	\$ -	\$ 23,650	\$ 24,286	\$ 47,936
	Total	\$ 489,612	\$ 38,988	\$ 76,030	\$ 117,418	\$ 722,047

Table 6.4: Equipment costs. Capital equipment quotes are confidential and can be provided upon request.

Capital Equipment					
	Qty	Item	Unit Price	Total Cost	Vendor
1	8 ea.	2" OAPs Hi-Precision Quality			AOS
2	1 ea.	APP Coronagraph			
3	1 ea.	Focal Plane Mask			
4	1 ea.	K Mirrors Rotator			
5	1 ea.	Deformable Mirror (DM1)			BMC
6	1 ea.	Artificial Source			Fianium
7	1 ea.	Stacis Optical Table			TMC
8	1 ea.	OCAM2K Camera			First Light
9	2 ea.	IXON 888 Camera			Andor
10	1 ea.	PI 330 Fast Tip-Tilt Stage			PI
11	2 ea.	Real Time Computer			Custom
12	1 ea.	PCIe Expansion			Custom
13	1 ea.	Instrument Control Computer			Custom
14	1 ea.	AO Operations Computer			Custom
			Total	\$ 1,109,718	
Non-Capital Equipment					
15	14 ea.	Flats	\$ 1,000	\$ 14,000	Thorlabs
16	2 ea.	PIAA	\$ 2,000	\$ 4,000	
17	1 set	K Mirrors	\$ 3,000	\$ 3,000	Thorlabs
18	1 ea.	Atmospheric Phase Mask	\$ 4,000	\$ 4,000	
19	1 ea.	Shear Plate/Custom Alignment Tool	\$ 1,000	\$ 1,000	
20	1 ea.	Etched Lyot and Pupil Masks	\$ 1,000	\$ 1,000	In-house
21	8 ea.	MMOA-2 Mount	\$ 3,035	\$ 24,280	AOS
22	8 ea.	Flat Mounts K series	\$ 500	\$ 4,000	Thorlabs
23	1 lot	Fabricated Items	\$ 2,600	\$ 2,600	In-house
24	1 lot	Miscellaneous Optics	\$ 4,604	\$ 4,604	Various
25	1 lot	Shipping Crates	\$ 6,000	\$ 6,000	Various
26	2 ea.	Transportable Storage 8 TB	\$ 2,395	\$ 4,790	Custom
27	2 ea.	UA Fixed Storage 136 TB	\$ 20,000	\$ 40,000	Custom
28	1 lot	Various Spares	\$ 12,795	\$ 12,795	Various
29	1 ea.	Diverging Lens for Interferometer	\$ 3,003	\$ 3,003	Zygo
			Total	\$ 129,071	



MagAO-X PDR

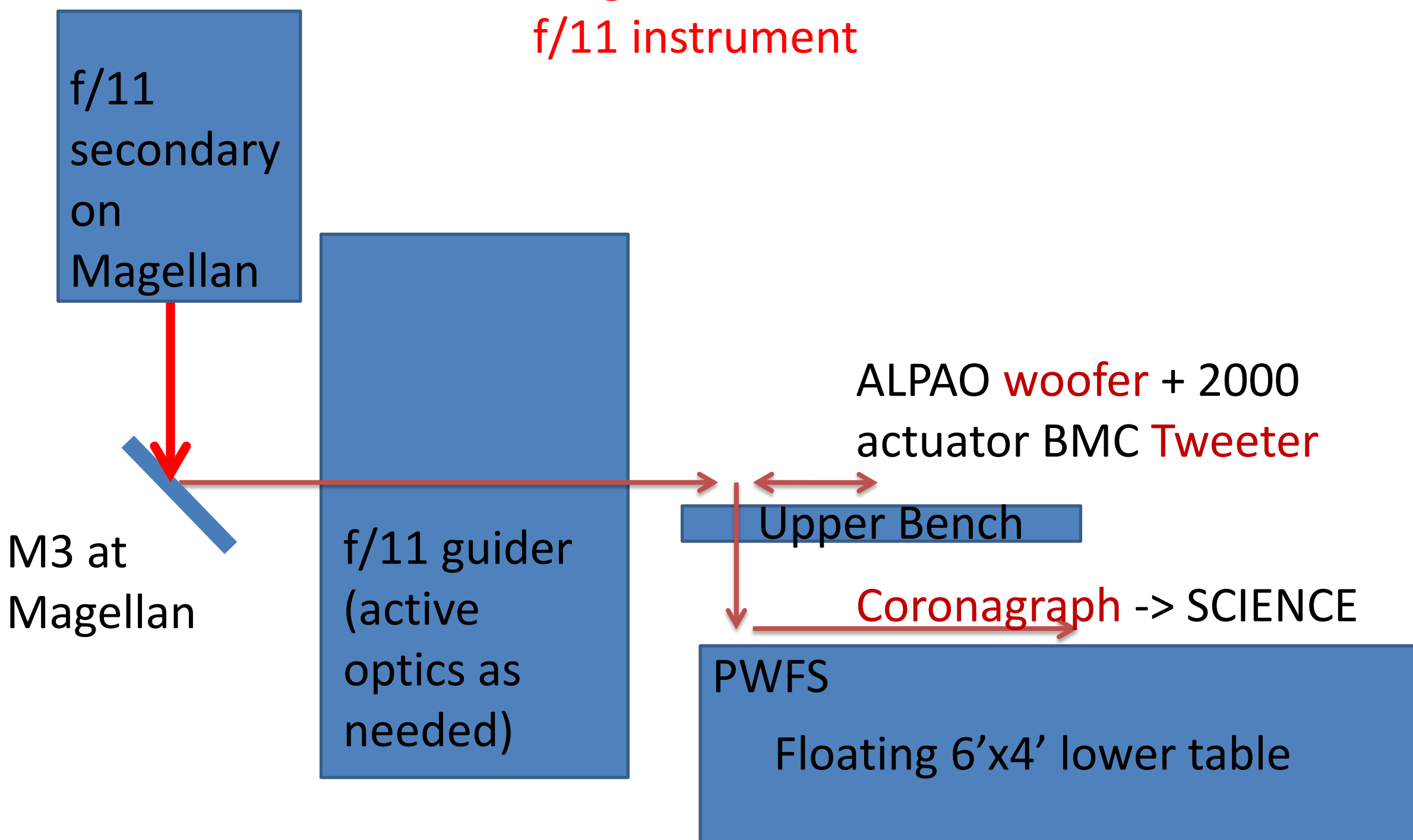
Appendix A1: Optical interface to Magellan

Laird Close

4/18/2017



Conceptual design of f/11 MagAO-X optics with Coronagraph



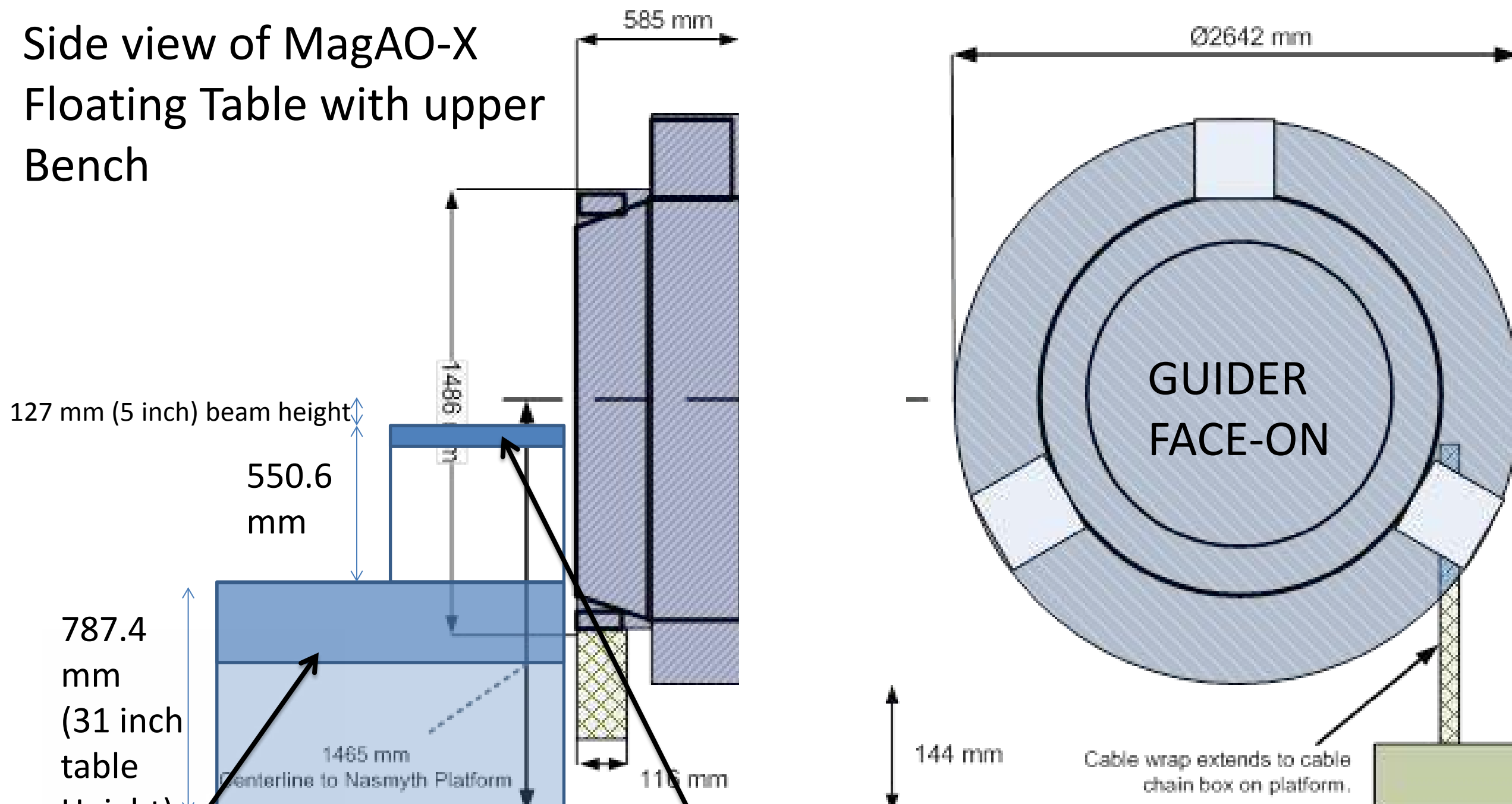
MagAO-X Summary:

~80% Strehl at 0.65 microns + PIAACMC coronagraph with **Contrasts of 10^{-5} - 10^{-6}** @50 mas and 10⁻⁶ @150 mas on a 5th mag star in median conditions. Also can feed MKID or RHEA IFS R=60,000 (PI Ireland)



9.6mm air gap between table and f/11 guider for 125mm back focal dist.

Side view of MagAO-X
Floating Table with upper
Bench



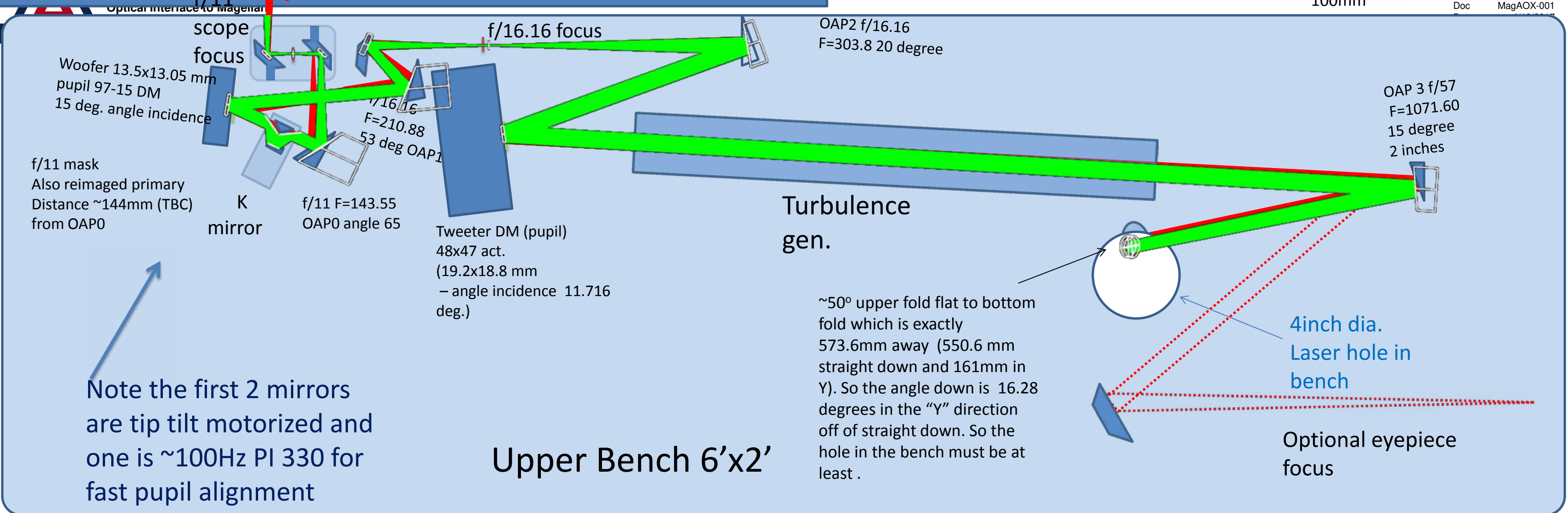
Lower 6'x4'x1' TMC research grade optical top

Upper 2'x6'x4" TMC research grade optical breadboard (aligned with Table)

F11 guider

100mm

Doc MagAOX-001



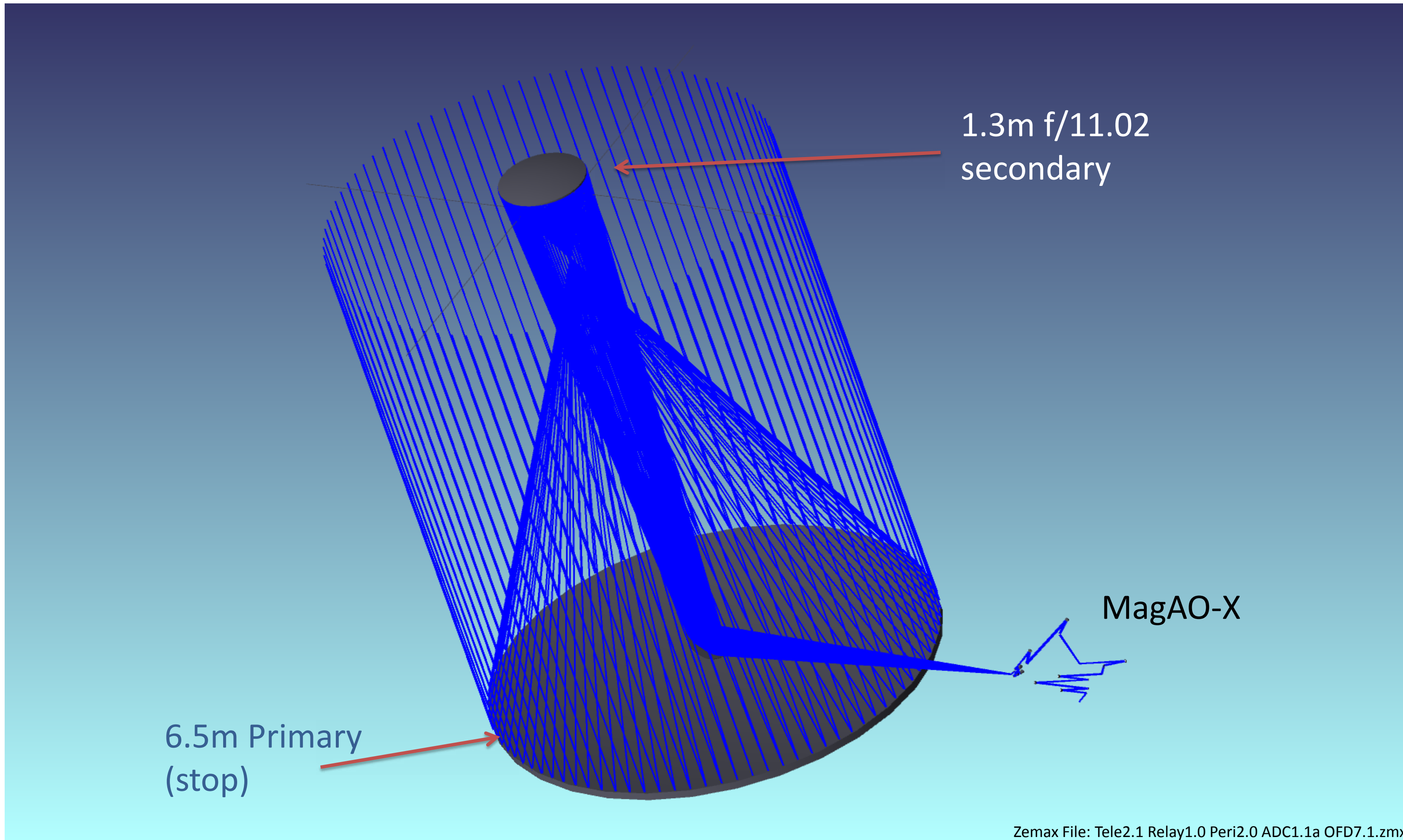
Zemax design in Green – agrees with our analytical optical design, OAPs and pupils correct in ZEMAX.

OPTICAL DESIGN

- Zemax design by Oli Durney (Senior Optical Engineer Steward Observatory) from initial analytical design
- The design is all reflective (save the ADCs)
- All the powered optics are OAPs (eliminates ghosts and chromaticity)
- The ADC design is diffraction-limited from 1-2 airmasses and from 0.6 to 1.8 microns. The ADC is commonpath with the PWFS and the science cameras.
- The design was first analytically done by Laird Close and then done with zemax by Oli Durney. Both designs are in excellent agreement.
- The true aperture stop (the primary mirror) is relayed to the Woofer pupil to the Tweeter pupil to the first coronagraphic pupil to the Lyot stop.
- The first coronagraphic focal plane is f/67 and is the location of the coronagraphic mask
- The final focal plane is after the Lyot stop and is also f/67 yielding a 6mas/pixel platescale on the Ultra 888 science camera.
- The optical quality of the on-axis beam has a Strehl 100% (with perfect optics) over any broad band astronomical filter that we would use (such as r',i',z',J, H).

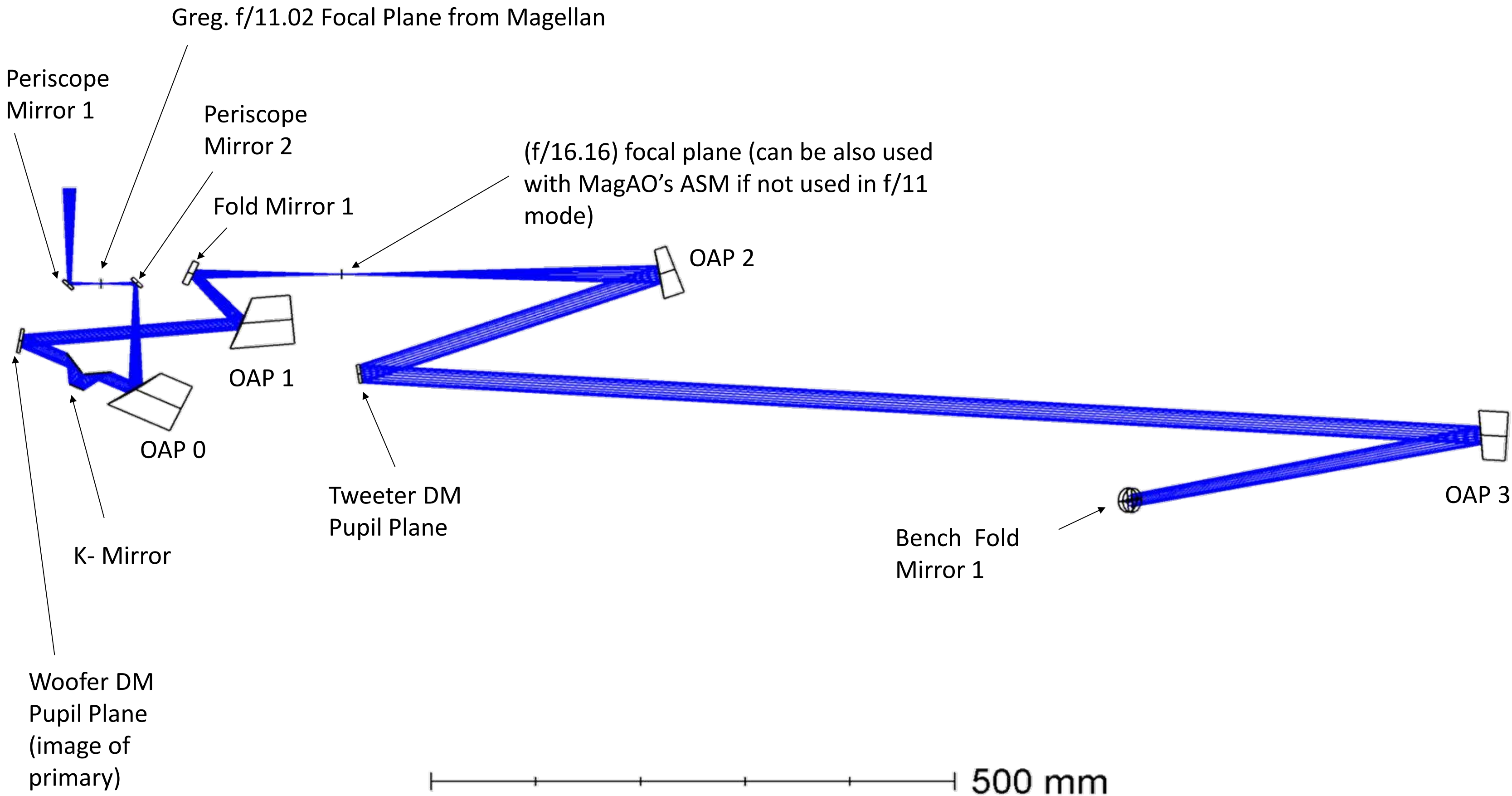


Shaded Model of f/11 + MagAO-X



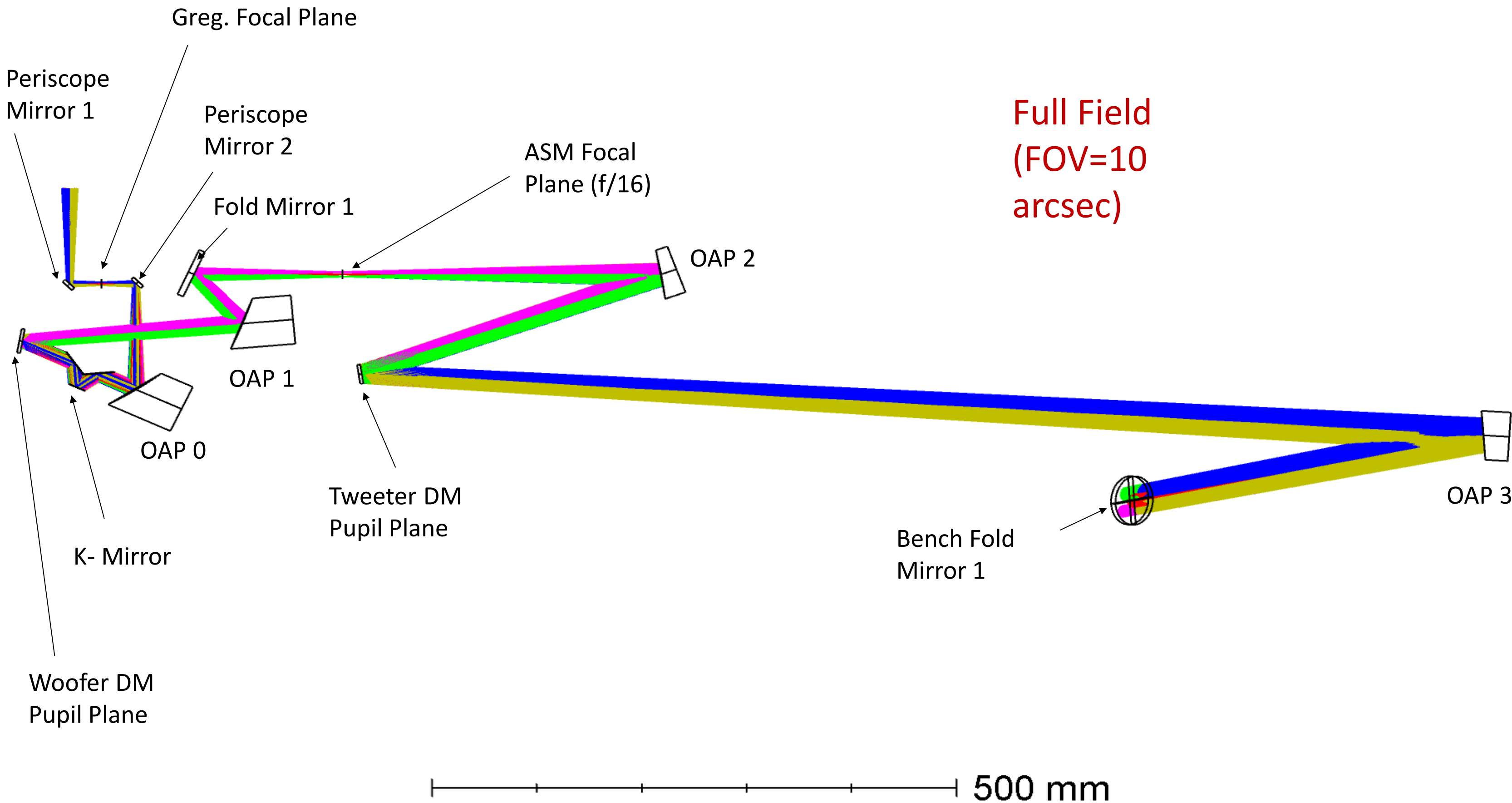


Upper Bench Optical Design (on-axis)



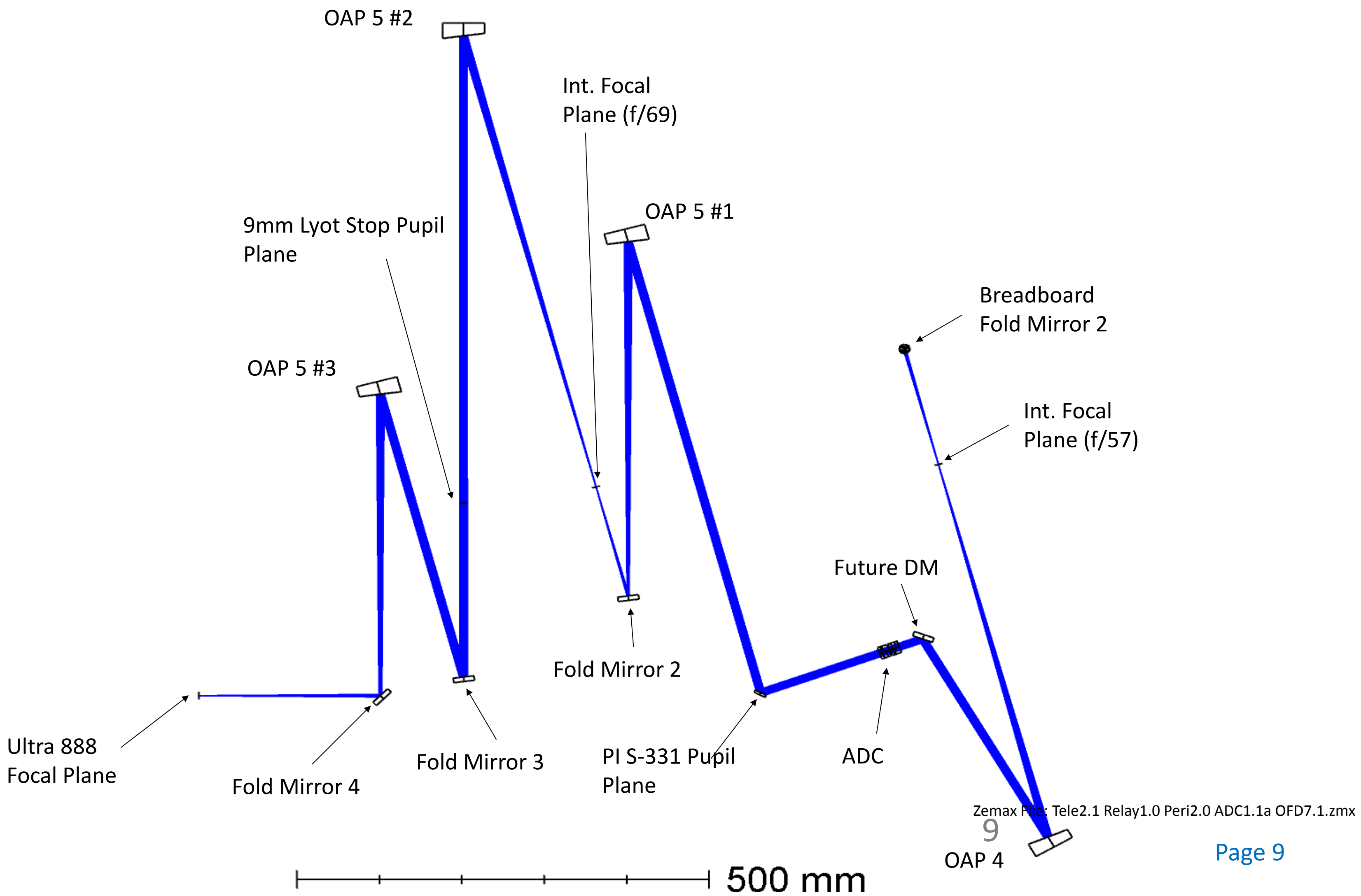


Upper Bench Optical Design (10" FOV)



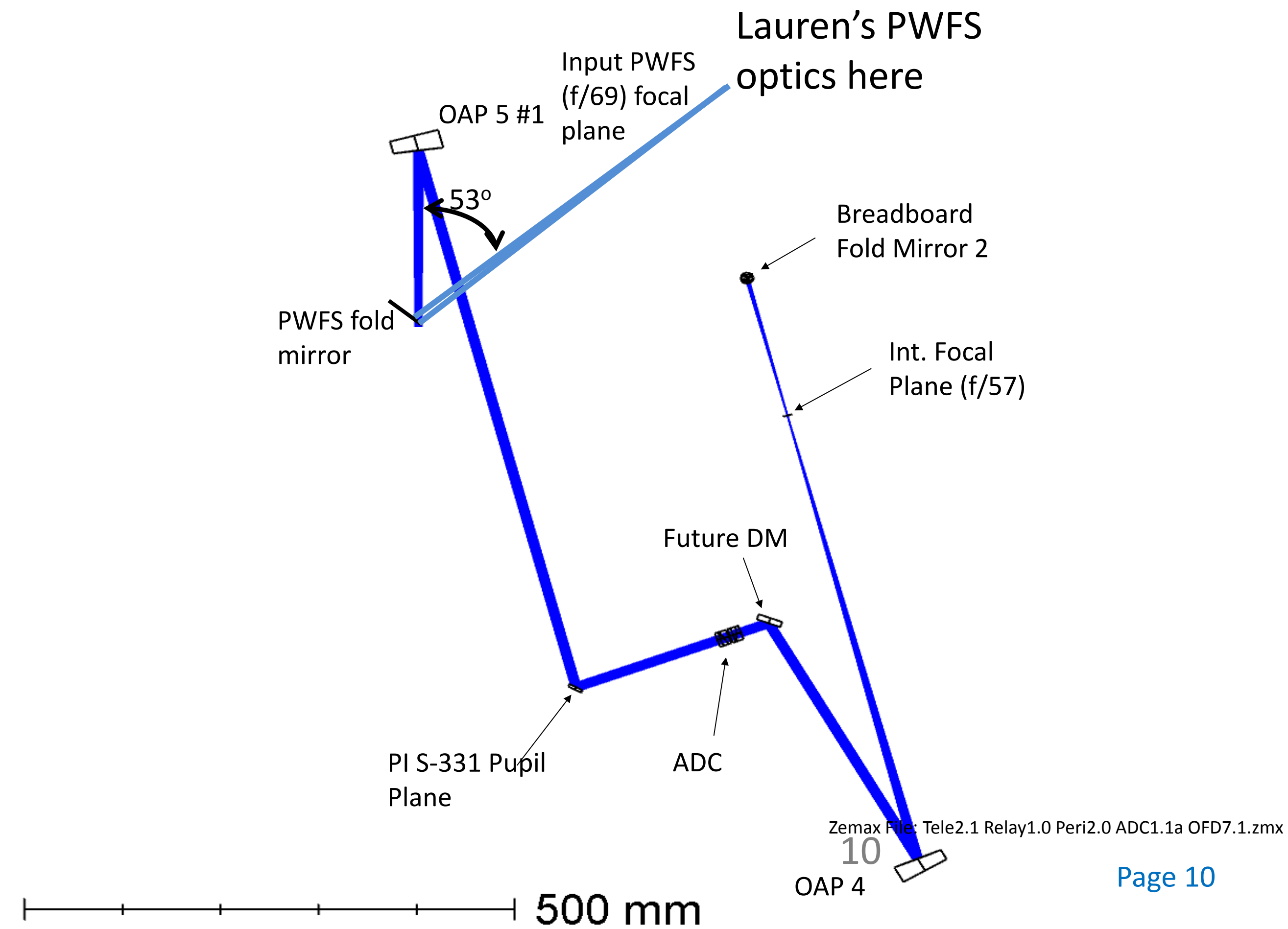


Lower Table Optical Design On-Axis

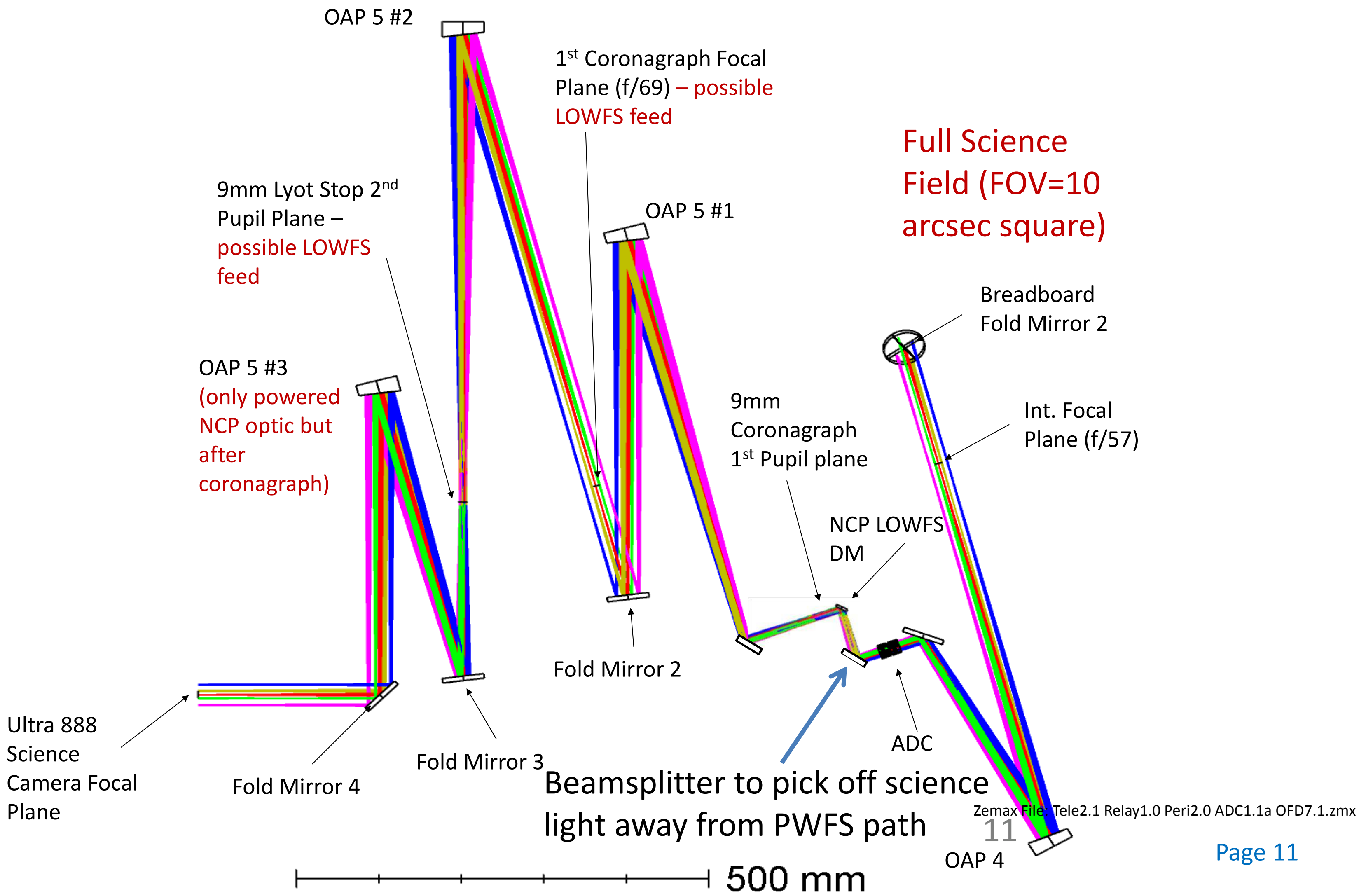




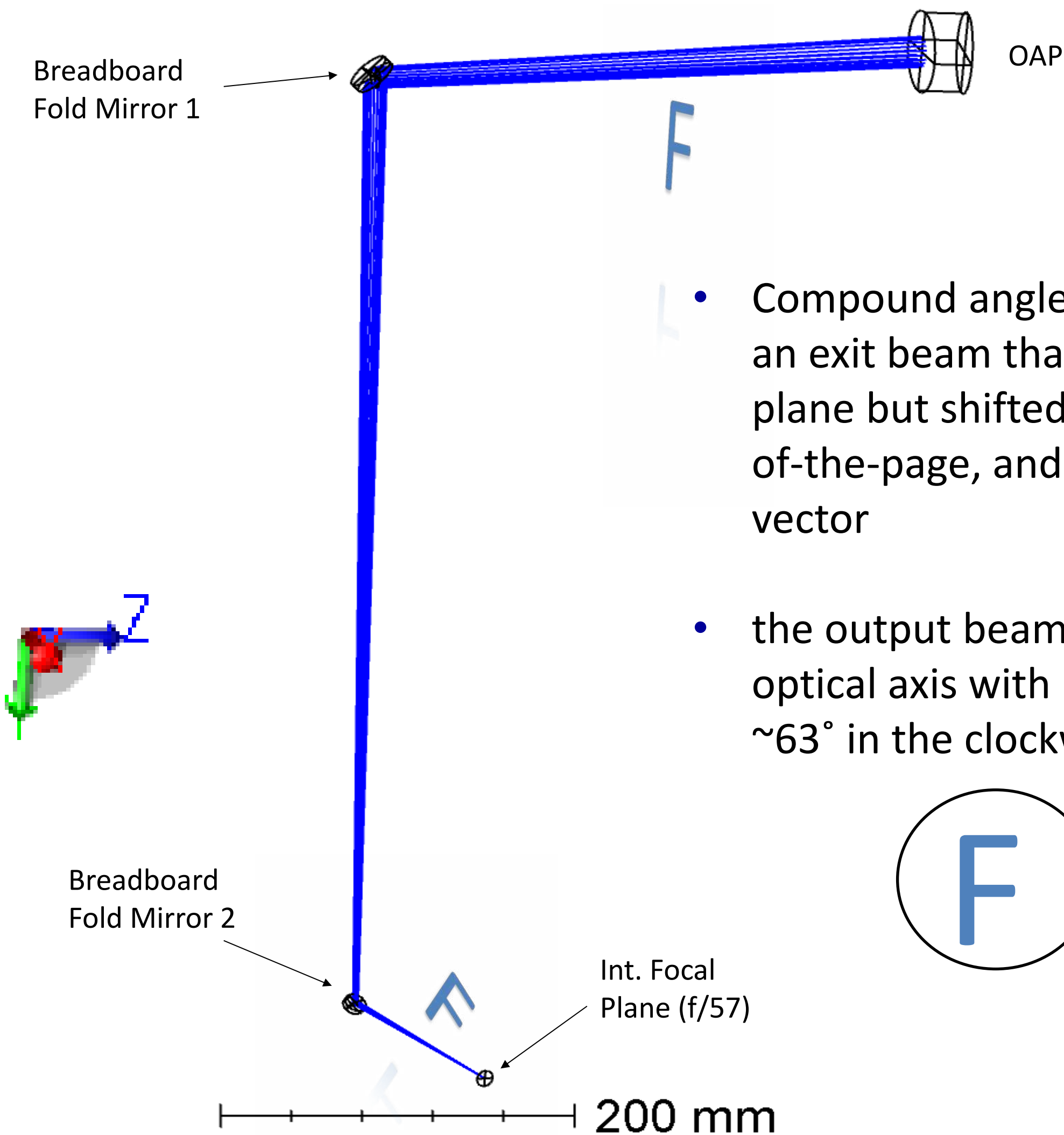
Lower Table Optical Design with PWFS



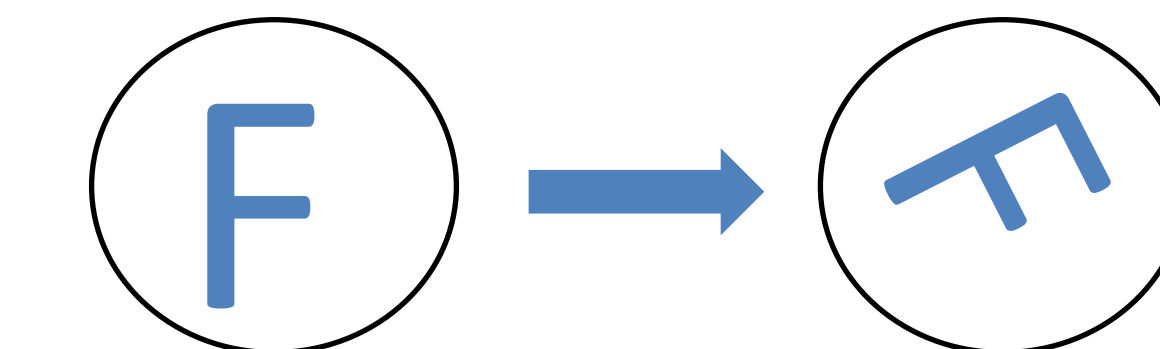
Lower Table Science Full FOV



Bench to Table Periscope

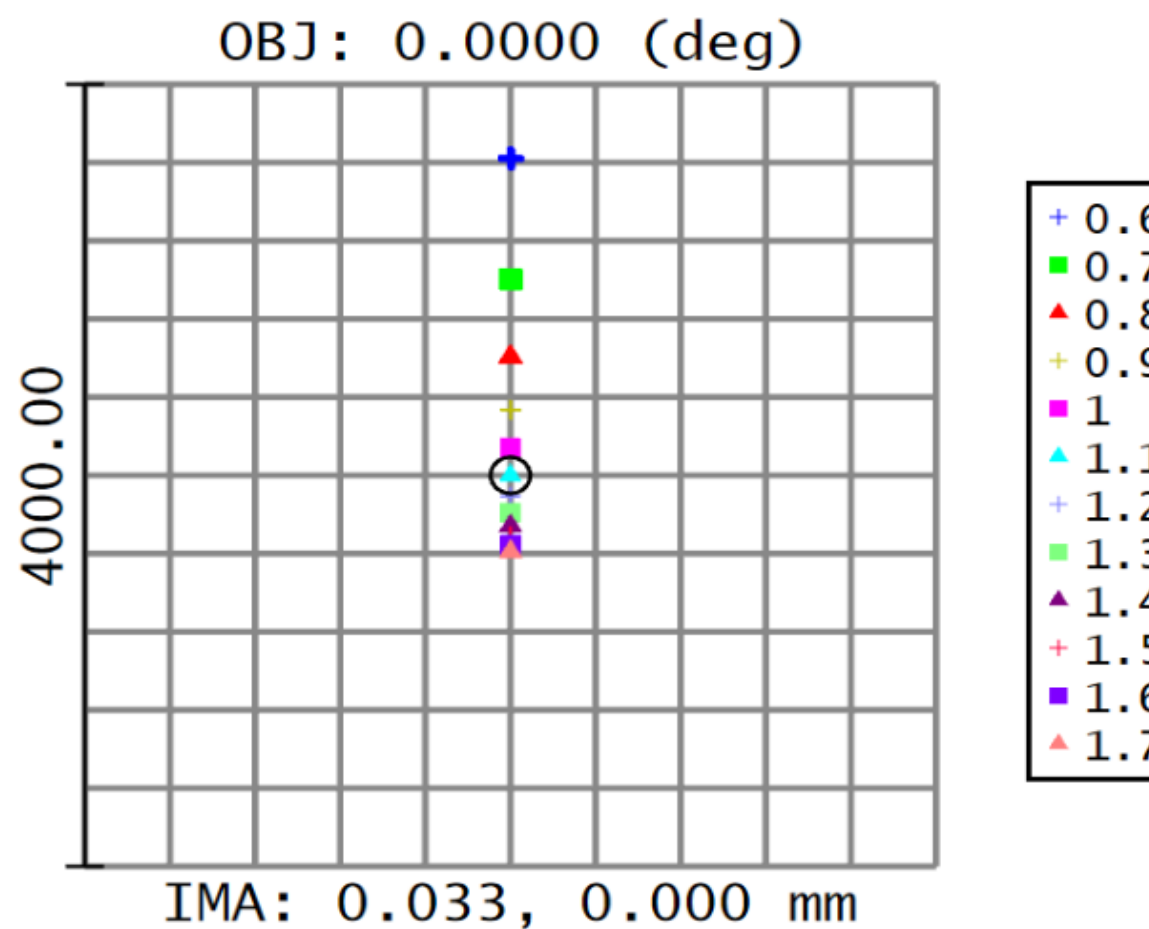


- Compound angles for both BBFM1 & 2 result in an exit beam that is parallel with the input beam plane but shifted 550.6 mm lower, 161 mm out-of-the-page, and rotated in its output direction vector
- the output beam is also rotated about the optical axis with respect to the input beam by ~63° in the clockwise direction.

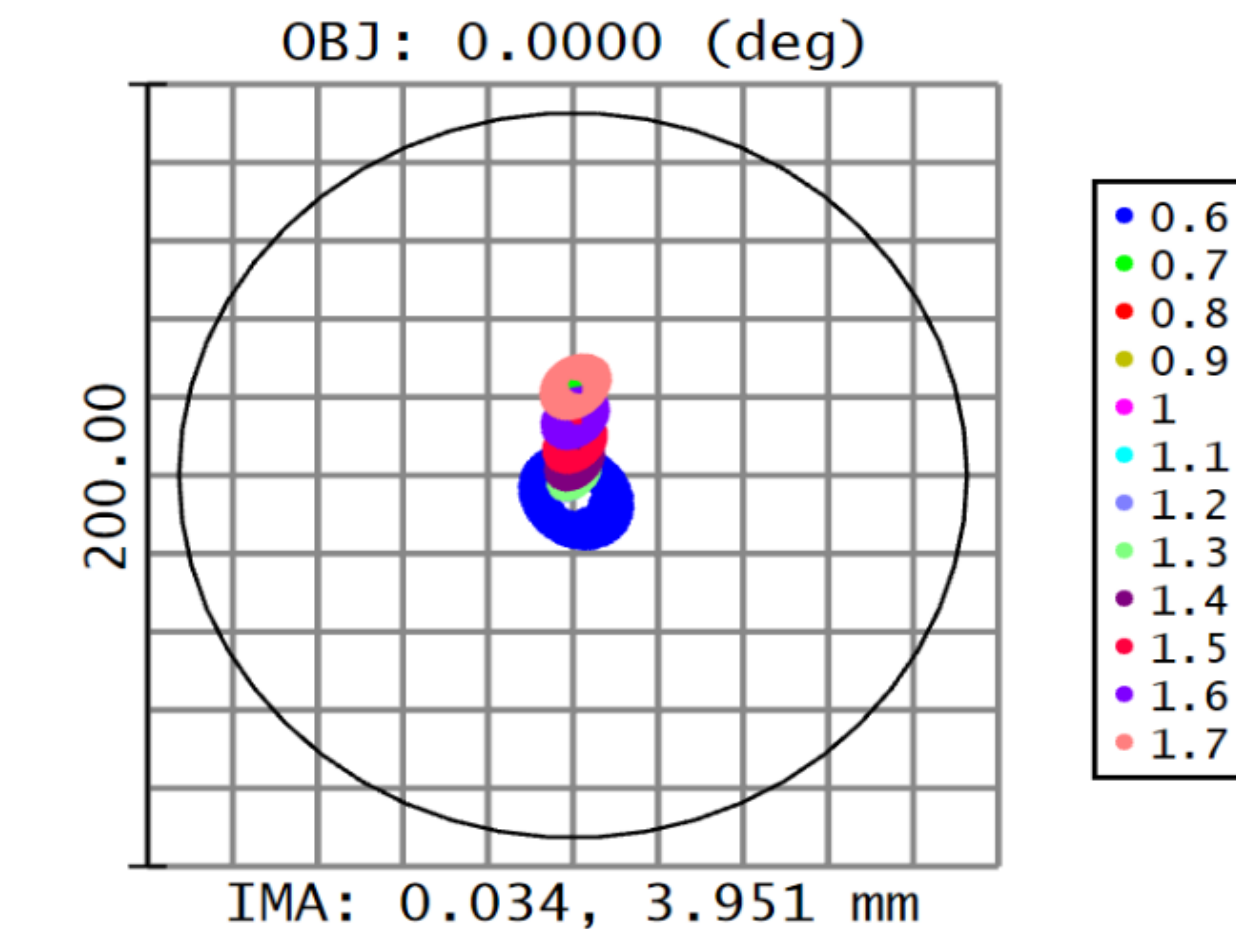


Spot Diagrams for Zenith Z=40° w/ ADC

No ADC Correction



ADC Correction (Current Design)



Surface TMA: Ultra 888 Focal Plane

Spot Diagram

Magellan With f/11 Secondary
2/16/2017
Units are μm . Airy Radius: 92.64 μm . Legend items refer to Wavelengths
Field : 1
RMS radius : 620.382
GEO radius : 1635.77
Scale bar : 4000 Reference : Chief Ray

Steward Observatory
933 N. Cherry Ave.
Tucson, AZ 85721

Tele2.1 Relay1.0 Peri2.0 ADC1.1a OFD5.5.zmx
Configuration 7 of 7

Surface TMA: Ultra 888 Focal Plane

Spot Diagram

Magellan With f/11 Secondary
2/16/2017
Units are μm . Airy Radius: 92.65 μm . Legend items refer to Wavelengths
Field : 1
RMS radius : 12.594
GEO radius : 30.627
Scale bar : 200 Reference : Chief Ray

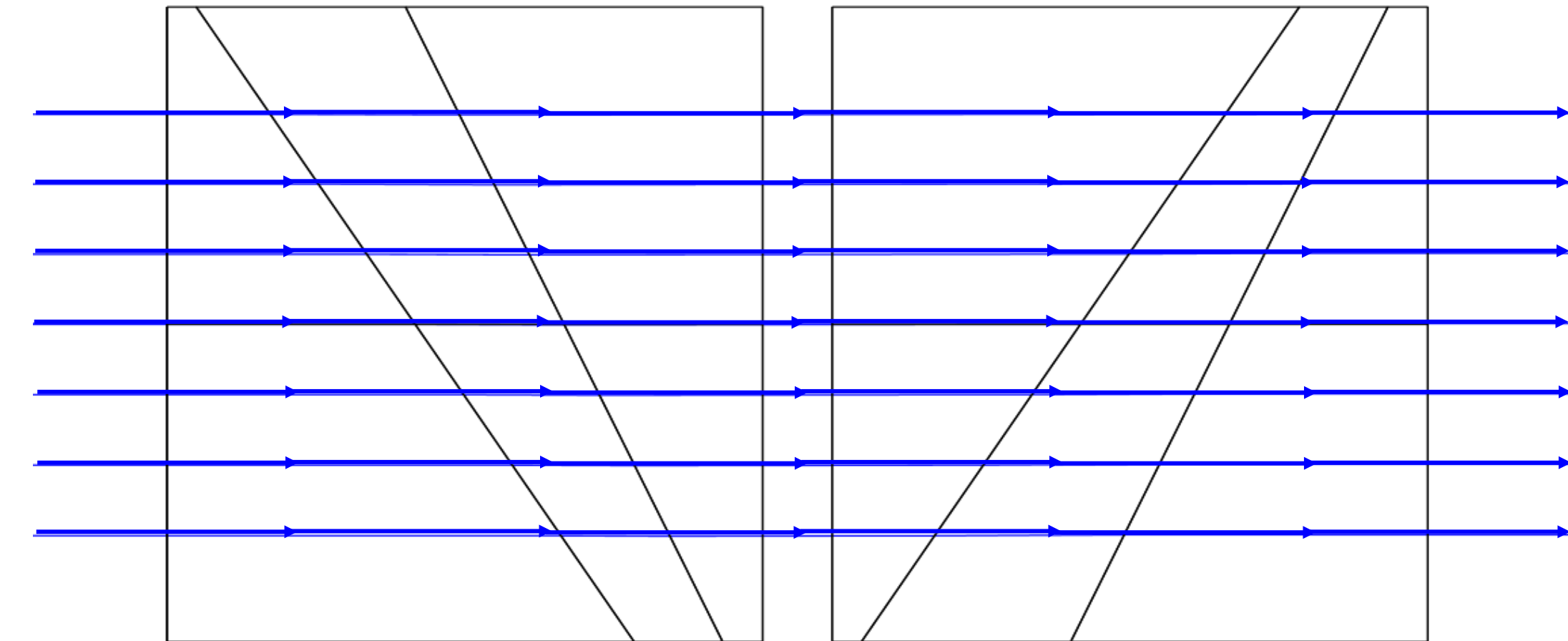
Steward Observatory
933 N. Cherry Ave.
Tucson, AZ 85721

Tele2.1 Relay1.0 Peri2.0 ADC1.1a OFD5.5.ZMX
Configuration 7 of 7

ADC Prism Design Layouts

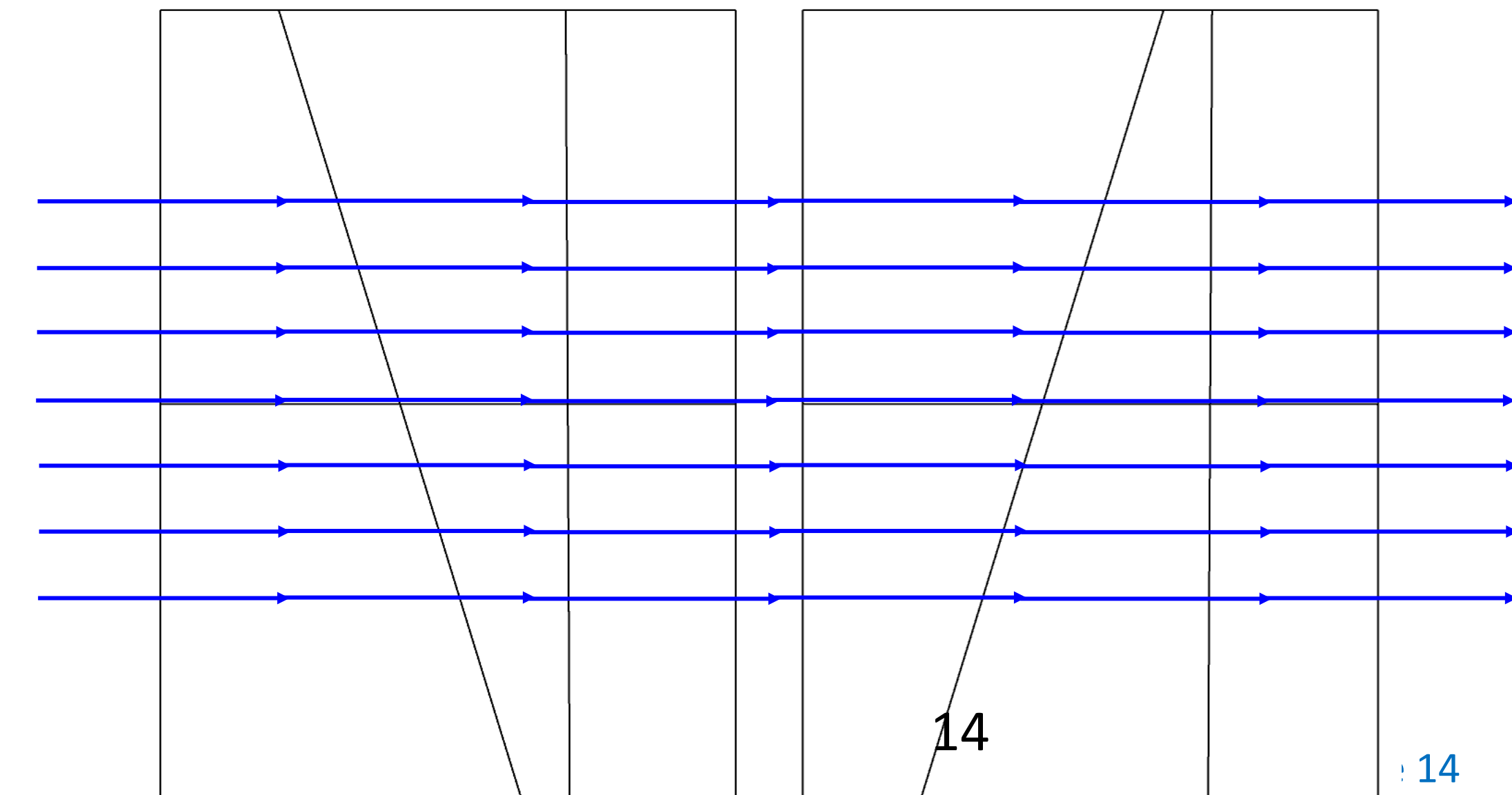
Current ADC Design

- $\phi = 14 \text{ mm}$
- S-PHM53, S-TIM8, N-KZFS4
- CT = 5.0, 3.0, 4.0 mm
- $\theta = 57.785^\circ, 65.474^\circ$



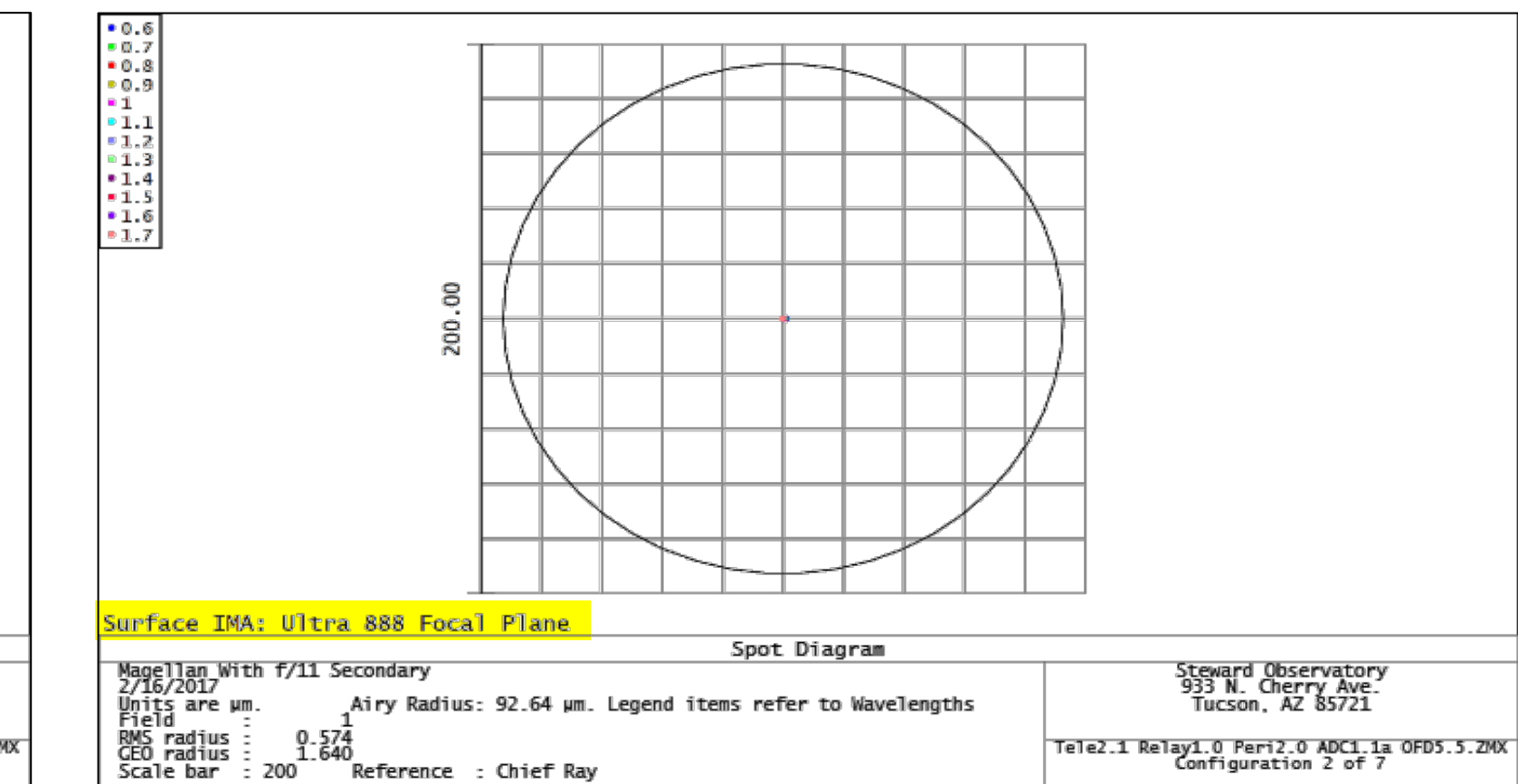
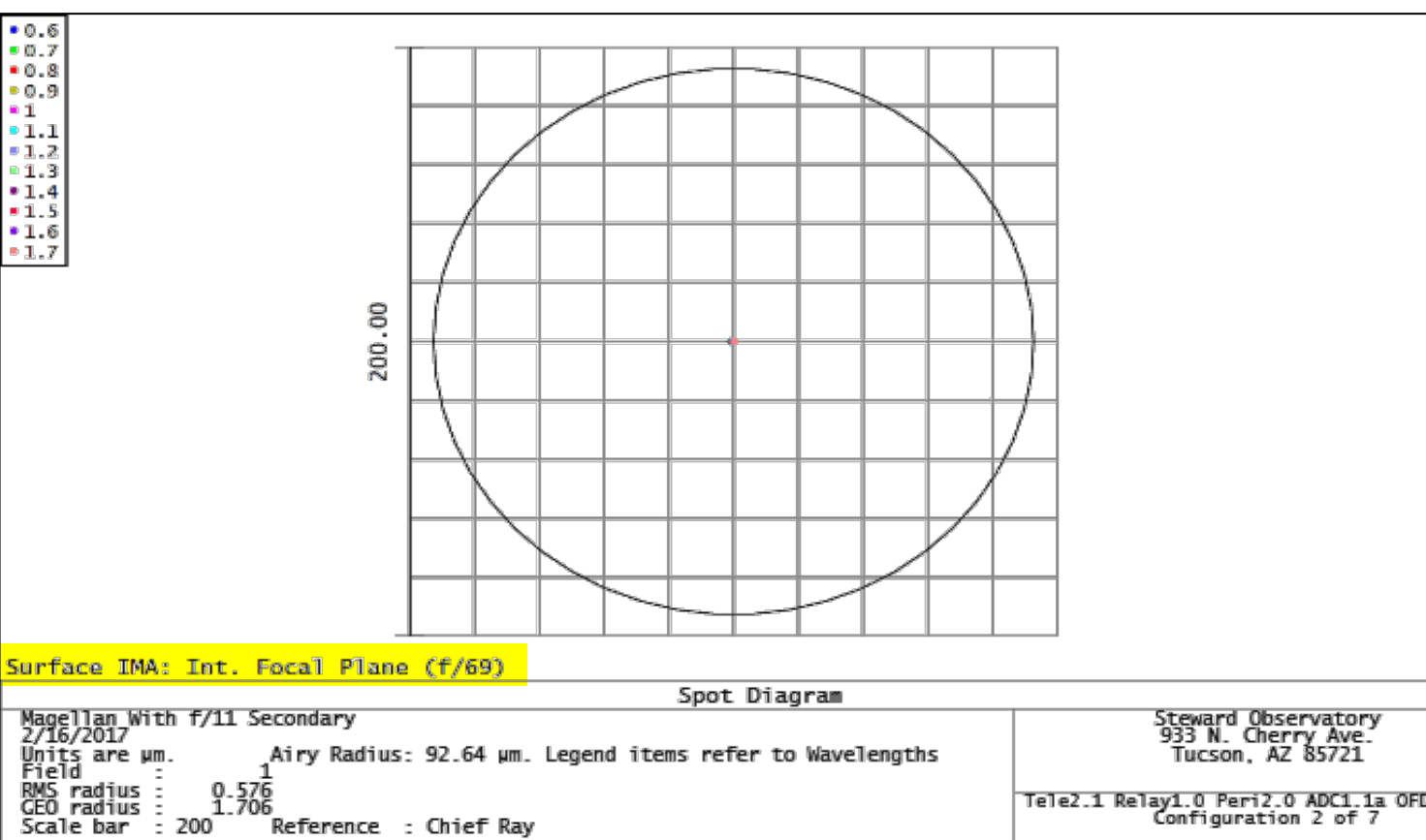
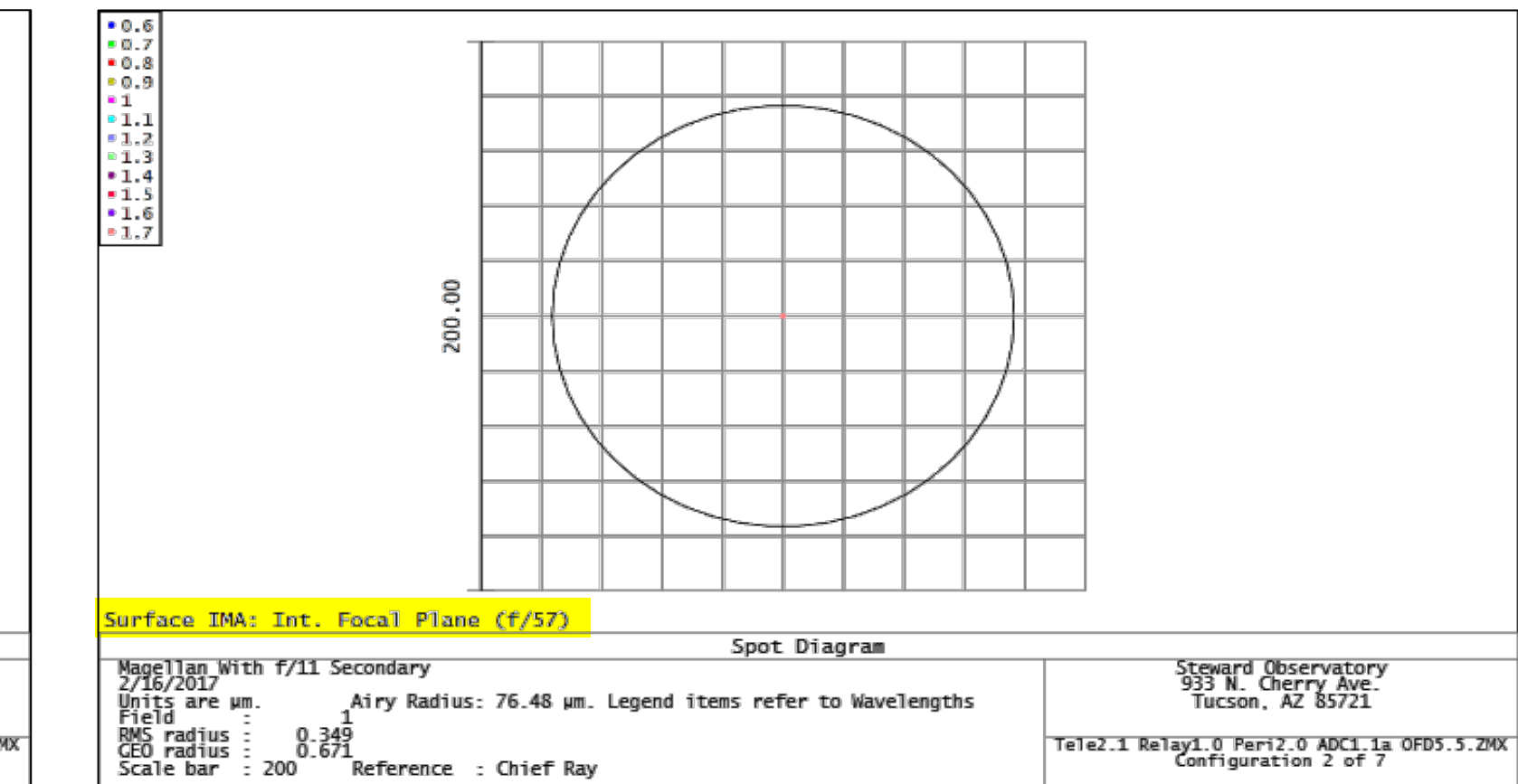
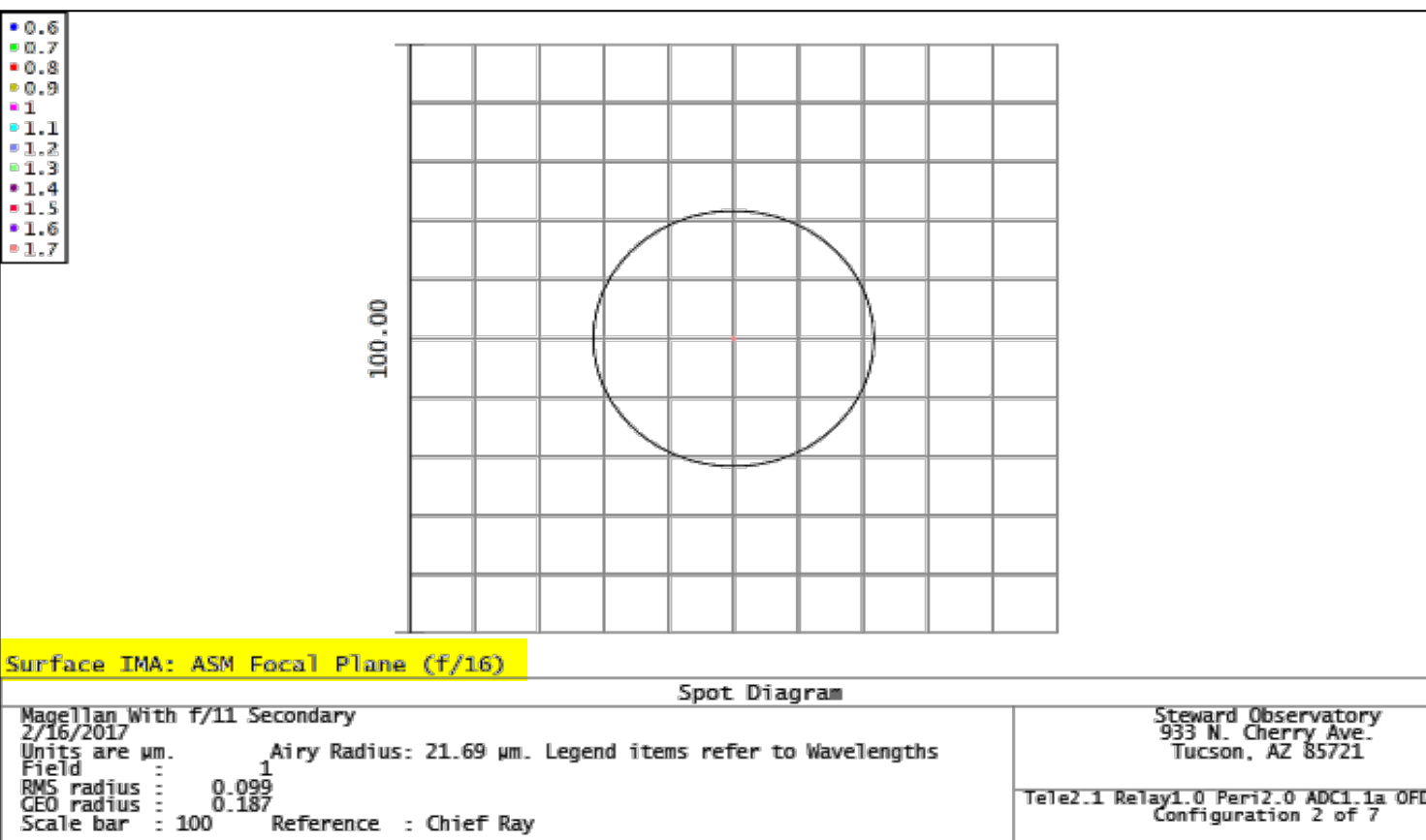
New ADC Design

- $\phi = 18 \text{ mm}$
- S-PHM53, S-TIM8, N-KZFS4
- CT = 5.0, 3.5, 3.5 mm
- $\theta = 73.687^\circ, 0.260^\circ$



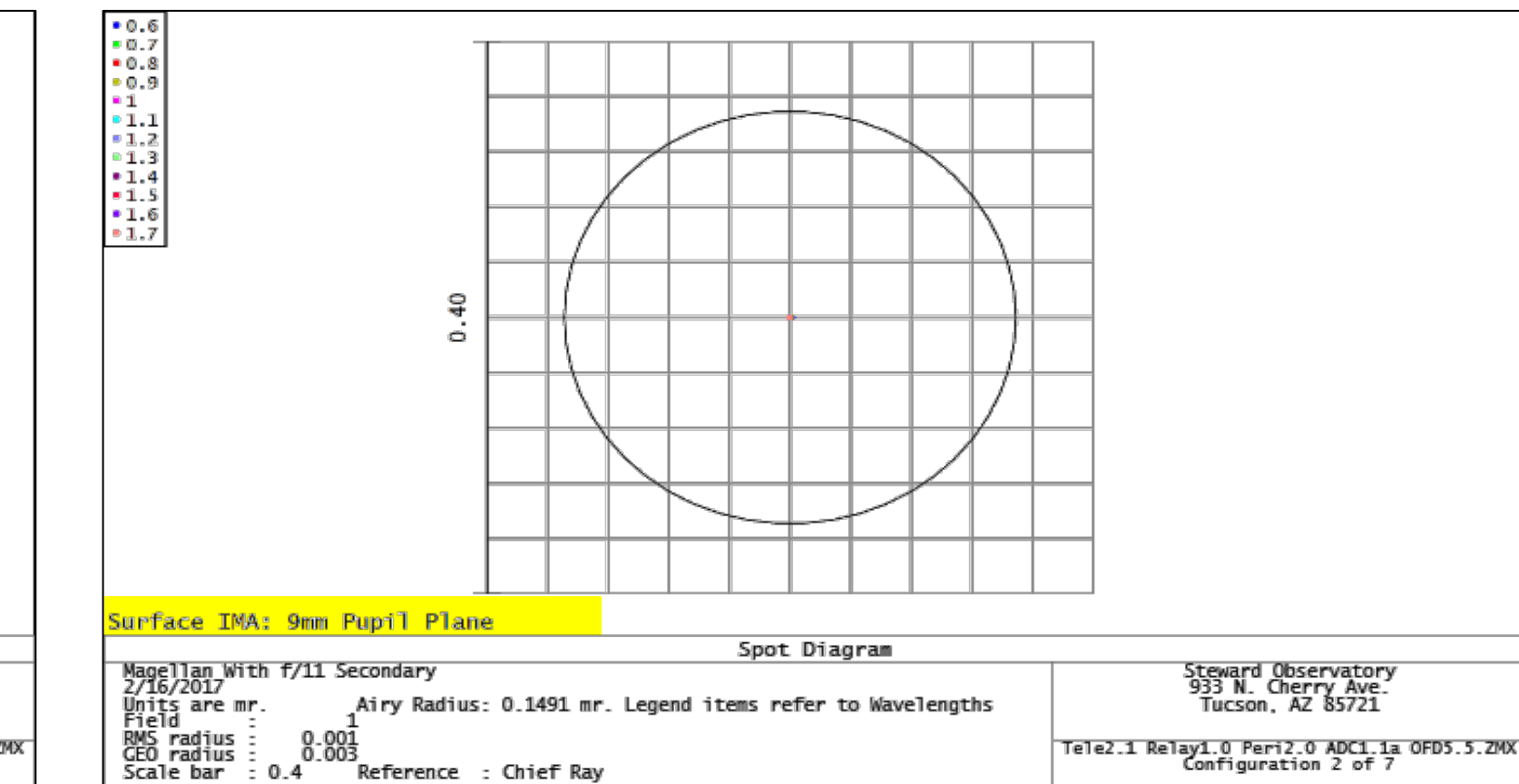
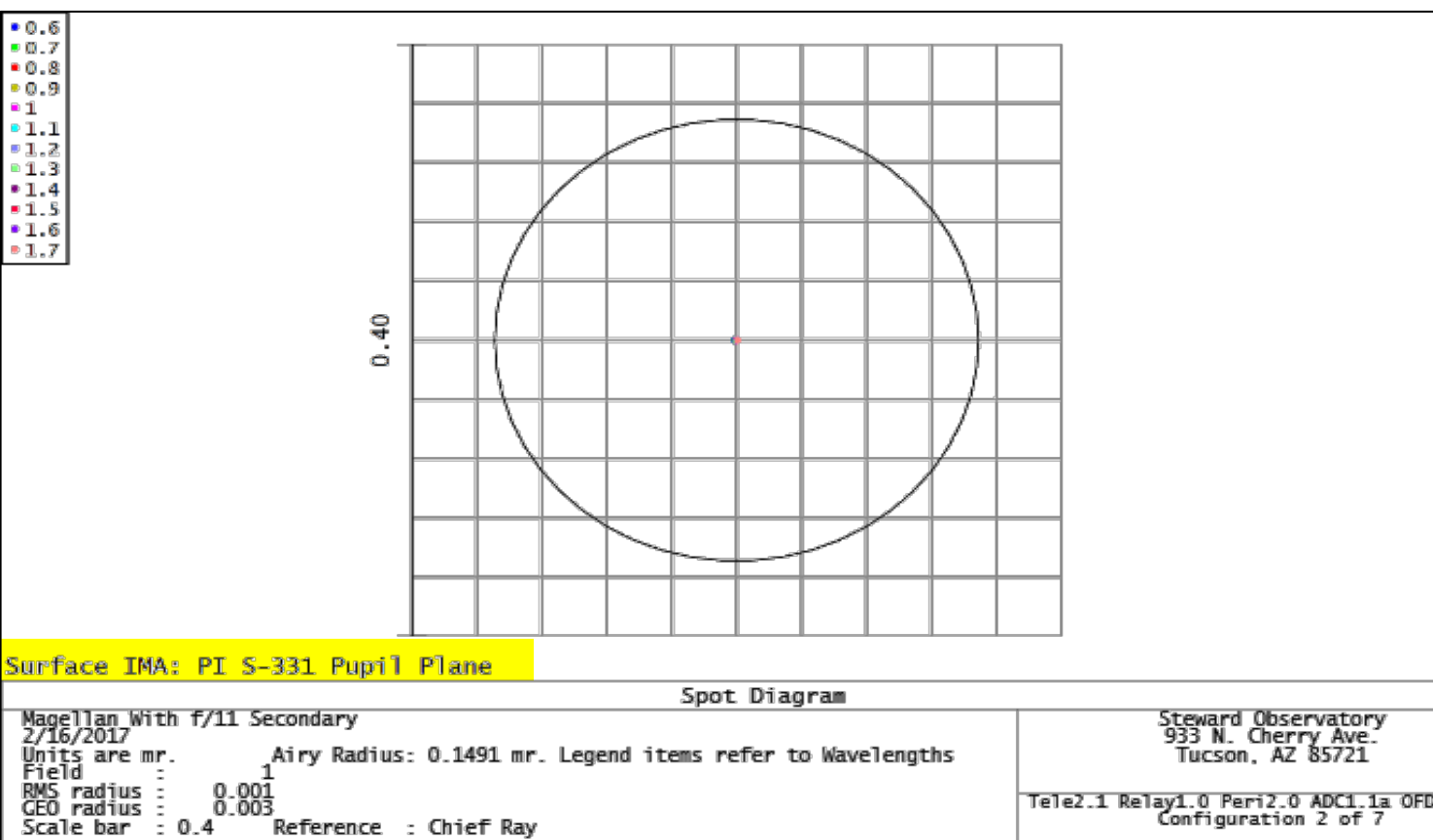
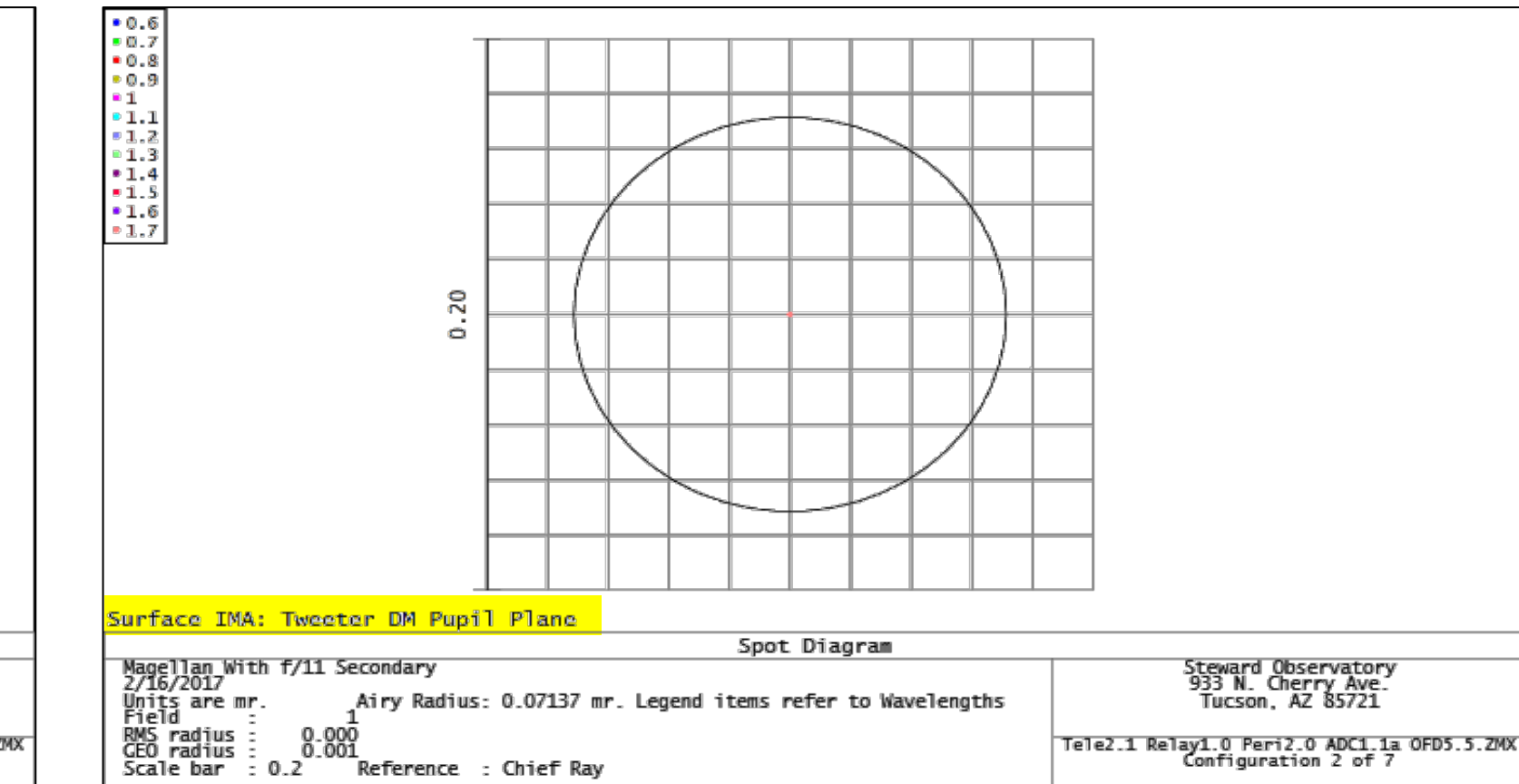
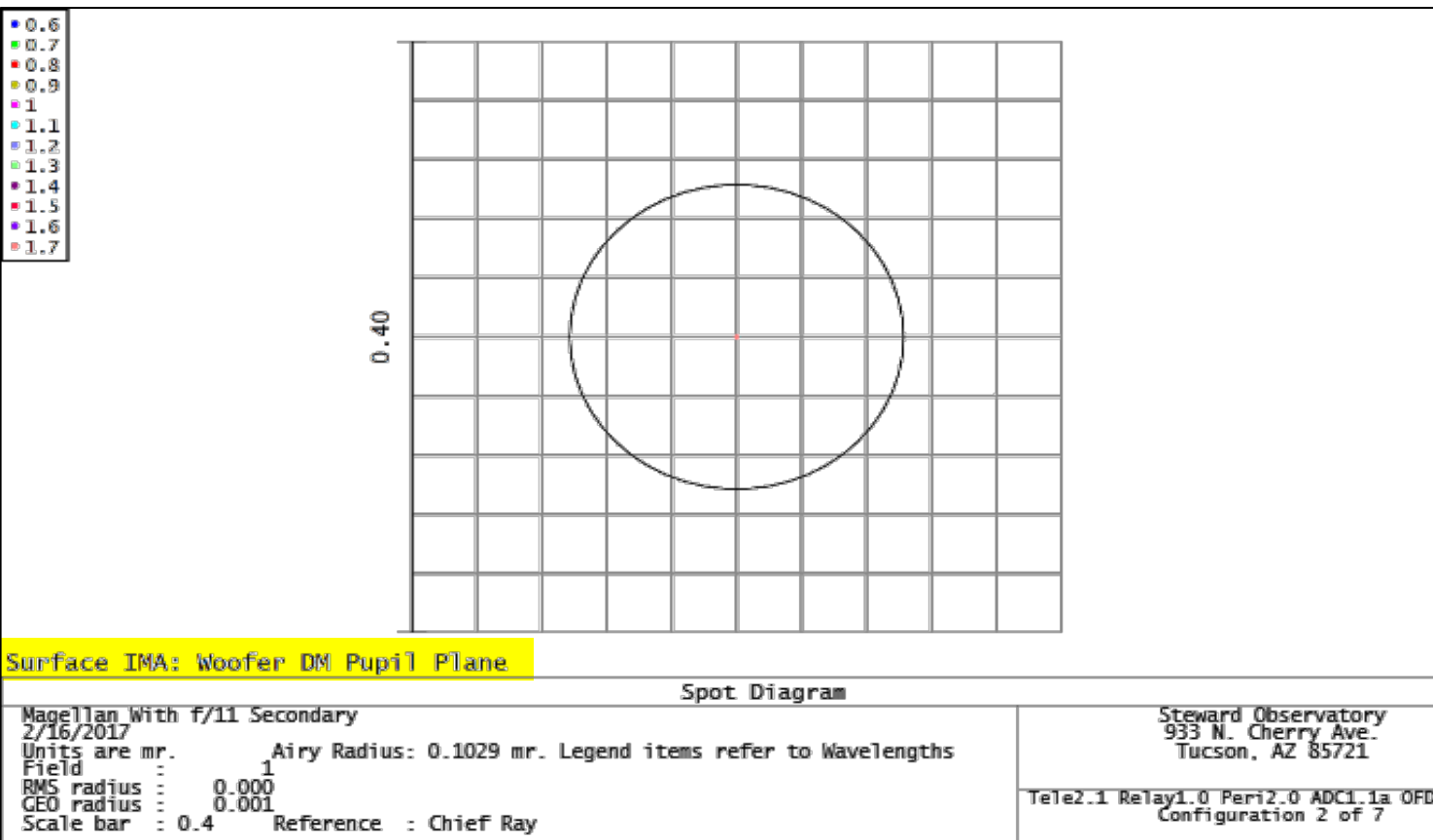


Spot Diagrams at Focal Planes

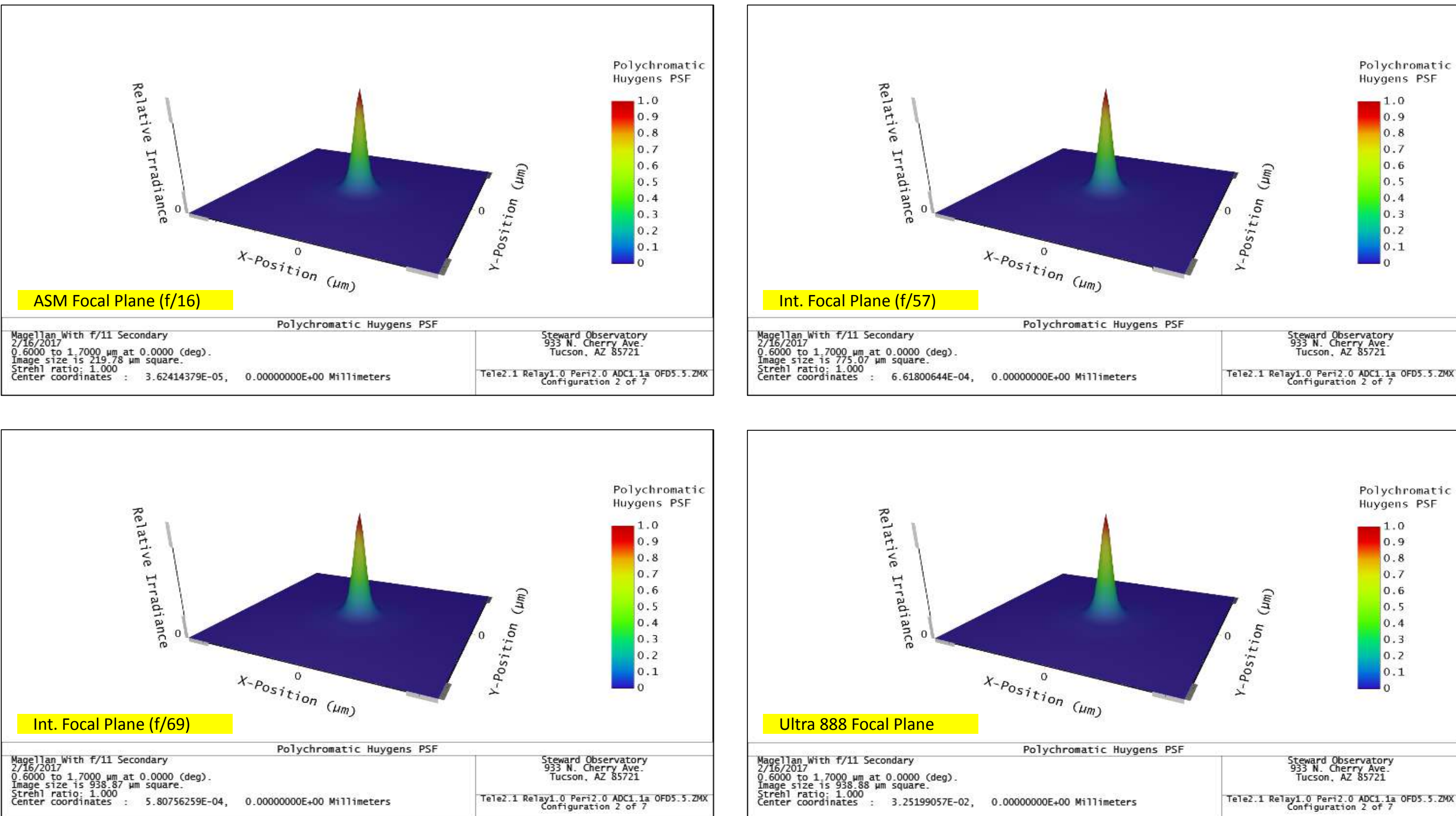




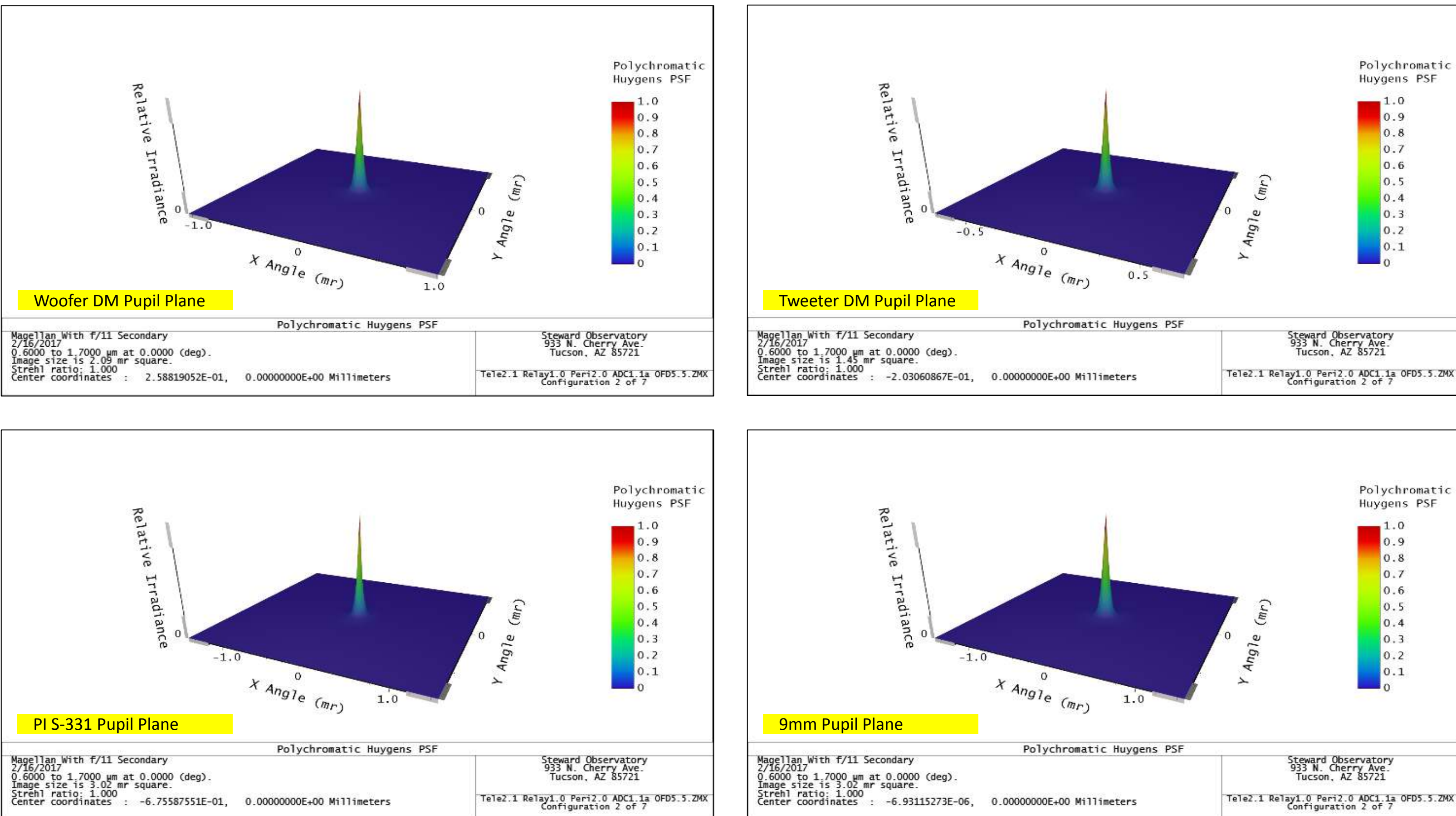
Spot Diagrams at Pupil Planes



PSF at Focal Planes



PSF at Pupil Planes





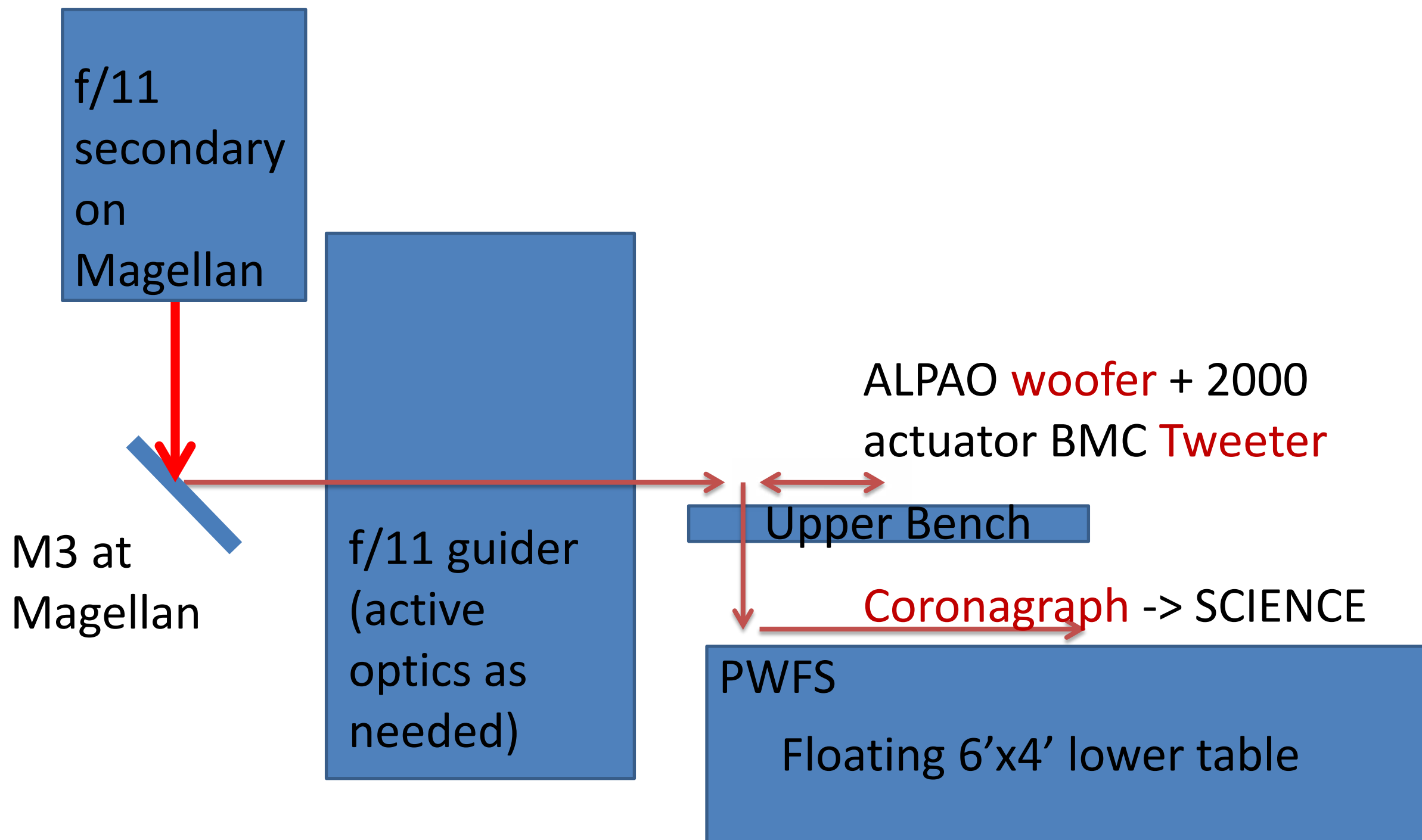
MagAO-X PDR

Appendix A2: Mechanical Interface to Magellan

Laird Close

4/18/2017

Conceptual design of f/11 MagAO-X optics with Coronagraph

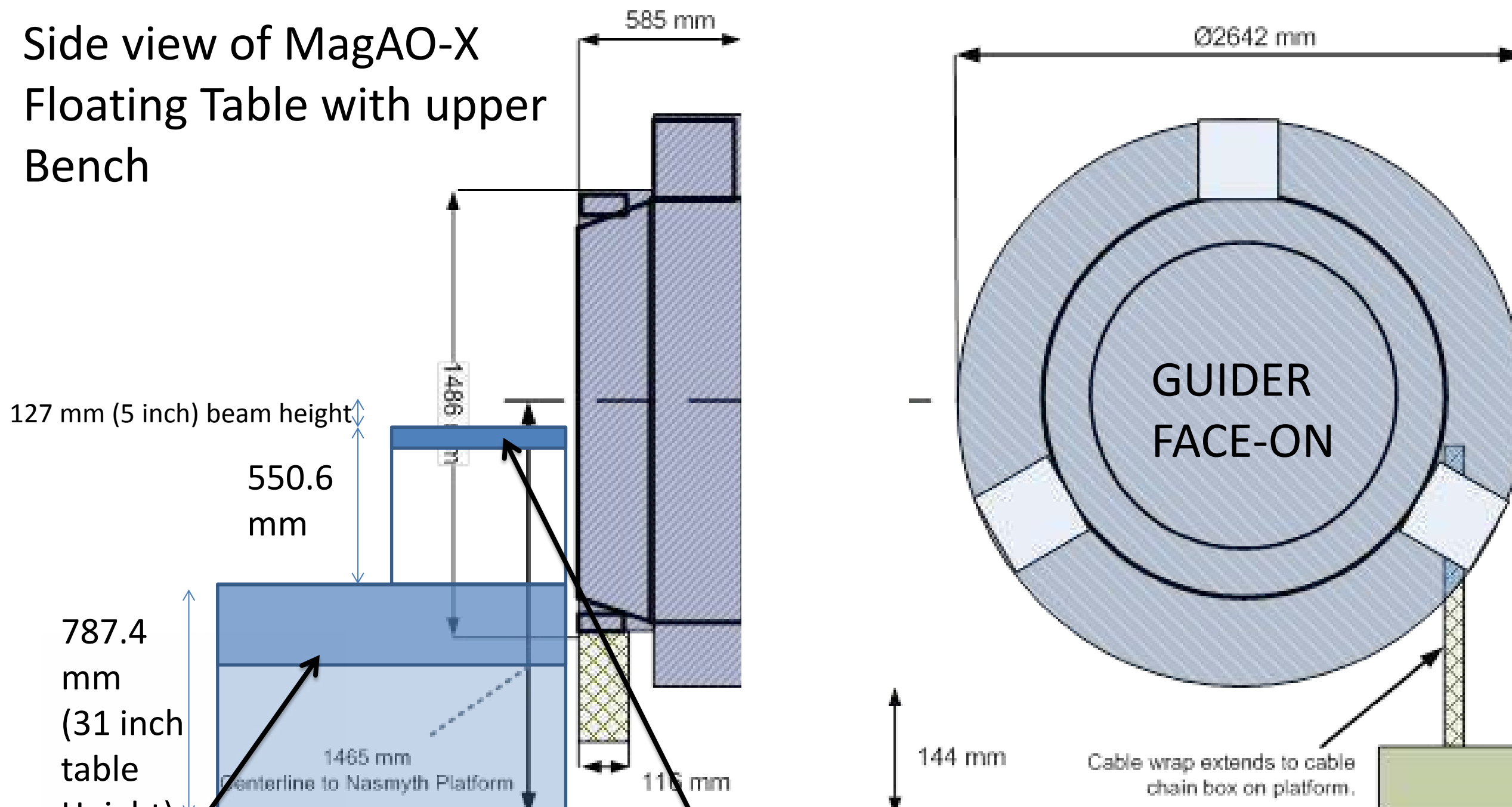


MagAO-X Summary:

~80% Strehl at 0.65 microns + PIAACMC coronagraph with **Contrasts of 10^{-5} - 10^{-6}** @50 mas and 10⁻⁶ @150 mas on a 5th mag star in median conditions. Also can feed MKID or RHEA IFS R=60,000 (PI Ireland)

9.6mm air gap between table and f/11 guider

Side view of MagAO-X
Floating Table with upper
Bench



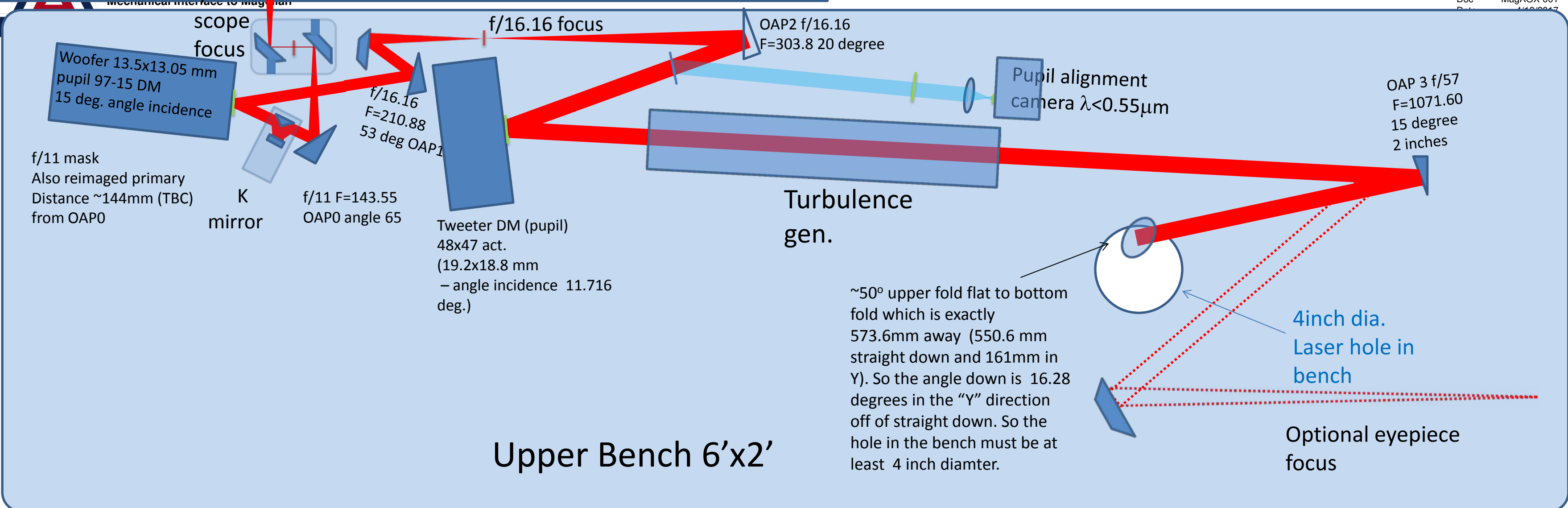
Lower 6'x4'x1' TMC research grade optical top

Upper 2'x6'x4" TMC research grade optical breadboard (aligned with Table)

F11 guider

100mm

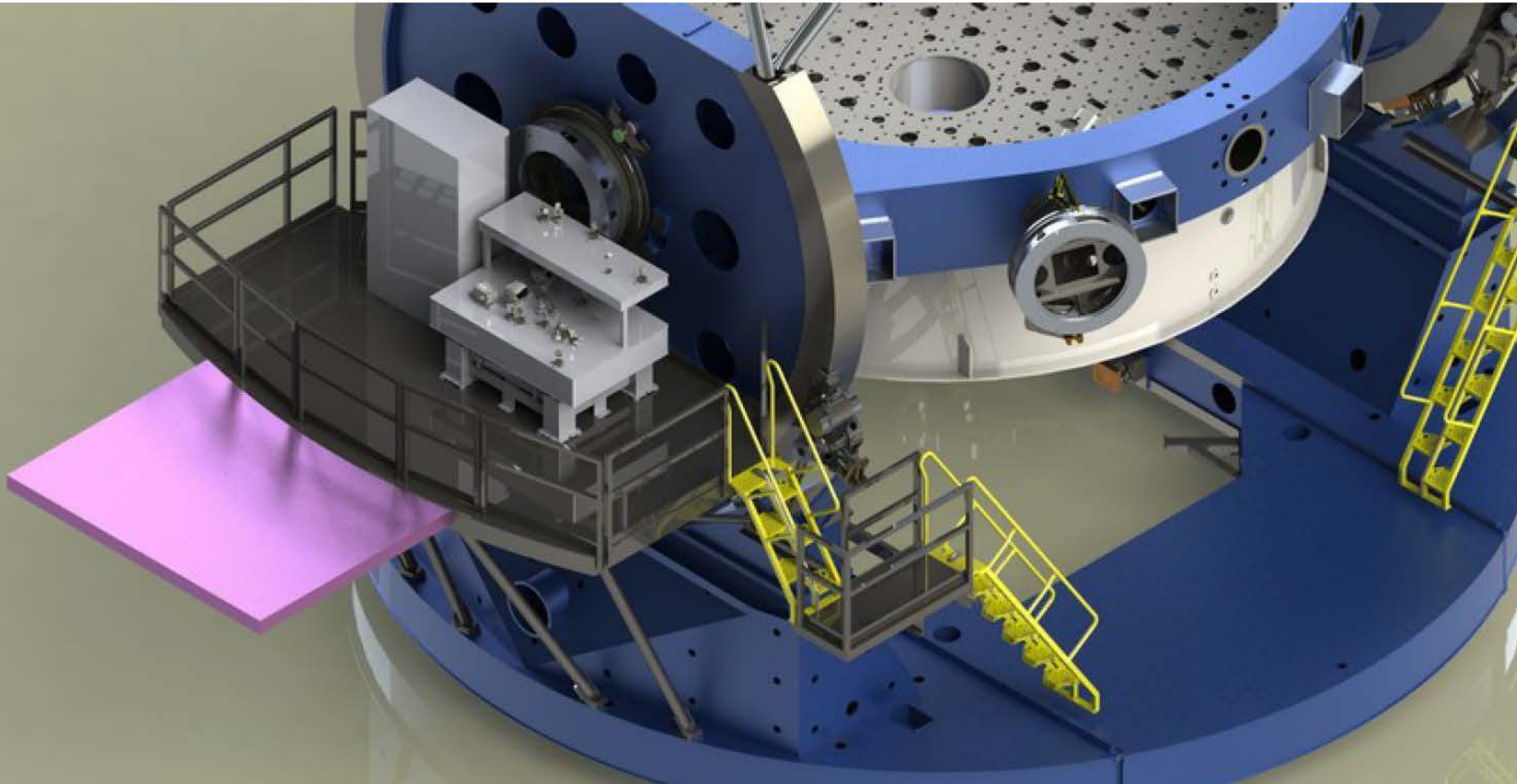
Doc
Rev
MagAOX-001
11/09/2017



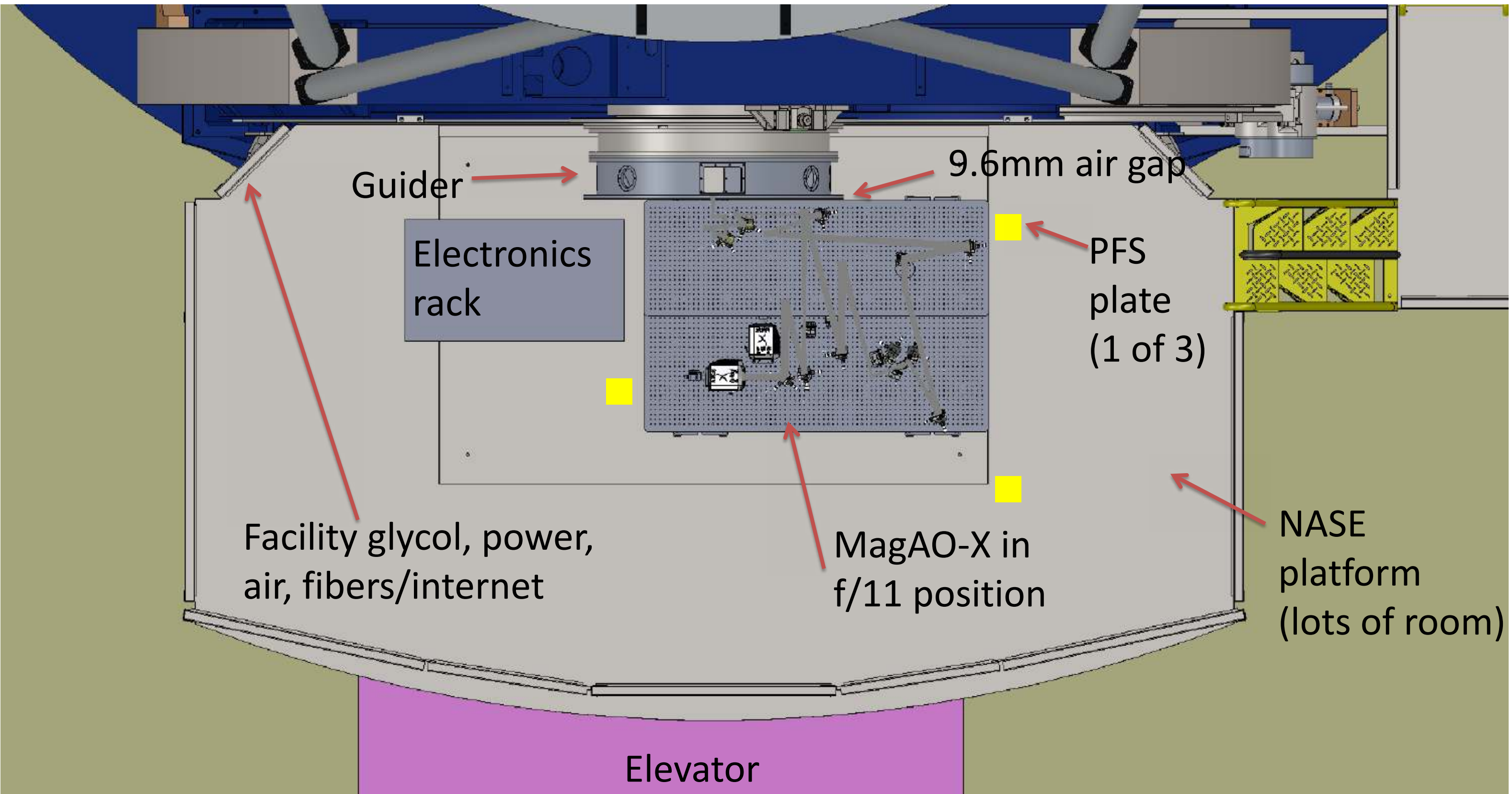
Analytical concept of the f/11
feed to the Woofer and Tweeter
on the upper bench



Completed Design At Magellan



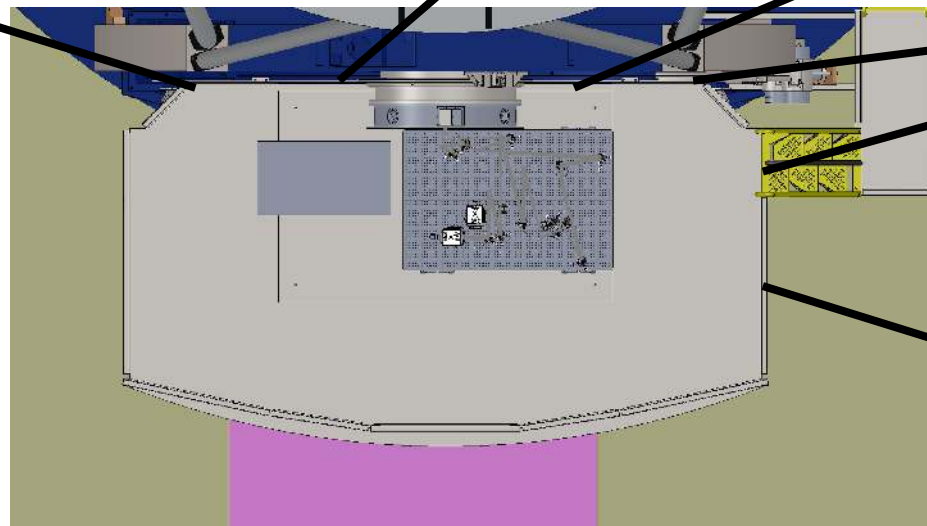
MagAO-X fits on the NASE





A.3 Electrical Interfaces

Jared R. Males



Existing NEMA 5-15 outlets on NASE
Orange = UPS (12x, 80 A total)
White = Direct (12x, 66 A total)

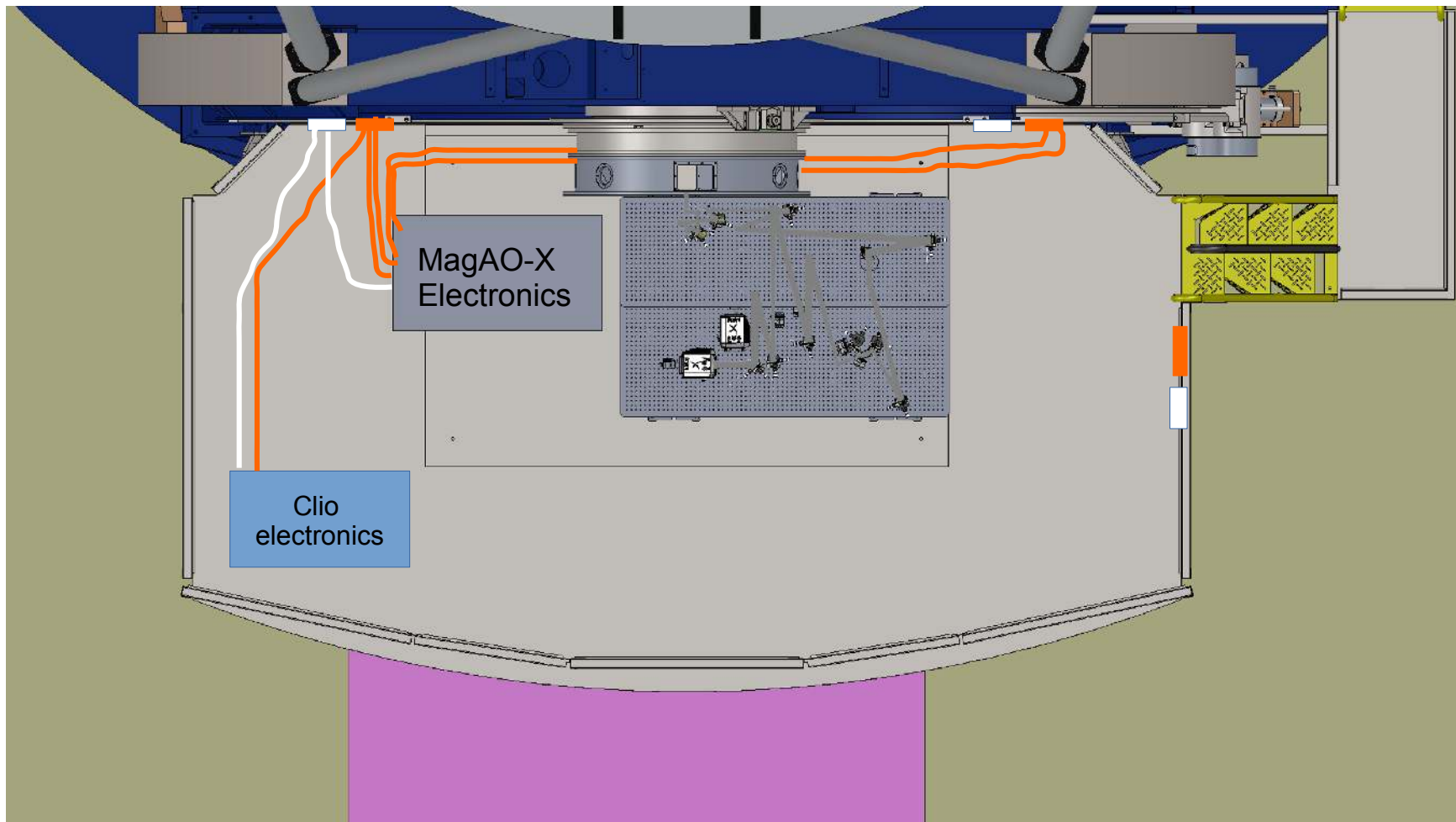


MagAO-X Needs:

- Electronics Rack: 4x 15A = on UPS
- 1x 15A on direct

Clio Electronics

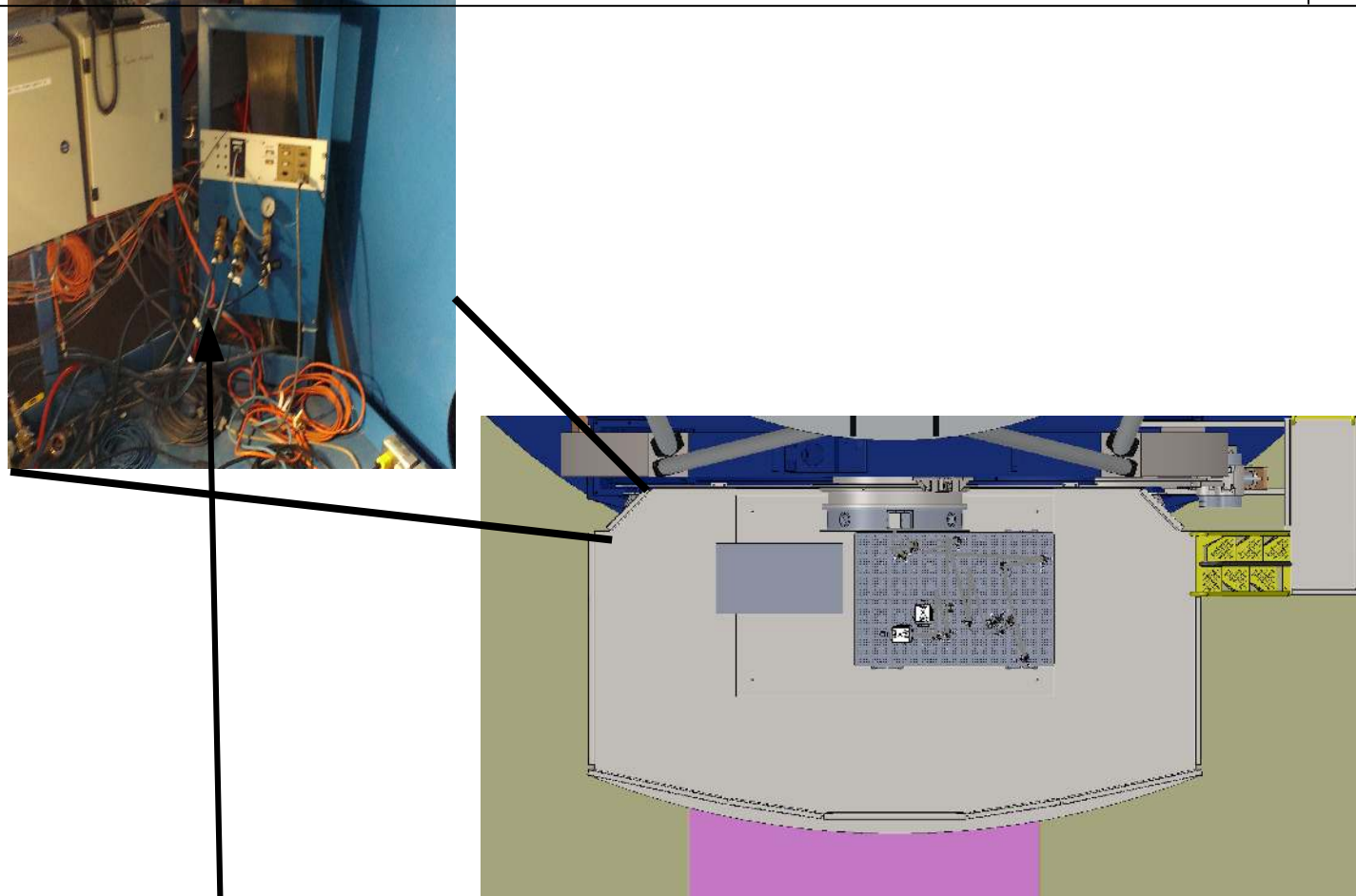
- 1x UPS
- 1x Direct



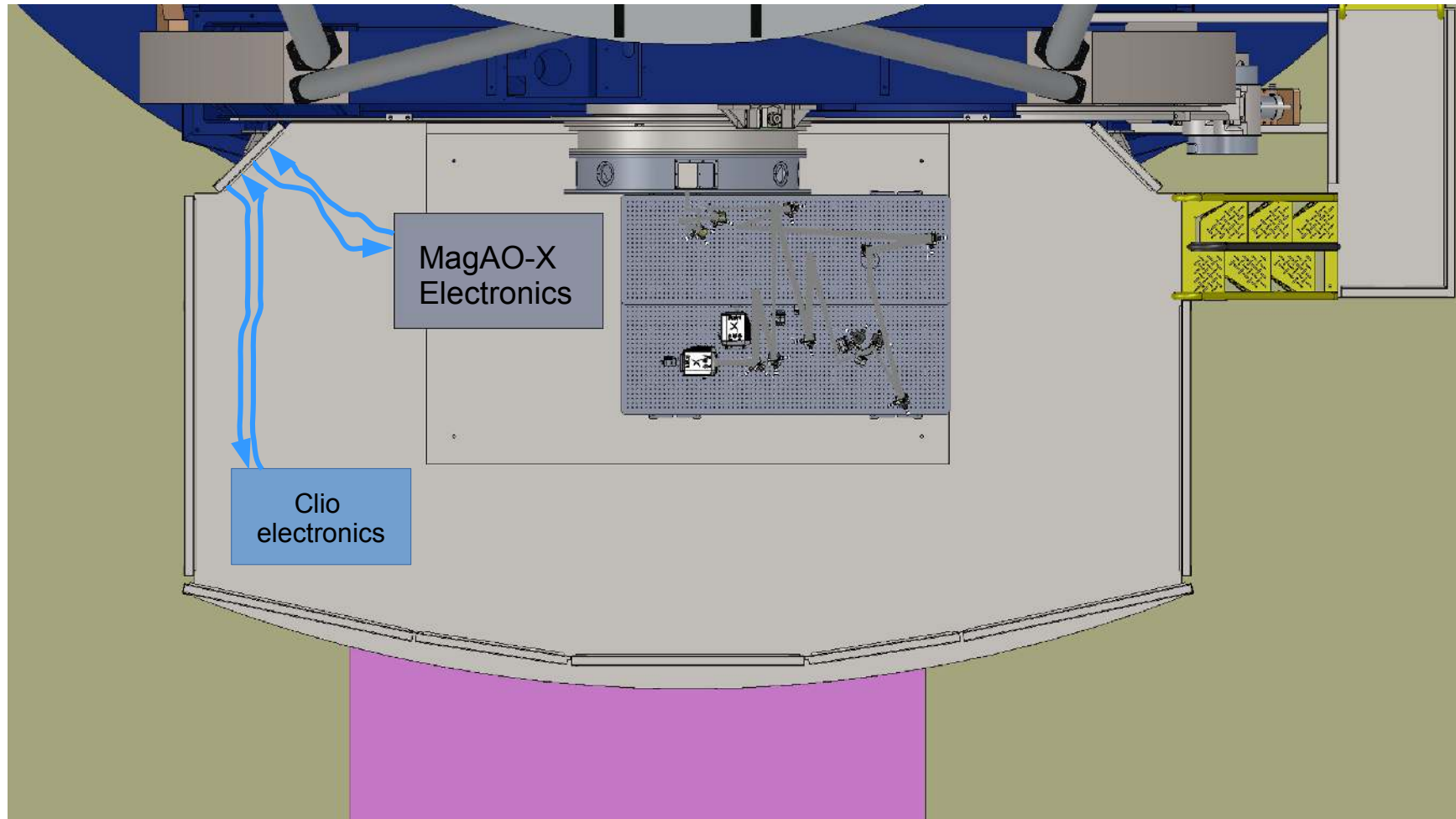


A.4 Cooling Interfaces

Jared R. Males



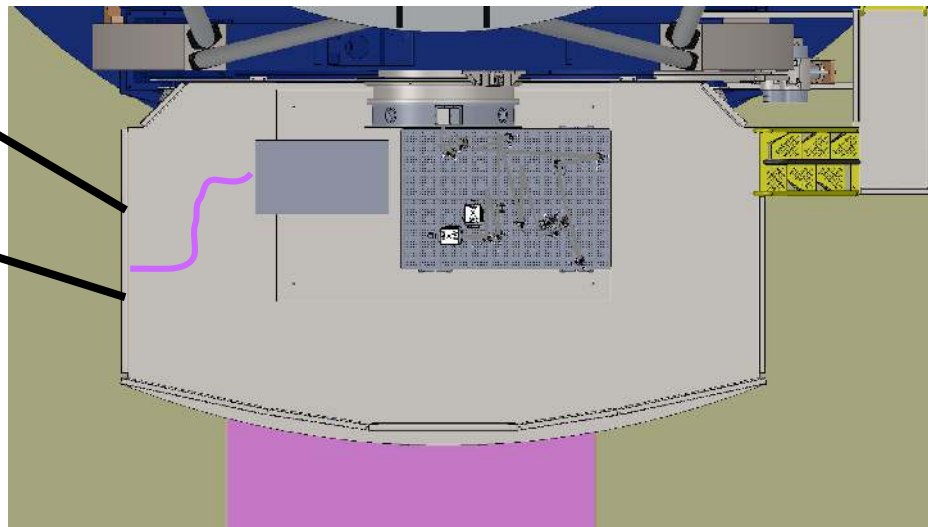
Existing facility glycol, 2x supply and 2x return



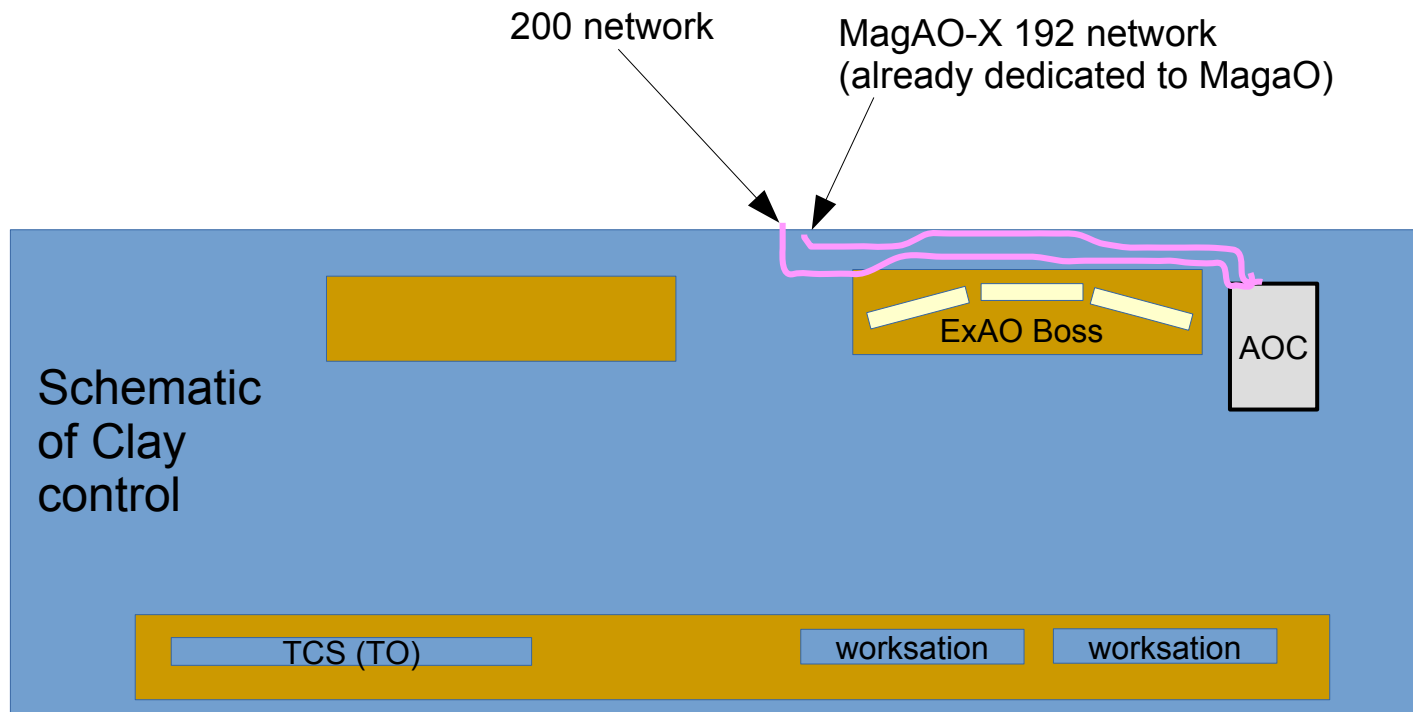


A.5 Software Interfaces

Jared R. Males



Fiber junction box with 4x pairs 10Gb/s fiber routed to equipment room.



Astronomer(s) occupy
these workstation (s),
use browser to connect
to AOC